NATIONAL AERONAUTICS AND SPACE ADMINISTRATION

Space Programs Summary No. 37-39, Volume III

for the period March 1, 1966 to April 30, 1966

The Deep Space Network

JET PROPULSION LABORATORY
CALIFORNIA INSTITUTE OF TECHNOLOGY
PASADENA, CALIFORNIA

May 31, 1966

Preface

The *Space Programs Summary* is a six-volume, bimonthly publication that documents the current project activities and supporting research and advanced development efforts conducted or managed by JPL for the NASA space exploration programs. The titles of all volumes of the *Space Programs Summary* are:

Vol. I. The Lunar Program (Confidential)

Vol. II. The Planetary–Interplanetary Program (Confidential)

Vol. III. The Deep Space Network (Unclassified)

Vol. IV. Supporting Research and Advanced Development (Unclassified)

Vol. V. Supporting Research and Advanced Development (Confidential)

Vol. VI. Space Exploration Programs and Space Sciences (Unclassified)

The *Space Programs Summary*, Vol. VI consists of an unclassified digest of appropriate material from Vols. I, II, and III; an original presentation of technical supporting activities, including engineering development of environmental-test facilities, and quality assurance and reliability; and a reprint of the space science instrumentation studies of Vols. I and II.

W. H. Pickering, *Director*
Jet Propulsion Laboratory

Space Programs Summary No. 37-39, Volume III

Prepared under Contract No. NAS 7-100, National Aeronautics & Space Administration

Contents

Contents (Cont'd)

I. Introduction

The Deep Space Network (DSN), established by the NASA Office of Tracking and Data Acquisition, is under the system management and technical direction of JPL. The DSN is responsible for two-way communications with unmanned spacecraft travelling from approximately 10,000 miles from Earth to interplanetary distances. Tracking and data-handling equipment to support these missions is provided. Present facilities permit simultaneous control of a newly launched spacecraft and a second one already in flight. In preparation for the increased number of U.S. activities in space, a capability is being developed for simultaneous control of either two newly launched spacecraft plus two in flight, or four spacecraft in flight. Advanced communications techniques are being implemented to provide the possibility of obtaining data from, and tracking spacecraft to, planets as far out in space as Jupiter.

The DSN is distinct from other NASA networks such as the Scientific Satellite Tracking and Data Acquisition Network (STADAN), which tracks Earth-orbiting scientific and communication satellites, and the Manned Space Flight Network (MSFN), which tracks the manned spacecraft of the *Gemini* and *Apollo* programs.

The DSN supports, or has supported, the following NASA space exploration projects: (1) *Ranger, Surveyor, Mariner,* and *Voyager* Projects of JPL; (2) *Lunar Orbiter* Project of the Langley Research Center; (3) *Pioneer* Project of the Ames Research Center, and (4) *Apollo* Project of the Manned Spacecraft Center (as backup to the Manned Space Flight Network). The main elements of the network are: the Deep Space Instrumentation Facility (DSIF), with space communications and tracking stations located around the world; the Ground Communications System (GCS), which provides communications between all elements of the DSN; and the JPL Space Flight Operations Facility (SFOF), the command and control center.

The DSIF tracking stations are situated such that three stations may be selected approximately 120 deg apart in longitude in order that a spacecraft in or near the ecliptic

plane is always within the field of view of at least one of the selected ground antennas. The DSIF stations are:

Station No.	*Name*	*Location*
11	Goldstone, Pioneer	Barstow, California
12	Goldstone, Echo	Barstow, California
13	Goldstone, Venus (research and development)	Barstow, California
14	Goldstone, Mars (under construction)	Barstow, California
41	Woomera	Island Lagoon, Australia
42	Tidbinbilla	Canberra, Australia
51	Johannesburg	Johannesburg, South Africa
61	Robledo	Madrid, Spain
62	Cebreros (under construction)	Madrid, Spain
71	Spacecraft Monitoring	Cape Kennedy, Florida
72	Spacecraft Guidance and Command (under construction)	Ascension Island

JPL operates the U.S. stations, and will operate the Ascension Island Station. The overseas stations are normally staffed and operated by government agencies of the respective countries, with the assistance of U.S. support personnel.

The Spacecraft Monitoring Station supports spacecraft final checkout prior to launch, verifies compatibility between the DSN and the flight spacecraft, measures spacecraft frequencies during countdown, and provides telemetry reception from lift-off to local horizon. The other DSIF stations obtain angular position, velocity (doppler), and distance (range) data for the spacecraft, and provide command control to (up-link), and data reception from (down-link), the spacecraft. Large antennas, low noise phase-lock receiving systems, and high-power transmitters are utilized. The 85-ft diameter antennas have gains of 53 db at 2300 Mc, with a system temperature of 55°K, making possible the receipt of significant data rates at distances as far as the planet Mars. To improve the data rate and distance capability, a 210-ft diameter antenna is under construction at the Goldstone Mars Station, and two additional antennas of this size are planned for installation at overseas stations.

In their present configuration, all stations with the exception of Johannesburg, are full S-band stations. The Johannesburg receiver has the capability for L- to S-band conversion. The Spacecraft Guidance and Command Station will be basically full S-band when it becomes operational.

It is the policy of the DSN to continuously conduct research and development of new components and systems and to engineer them into the network to maintain a state-of-the-art capability. Therefore, the Goldstone stations are also used for extensive investigation of space tracking and telecommunications techniques, establishment of DSIF/spacecraft compatibility, and development of new DSIF hardware and software. New DSIF-system equipment is installed and tested at the Goldstone facilities before being accepted for system-wide integration into the DSIF. After acceptance for general use, it is classed as Goldstone Duplicate Standard (GSDS) equipment, thus standardizing the design and operation of identical items throughout the system.

The GCS consists of voice, teletype, and high-speed data circuits provided by the NASA World-Wide Communications Network between each overseas station, the Spacecraft Monitoring Station, and the SFOF. Voice, teletype, high-speed data, and video circuits between the SFOF and the Goldstone stations are provided by a DSN microwave link. The NASA Communications Network is a global network consisting of more than 100,000 route mi and 450,000 circuit mi, interconnecting 89 stations of which 34 are overseas in 18 foreign countries. It is entirely operationally oriented and comprises those circuits, terminals, and switching equipments interconnecting tracking and data acquisition stations with, for example, mission control, project control, and computing centers. Circuits used exclusively for administrative purposes are not included.

During the support of a spacecraft, the entire DSN operation is controlled by the SFOF. All spacecraft command, data processing, and data analysis can be accomplished within this facility. The SFOF, located in a three-story building at JPL, utilizes operations control consoles, status and operations displays, computers, and data-processing equipment for the analysis of spacecraft performance and space science experiments, and communication facilities to control space flight operations. This control is accomplished by generating trajectories and orbits, and command and control data, from tracking and telemetry data received from the DSIF in near-real time. The SFOF also reduces the telemetry, tracking, command, and station performance data recorded by the DSIF into engineering and scientific information for analysis and use by scientific experimenters and spacecraft engineers.

II. DSN Systems Design

A. The NASCOM Teletype Message Switching System

J. Walker

The Deep Space Network Ground Communications System (DSN/GCS) as previously discussed is a large, complex array of equipment and facilities which are intended to perform many functions. It consists, in part, of a particular configuration of the NASA Communications Network (NASCOM). In general, NASCOM furnishes the DSN/GCS with communications channels between the Space Flight Operations Facility (SFOF) at Pasadena, and various world-wide DSN Deep Space Stations (DSS). NASCOM has added to its existing number of communications services an automated message switching network. Due to the magnitude of communications service provided by NASCOM, it is essential to have an understanding of its capabilities.

Until now, the DSN has requested that NASCOM provide a number of discrete circuits between each DSS and the SFOF. However, NASCOM services many users in addition to the DSN. These include the various tracking stations which support the Manned Space Network (MSN) and the Satellite Tracking and Data Acquisition Network (STADAN). Consequently, providing discrete circuits between its many users has become costly.

For example, a single teletype circuit between the SFOF and Australia costs about $400,000 per year to rent from the carriers. The obvious solution to the cost problem would be to allow the various users to share a smaller number of common circuits. However, particularly during orbital missions, the problem associated with switching these circuits among the various stations becomes complex. For this reason, it was decided that manual switching of the various teletype circuits would not provide levels of circuit reliability suitable for mission support.

In order to reduce over-all communications costs and to increase reliability, NASCOM has developed an automated message switching network which allows its many users to share common communications teletype channels. The NASCOM TTY Message Switching System utilizes communications-oriented computers, or Communications Processors (CP) to provide these automated switching functions.

The CP system might be likened to the commercial dial telephone system in that the following similarities exist:

(1) The NASCOM System consists of a number of central switching centers, each of which services

its various simultaneous users. The NASCOM switching centers are located at London, England; Canberra, Australia; Honolulu, Hawaii; and Greenbelt, Maryland. This concept is illustrated by Fig. 1.

(2) The process of sending a message from one place to another requires a teletype header, or address, similar to a telephone number. In both cases, this action serves to establish a connection between the sender and the receiver.

(3) When the message is completed, a sequence of teletype characters is required to terminate the call. This function is similar to hanging up the telephone, thereby disconnecting the sender and receiver and releasing the circuit for use by someone else.

Thus, the system can service numerous users, and by using circuits on a message basis, cut total circuit quantities. The usage of CP provides this function automatically. The cost of the CP is amortized in a short time due to the decrease in number of rental circuits.

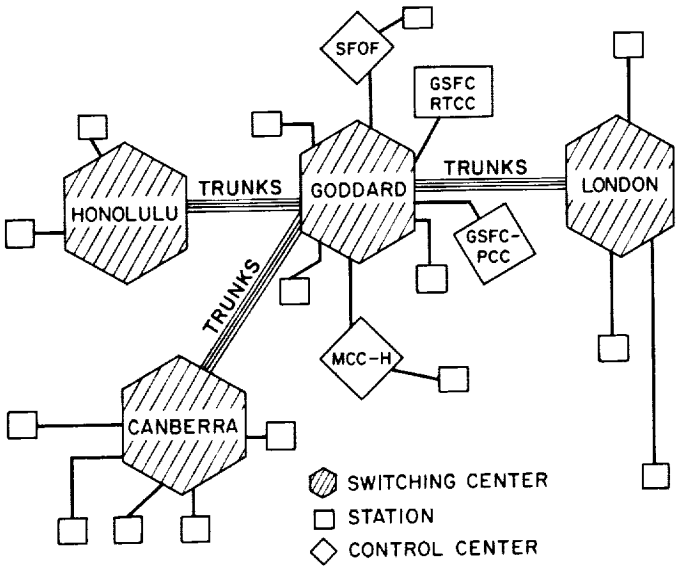

NOTES:
1. COMMUNICATIONS PROCESSOR LOCATED AT EACH SWITCHING CENTER
2. ALL TRAFFIC TWO WAY; i.e. FULL DUPLEX TRUNKS

Fig. 1. Basic star network configuration

B. An Application of the Model: Error Transmission

D. C. Card

A matter of primary concern to the user of a data-transmission system is the propagation of error in the functions which he is attempting to measure. Given here is a simplified idealization of the DSN Communications System model (see SPS 37-37, Vol. III, pp. 3–5) which is presented as an example of the use of the model.

Consider a system which handles digital data throughout; however, the input data are quantized samples of analog measurements. The user wishes to represent the measured function as faithfully as possible. Assume that the sampled function is bandwidth-limited such that, ideally, it could be reconstructed from the analog samples.

Assume that the sampled function is represented by n intervals, and that

a = magnitude in signal units (e.g., volts) of one interval

A = peak-to-peak amplitude of total signal deviation

thus, $a = A/n$.

For equal intervals, it is well-known that the mean-squared quantization noise, N_q, in signal units, has the form

$$N_q = a^2/12 . \tag{1}$$

In numerical units, for an N-bit binary word, the fractional quantization interval is $1/2^N$. The normalized rms quantization error becomes

$$\varepsilon_{q\,\mathrm{num}} = \frac{1}{2\,(3)^{1/2}} \cdot \frac{1}{2^N} = \frac{1}{2^{N+1}\,(3)^{1/2}} . \tag{2}$$

The function of the final stages of the receiver elements is to make a binary decision, at the appropriate times, upon the message stream, which is presented. If it is assumed that the decision-level, in amplitude say, is $A/2$, where A is the peak signal amplitude. It can be shown that the probability of making an error on each decision is

$$p = \frac{1}{2}\left(1 - \mathrm{erf}\,\frac{A}{2\sigma\,(2)^{1/2}}\right), \tag{3}$$

where σ is rms noise power (in signal units).

The relative weight of the nth bit in an N-bit word, compared to full-scale, is $2^n/2^{N-1}$, where $0 \leq n \leq N-1$. If it is assumed that the occurrences of errors are independent events, with the binary error probability P_b determined by S/N conditions, the mean-squared error due to single bit errors in a word is (relative to full scale)

$$\overline{e^2} = \frac{P_b}{2^{2(N-1)}} \sum_{n=0}^{N-1} 2^{2n} = \frac{4P_b(v_q^2 - 1)}{3v_q^2}, \tag{4}$$

where $v_q = 2^N$, the number of quantizing increments.

The relation between S/N and bit error is found, using the mean-squared message power, $\overline{m^2(t)}$, relative to full scale:

$$(S/N)_b = \frac{\overline{3m^2(t)}\, v_q^2}{4P_b(v_q^2 - 1)}. \tag{5}$$

Since quantizing noise and digital transmission errors are independent, the over-all message/noise ratio for binary PCM systems is

$$(S/N)_{PCM} = \frac{\overline{m^2(t)}}{N_q + \overline{e^2}} = \frac{\overline{3m^2(t)}\, v_q^2}{4P_b(v_q^2 - 1) + 1}. \tag{6}$$

If the digital system includes L regenerative digital links, then it is known that the total probability of bit error is given by

$$P_{bL} = \frac{1}{2}[1 - (1 - 2P_b)^L] \tag{7}$$

– and for $P_b << 1/2$. (P_b is the bit error probability of each link) we have

$$P_{bL} \simeq LP_b. \tag{8}$$

Because of the complicated relationships for performance of receivers near threshold, we will not develop the formulas here, but only assume values of the parameters as presented to the discriminator.

Let the binary representation be N-bit words, and $v_q = 2^N$; let p at the receiver (in principle, from Eq. (3)) be $p \equiv P_b = 10^{-4}$. Assume $\overline{m^2(t)} = 1/4$. Assume that there are three regenerative links between the discriminator and the receiver, each with $P_b = 10^{-4}$. Since $v_q^2 - 1 \simeq v_q^2$, we find

$$\overline{e^2}_{\text{system}} = \frac{4(4 \times 10^{-4})}{3} \simeq 5.3 \times 10^{-4};$$

thus, the rms *relative* analog equivalent error is

$$e \simeq 2.3 \times 10^{-2}$$

The analog equivalent system message-to-noise ratio is found to be

$$(S/N)_{\text{system}} = \frac{(0.25)}{N_q + (5.3 \times 10^{-4})} \simeq 10^2$$

where $N_q = 1/(3v_q^2) \simeq 19.7 \times 10^{-4}$. This calculation represents the relevant noise parameters on data which is "out-put" to the user without noise. Further developments will include both refinements of this model and the propagation of error through a noisy computation link.

C. Deep Space RFI Study

R. B. Hartley

A detailed study of radio frequency interference (RFI) within the DSN has been initiated. Limited available frequency allocations and increased spacecraft activity, especially broad-band television and ranging signals, necessitate our learning more about the mechanism of interference.

The study is to be undertaken in two parts. The first part, a study of the *Surveyor* Project, its telecommunications requirements, and interference considerations, will serve to identify and develop the tools necessary to deal with problems of RFI. The second part will be devoted to a generalization of these results in the form of an "RFI Manuel" which can be applied to other spacecraft projects.

The study will include the characteristics of various spacecraft communication systems, their tendency to create interference, and their susceptibility to interference. Also to be considered are various DSIF subsystems and their relationship to RFI. The RFI Manual will describe useful methods for insuring interference-free communications.

III. Tracking and Navigational Accuracy Analysis

A. DSN Inherent Accuracy Project

T. W. Hamilton

The DSN Inherent Accuracy Project was formally established by the DSN Executive Committee in July, 1965. Its goals are:

(1) To determine (and verify) the inherent accuracy of the DSN as a radio navigation instrument for lunar and planetary missions.

(2) To formulate designs and plans for refining this accuracy to its practical limits.

Meeting of these goals is a cooperative job of two JPL Divisions: Telecommunications (33) and Systems (31). To accomplish these goals, the Project holds regular monthly meetings to coordinate and to initiate activities that are relevant. The Project Leader and his Assistant are authorized to task Project members to conduct analyses of proposed experiments, prepare reports on current work, and write descriptions of proposed experiments. Further, the Project is authorized to deal directly with flight projects utilizing the DSN regarding data gathering procedures which bear on inherent accuracy.

The Project Leader and his Assistant are from Divisions 33 and 31, respectively, and report to the DSN Executive Committee.

Most of the technical work directly related to the Inherent Accuracy Project will be reported in the following five *SPS* sections: III-B, C, D, E, and F.

B. DSIF Data Types and Tracking Modes

D. W. Trask

In support of lunar and planetary missions, the DSIF network provides angle data (local hour angle and local declination), as illustrated in Fig. 1, and S-band (2300

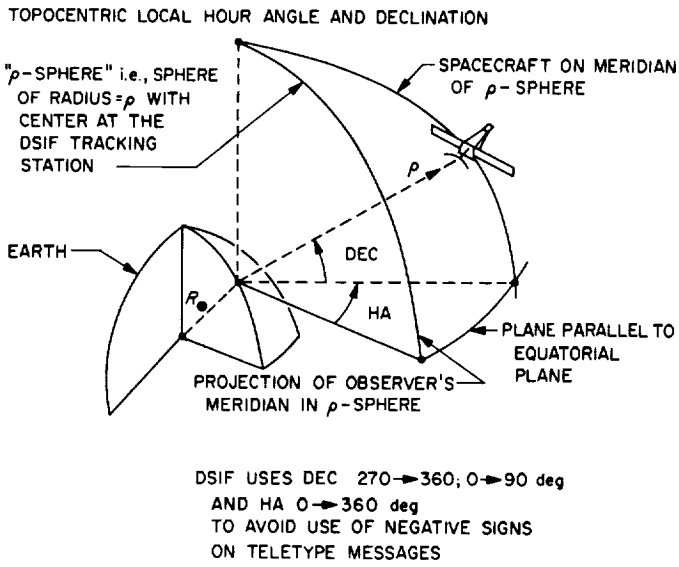

Fig. 1. Topocentric angle data provided by DSIF station

MHz) doppler. The angle data are valuable during the early portion of the flight when the trajectory geometry is varying rapidly. However, after the first few hours, the information gained by the continued use of the angle data is overshadowed by that provided by two-way doppler. The two-way doppler is a measure of the radio velocity (V_R) of the spacecraft relative to the tracking station.

A simplified two-way doppler configuration is depicted in Fig. 2. The tracking station transmits the signal to the spacecraft; the signal received at the spacecraft is shifted in frequency by the well known doppler effect; the spacecraft then retransmits the received signal. The signal received at the ground receiver has been further doppler-shifted by the radial velocity of the receiver with respect to the spacecraft. The difference between the received frequency and the current transmitter frequency is called the doppler tone.

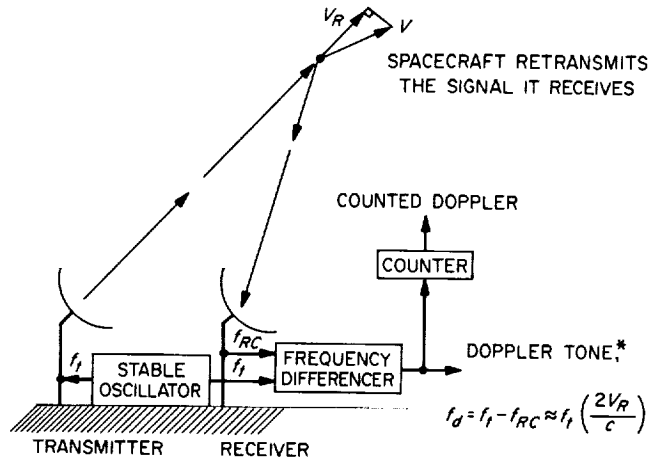

*THE DOPPLER TONE f_d IS A MEASURE OF THE RADIAL SPEED V_R

Fig. 2. Two-way doppler data provided by DSIF station

In practice, the doppler tone is continuously counted, and this continuous count is sampled at rates from one per second to one per minute. The one-sample per minute mode is utilized during most of the flight, while the higher sample rates are used during injection, during lunar or planetary encounter, and during spacecraft maneuvers. These continuous-count samples of doppler tone are differenced to obtain a data type known as counted two-way doppler which is actually the range difference that occurred during a sample interval. These relatively high sample rates are utilized for data monitoring purposes, i.e., to catch blunder points and to uncover unusual data noise characteristics. In actual practice during the orbit determination process, the range differences are currently being utilized over 10-min intervals; in the future, they will be used over intervals of 10^4 sec and higher. By combining these doppler measurements taken over a specified interval of time at several stations, the spacecraft orbit is reconstructed and its future course can be accurately predicted.

The DSIF network is capable of taking other doppler types, as illustrated in Fig. 3. In general, the qualities of the f_1 and f_3 types are not competitive with the f_2; however the f_1 data can be valuable in certain situations where the probe accelerations are high. The equations and associated block diagrams for these S-band doppler types were delineated by F. Borncamp in *SPS 37-27*, Vol. III, pp. 25–31.

C. Timing: DSIF Two-Way Doppler Inherent Accuracy Limitations

D. W. Trask and P. M. Muller

1. Introduction

This is the second in a series of articles on the accuracy limitations inherent to the DSIF data type that is referred to as two-way doppler. In practice, the doppler is

TYPES

a. ONE-WAY DOPPLER (f_1):
SPACECRAFT (S/C) TRANSMITS TO THE DSIF STATION WHICH OPERATES ONLY IN THE RECEIVE MODE.

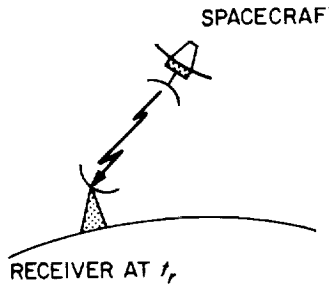

b. COHERENT THREE-WAY DOPPLER (f_{c3}):
$f_r(f_r)$ AND $f_x(f_x)$ ARE COHERENTLY DIFFERENCED AT THE RECEIVING STATION; THIS CONFIGURATION WAS USED DURING THE *Mo II* (VENUS) MISSION BY UTILIZING THE MICROWAVE LINK BETWEEN TWO OF THE GOLDSTONE STATIONS; i.e., DSIF 12 TRANSMITTED, AND DSIF 11 RECEIVED; THE S/C TRANSPONDER RECEIVES THE INCOMING SIGNAL, MULTIPLIES IT BY 240/221, AND RETRANSMITS IT TO THE GROUND STATION FOR f_{C3}, f_2, AND f_3.

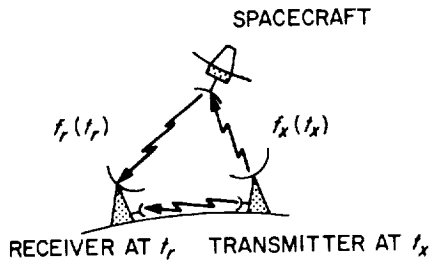

RECEIVER AND TRANSMITTER ARE DIFFERENT STATIONS

c. TWO-WAY DOPPLER (f_2):
A SPECIAL CASE OF COHERENT THREE-WAY DOPPLER, WHERE THE SAME DSIF STATION IS THE TRANSMITTING AND RECEIVING STATION.

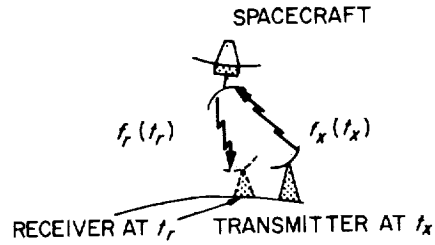

RECEIVER AND TRANSMITTER ARE THE SAME STATIONS

d. THREE-WAY DOPPLER (f_3):
NORMALLY THE TRANSMITTING AND RECEIVING STATIONS ARE LOCATED ON DIFFERENT CONTINENTS, AND NO MICROWAVE LINK IS AVAILABLE TO ALLOW THE COHERENT DIFFERENCING OF $f_r(f_r)$ AND $f_x(f_x)$.

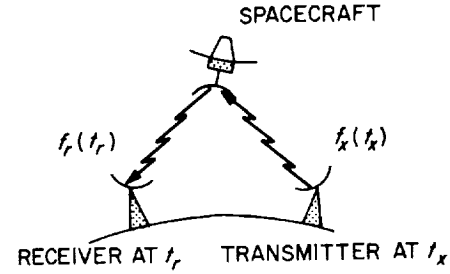

RECEIVER AND TRANSMITTER ARE DIFFERENT STATIONS

Fig. 3. Types of doppler data provided by DSIF network

continuously counted and sampled at fixed intervals. The observable that is then used by the Orbit Determination Program is the range difference between the observer and the spacecraft which is accumulated over a fixed count interval. Although the accuracy of this data type has consistently exceeded the quality necessary for the successful fulfillment of the current Earth-based radio guidance role to which the DSIF has been committed, an effort is continually in progress to improve the quality of this data so that expected needs of future missions may be met. This article discusses some of the timing aspects of this effort.

Time is usually considered to be the uniform independent argument for all orbit determination work. Ultimately, frequency stability, relative station-timing, ephemeris sources, and several other considerations become related. There is considerable interest in all of these problems at NASA and JPL. The ultimate goal is to determine the inherent limitations to the doppler and range measurements and to achieve the best practical balance of errors.

2. Time Systems and Agencies; Definitions

(1) *B.I.H.*—The International Bureau of Time (Bureau International de l'Heure) in Paris, France, which is the coordinating agency for time transmissions and related matters. The results of research are published in the *Bulletin Horaire.*

(2) *UT1.*—The true instantaneous Universal Time, which is the rotational position of the Earth. It is *derived* directly from the Sidereal Time observed at various observatories; being determined by accurate measurement of star transits. The equations relating Sidereal Time may be found in Ref. 1 or in the article by Moyer later in this *SPS*. *UT*1 is not a uniform time-scale because the Earth is generally slowing down.

(3) *UT0 (UT Zero).*—The Universal Time which is observed by a station directly, using the instantaneous pole of rotation, and no special corrections or derivations.

(4) *UT2.*—This is obtained by subtracting the predicted seasonal variations out of *UT*1. The result is a more uniform time scale. The *B.I.H.* decides upon the correction to be applied. *UT*2 is also defined to be Greenwich Civil Time.

(5) *A.1, NBS(A), or AT.*—Atomic Time in the United States is defined to have a second of length 9,192,631,770 ±20 cyc of the U.S. Frequency Standard in Boulder Colorado, a Cesium Resonator. The initial epoch of Atomic Time was 0 hours 1 January 1958 Greenwich Civil Time (*UT*2). At that moment $AT = UT2$. The length of the Atomic Second was chosen to equal the best estimate of the Ephemeris Second (as determined prior to 1958). This is a uniform time-scale.

(6) *ET.*—Ephemeris Time is theoretically defined in terms of the Solar Ephemeris. The Moon is more accurately observed, and it is tied to the Sun by gravitational theory. The working definition considers *ET* to be the time-argument which one must put into the Improved Brown Lunar Theory, so that an observation of the Moon shall agree with the theory. The time obtained is the Ephemeris Time of the observation. Currently, *ET* is some 36 sec ahead of Universal Time. *ET* may or may not be a uniform-time in reality, but it is presently assumed to be so.

(7) *UTC.*—Universal Time Coordinated is a uniform time derived by fixed-frequency-ratio offset from Atomic Time. Its rate is purposely set to agree as closely with *UT*2 as may be predicted. This is the time scale which virtually all radio-time signals follow. See the article by Moyer in this *SPS* (under *UTC*) and Table 1 of this article for the equations between *A*.1 and *UTC* as well as other information. The offset is predicted in advance, goes into effect on the first of the year, and is much publicized by the *B.I.H.* and other agencies. In addition to offset

Table 1. WWV Events 1962.0 to present

Date	Event
1 Jan 62	$S = +130 \times 10^{-10}$
1 Nov 63	*T* retarded 100 ms
1 Jan 64	$S = +150 \times 10^{-10}$
1 April 64	*T* retarded 100 ms
1 Sept 64	*T* retarded 100 ms
1 Jan 65	*T* retarded 100 ms
1 Mar 65	*T* retarded 100 ms
1 July 65	*T* retarded 100 ms
1 Sept 65	*T* retarded 100 ms
1 Jan 66	$S = +300 \times 10^{-10}$

S = Slope-offset of WWV from A.1 — T = WWV clock time (UTC)
$F_{WWV} = F_{Cesium} \cdot (1 - S)$ — F = frequency
1 sec Atomic Time = 9,192,631,770 ± 20 cyc of cesium frequency
1 second of UTC = 9,192,631,770 cyc of Offset Clock.

frequency, *UTC* will usually undergo periodic step-adjustments. If the error (*UTC-UT2*) grows larger than about 0.1 sec, the *B.I.H.* will announce a step-adjustment for the first day of a given month. At that time, all coordinated time signals will be advanced or retarded by the stated amount (usually 0.100 sec). An effort is made to keep *UTC* within 0.100 sec of *UT2*. The appearance of *UTC* with respect to Atomic Time may be found plotted in Fig. 4. A listing of *UTC* events as tabulated by the U.S. Naval Observatory and radio station *WWV* comprises Table 1. The relationship between *UTC* and *UT1* is plotted on Figs. 5 and 6.

(8) ***U.S.N.O.***—United States Naval Observatory. This is the U.S. agency for observing Star Transits, determining Sidereal and Universal Time, and publishing the necessary documents to make this information available and understandable. Weekly bulletins are published, covering all of the above time scales and giving current values. They also have a large series of reprints of Journal articles covering the above points, and many others, in detail. Dr. Markowitz is the present director of the Time Service, and his associates are Dr. Lidback and Dr. Hall. Their assistance has made it possible for us to understand the statements made in this article. Credits are also given in Ref. 2, together with a partial listing of the available reprints.

(9) ***WWV, WWVH, NBA,...*** Call letters of radio stations broadcasting *UTC* on carrier frequencies mainly between 5 and 20 MHz.

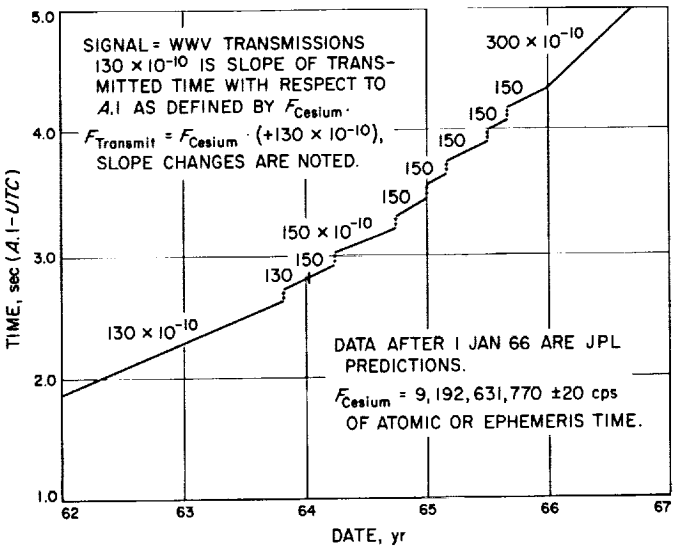

Fig. 4. Plot of A.1-signal (UTC)

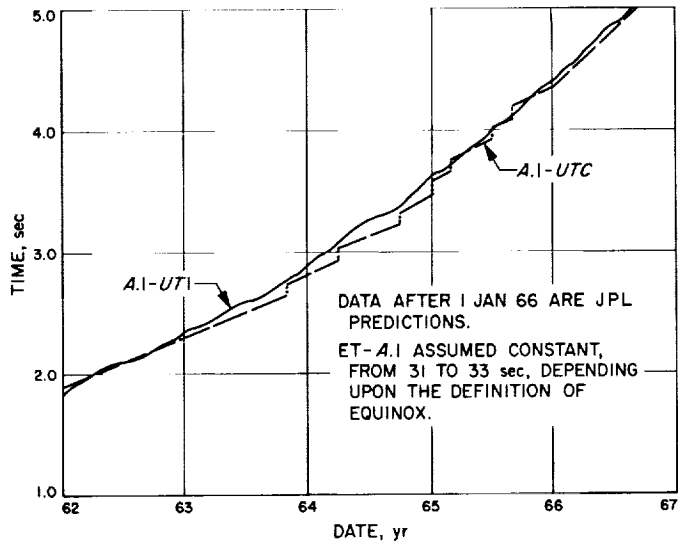

Fig. 5. Plot of A.1-UTC and (UT1)

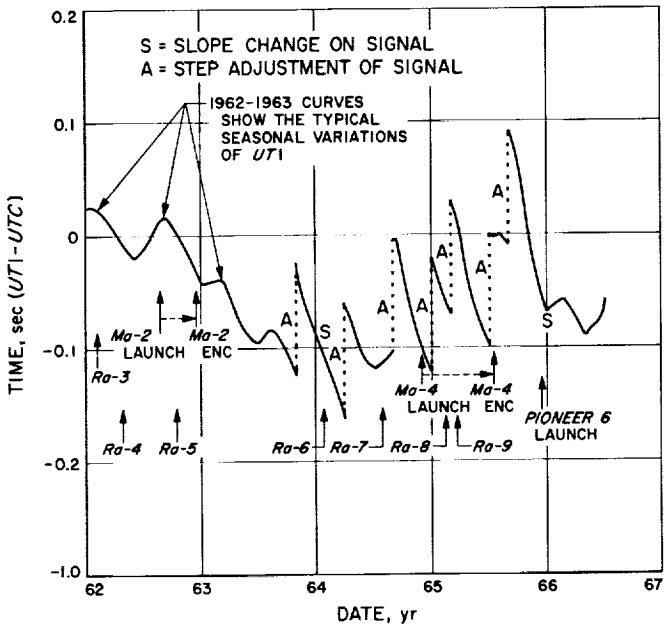

Fig. 6. Plot of UT1-signal (UTC)

(10) ***WWVB, WWVL,...*** The call letters of stations broadcasting *UTC* or *A.1* on Very Low Frequencies (VLF) between 15 and 60 kHz. The primary purpose of these transmissions is to research the feasibility of making a single time service available world-wide. The achievement of this goal will allow microsecond timing and synchronization of distant clocks. For further information, see Ref. 3.

3. Timing Used in the Orbit Determination Process

Three types of time are used when computing an orbit; namely, Ephemeris Time (*ET*, used to look up positions of the celestial bodies), Universal Time (*UT*, used to determine the location of a tracking station in space), and Station Time (t_s, the time tag that is associated with the actual tracking data). The behavior of these times with respect to a uniform time is heuristically illustrated in Fig. 7, where the abscissa is a uniform time defined for purposes of this discussion as *A*.1 (Atomic Time), and the ordinate represents units in one of the above three time systems.

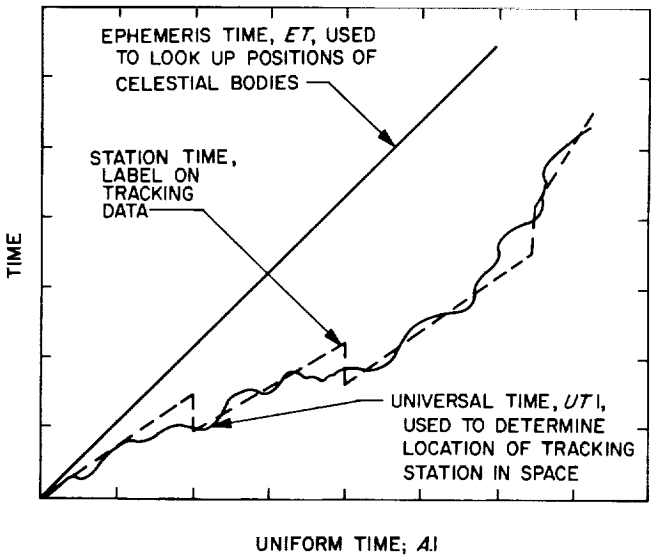

Fig. 7. Relationship of time systems in the orbit determination process

Any uniform time (the second is invariant in length) will appear in Fig. 7 as a straight line, as in the case of Ephemeris Time. It is assumed in the JPL Double Precision Orbit Determination Program (DPODP) that the time which is used as the independent argument when integrating the equations of motion is a uniform time and identical to *ET*. It is further assumed in the Single Precision Orbit Determination Program (SPODP) that *A*.1 = *ET* = constant. Universal time (*UT*1) on the other hand is a non-uniform time. It represents the instantaneous angular position of the Earth in space and as such is affected by tidal action and other forces which cause anomalies in the Earth's rotational rate (Ref. 4). The DSIF tracking stations synchronize their clocks to the time broadcast by the various time-standard stations, often referred to as WWV time or more appropriately *UTC*. *UTC* is uniform over defined time intervals. It represents an approximation to another type of universal time, i.e., *UT*2. The length of the second (slope of the line in Fig. 7) used by *UTC* is determined from the predicted behavior of *UT*2, and in general the *UTC* second will not be identical to the ephemeris second. As seen above, it is necessary to introduce discontinuities in *UTC* time periodically. This happened three times during the *Mariner IV* mission between launch and planet encounter. A history of these discontinuities and slope changes is presented in Table 1.

Most users receive the time-scale *UTC* (offset and stepped by international agreement). This time is not equal to either *ET* or *UT*1 which the orbit determiner requires. For the extremely tight requirements imposed by processing Earth-based radio data, the user must consider conversion between the various scales at his disposal so as to obtain the best values of *ET* and *UT*1. These considerations are surprisingly important.

Ephemeris time, which we know to within about 1 second absolute and perhaps 0.1 seconds change per year, can cause errors in orbit determination (OD). If the *ET* is wrong, all bodies in the solar system are looked up at the wrong time, and their positions are wrong. For a long planetary mission, the accumulated errors due to incorrect ephemerides will perturb the orbit in complex ways as well as add a planet-miss error due to the target ephemeris error. These questions are under study at the present time.

4. Effects of Timing Errors*

a. Uncertainties in UT1 − t_s. The lack of precise knowledge of the relationships among the three times illustrated in Fig. 7 can result in a degradation in the apparent quality of the tracking data, incorrect solutions for the tracking station locations, and an erroneous prediction of the spacecraft coordinates near planetary or lunar encounter. The latter two effects are related in the case of an error between t_s and *UT*1. Two limiting cases are illustrated in Fig. 8 for a spacecraft tracked by a single station. In both instances, the orbit determination process is not aware of any error in the timing relationships.

For Case 1, the orbit determination process assumes the tracking station location is known perfectly and

*The authors wish to express their appreciation to Mr. T. W. Hamilton for the many helpful discussions on the topics included in this section.

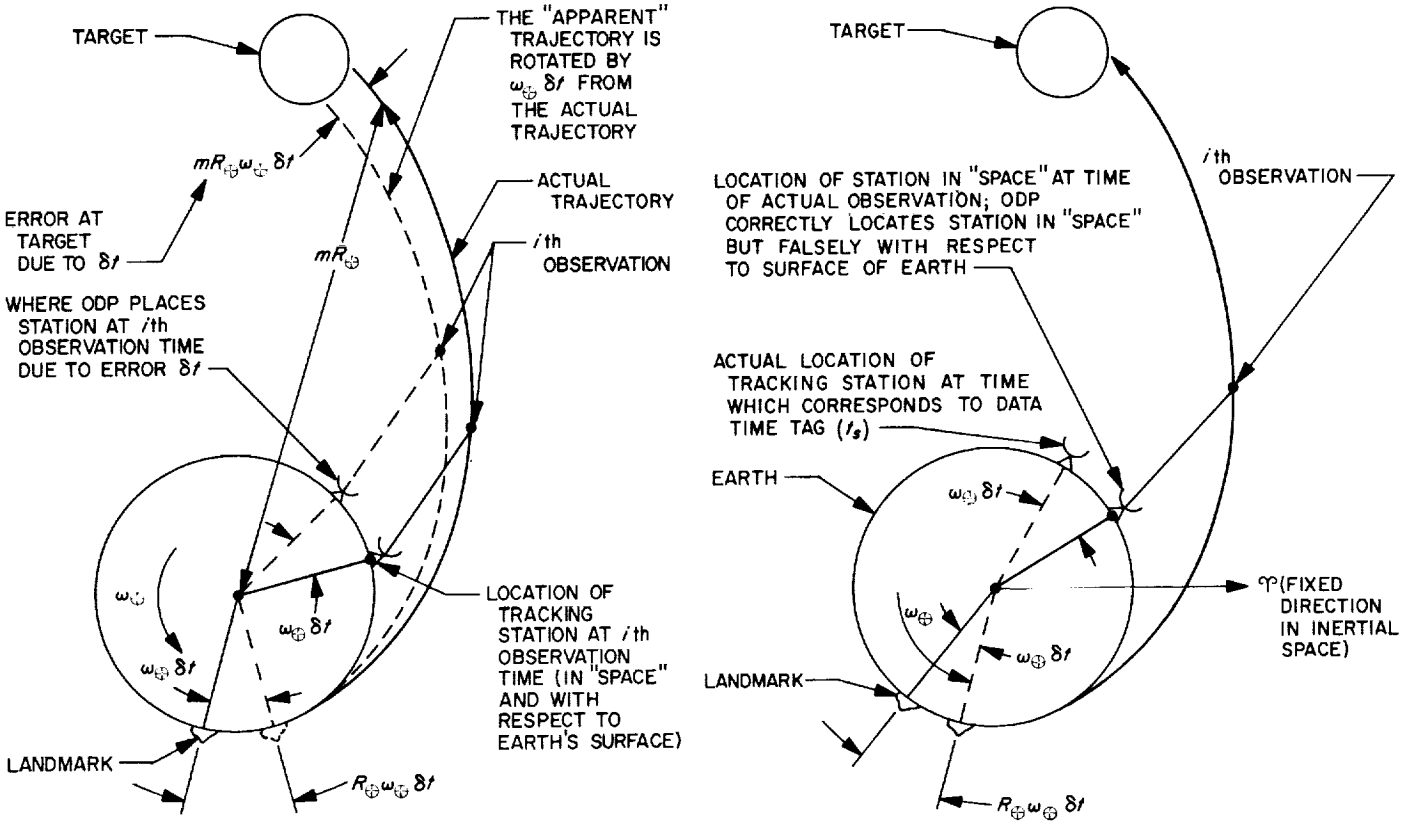

Fig. 8. Effect of an error (Δt_s) in $UT1$-t_s

determines the orbit. This will cause the spacecraft trajectory to rotate in space such that for a lunar mission the coordinates near encounter will be in error by 25 km for each second of error in $UT1$-t_s. Midcourse maneuver preparations during a mission represent an example of this situation where only near-Earth tracking data is available to determine the orbit and predict the trajectory near the target body.

If on the other hand it is assumed as in Case 2 that the orbit is perfectly known while solving for the longitude of the tracking station, the DSIF station will shift 400 meters in longitude for each second of time error in the quantity $UT1$-t_s. This situation is approximated during the cruise phase of a planetary mission after the spacecraft orbit has been "defined in space" due to the influence of the Sun or similarily in a lunar flight as the spacecraft approaches the Moon.

The above discussion does not differentiate between an error in $UT1$ or in t_s with respect to an "absolute reference time." In the case of an orbit program, this reference time is ET (or $A.1$). When processing data, the ODP is basically dependent on the station tags. That is, the $UT1$ and ET corresponding to the time tag is associated with the data point. Therefore, an error in t_s-$A.1$ (or ideally t_s-ET) differs from an $UT1$-$A.1$ error in that the former causes a "shift" in the ephemeris bodies at the time the OD program believes the data point to be taken. However, this effect is of secondary importance for the examples considered in this section.

The quantity $UT1$-$A.1$ is determined by the U.S. Naval Observatory (USNO) time service from nightly observations of star transits (Ref. 2). These results (good to 3 msec, 1σ) are averaged and published weekly in the USNO Bulletin (Ref. 2). Final times covering 1-yr intervals (good to from 1 to 2 msec, 1σ) are published roughly a year after the interval. JPL uses the USNO data and typically predicts the $UT1$-$A.1$ behavior from 2 weeks to 1 month in advance when supporting a lunar or planetary mission. The estimated uncertainty on $UT1$-$A.1$ from these sources is shown in Table 2. Although relatively little is known about the exact behavior of $UT1$-$A.1$ to the sub-msec level (5 msec is a typical uncertainty for a night's observation), the correlation widths associated with the errors quoted in Table 2 are probably on the order of weeks and longer.

Table 2. $UT1-A.1$ uncertainties

Date when $UT1-A.1$ was determined	One-sigma error, msec	Worst case, msec
3 months in advance	20	50
1 month in advance	10	25
USNO weekly bulletins, preliminary-times	3	10
1 year later, USNO final times	1.5	5

The error in range differences measured by the DSIF due to "mislocating" the DSIF stations in "space" is a function of the error, δt, in $UT1 - t_s = (UT1 - A.1) - (t_s - A.1)$. A "bias" in $UT1 - t_s$ would show up in the OD solutions as a shift in station longitude. This discussion will limit itself to the assumed unknown "daily" variation of $UT1 - t_s$ as presented in Table 3. The ability of the stations to synchronize themselves to the NBS timing signals is a limiting factor until time synchronization by use of the ranging system is available. After that, the variations of $UT1 - A.1$ dominate.

The error in range difference (RD) due to δt is given by (where the doppler count interval is centered about the "zenith"):

$$\Delta\rho \approx r_s\, \omega_\oplus^2 [\cos \delta_L]\, T_c\, \delta t$$

where

r_s = distance of DSIF station from the Earth's spin axis. (See subsequent *SPS* article by Hamilton and Melbourne; Sect. E, Fig. 14, p. 18.)

$\omega_\oplus$ = rotation rate of Earth, rad/sec.

δ_L = local declination of the spacecraft as viewed from the tracking station (generally $\delta_L < 30$ deg).

T_c = doppler count time over which RD is accumulated, $\sim$ sec.

δt = error in knowledge of $UT1 - t_s$, $\sim$ sec.

The predicted behavior of $\Delta\rho$ due to the δt of Table 3 is presented in Fig. 9 for $T_c = 10^4$ sec, starting with *Ranger* 3 and projecting into the 1970's. Event markers for the *Ranger* 3-9 (lunar) missions as well as for the launch and target encounter of the *Mariner II* (Venus) and *Mariner IV* (Mars) missions are superimposed on this figure. To realize a $\Delta\rho < 0.1$ m, δt must be less than 0.3 msec/day.

b. Effects of time synchronization errors on target orbiter tracking. The effect of time synchronization errors between stations is pronounced when considering the tracking of such missions as lunar and martian orbiters. The following discussion assumes a circular orbit about the target body which has been determined by data from

Table 3. Predicted "daily" variation in $\delta t = UT1 - t_s$

Year	Comments	Station synchronization to A-1, $\sigma_{(t_s - A.1)}$ msec	"Daily" $\sigma_{(UT1 - A.1)}$ msec	"Daily" $\sigma_{\delta t}$, msec
1962	Each DSIF station resynchronized to UTC time standard stations at start of each tracking pass	2–5	0.2	2–5
1965	Each DSIF station resynchronized to UTC time standard stations at start of each tracking pass	1–3	0.2	1–3
1968	DSIF net internally synchronized by use of DSIF-S/C ranging system; sync monitored by rubidium frequency standards	0.003–0.010	0.2	0.2
1971	As above, but hydrogen masers used as frequency standards	0.001–0.003	0.1	0.1

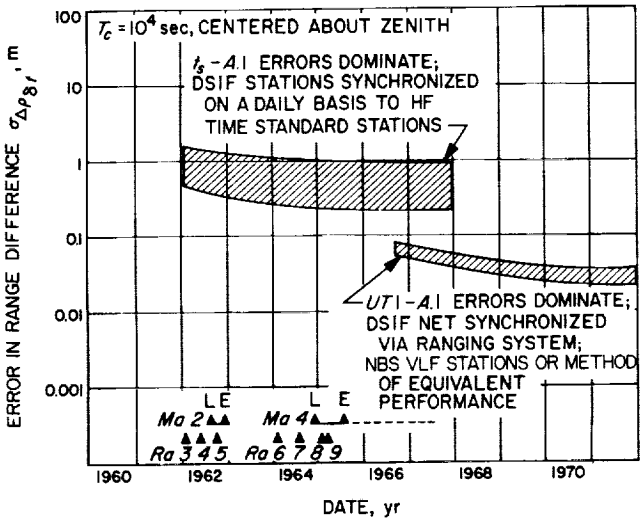

Fig. 9. Range difference error due to UT1-t_s uncertainties

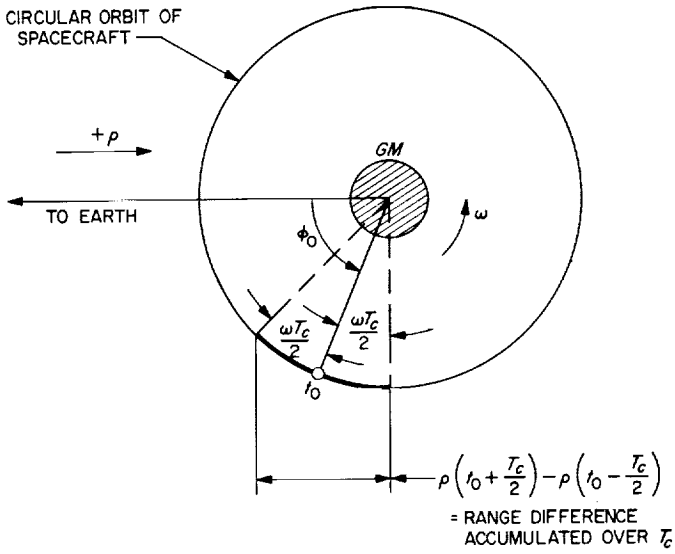

Fig. 10. Tracking geometry for target orbiter

DSIF stations whose tracking data time tags are all perfectly synchronized. The error in range differences produced by a "non-synchronized station" is analyzed for the case illustrated in Fig. 10, and is

$$\Delta\rho = -2\left[\frac{2\pi\,(GM)}{P}\right]^{1/3}\cos\phi_0\left[\sin\frac{\pi T_c}{P}\right]\Delta t_s$$

where

T_c = doppler count time over which the range difference $RD\,(t_0) \equiv \rho\,(t_0 + T_c/2) - \rho\,(t_0 - T_c/2)$ is accumulated.

P = period of spacecraft orbit about the target body $= 2\pi/\omega$.

GM = universal gravitational constant times the mass of the target body (Moon or Mars).

ϕ_0 = angle, as viewed from the center of the target body, between the Earth and the spacecraft at t_0.

Δt_s = synchronization error $= t_s - t_{standard}$, $t_{standard}$ corresponds to time tags of synchronized stations.

$\Delta\rho$ = error in observed RD due to Δt_s, i.e., $\Delta\rho = RD\,(t_0) - RD\,(t_0 + \Delta t_s)$ where $RD\,(t_0)$ corresponds to the observed RD, and $RD\,(t_0 + \Delta t_s)$ corresponds to the computed RD based upon the "computed" orbit and the time tag which is off by Δt_s from the time tags of the tracking stations which determined the "computed" orbit.

The time synchronization requirement to maintain $|\Delta\rho| < 0.1$ meter is illustrated in Fig. 11 for the doppler count interval centered about the sub-Earth point ($\phi_0 = 0$, this maximizes $\Delta\rho$, other things being equal). Although the error in RD is reduced as T_c/P decreases, the error from data point to data point is highly correlated so long as Δt_s is relatively stationary (the rubidium

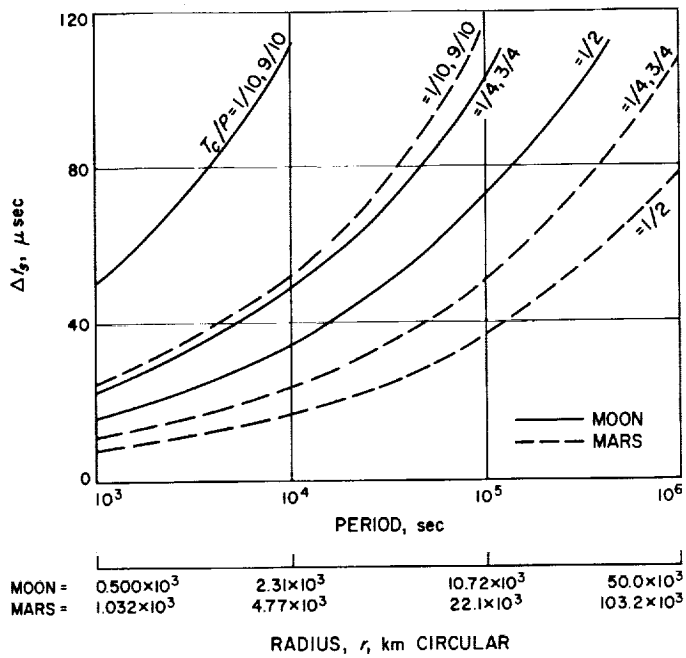

Fig. 11. Time synchronization requirement Δt_s for $\Delta\rho \leq 0.1$ meter with circular orbit $\phi_0 = 0$

standards currently used by DSIF are capable of controling the drift on Δt_s to 1 μsec over 1 day). With this in mind, station synchronization requirements of from 20 to 40 μsec are sensible for the orbiter missions envisioned, and station synchronization below 10 μsec will be useful.

5. Proposed Methods for Improving Synchronization

At present, all of the DSIF stations are not in general synchronized to the same time standard broadcasting station. These time standard transmitting stations have differed among themselves on the order of 1 to 3 msec. The present procedure will not be adequate in the near future where mission requirements will dictate that the DSIF stations be synchronized with respect to each other within 20 to 40 μsec. A number of methods have been proposed to improve the time synchronization of the DSIF stations. Among these are the following:

(1) Utilize spacecraft telemetry events which occur in view of more than one tracking station. This method has been tried on an experimental basis during *Ranger* missions. The synchronization available by this method was limited to between 1 and 2 msec by the available bandwidth.

(2) Introduce a slight step change in transmitter frequency when the spacecraft is in view of more than one station. This was tried on an experimental basis during *Ranger IX* and has the potential of synchronizing the stations to a few microseconds. On a predetermined time pulse, the two stations initiated the counting of a constant frequency. The counters were automatically stopped upon detection of the frequency shift. A limiting factor to this method is the degree to which time delays introduced by the station hardware can be calibrated.

(3) Starting with the Langley *Lunar Orbiter* (LLO), the ranging system can provide timing synchronization by essentially a procedure equivalent to (2).

(4) Time signals can be transferred among stations via communications satellites in a manner such that path length uncertainties will essentially cancel.

(5) Atomic or crystal calibration standards can be transported around the DSIF net at regular intervals.

(6) The VLF radio transmission system under test by NBS would allow maintenance of sync (to 10 μsec for strong signal at receiver) after one of the above methods has succeeded in determining one time epoch.

During *Ranger III*, the overseas DSIF stations were probably synchronized to the National Bureau of Standards time standard stations within 3 to 5 msec, while 2 to 3 msec was realized at the Goldstone, California, stations. By the time of the Langley *Lunar Orbiter* and with the use of the ranging system, it should be possible to synchronize the DSIF net to within 3 to 10 μsec. The use of the very low frequency (VLF) NBS stations is being investigated.

The range difference error due to the ability to synchronize the DSIF stations (per Table 3) is shown in Fig. 12 where a doppler count time equal 10^4 sec is assumed for both the lunar and martian cases. The $\Delta\rho$ regions are bounded on the top by the "loose" synchronization and a spacecraft orbital period, $P = 2 \times 10^4$ sec, while the bottom bound represents $P = 1 \times 10^5$ sec and the "tighter" time synchronization assumption. Notice that under these assumptions, $\Delta\rho < 0.1$ meters when the DSIF ranging system is used to synchronize the tracking data.

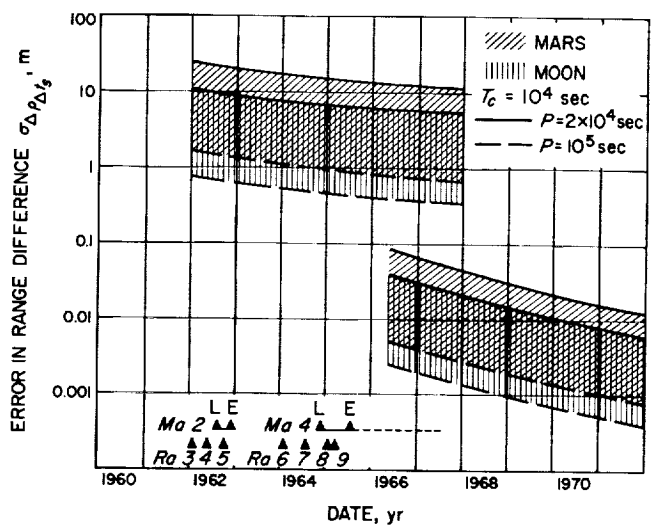

Fig. 12. Tracking station synchronization

6. Conclusions

Timing is a non-trivial problem in Orbit Determination. We hope that the definitions supplied above will be of help. Note the references, for they constitute the primary sources of information and the current state of research.

There are four main error sources in the timing systems. First, the station clocks must be synchronized to one

another. Second, the reference between the universal station time and *UTC* (*A*.1 in the future) must be known. Third, we must have *UT*1 − *A*.1 or equivalent, so that *UT*1 may be tied to station time. Fourth, we must determine *ET* − *A*.1 or equivalent.

Prior to 1966, the stations were synchronized to about 3 msec, *UT*1 was known to the same accuracy, and *ET* was determined within about 1 sec, all with respect to *A*.1. Of these, the ability to synchronize the stations in the DSIF network to within 3 to 10 μsec is the major near-term improvement. This is particularly important in the case of target orbiters such as the Langley *Lunar Orbiter* mission which is scheduled to take place in the last half of 1966.

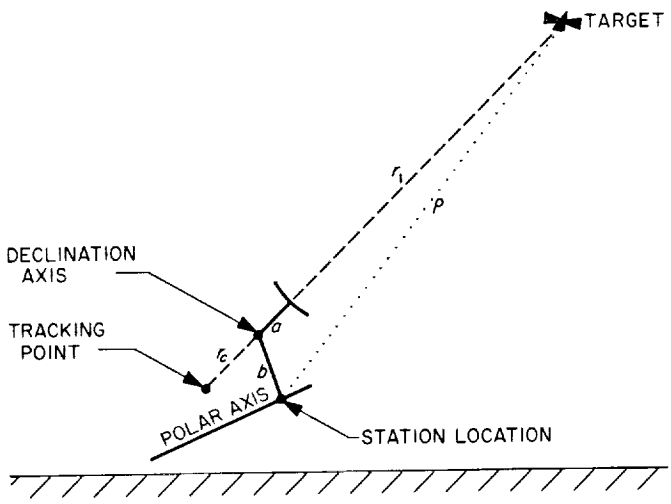

Fig. 13. Ha-Dec antenna geometry

D. Ha-Dec Tracking Data Corrections

R. L. Motsch

The current Orbit Determination Program (ODP) scheme for processing tracking data contains assumptions that do not allow for the proper handling of range measurements. The necessary corrections to the ODP for handling raw range data are presented in this article. The effect of the range corrections on doppler data is derived, and numerical examples are given.

1. Source of Range Error

In the current scheme of processing tracking measurements, it is assumed that (1) the axes of antenna rotation intersect at a point termed the station location, and (2) the dish vertex and the antenna tracking point are coincident with the station location. These assumptions each produce errors in range measurements, for in reality (see Ref. 5):

(1) The axes of antenna rotation are separated a distance b in the plane of the declination gear.

(2) The vertex of the dish lies ahead of the declination axis a distance a along the RF axis.

(3) The tracking point of the antenna lies a distance r_c behind the declination axis along the RF axis.

These statements are summarized in Fig. 13.

2. Effective Range Correction

Recent studies[1] have shown that the total range error (ε_R) made due to current assumptions concerning antenna configuration and motion is given by:

$$\varepsilon_R = r_c - \frac{b^2 + 2b\,(R - r_c)\cos\delta}{\rho + (R - r_c)} \qquad (1)$$

where a is the perpendicular distance between the vertex of the dish and the declination axis, b is the perpendicular distance between the declination axis and the polar axis, r_c is the tracking calibration constant, δ is the target local declination, R is the "raw" range measurement, and ρ is the true range (i.e., station-location-to-target distance), given by:

$$\rho = [b^2 + (R - r_c)^2 + 2b\,(R - r_c)\cos\delta\,]^{1/2}$$

Eq. (1) is an exact representation of the total range error. If we make the assumption that $\rho \approx R - r_c$, we obtain the simpler expression:

$$\varepsilon_R \approx r_c - \frac{b^2}{2\,(r - r_c)} - b\cos\delta\,.$$

[1]Motsch, R., Palmiter, H., *"Tracking Data Error Corrections for Ha-Dec Antennas,"* 30 March 1966 (internal communication).

By noting that $b^2/2(R - r_c)$ is insignificantly small for all realizable R, we obtain as our final expression for the range error:

$$\varepsilon_R \approx r_c - b\cos\delta \tag{2}$$

Computer studies show that the worst-case error made by using Eq. (2) as an approximation to ε_R is in the order of millimeters. Hence, as our estimate of ρ, we will use:

$$\rho \approx R - r_c + b\cos\delta \tag{3}$$

3. Effect of Range Error on Doppler Data

Since a measurement of doppler shift is the frequency equivalent of a measurement of range-rate, a *time-varying* error in the value of range must be reflected as an error in the doppler data. Taking the time derivative of Eq. (2) we have:

$$\varepsilon_R \approx +b\dot{\delta}\sin\delta \tag{4}$$

Hence, the corrected value of range-rate ($\dot{\rho}$) referenced to the actual station location as shown in Fig. 13 is given by:

$$\dot{\rho} \approx \dot{R} - b\dot{\delta}\sin\delta \tag{5}$$

Here R, and thus $\dot{R}$, are defined in terms of measurement of range directly, so we are dealing with a data type of a somewhat different sort from doppler data. But, (from Fig. 13):

$$R - r_c = r_1 + a \tag{6}$$

Thus:

$$\dot{R} = \dot{r}_1 \tag{7}$$

We are now on a consistent basis, with:

$$\dot{\rho} \approx \dot{r}_1 - b\dot{\delta}\sin\delta \tag{8}$$

where r_1 is the physical distance between the dish vertex and the target.

4. Error Magnitudes

From Eqs. (3) and (8), we see that the range and doppler errors are given, respectively, by:

$$\varepsilon_\rho = \rho - R = -r_c + b\cos\delta \tag{9}$$

$$\varepsilon_{\dot{\rho}} = \dot{\rho} - \dot{r}_1 = -b\dot{\delta}\sin\delta \tag{10}$$

Since the calibration constant (r_c) can be measured independently and, assuming no errors in measurement, can be removed from the tracking data as a constant bias, we can consider the range and doppler errors as functions of declination only.

For other than near-Earth probes, declination is essentially constant over any one pass, thus we can assume no error in doppler measurements and a constant error in range measurements. Worst-case conditions for a near-Earth probe occur during the first pass, when declination is changing most rapidly. Table 4 displays first-pass data for a projected *Surveyor* mission, assuming an 85-ft Ha-Dec antenna whose b distance is 6.706 meters. Theoretical worst-case conditions are given in Table 5 for the same antenna assumptions as in Table 4. Note that only the error magnitudes are given. The maximum signed-errors vary with station latitude.

Table 4. Error magnitude for typical Surveyor mission

Data	15 min		Set
	Rise	Extreme	
δ, deg	22.4	−22.0	−23.6
$\dot{\delta}$, rad/sec	−0.00075	−0.00034	0.00000
ε_ρ, meters	6.200	6.218	6.145
$\varepsilon_{\dot{\rho}}$, cps	0.029	0.013	0.000

The $\varepsilon_{\dot{\rho}}$ data is derived using a 15.3 cps/meter conversion factor for S-band tracking, per W. R. Wollenhaupt, *DSIF Observable Doppler Equations*, June 9, 1964.

Table 5. Error magnitudes for theoretical worst case

Data	Range worst case	Doppler worst case
δ, deg	0.0	90.0
$\dot{\delta}$, rad/sec	0.00122	0.00122
ε_ρ, meters	6.706	0.000
$\varepsilon_{\dot{\rho}}$, cps	0.000	0.125

5. Conclusions

The omission from the ODP of the antenna motion correction makes previous early first-pass tracking data in error. The possible error contributions to both range and doppler tracking data are significant in terms of present-day tracking capabilities, and steps are being taken to incorporate these corrections in the ODP. Similar analysis on other antenna configurations is now underway.

E. Information Content of a Single Pass of Doppler Data from a Distant Spacecraft

T. W. Hamilton and W. G. Melbourne

1. Introduction

On a typical pass of two-way tracking of a distant spacecraft, the doppler frequency is continuously counted from the time of initial "lock" until the end of the pass. The cumulative count is read out at regular intervals, typically 1 min. The data are sometimes "compressed" by forming first differences from every Kth sample and dividing by KT_s, where T_s is the original readout or sampling interval. Such "doppler frequencies" are interpreted as the space probe radial velocity with respect to the tracking station.

On a planetary mission such as *Mariner IV*, over 200 passes containing more than 500 samples in each pass can easily be accumulated. It is desirable that each pass be "compressed" into a smaller set of numbers characterizing the *trajectory-determining* information—here we will not be concerned with the higher-frequency information content relating to system noise, spacecraft oscillations, and atmospheric effects. Besides radically reducing the subsequent data-handling costs, such a compression can allow a better physical understanding of the nature of the navigational information in each pass. Such understanding is useful in allocating other system errors and in efficiently predicting navigational accuracies over a spectrum of mission situations.

It has been shown by J. O. Light (*SPS 37-33*, Vol. IV, pp. 8–16) that the "velocity parallax" due to the tracking station's rotation with the Earth is the most powerful factor in the doppler information for redetermining the orbit following a midcourse maneuver relatively near the Earth. In this article, it is established that a full pass of doppler data can meaningfully be interpreted as measuring the probe's mean geocentric *radial velocity*, its *right ascension*, and the cosine of its *declination*. For many mission situations, the latter two angles are extremely important in the navigational accuracies attainable. Thus the importance of tracking relatively near to the horizon is established since the accuracy of the right ascension and declination determinations is critically dependent on the fraction of the full pass included in the tracking. Subsequent articles will deal with this subject in greater depth and will treat other data noise models than the conservative one used here.

2. Calculation of the Observable

In Fig. 14, the observer (tracking station) is rotating about the z-axis at a distance of r_s with an angular rate ω. The probe, P, has coordinates $\mathbf{r}$ and $\dot{\mathbf{r}}$ relative to the x-y-z inertial frame. Since we are dealing with a distant probe, $r_s/r << 1$ and $z_0/r << 1$. The range from observer to the probe, ρ, is obtained from

$$\rho^2 = (x - r_s \cos\theta)^2 + (y - r_s \sin\theta)^2 + (z - z_0)^2. \qquad (1)$$

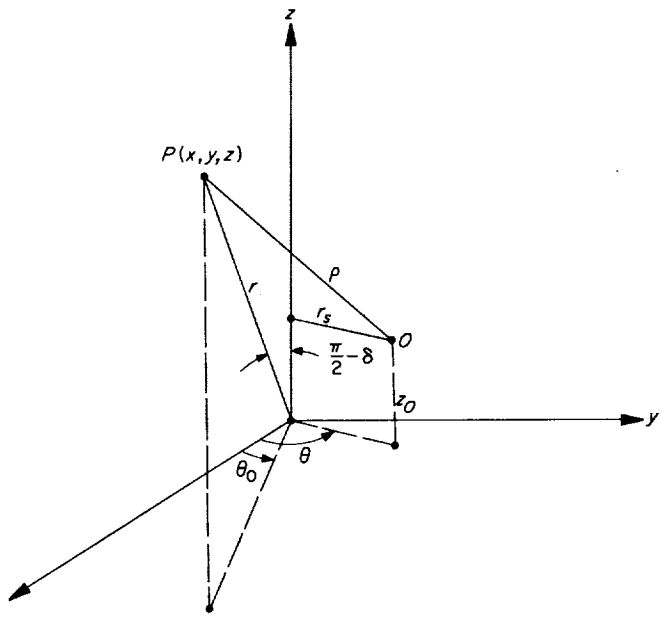

Fig. 14. Coordinates of probe, P, and observer, O

The range rate is composed of two parts, the motion of P and the motion of O; hence

$$\dot{\rho} = \frac{\partial \rho}{\partial t} + \frac{\partial \rho}{\partial \theta}\frac{d\theta}{dt}$$

or

$$\rho\dot{\rho} = (x - r_s \cos\theta)(\dot{x} + \omega r_s \sin\theta) + (y - r_s \sin\theta)(\dot{y} - \omega r_s \cos\theta) + \dot{z}(z - z_0) \qquad (2)$$

By expanding in powers of r_s/r and z_O/r, we obtain the following expression

$$\dot{\rho} = \dot{r} + \omega r_s\left(\frac{x}{r}\sin\theta - \frac{y}{r}\cos\theta\right) + \frac{r_s}{r}\left[\dot{r}\left(\frac{x}{r}\cos\theta + \frac{y}{r}\sin\theta\right) - \dot{x}\cos\theta - \dot{y}\sin\theta - \omega r_s\left\{\frac{xy}{r^2}\cos 2\theta + \left(\frac{y^2 - x^2}{r^2}\right)\frac{\sin 2\theta}{2}\right\}\right]$$
$$+ \frac{z_O}{r}\left[\frac{z}{r}\left\{\dot{r} + \omega r_s\left(\frac{x}{r}\sin\theta - \frac{y}{r}\cos\theta\right)\right\} - \dot{z}\right] + 0\left[\frac{r_s^2}{r^2}, \frac{z_O r_s}{r^2}, \frac{z_O^2}{r^2}\right]. \quad (3)$$

The observed $\dot{\rho}$ is given by the geocentric range rate, $\dot{r}$, plus a term of the form

$$\frac{r_s\,\boldsymbol{\omega}\cdot(\mathbf{r}\times\mathbf{r}_s)}{r r_s}$$

($r_s\omega$ is about 400 m/sec for a 30 deg latitude station), plus terms in the small parameters r_s/r, z_O/r. For a probe at $r = 0.03$ AU, these small parameters are about 10^{-3}. It is our intent to show that the expression below, obtained by letting $r \to \infty$ in Eq. (3), exhibits the important characteristics necessary to an understanding of the information content in a pass of doppler tracking data;

$$\dot{\rho} = \dot{r} + \omega r_s \cos\delta \sin(\theta - \theta_O), \text{ where } \theta - \theta_O = \omega(t - t_O). \quad (4)$$

In calculations with real data, no such approximations are made. The subsequent error analysis uses (4) because it is a simple and remarkably accurate description of the real situation.

3. Regression Analysis

The precision to which the right ascension, declination and geocentric radial velocity of the probe can be obtained from a single pass of data will now be described.

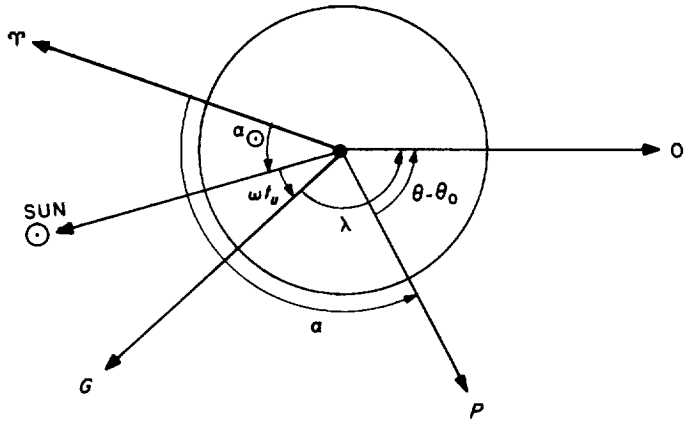

Fig. 15. Equatorial projection of coordinates in Fig. 14

Our basic data equation in (4) has been expressed in terms of the observable $\dot{\rho}$ and the angle θ. It is convenient to express θ in terms of the measurable quantity universal time, t_u, which determines the instantaneous angular orientation of the Earth about its axis of rotation. From Fig. 14 we note that θ is measured in the equatorial plane. From the equatorial projection in Fig. 15 it follows that $\theta - \theta_O$ is given by

$$\theta - \theta_O = \omega t_u + \alpha_\odot + \lambda - \alpha \quad (5)$$

where

- ♈ is the mean vernal equinox of 1950.0,
- $\alpha_\odot$ is the instantaneous right ascension of the mean Sun,
- ω is the mean rotation rate of the Earth of date,
- t_u is the true universal time,
- λ is the longitude of the observer O measured in an easterly direction from Greenwich,
- α is the instantaneous right ascension of the space probe, P.

The right-hand members of (5) have error components of diverse size, and so it is important that we describe our assumptions concerning each of these errors. The quantity ω is assumed to be known exactly. There are, of course, stochastic fluctuations in ω which lead to changes in the rate of t_u as measured by a "Newtonian" clock; however, from observational data on this fluctuation it may be shown that the accumulated effect of an error in ω over one pass has a negligible effect relative to other error sources. The quantity t_u is approximated by the so-called $UT.1$ time which is the best estimate of true universal time. We assume that $UT.1$ is measured exactly but that it has an unknown stochastic error ξ, which is probably less than $0^s.002$ and effectively constant over one pass. We assume that $\alpha_\odot$ is known exactly. The longitude of the observer is assumed to have a small unknown bias ε_λ. In addition, the distance of O off the spin axis r_s, is assumed to have a small unknown bias ε_{r_s}.

The problem is to find α, δ and $\dot{r}$ at the instant P crosses the meridian of $O(\theta = \theta_o)$ and to find the precision in the estimates of these quantities in the presence of data noise, the timing error ξ, and the small unknown biases in λ and r_s. We assume here that $\dot{\mathbf{r}}$, α and δ are constant over one pass, and that $|\dot{\mathbf{r}}|/\omega r << 1$, $r_s/r << 1$, and $z_o/r << 1$, so that the simplified data expression in (4) is valid. Later reports will deal with the additional information gained from the small departures from these assumptions which occur in actual missions.

In order to put our data equation in a convenient form for regression analysis, we define the quantity α^* to be a specified value of the right ascension of $P(x, y, z)$ which from a-priori information is known to be near the true value, α. The small quantity ε_α given by $\varepsilon_\alpha = \alpha - \alpha^*$ is to be determined from measurements. Similarly, we define λ^* to be the a-priori value of the longitude of O and ε_λ is given by $\varepsilon_\lambda = \lambda - \lambda^*$. We also define $\xi = t_u - t_u^*$, where t_u is the true universal time, and t_u^* is $UT.1$. Next, we define t by the relation

$$\omega t = \omega t_u^* + \alpha_\odot + \lambda^* - \alpha^* \tag{6}$$

We note that t is an observable. The equation for θ in (5) now becomes

$$\theta - \theta_o = \omega(t - t_o) \tag{7}$$

where t_o is given by

$$\omega t_o = \varepsilon_\alpha - \varepsilon_\lambda - \omega\xi \tag{8}$$

Our a-priori choices for α, λ and t_u are such that ωt_o is a small quantity which is to be estimated from the observations.

Since ωt_o is small, using (4) and (8), the data equation becomes

$$\dot{\rho} = a + b\sin\omega t + c\cos\omega t + n(t) \tag{9}$$

where

$$a = \dot{r},$$

$$b = r_s\omega\cos\delta\cos\omega t_o \doteq r_e\omega\cos\delta,$$

$$c = r_s\omega\cos\delta\sin\omega t_o \doteq \omega t_o r_s\,\omega\cos\delta$$

and $n(t)$ is the data noise. We assume that a pass is symmetric about $t = t_o \approx 0$ and that N observations are made at equally spaced time intervals over the pass. Further, we assume white gaussian noise of mean zero and variance $\sigma_{\dot{\rho}}^2$. The maximum likelihood estimates of a, b and c are given by

$$\hat{a} = \frac{1}{2\psi(1-\rho_{13}^2)}\left[\int_{-\psi}^{\psi}\dot{\rho}(\phi)\,d\phi - \frac{2\sin\psi}{\psi\left(1+\frac{1}{2\psi}\sin 2\psi\right)}\int_{-\psi}^{\psi}\dot{\rho}(\phi)\cos\phi\,d\phi\right] \tag{11}$$

$$\hat{b} = \frac{1}{\psi\left(1-\frac{1}{2\psi}\sin 2\psi\right)}\int_{-\psi}^{\psi}\dot{\rho}(\phi)\sin\phi\,d\phi \tag{12}$$

$$\hat{c} = \frac{1}{2\psi(1-\rho_{13}^2)}\left[\frac{2}{\left(1+\frac{1}{2\psi}\sin 2\psi\right)}\int_{-\psi}^{\psi}\dot{\rho}(\phi)\cos\phi\,d\phi - \frac{2\sin\psi}{\psi\left(1+\frac{1}{2\psi}\sin 2\psi\right)}\int_{-\psi}^{\psi}\dot{\rho}(\phi)\,d\phi\right] \tag{13}$$

where ψ is the half-width of the pass, i.e., $-\psi \leq \theta \leq \psi$. Here, we have replaced the summations in our discrete process by integrations since N is in practice large and since we are not interested in an actual evaluation of the constants. We observe that due to our assumption of a symmetric pass with $t_o \approx 0$, $\hat{b}$ is uncorrelated with $\hat{a}$ and $\hat{c}$

but that $\hat{a}$ and $\hat{c}$ are strongly correlated. In fact, the covariance matrix Λ of these estimates is given by

$$\Lambda = \begin{pmatrix} \dfrac{1}{1-\rho_{13}^2} & 0 & \dfrac{-2\sin\psi}{\psi\left(1+\dfrac{1}{2\psi}\sin 2\psi\right)(1-\rho_{13}^2)} \\ 0 & \dfrac{2}{\left(1-\dfrac{1}{2\psi}\sin 2\psi\right)} & 0 \\ \dfrac{2\sin\psi}{\psi\left(1+\dfrac{1}{2\psi}\sin 2\psi\right)(1-\rho_{13}^2)} & 0 & \dfrac{2}{\left(1+\dfrac{1}{2\psi}\sin 2\psi\right)(1-\rho_{13}^2)} \end{pmatrix} \frac{\sigma_{\dot{\rho}}^{*2}}{N} \tag{14}$$

where ρ_{13} is the correlation between $\hat{a}$ and $\hat{c}$ and given by

$$\rho_{13} = \frac{-2^{1/2}\sin\psi}{\psi\left[1+\dfrac{1}{2\psi}\sin 2\psi\right]^{1/2}} \tag{15}$$

Note that for $0 \leq \psi \leq \pi/2$, ρ_{13} lies in the range $-1 \leq \rho_{13} \leq -0.9$ which reflects the non-orthogonality of the even-functions 1 and $\cos\phi$ over intervals symmetric about $\phi = 0$.

Fig. 16 shows the variation of the precision of these estimates with the half-width of the pass ψ. Notice that as ψ is reduced from 90 deg, the precisions of $\hat{a}$ and $\hat{c}$ are severely degraded whereas the precision of $\hat{b}$ deteriorates more gradually. These phenomena are easily explained from an examination of (9). Notice that $\hat{a}$ and $\hat{c}$ for small ψ are difficult to separate. The dashed curve gives the precision of $\hat{c}$ when a is assumed perfectly known. This case may be obtained from (14) by setting $\rho_{13} = 0$ and will be referred to in the sequel. Notice for this special case that $\sigma_{\hat{c}}$ remains relatively flat compared to $\sigma_{\hat{b}}$ and for small ψ, $\sigma_{\hat{b}}$ is substantially degraded relative to $\sigma_{\hat{c}}$. Again, (9) shows that an error in b is most easily seen at $\omega t = \psi = 90$ deg whereas the effect of an error in c is maximized at $\omega t = 0$.

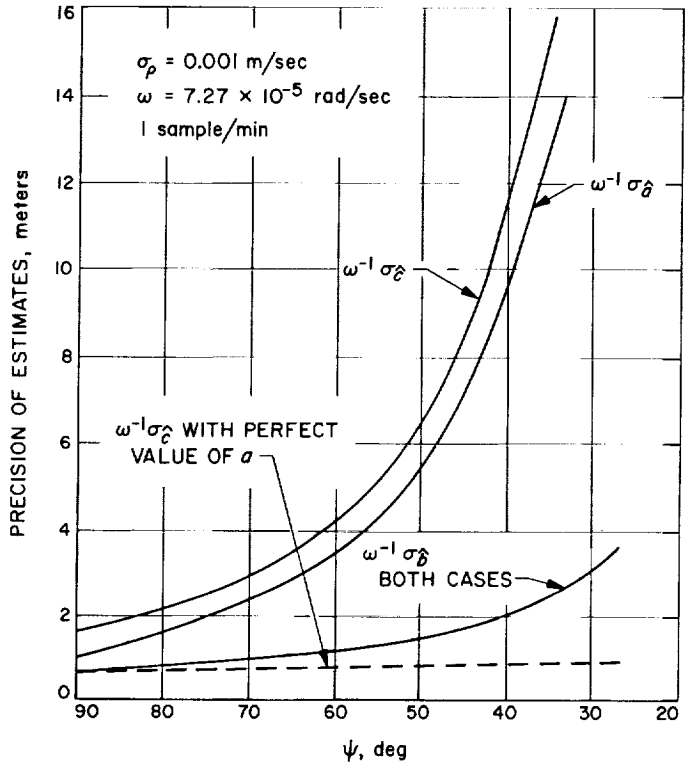

Fig. 16. Precision of parameter estimates $\hat{a}$, $\hat{b}$, $\hat{c}$, with half-width of pass ψ

The determination of $\dot{r}$ follows directly from a. For α, we have from (10) that

$$\omega\hat{t}_0 = \hat{c}/\hat{b} \tag{16}$$

and it follows since $\hat{c}$ and $\hat{b}$ are uncorrelated that the variance of ωt_0 is given by

$$\sigma_{\omega\hat{t}_0}^2 = \hat{b}^{-2}\sigma_{\hat{c}}^2 + (\omega\hat{t}_0)^2 b^{-4}\sigma_b^2 \doteq \hat{b}^{-2}\sigma_{\hat{c}}^2 \tag{17}$$

since ωt_0 is near zero. The estimate for α now follows from (8) provided ϵ_λ and ξ are given.

Since ξ, ϵ_λ, and t_u are uncorrelated, it follows from (8) that the variance of $\hat{\alpha}$ is given by

$$\sigma_{\hat{\alpha}}^2 = \sigma_{\omega\hat{t}_0}^2 + \omega^2\sigma_\xi^2 + \sigma_\lambda^2 \tag{18}$$

From the coefficient $\hat{b}$, we obtain an estimate of $\cos\delta$ provided r_s is given. Further, the variance of $\hat{\delta}$ is given by

$$\sin^2\hat{\delta}\,\sigma_{\hat{\delta}}^2 = (r_s\omega)^{-2}\,\sigma_{\hat{b}}^2 + r_s^{-2}\cos^2\hat{\delta}\,\sigma_{r_s}^2 \qquad (19)$$

Finally, the correlation in $\hat{a}$ and $\hat{c}$ is easily removed by choosing a linear combination of these quantities which diagonalizes the covariance matrix Λ. The magnitudes of the eigenvectors, $\hat{a}'$, $\hat{b}'$, $\hat{c}'$, are given by

$$\begin{cases} \hat{a}' = \hat{a}\cos\Gamma + \hat{c}\sin\Gamma \\ \hat{b}' = \hat{b} \\ \hat{c}' = \hat{c}\cos\Gamma - \hat{a}\sin\Gamma \end{cases} \qquad (20)$$

where Γ is found to be

$$\tan 2\Gamma = \frac{-4\sin\psi}{\psi\left(1 - \frac{1}{2}\sin 2\psi\right)} \qquad \left(0 \leq -\Gamma \leq \frac{\pi}{2}\right) \qquad (21)$$

Note that $45° \leq -\Gamma \leq 56°$ for $0 \leq \psi \leq 90°$. The eigenvalues $\sigma_{a'}^2$, $\sigma_{b'}^2$, and $\sigma_{c'}^2$ are given by

$$\begin{cases} \sigma_{\hat{a}'}^2 = \dfrac{\sigma_{\hat{a}}^2 + \sigma_{\hat{c}}^2}{2} + \dfrac{1}{2}\left[(\sigma_{\hat{a}}^2 - \sigma_{\hat{c}}^2)^2 + 4\sigma_{\hat{a}}^2\,\sigma_{\hat{c}}^2\,\rho_{13}^2\right]^{1/2} \\ \sigma_{\hat{b}'}^2 = \sigma_{\hat{b}}^2 \\ \sigma_{\hat{c}'}^2 = \dfrac{\sigma_{\hat{a}}^2 + \sigma_{\hat{c}}^2}{2} - \dfrac{1}{2}\left[(\sigma_{\hat{a}}^2 - \sigma_{\hat{c}}^2)^2 + 4\sigma_{\hat{a}}^2\,\sigma_{\hat{c}}^2\,\rho_{13}^2\right]^{1/2} \end{cases} \qquad (22)$$

Fig. 17 shows the behavior of these eigenvalues as a function of ψ. The effect of the correlation in $\hat{a}$ and $\hat{c}$ now is cast completely into $\sigma_{\hat{a}'}$. The precision of $\hat{c}$ goes as essentially $1/N^{1/2}$.

4. Interpretation of the Results

In Sec. 3 above, we concluded that the estimate of geocentric radial velocity of the probe and its precision follow directly from the coefficient $\hat{a}$ and its variance $\sigma_{\hat{a}}^2$. For the right ascension and declination, these determinations are not as straightforward, for we have seen that the precision of these determinations depends on our knowledge of the station location and also timing in the case of right ascension.

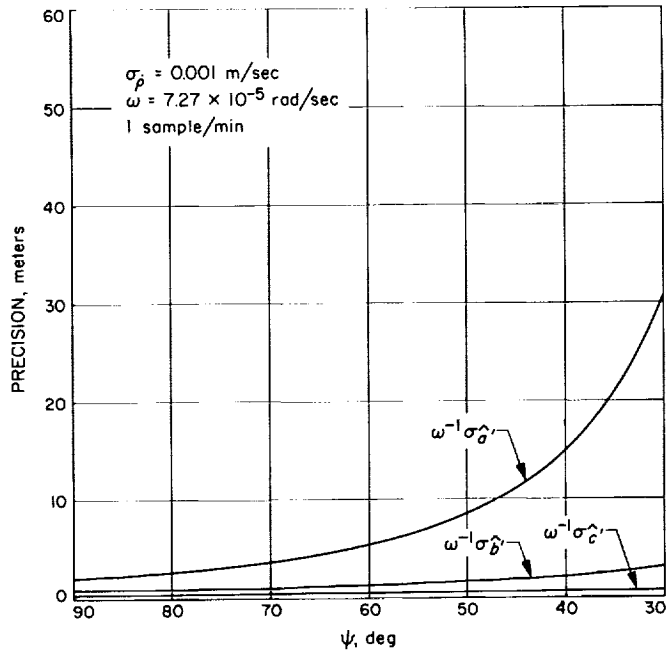

Fig. 17. Behavior of eigenvalues as a function of ψ

Let us first address ourselves to the problem of station location. We note in passing that (3) provides an explanation for the observed fact in actual missions that the component of the position of O parallel to the spin axis is not well determined nor, conversely, does a small error in this component seriously affect the results.

For the distance off the spin-axis r_s, it follows from (10) that r_s will be strongly determined for probe declinations near zero; in fact, for this case we have

$$\sigma_{r_s} = \omega^{-1}\,\sigma_{\hat{b}} \qquad (\delta = 0) \qquad (23)$$

Referring to Fig. 16, we see for a full pass ($\psi = 90°$) and for $\sigma_{\dot{\rho}} = 1$ mm/sec, that r_s is determined to 1 meter. Furthermore, in an actual mission the probe P is being accelerated by other bodies (e.g., the Sun) whose geocentric right ascensions and declinations are precisely known; this effect enables one to obtain a good separation of the instantaneous declination and the spin axis bias when observations are taken over a sufficiently wide span of the trajectory of P. In any case, a precision of 1 meter for r_s, for $\sigma_{\dot{\rho}} = 1$ mm/sec, emphatically demonstrates that in order to realize this precision, one must be careful to insure that all error sources of this magnitude are incorporated in the mathematical model used in the actual orbit determination process. This includes such effects as antenna motion, nutation and wandering of the pole of the

Earth, tidal deformations of the Earth, and ionospheric effects.

In the case of station longitude bias, the problem is coupled with errors in universal time. An error of 0^s.002 in time is equivalent to about 1 meter in a longitude direction for the station. For two different stations on the surface of the Earth, the relative longitude is not affected by *UT*.1 errors provided they can synchronize the observations. As in the case of r_s determinations, if one knows the right ascension of P by "independent" means (e.g., from observations of a *Ranger* spacecraft near lunar impact) more precisely than ωt_0 can be determined, we obtain a strong determination of the bias in λ. For this case, it follows from (8) that

$$\sigma_\lambda^2 = \sigma_{\omega t_0}^2 + \omega^2 \sigma_\xi^2 \qquad (\varepsilon_\alpha = 0) \tag{24}$$

For, $\sigma_{\dot\rho}^{\cdot} = 1$ mm/sec and $\sigma_\xi = 0^s.002$, $r_s\sigma_\lambda$ is about 2 meters. Here, we have used (17) to evaluate $\sigma_{\omega\hat{r}_0}$ from σ_ε using the $\psi = 90$ deg point on Fig. 16. If $\dot r$ of P also is predicted independently the value of $\sigma_{\dot\xi}$ should move toward the dashed curve in Fig. 16. Hence, we would ultimately expect λ to be determined to a precision commensurate with σ_ξ. Fig. 18 shows actual Goldstone-Woomera relative longitude determinations from *Rangers 6–9*. In these flights, software accuracy limitations cause $\sigma_{\dot\rho}^{\cdot}$ to be degraded to about 10 mm/sec.

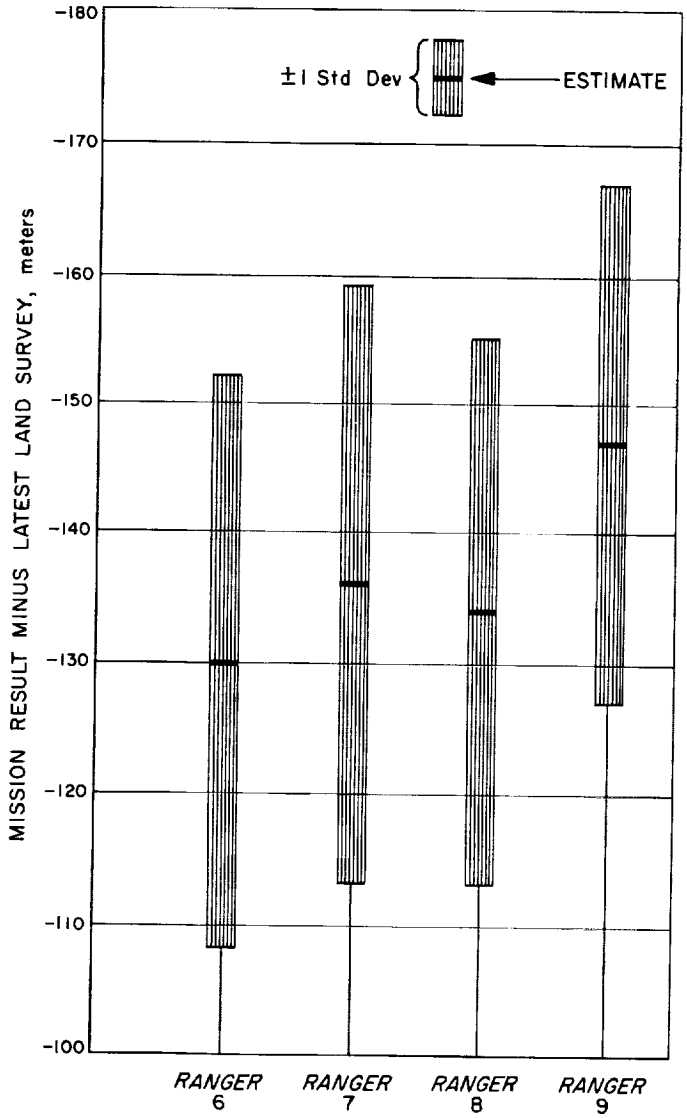

Fig. 18. Goldstone station location relative to longitude difference of Woomera, with time correction

Finally, if we assume that the station locations have become sufficiently well established so that the biases ε_λ and ε_{rs} are not the dominant error sources, it follows that (18) and (19) and Fig. 16 may be used to obtain the precision with which α and δ can be estimated from one pass of doppler data. The timing error also is not dominant provided $\sigma_{\dot\rho}^{\cdot} \geqq 1$ mm/sec. Taking $\psi = 80$ deg and multiplying by $(2)^{1/2}$ to allow for the contingencies of timing and station location errors we have the result that

$$\sigma_\alpha = 5 \times 10^{-7} \text{ radians} \tag{25}$$

$$\sin\delta\sigma_\delta = 2.5 \times 10^{-7} \text{ radians} \tag{26}$$

These accuracies are equivalent to about 0.″1 arc which is similar to the accuracy of angular data obtained from astronomical observations. In addition, $\dot r$ is determined to

$$\sigma_{\dot r}^{\cdot} = 0.1 \text{ mm/sec} \tag{27}$$

Hardware performance in the near future will have accuracies of better than $\sigma_{\dot\rho}^{\cdot} = 1$ mm/sec, probably around 0.1 mm/sec. Although a more careful analysis of our limiting error sources is required for such systems, it is clear that it may be possible to significantly reduce the numbers in (25), (26), and (27).

Acknowledgments. The authors have benefited from many conversations with members of the Systems Analysis Section in arriving at the results described above. Particular acknowledgment is due to J. D. Anderson and J. O. Light.

F. A Post-Flight Tabulation of the *Mariner IV* Real-Time Orbit Determination Errors

G. W. Null

1. Tracking Data: Validity and Usage

Two-way DSIF doppler data was the only type used in determining the orbits during the *Mariner IV* Mars mission. This data was taken continuously during critical phases of the mission, such as pre-midcourse and closest approach to Mars, and it was otherwise averaged over 24 hr to 5 days. Data was taken from Goldstone, California; Johannesburg, S. A.; Woomera and Canberra, Australia; and Madrid, Spain.

The data time span considered here is from launch on November 28, 1964 to October 1, 1965, which is 2.5 months past Mars closest approach (July 15, 1965). There is, of course, a reasonable chance of obtaining more tracking data when *Ma-4* passes by the Earth in late 1967. The data was coherent and did not involve any use of microwave links to achieve coherency as was the case for *Mariner II*. No observable biases due to equipment were observed in the data, and the bias due to lack of knowledge of the refraction correction was minimized by only allowing data above 17 deg elevation in the orbit fits. High-frequency noise on the data was less than 0.02 cps for doppler counted over 60 sec. At the S-band frequency of 2295 mc this accuracy is equivalent to 0.12 cm/sec error in the range rate of the probe relative to the tracking station. It was possible to increase this resolution by either counting over larger counting intervals (accomplished by data processing of the original 60-sec sampled data) or by multiplying the doppler frequency to be counted by a factor (for *Ma-4* a factor of 8) before the counting was performed. Thus the data noise was generally less than 0.003 cps S-band (0.02 cm/sec) as seen in the orbit residuals; 0.003 cps represents the limiting accuracy of the existing single-precision orbit determination program (ODP) to compute tracking data. The principal advantage to *Ma-4* of such small data noise is to be able to see biases in the orbit residuals more clearly.

Unfortunately, the physical model of the universe in the ODP is not exact, and this fact prohibits making the best use of the data. Since the ODP takes into account only those error sources formally implemented in a deterministic solution model and since the accuracy claimed by the ODP for its answers is directly proportional to the accuracy the user claims for his data (assuming that no a-priori information is used), the ODP for planetary cases would give grossly optimistic accuracy estimates if the input data accuracy estimate (data weight) were the same as the high-frequency noise on the data. This has been confirmed by actual experience with *Ma-2* and *Ma-4*. Furthermore, if the no a-priori answers obtained from tracking data are combined with a-priori constants which have reasonable associated statistics (such as the astronomical unit, station locations, and the solar pressure coefficients) as is actually done for most orbits, the a-priori constant values will by outweighed by the no a-priori values. Thus, an error in the actual orbit itself can be induced by data weights which are too small. To avoid this error as much as possible and to produce ODP statistics (tracking data + a-priori) which are reasonable, a semi-arbitrary range rate weight of $\sigma_{\dot{\rho}} = 3$ cm/sec was chosen for 60-sec sampled data. Note that this is approximately 30 times larger than the noise seen on 60-sec counted S-band doppler and more than 150 times the noise on the 600-sec S-band data typically used in orbits. When 600-sec counted data is used (data points 600 sec apart), the $(N)^{1/2}$ rule is used; and a weight of $\sigma_{\dot{\rho}} = 3/(10)^{1/2} \cong 1$ cm/sec is used. This weighting scheme assumes that low-frequency biases due to program insufficiencies and physical model errors are the dominating error source and that data noise is so small as to be a negligible error source.

It is obvious that using large data weights to compensate for orbit errors is not an optimum procedure. Unfortunately, it is the only one currently available and was therefore used both for *Ma-2* and *Ma-4*. The error sources for *Ma-4* and the planned remedies for them will be discussed in the following section. In the absence of valid statistical descriptions of the orbit solutions by the ODP, the labeling of solution parameters with statistical error estimates becomes a matter of engineering judgment. In making those judgments, particular attention is paid to the following:

a. The stability of a parameter being solved for when the conditions of the problem are varied. For example: (1) Other important parameters can be frozen at various values, and the effect on the parameter under test noted. (2) Solutions may be made using data from a single tracking station; by comparing several solutions of this type, a definite test can be made for the presence of bad tracking data.

b. The ability of the ODP to predict future measurable events. For example, Mars occultation times and future doppler observables.

c. The ability of the ODP to predict future events which are not directly observable. These are assumed to be well determined after the conclusion of the mission; the near-Mars orbit is believed to be such an observable.

2. The Ma-4 Post-Flight Encounter Orbit Tracking from E — 5 to E + 5 Days

This section will present a representative orbit computed after the flight on October 30, 1965. The epoch to which the initial position and velocity were referenced was on July 10, 1965 (5 days before encounter).

a. A-priori one-sigma statistics input to the Orbit Determination Program (ODP).

(1) *Geocentric position and velocity of the probe:*
$\tilde{\sigma}_{pos}$ = 10,000 km spherical uncertainty;
$\tilde{\sigma}_{vel}$ = 10 m/sec spherical uncertainty.
A-priori values were taken from cruise tracking.

(2) *Mass ratio of Mars to the Sun* (M_m):
$\tilde{\sigma}_{M_m} = 2\%$;
a-priori value $0.32280422 \times 10^{-6}$.

(3) *Solar pressure coefficient:*
$\tilde{\sigma}_{(1+G)} = 5\% \cong 5\%$ of the total solar pressure force;
a-priori value for $1 + G = 1.2067$.

(4) *Astronomical unit:*
$\tilde{\sigma}_{AU}$ = 2,000 km;
a-priori value = 149598500 km.

(5) *Station locations:*
$\tilde{\sigma}_{pos}$ = 50 meters spherical;
a-priori values from surveys, *Ranger* results, and pre-*Ma-4* encounter solutions.

b. The best available encounter orbit. When a solution was made using the a-priori conditions and statistics described in Sect. 2a, above, the results were as follows: The geocentric position changed by slightly less than 1,000 km, the geocentric velocity by approximately 1 m/sec, the solar pressure by 0.005%, and the station locations by less than 10 meters. The solution for the astronomical unit and mass of Mars with their associated ODP one-sigma statistics was:

$$AU = 149597470. \pm 240 \text{ km}$$

$$M_m = (0.322728 \pm 0.000015) \times 10^{-6}$$

The encounter orbit parameters are:

E = time of closest approach = TCA = July 15, 1965, $01^h00^m\ 58^s.180$

$\mathbf{B}$ = a vector from the center of Mars normal to the incoming asymptote

$$B = 15251.5 \pm 15 \text{ km}$$

$$\mathbf{B} \cdot \mathbf{T}_c = 8141.6 \pm 20 \text{ km}$$

$$\mathbf{B} \cdot \mathbf{R}_c = 12896.6 \pm 20 \text{ km}$$

$\mathbf{T}_c$ is a unit vector in the plane of the ecliptic normal to the incoming asymptote $\mathbf{S}$; $\mathbf{R}_c$ makes up a right-handed *RST* coordinate system. Tracking data used in the fit was 600-sec counted doppler, except that 60-sec counted doppler was used from $E - 4$ hr to $E + 4$ hr.

c. Effects of uncertainties in component values.

(1) In a variety of other encounter orbits, the solutions for the encounter orbit ($\mathbf{B}$, TCA, etc.) and the mass of Mars remained very stable. The range of values for the $\mathbf{B} \cdot \mathbf{T}_c$ and $\mathbf{B} \cdot \mathbf{R}_c$ components from the values quoted above was less than 5 km in all cases, the range of values about TCA was less than 2 sec, and finally the range of values for M_m from the quoted value was less than 0.01%.

(2) For reasons probably connected with the stability of the single precision computer program, a solution which included the astronomical unit (AU) always resulted in larger residuals between computed and observed data than a solution which did not include the AU. However, the numerical value of the AU solution fell within a range of 200 km of the quoted value. Computer runs have shown that even if AU is frozen at a value of 149598500. km which is 1000 km higher than the quoted solution, the target orbit and M_m remain within the ranges given above. This would indicate, since AU is an ephemeris parameter, that ephemeris error does not affect the quoted solution significantly. Monte Carlo simulation studies changing the look-up argument between Universal Time and Ephemeris Time by 20 sec showed similar results.

(3) Even for orbits using data from midcourse through $E + 5$ days, the range of values about $\mathbf{B}$ is less than 50 km, the range of M_m is less than 0.1%, and the range of AU is less than 1000 km. This is surprising since, in most of these runs, no provision was made to solve for the Earth-Mars ephemeris errors and since the single-precision ODP is not adequate for making such orbits.

(4) The uncertainty in the radius of Mars obtained by astronomical measurements is approximately 50 km.

The observed enter-occultation time of the radio signal compared favorably with that predicted by using the encounter orbit and an average value of R_{Mars} (3378 km), thus indicating the orbit is good to at least 50 km.

(5) In conclusion, it seems from the preceding four points that the encounter orbit is well-determined and that the following one-sigma uncertainties might reasonably be attached:

$$\sigma_{\mathbf{B}\cdot\mathbf{T}_c} = \sigma_{\mathbf{B}\cdot\mathbf{R}_c} = 20 \text{ km}$$
$$\sigma_B = 10 \text{ km}$$
$$\sigma_{TCA} = 10 \text{ sec}$$
$$\sigma_{M_m} = 0.02\% \text{ of } M_m$$
$$\sigma_{AU} = 500 \text{ km}$$

3. Evaluation of Combined Pre-Midcourse Orbit and Maneuver Errors

a. The aiming point for the midcourse maneuver, made Dec. 5, 1964 (launch + 7 days) was:

$$B = 12011 \text{ km}$$
$$\mathbf{B}\cdot\mathbf{T}_c = 6007 \text{ km}$$
$$\mathbf{B}\cdot\mathbf{R}_c = 10401 \text{ km}$$
$$\text{TCA} = 01^h\ 47^m$$

b. The actual achieved target point, from Sect. 2 was:

$$B = 15251 \text{ km}$$
$$\mathbf{B}\cdot\mathbf{T}_c = 8142 \text{ km}$$
$$\mathbf{B}\cdot\mathbf{R}_c = 12897 \text{ km}$$
$$\text{TCA} = 01^h\ 01^m$$

c. The combined orbit errors, i.e., actual − desired values, were

$$\Delta B = +3240 \text{ km}$$
$$\Delta\mathbf{B}\cdot\mathbf{T}_c = +2135 \text{ km}$$
$$\Delta\mathbf{B}\cdot\mathbf{R}_c = +2496 \text{ km}$$
$$\Delta\text{TCA} = -46 \text{ min}$$

The actual error was approximately three-fourths of the specified one-sigma requirement set by the *Ma-4* Project in Functional Specification MC-4-170A. The one-sigma requirement on pre-midcourse orbit determination accuracy is given in MC-4-111 as 2250 km one-sigma. This error is hard to separate from maneuver equipment error since the estimated orbit error is a strong function of AU and solar pressure estimates. However, preliminary results have shown that an error of +1000 to 1500 km in $\mathbf{B}\cdot\mathbf{T}_c$ and an error of +300 km in $\mathbf{B}\cdot\mathbf{R}_c$ to be the most likely pre-midcourse orbit error. These error estimates were obtained by differencing the pre-midcourse orbit used to compute the maneuver and the "best" post-flight run using pre-midcourse tracking data. Much work remains if more definite numbers are required.

4. Cruise Orbit Determination Errors

Orbits were performed at an average of one every 2 weeks during the cruise phase (midcourse to $E - 5$ days) of the mission. During the first few months of the flight, the data was not strong enough to solve for AU so that essentially the AU was frozen at the JPL Venus radar-bounce value of 149598500 (±500 km 1σ). Later it was possible to loosen the a-priori on AU somewhat, allowing the data to participate more fully in determining AU. Since the solution for AU tended to change somewhat from week to week, there was a corresponding jumpiness in the target parameters. This was intensified when approximately 1 month before encounter, the mass of Mars was added to the solution set. Thus there was no set of runs done in real time during cruise which used the same a-priori assumptions.

The plots (Figs. 19–21) of real-time orbit errors show trends consistent with the above procedures in that the orbits are stable for the first few months and then tend to jump around late in the mission. Two other curves are also shown in each of these figures. These curves represent systematic sets of runs done after the end of the mission in which all a-priori conditions were held constant and data was added in 1-month blocks. The parameters solved for in these runs were initial positions, initial velocity, a solar pressure coefficient, and station location. For one set of runs, AU was frozen at the JPL Venus bounce AU value of 149598500 km; and for the other set, AU was frozen at the value obtained from the *Ma-4* encounter fit

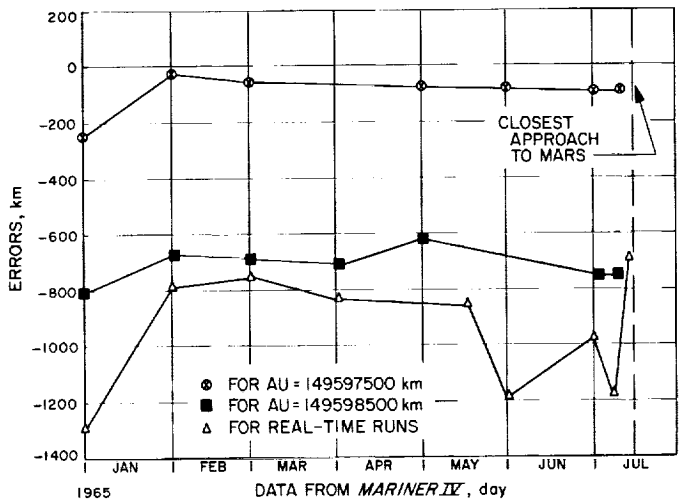

Fig. 19. Errors in predicting encounter parameters $B \cdot T_c$

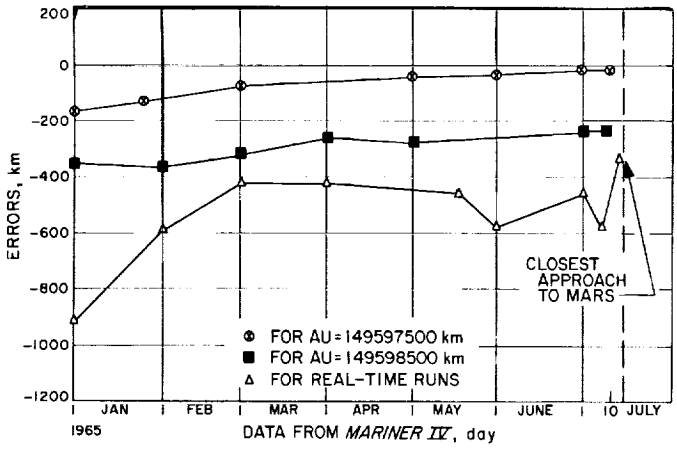

Fig. 20. Errors in predicting encounter parameters $B \cdot R_c$

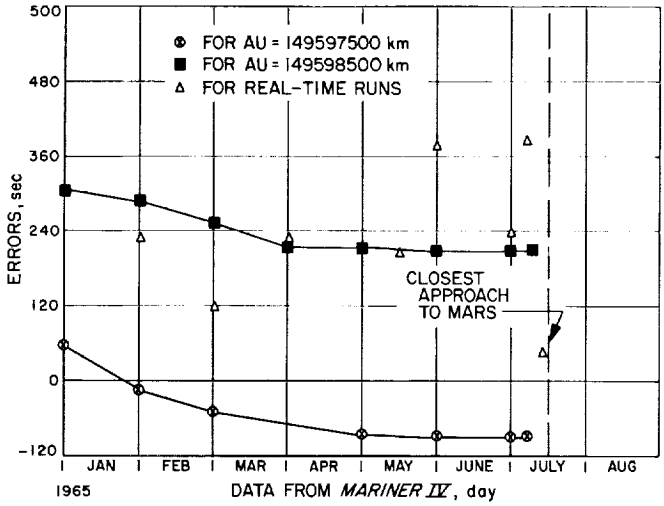

Fig. 21. Errors in predicting time of closest approach

(149597500 km). All available features of the program were used in these latest runs including improved timing equations, an improved estimate of the solar pressure from telemetry, and the use of solar pressure forces in two components normal to the Sun-probe line. These forces were needed to approximate the forces induced by moving solar vanes on the ends of the solar panels. Since the telemetry measurements of these vane positions gave better knowledge of the normal solar forces than was possible by solving for these forces with tracking data, the corresponding constants were included in the trajectory but not the parameter solution list.

As for the real-time runs, it is seen that there are errors of 500 to 1000 km throughout cruise even though the consistency of the orbits is high for certain portions of the flight.

The remarkable reduction of target prediction error when AU = 149597500 km is used enhances the validity of the otherwise suspect encounter AU solution. Other recent results from Venus bounce observations give a result of AU = 149598000. Therefore, since $\partial B/\partial AU = 0.6$, it is likely that the real-time AU value of 149598500 km produced an error of from 300 to 600 km.

5. Near-Encounter Orbit Errors (Epoch 0^h, July 10, 1965; Tracking Data from 0^h, July 10)

This section will present the errors in the orbits performed starting at closest approach $E - 10$ hr. Note that the errors at that time are roughly those existing at the end of the cruise plots (Figs. 19–21). A-priori sigmas were possibly somewhat tighter on position and velocity than would seem wise in the light of post-flight analysis. However, during the mission there had been no evidence of an error of the size that actually existed. During the last 5 hr before encounter, two computers were operating. One computer was using $\tilde{\sigma}_{pos} = 500$ km and $\tilde{\sigma}_v = 0.1$ m/sec while the other used $\tilde{\sigma}_{pos} = 200$ km and $\tilde{\sigma}_v = 0.1$ m/sec; both methods gave equivalent results. Later, at approximately $E - 1$ hr, both computers used the looser a-priori. The errors in several representative orbits are shown in Fig. 22. It is intended to do considerably more work in making systematic runs similar to the two cruise sets of runs of Sect. 4, above.

Operationally, the orbit errors during the period from $E - 10$ hr through $E + 5$ hr did not result in any deg-

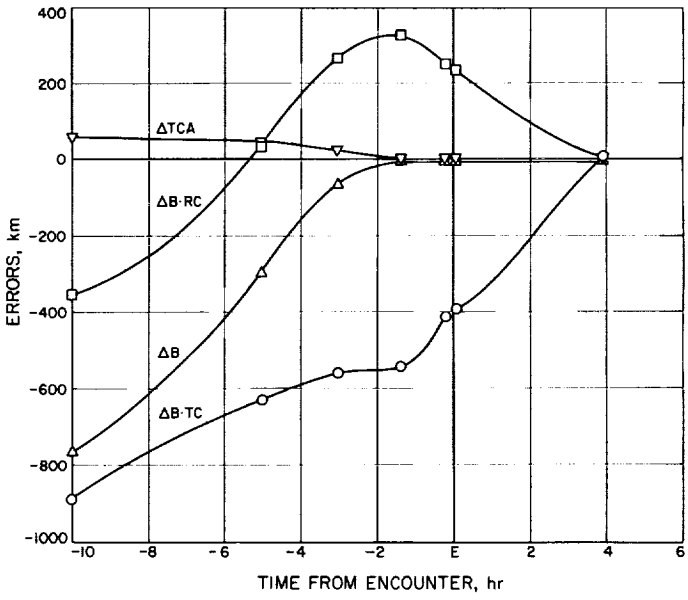

Fig. 22. Errors in predicting encounter quantities

radation of the scientific results from *Ma-4* including the TV pictures and the Mars occultation data.

6. Conclusions

a. Operationally, the orbit determination error met the error specifications set by the Ma-4 Project, and did not degrade the performance of the mission significantly.

b. The orbit errors during the cruise and near-encounter portion of the mission were three or four times larger than had been expected. Some of the more probable causes are:

(1) ODP computations are mainly done in single-precision (8-digit) arithmetic. This causes some instability in the cruise orbits but is not a major error source.

(2) Solar pressure forces caused by solar vane positions were not mechanized in ODP until after encounter. These forces cause a 200-km target error.

(3) Telemetry data indicated random forces of 0.5% of the solar pressure force due to valve leakage from the attitude control system. The leak rate was found to vary occasionally when a valve was actuated. From the limit-cycle telemetry, it is possible to verify frequent changes in the leak rate of 0.5% of the solar pressure force. The solar pressure force averaged 4 dynes on the 260 kg *Ma-4* spacecraft. The time-averaged translational force due to the total leak rate was probably no greater than 3% of the solar pressure force. Preflight ground measurements of leak rate on the valves flown on *Ma-4* usually showed leak rates in the range of 0.5% to 2% of the solar pressure force; 1% of the solar pressure force would map into a *B*-plane error of 200 km.

(4) Planetary ephemeris errors are a possible error source which, exclusive of the AU uncertainty, are believed to be accurate to 130 km (one standard deviation).

(5) AU error is the most likely major error source and probably accounts for 500 km or more of the target error.

c. In the light of the above mentioned error sources, it is understandable that the cruise data was difficult to fit and that the residuals should show long-term trends with maximum amplitude of 0.05 cps S-band (0.3 cm/sec range rate). Taking this disturbance into account, it is also plausible that the stability of the cruise orbit results might deteriorate when two highly correlated effects such as solar pressure and the AU are simultaneously solved for.

d. A definite analysis of the Ma-4 orbit errors cannot be completed until proper computer programs are available to analyze the data. This will require the new double-precision orbit program (DPODP), scheduled for completion in early 1967. In the meantime the investigation will be carried out with improved versions of the current ODP. The attitude control forces cannot be "fit out" of the solution perfectly even with the DPODP because of their non-deterministic character.

e. The mass of Mars and AU solutions are reasonably consistent with earlier experimenters. In Figs. 23 and 24, bar-graph plots show the various values by the dark lines and the probable error by the length of the bar away from the value line. All AU solutions except that for *Ma-4* use Venus radar bounce data taken near the Earth–Venus conjunctions. No value is given for the *Ma-2* 1962 Venus flight. The definitive *Ma-2* AU solution will probably be published in the next year. For *Ma-2*, the encounter AU solution was a factor-of-25 weaker than the *Ma-4* encounter solution. Thus to obtain a stronger *Ma-2*

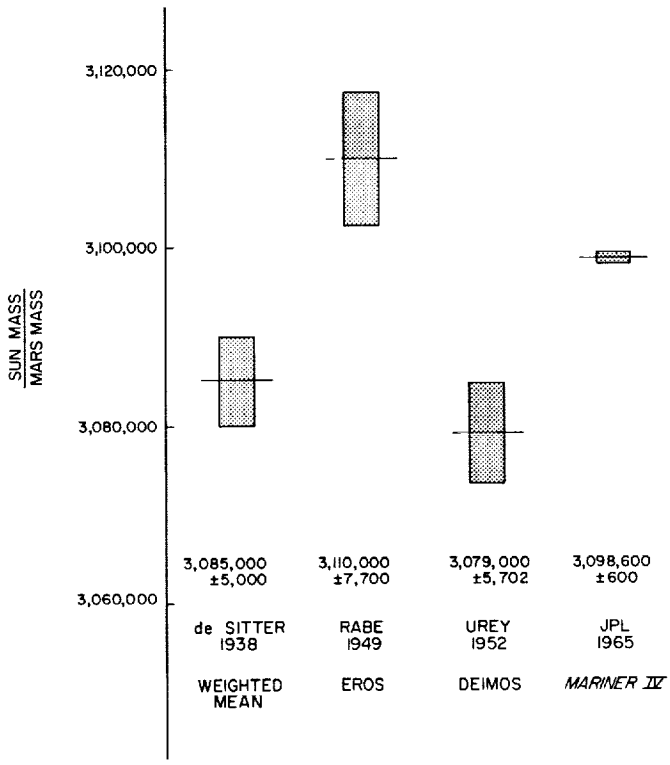

Fig. 23. Probable error in estimates of mass of Mars

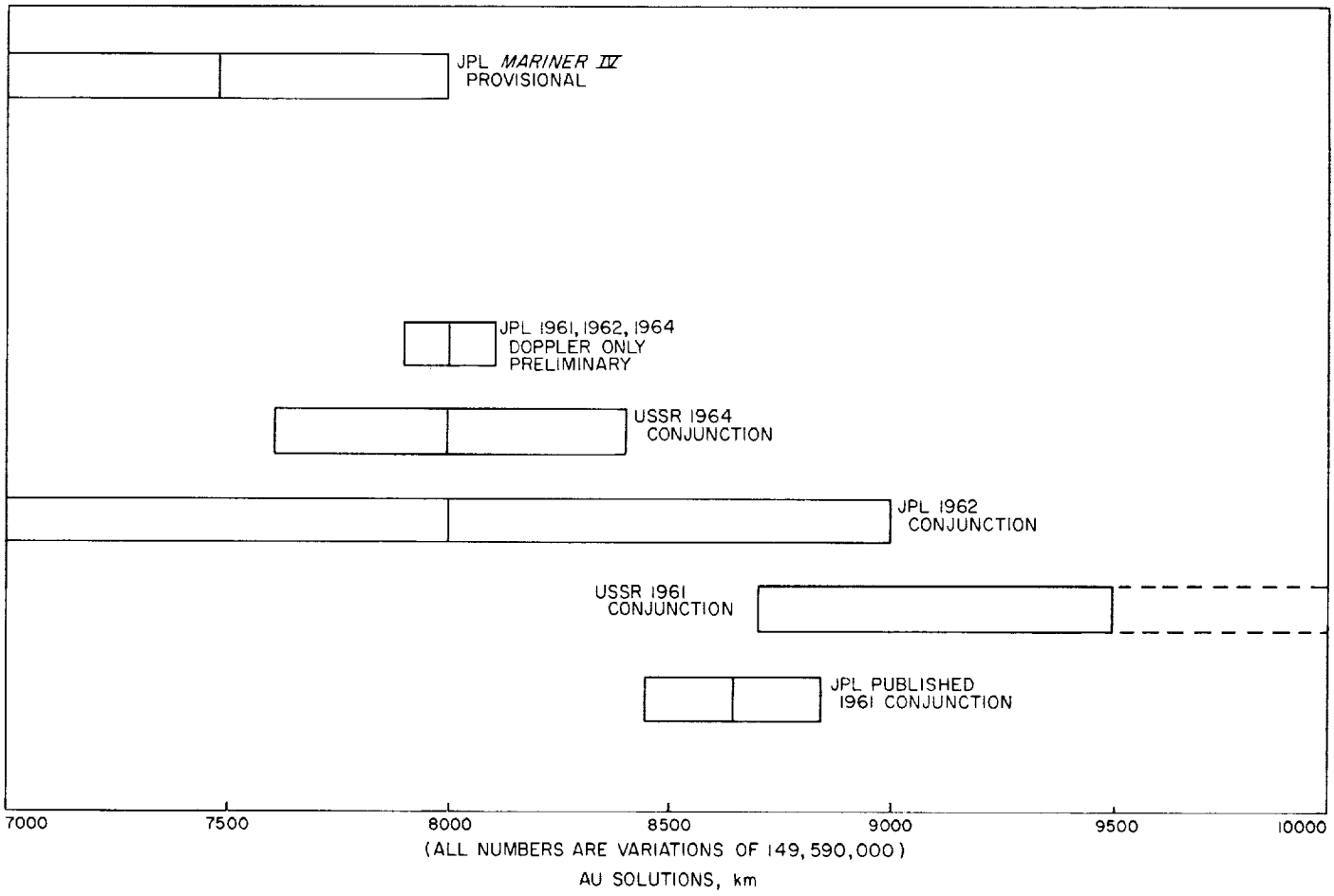

Fig. 24. Probable error in estimates of astronomical unit

AU solution, the cruise and encounter data must be combined in one orbit. The delay in achieving a high accuracy *Ma-2* AU solution has been caused by difficulties in making the combined solutions. The *Ma-4* combined solutions will also be released within 1 year. The JPL Venus bounce value marked "provisional" is not yet published and is quoted with the permission of Dr. D. Muhleman, formerly of JPL. This solution is considered to be more accurate than the 1961 JPL value since it uses a double-precision computer program, solves for the Venus ephemeris as well as the AU, and has data from three conjunctions. The 1961 solution was in single precision and did not solve for ephemeris corrections. All values are for a value of the speed of light of $c = 299792.5$ km/sec. The speed of light is considered to be a defined constant in orbit and planetary bounce work so that lengths are really determined in light-seconds and translated to meters for more convenient use.

The *Ma-4* mass of Mars solution shown in Fig. 23 is one order of magnitude more accurate than any previous determination. Analysis of tracking data from future Mars spacecraft will permit a definite check of the validity of the *Ma-4* solutions.

G. Velocity Estimation Accuracy Versus Doppler Sample Rate II. Exponentially Correlated Noise

D. W. Curkendall

In *SPS 37-38*, Vol. III, pp. 20–24, the effect of the doppler sampling rate on velocity estimation errors was investigated. The analysis was limited to the assumption that the noise corrupting the data was white phase-jitter on the incoming doppler wave. That is, the noise assumed had a correlation time of zero. This restriction is relaxed here, and the analysis is performed using an exponentially correlated noise model.

In order to make this note reasonably self-contained but without unnecessary repetition of the last volume's entry, the tracking and processing model is once again developed, but results obtained from the white noise model are quoted without justification.

As before, several methods of taking and processing the data will be treated. Given particular emphasis are the following cases:

(1) Destructively-counted doppler

(2) Continuously-counted, differenced doppler

(3) Continuously-counted, total count doppler

In each case, both the minimum variance (MV) and the uniformly weighted (UW) estimates are considered.

As was found in *SPS 37-38*, Vol. III, the destructive counting data destroys much of the inherent accuracy of the doppler system. The analysis also shows that, even though MV estimates yield similar results for either (2) or (3), the UW estimate utilizing the data as total-count doppler can be made considerably more powerful than the corresponding estimate employing differenced data.

1. The Basic Model

Consider the one-dimensional situation where the spacecraft is moving radially with constant but unknown speed, v, relative to a tracking station which is placed at the center of the Earth. This station is receiving a continuous signal whose frequency is directly proportional to v. There exists a device which integrates this frequency, yielding a phase measurement which is corrupted by exponentially correlated noise, i.e.,

$$\Phi_i = \phi(t_i) + \varepsilon(t_i)$$

where

Φ_i = measurement of phase at $t = t_i$,

$\phi(t_i)$ = true phase at t_i,

$\varepsilon(t_i)$ = noise on the measurement with $E[\varepsilon(t_i)\,\varepsilon(t_j)] = \sigma^2 e^{-|t_i - t_j|/\tau}$

where $E[\cdot]$ denotes the expected value of $[\cdot]$, and τ is the correlation time of the process.

What we basically wish to do is to obtain an understanding of our ability to determine from the tracking data the value of the unknown velocity of the spacecraft, v. In each case considered, the total observation time, T, will be held fixed and the resultant orbit accuracy will be expressed as a function of the number of data points, N, taken during T.

2. How Data Is Taken and Processed

a. Continuously counted data. Here, the total interval over which the spacecraft is observed, T, is broken into N measurements of the integral of the frequency. These measurements are spaced at even intervals, $\Delta t = T/N$. If this data is to be used as "differenced" doppler, each observation is formed

$$y_i = \frac{\Phi_i - \Phi_{i-1}}{\Delta t} = (\Phi_i - \Phi_{i-1})\, N/T \tag{1}$$

If, however, a total count scheme is used, each measurement is differenced back to the original measurement to obtain the observation

$$y_i = \Phi_i - \Phi_0 \tag{2}$$

b. Destructive count data. In a practical destructive counting mechanization, a gate on the doppler counter is opened at an even time (GMT) and the time it takes for precisely n cycles of doppler to be counted is measured. The system then resets and stays idle until the next even GMT arrives. At this time the sequence is reinitiated. The essential feature of this system is that gaps appear in the counting sequence, destroying the coherence between successive observations. It is sufficient for our purposes here to analyze a similar counting scheme that retains this feature. In this equivalent scheme, phase measurements are taken according to the following schedule:

(1) at $t = t_{11} = 0$

(2) at $t_{12} = \Delta t\,(1 - \alpha)$ where $0 < \alpha < 1$

(3) at $t_{21} = \Delta t$, $t_{22} = \Delta t\,(2 - \alpha)$, etc.

(4) Additional measurements are made until the allowed length of time, T, has elapsed as is shown in Fig. 25.

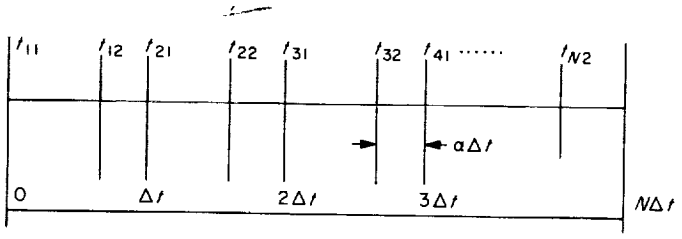

Fig. 25. Measurement scale

Each pair of measurements is differenced and divided by $\Delta t\,(1 - \alpha)$

$$y_i = \frac{\Phi_{i2} - \Phi_{i1}}{\Delta t\,(1 - \alpha)} \tag{3}$$

If the measurements given by (3) are combined in a single observation vector, then

$$\mathbf{y} = \begin{bmatrix} y_1 \\ y_2 \\ \cdot \\ \cdot \\ \cdot \\ y_N \end{bmatrix} = \frac{1}{\Delta t\,(1 - \alpha)} \left\{ \begin{bmatrix} \phi_{12} - \phi_{11} \\ \phi_{22} - \phi_{21} \\ \cdot \\ \cdot \\ \cdot \\ \phi_{N2} - \phi_{N1} \end{bmatrix} + \begin{bmatrix} \varepsilon_{12} - \varepsilon_{11} \\ \varepsilon_{22} - \varepsilon_{21} \\ \cdot \\ \cdot \\ \cdot \\ \varepsilon_{N2} - \varepsilon_{N1} \end{bmatrix} \right\} \tag{4}$$

or

$$\mathbf{y} = A\upsilon + \boldsymbol{\varepsilon}$$

where A is the $N \times 1$ matrix of $\partial y_i/\partial \upsilon$, i.e., in this case

$$A^T = [1, 1, 1, \cdots 1]$$

Employing the well-known error variance equations, a MV estimate produces mean-squared error

$$Q_{MV}(N) = E\,[(\upsilon - \upsilon^*)^2] = (A^T \Lambda_\varepsilon^{-1} A)^{-1} \tag{5}$$

whereas a UW estimate gives error variance

$$Q_{UW} = (A^T W A)^{-1} A^T W \Lambda_\varepsilon W^T A\,(A^T W A)^{-1} \tag{6}$$

where

υ^* = estimate of υ

W = diagonal weighting matrix = $k^2 I$

and

$\Lambda_\varepsilon = E\,[\varepsilon\, \varepsilon^T]$ whose ij term

$$\lambda_{ij} = \frac{\sigma^2 N^2}{(1 - \alpha)^2 T^2} \{2e^{-|j-i|\beta/N} - e^{-|j-\alpha-i+1|\beta/N} - e^{-|j+\alpha-i-1|\beta/N}\} \qquad i \neq j$$

$$= \frac{\sigma^2 N^2}{(1 - \alpha)^2 T^2} \{2 - 2e^{-(1-\alpha)\beta/N}\} \qquad i = j \tag{7}$$

The term β is the ratio of total viewing time to the correlation time, T/τ. Eq. (7) is specifically written for the destructive count case but is valid for continuous count differenced data by letting α identically equal zero. The resulting Λ_ε for total count processing will be given below.

Because of the simple form of the A matrix, Eqs. (5) and (6) reduce to

$$Q_{MV}(N) = \sum_{i=1}^{N} \sum_{j=1}^{N} \lambda_{ij}^{-1} \tag{8}$$

$$Q_{UW}(N) = \frac{1}{N^2} \sum_{i=1}^{N} \sum_{j=1}^{N} \lambda_{ij} \tag{9}$$

where λ_{ij}^{-1} is the ij term of Λ_ε^{-1}

3. Results and Discussion

In *SPS 37-38*, Vol. III, pp. 20–24, each of the data taking and processing modes just described were analyzed under the assumption that white noise was corrupting the phase measurements. The differences arising (which were marked) were plotted and discussed. The overall effect of introducing physically realizable noise into the system (as opposed to white noise) is to modulate the differences between the data-taking and processing modes treated.

a. Destructive count data. The behavior of the mean-squared estimation error with increasing total number of samples N depends upon two factors:

(1) the relative size of the basic sample width Δt to the correlation interval, τ, *and*

(2) the relative size of the gap, $\alpha\,\Delta t$, to τ. When

$$\Delta t >> \tau$$

and

$$\alpha\,\Delta t >> \tau$$

then the mean-squared estimation error

$$Q(N) \approx \frac{2\sigma^2 N}{T^2(1-\alpha)^2} \tag{10}$$

when either a MV or UW estimate is employed. This is the same result obtained in *SPS 37-38*, assuming white noise. When

$$\Delta t >> \tau$$

but

$$\alpha\,\Delta t << \tau;\ \alpha << 1$$

Then, if a MV is formed,

$$Q(N) \approx \frac{12\sigma^2 N}{T^2(N+1)(N+2)} \tag{11}$$

but if UW estimation is used,

$$Q(N) \approx \frac{2\sigma^2}{T^2} \tag{12}$$

Eqs. (11) and (12) are identical to results obtained in *SPS 37-38*, Vol. III, for continuously counted data. What is occurring here is that when the data breaks $\alpha\,\Delta t$ are much smaller than τ, coherency in the successive samples is re-established. The phase error (see Fig. 25).

$$\varepsilon(t_{i2}) \approx \varepsilon(t_{i+1,1})$$

but $\varepsilon(t_{i2})$ is essentially uncorrelated with all other ε, thus we have the unusual case where destructive data behaves like continuously-counted data in the presence of white noise.

Fig. 26 illustrates these limiting conditions as well as the more general cases. These curves were obtained by

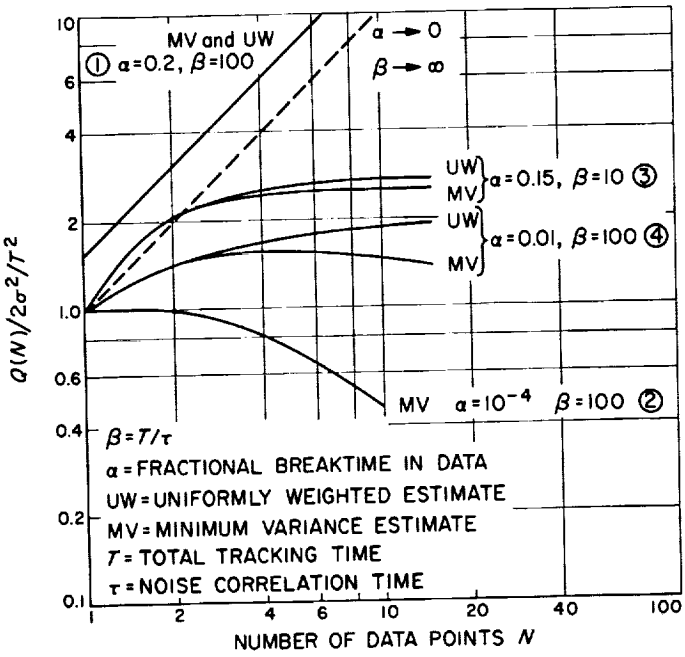

Fig. 26. Normalized error variance versus number of data points for destructive-count doppler

numerically solving (8) and (9). Here the ordinate gives the normalized error variance (i.e., $Q(N)$ divided by $2\sigma^2/T^2$) versus the number of samples, N. Curves one and two represent the cases just described. Curve three plots the variance for $\alpha = 0.15$ and $\beta = T/\tau = 10$ which exhibits the typical behavior of an initial rise and then a leveling-out as Δt nears τ. Note that the MV and UW estimates have nearly equal variances. The last two curves, four, represent the interesting case of an initial rise and a peaking-out followed by a small decrease as $\alpha\Delta t$ becomes smaller than τ but $\Delta t >> \tau$. The dotted line represents the limit as $\tau \to \alpha \to 0$.

b. Continuously-counted doppler. Fig. 27 plots typical results when continuous-count, differenced doppler data are used. Curves one and two represent the cases for $\beta = 10$, 20 and MV estimation. For small N, the plots follow the dotted curve, which is the white noise MV case taken from *SPS 37-38*. However, as Δt falls to near τ, a further increase in N yields but little improvement of Q. Curve three is for *UW* estimate and is given by the equation

$$Q(N) = \frac{2\sigma^2}{T^2}(1 - e^{-T/\tau}) \neq f(N) \qquad (13)$$

The plot shown is for $T/\tau >> 1$, which conceals the interesting property that as $\tau \to \infty$, $Q(N) \to 0$. Taken in conjunction, Eq. (13) and the dotted curve in Fig. 28 constitute a precise statement of the intuitively understood notion that noise processes whose correlation times are either very large or very small can easily be filtered in an orbit program. In this simplified one-dimensional analysis, the τ that is most damaging is when it nearly equals T. In general, the noise that is most difficult to filter is that which produces a "signature" on the doppler similar to that produced by the deterministic variations of the "A" matrix, ∂ (range rate)/∂ (injection conditions).

c. Total count doppler. In treating continuously-counted, total-count doppler, it is beneficial to estimate the original phase error ε_0 in addition to the velocity. For this case, Eq. (4) is modified to

$$y = A\begin{bmatrix} v \\ -\varepsilon_0 \end{bmatrix} + \varepsilon \qquad (14)$$

where

$$A^T = \begin{bmatrix} \frac{T}{N}, 2\frac{T}{N}, \cdots, N\frac{T}{N} \\ 1, \quad 1, \cdots, \quad 1 \end{bmatrix}$$

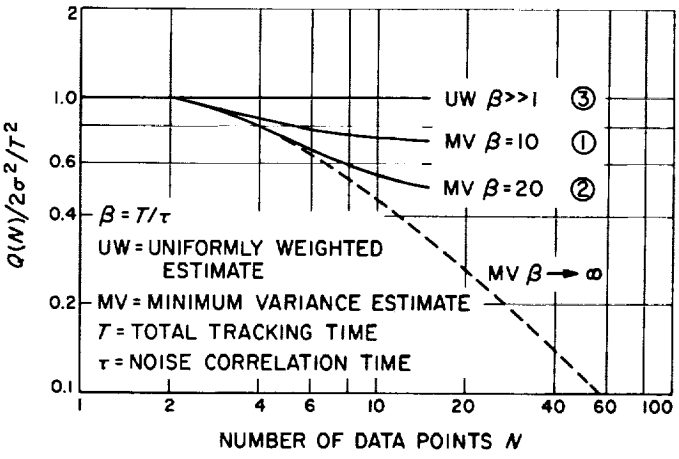

Fig. 27. Normalized error variance versus number of data points for continuously-counted differenced doppler

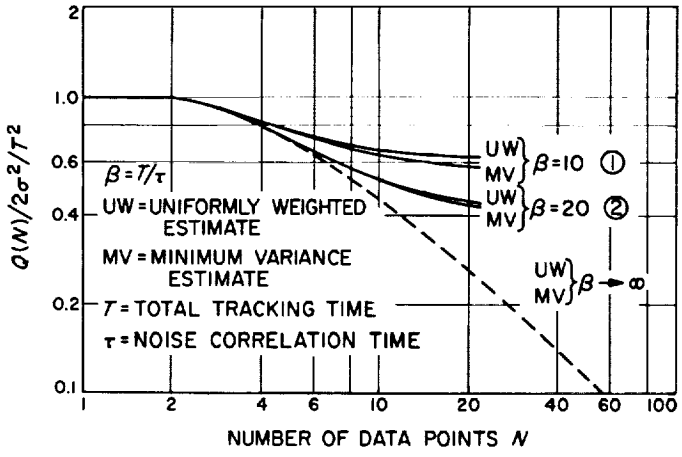

Fig. 28. Normalized error variance versus number of data points for continuously-counted total-count doppler

The ε is now simply the phase error at each read-out time; its covariance becomes:

$$\Lambda_\varepsilon = T^2\begin{bmatrix} 1 & r & r^2 & \cdots & r^{N-1} \\ & 1 & r & \cdots & r^{N-2} \\ & & 1 & \cdots & \cdot \\ & & & & \cdot \\ & & & & \cdot \\ & & & & r \\ & & & & 1 \end{bmatrix}$$

where $r = e^{-\beta/N}$

Fig. 28 contains the results from using this model with the additional feature that a-priori information was used in the estimation of ϵ_0 or was done in *SPS 37-38*. Plotted in the figure are two pairs of curves, one for $\beta = 10$ and a second for $\beta = 20$. Note that although the MV estimates are very similar to those obtained using differenced doppler, the UW estimate significantly outperforms its counterpart from the previous case.

4. Conclusions

Considering these results as a whole, it is possible to reach substantially the same conclusions that were reached for the more restrictive white noise model. That is,

(1) Except in special circumstances, the use of a destructive counting scheme seriously degrades the potential of the data through loss of coherence between points.

(2) The MV estimates using continuously counted, differenced or total count data, yield similar results. The error variance decreases until $\Delta t \simeq \tau$, after which no further significant improvement can be realized.

(3) The UW estimate using total count data significantly outperforms its differenced counterpart. Because simplicity often dictates that an orbit determination program be restricted to forming what are essentially UW estimates, this performance gain is considered a significant point if the major noise sources in the doppler data are in fact stationary in nature.

Most measurement error sources can be considered stationary, i.e., produce bounded phase errors in the accumulated doppler. The frequency standard is one source that does not fit this model under all circumstances. Results, both analytical and experimental, concerning the frequency standards will be presented in a later issue.

H. Computer Program Interfaces

D. W. Trask

In this section, the interactions are described between various computer programs used in processing and analyzing DSN tracking data. To illustrate how these programs fit together, the non-real-time processing of tracking data as illustrated in Fig. 29 is reviewed. The tracking data is received from the DSIF stations into an IBM 7044 computer. This computer is used basically as an input-output device in the Space Flight Operations Facility. The Systems Program within the 7044 compiles the incoming data on a mission log tape for future post-processing. It also contains a Pseudo-Residual Program (PRP), that compares the incoming tracking data with predicted values which are based on the best orbit computed to date. These differences or pseudo-residuals can be displayed in real time as either plots or in printed form. Periodically the mission log tape is processed by the Editor Program (EDTX) in the IBM 7094 where the tracking data is stripped off and placed on a magnetic tape for future post-processing. This tape serves as the input to a pair of tracking data editing programs (see Ref. 6), namely the Tracking Data Processor (TDP) and the Orbit Data Generator (ODG). These programs perform a series of bookkeeping operations on the data before it is passed on to the Orbit Determination Program (ODP).

The TDP is primarily a data logging program, while the ODG does most of the computational work. In particular, the TDP determines whether data messages are in an acceptable format, checks data condition codes (inserted at the tracking data stations) to determine whether the data is usable, makes crude checks on data values to see that they are realistic, converts all data into a common system of units and records all accepted data on disk and tape for further processing by the ODG. The ODG then makes more elaborate tests to determine whether data values are realistic, corrects angle and range observables to remove systematic equipment errors, computes "average doppler" from the raw counter readings, makes abitrary corrections to data values and time tags as specified by the user, appends to the data all auxiliary information needed by the ODP, and writes data on disk and tape for further processing by the ODP. At this point the data is ready to be processed by the ODP.

Currently JPL is using the Single-Precision Orbit Determination Program (SPODP, see Refs. 7, 8) which is a second-generation ODP that corrects a-priori estimates of injection parameters, physical constants, and station locations, and also minimizes the sum of weighted squares of residual errors between the observed and computed quantities. The SPODP output includes a complete printout of the orbit calculations, residuals formatted for automatic plotting by a Stromberg Carlson 4020 plotter, and predictions of future DSIF data to be used by the DSIF stations, PRP and postflight analysis programs such as

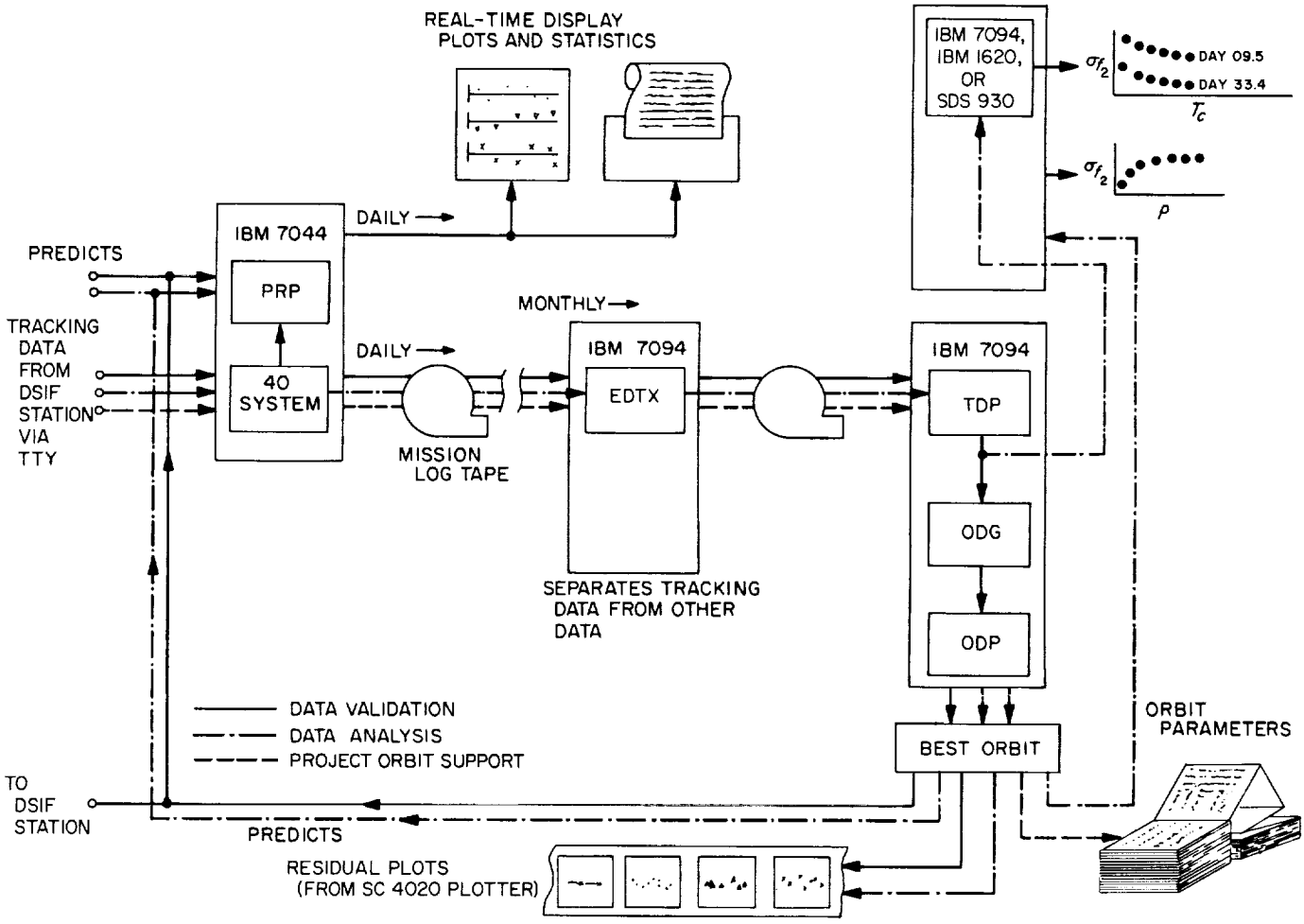

Fig. 29. Non-real-time tracking data processing system

the Residual Analysis Program (RAP) described below. JPL is currently developing a third-generation Orbit Determination Program called the Double-Precision Orbit Determination Program (DPODP) which has more accurate models, a significant increase in computational accuracy, and more flexibility than the current SPODP. Reports on the development of this program are a regular feature of *SPS*, Vol. III.

The output of the TDP as well as predictions from the best orbit determined by the SPODP are utilized by other programs for further post-processing of the tracking data to determine its noise characteristics. One of these programs now under development is RAP which computes the statistics of the various data types including their auto-correlation and spectral density functions.

In addition to the programs shown in Fig. 29, there is a family of programs designed to determine the orbit determination accuracies obtainable with the DSIF tracking data. Included in this family are:

(1) The Matrix Manipulation Program (MMP) designed to accept a tape of

$$\frac{\partial(\text{observable})}{\partial(\text{orbital element or physical constant})} \text{ partial}$$

derivatives and mapping matrices from the SPODP. The MMP is designed specifically for OD accuracy studies and can perform these runs for roughly 1/10 of the cost which would be incurred by using the SPODP.

(2) The Satellite Orbit Determination Studies (SODAS) program which uses a greatly simplified model over the SPODP to study OD characteristics for a spacecraft orbiting either the Moon or a planet.

I. Theoretical Basis for the DPODP: Time Transformations

T. D. Moyer

1. Introduction

This article is the second of a series which will present the theoretical basis for the Double-Precision Orbit Determination Program (DPODP). The first article described the program in general terms (*SPS 37-38*, Vol. III. pp. 24–26) and gave a list of detailed technical subjects to be covered in future articles, of which this is the first. This article describes the systems of time used in the DPODP and gives the formulas for transforming between these time scales.

2. Systems of Time

The DPODP utilizes five different systems of time as follows:

a. Ephemeris Time, ET. This is the uniform measure of time which is the independent variable for the equations of motion and hence the argument for the ephemerides of the planets, the Moon, and the probe.

b. Atomic Time, A.1. This is obtained from oscillations of the U.S. (cesium) Frequency Standard located at Boulder, Colorado. The value of A.1 was set equal to *UT2* on 1 January 1958, $0^h0^m0^s$ *UT2*. A.1 time increases at the rate of 1 second per 9,192,631,770 cycles of cesium, which is the best current esimate of the length of the ephemeris second.

c. Universal Time, UT (specifically UT0, UT1, or UT2). This is the measure of time which is the theoretical basis for all civil time-keeping. *UT* is defined in Ref. 1, p. 73 (the differences between *UT0*, *UT1*, and *UT2* will be defined below) as 12 hr plus the Greenwich hour angle of a point on the true equator whose right ascension measured from the mean equinox of date is:

$$R_U(UT) = 18^h38^m45^s.836 + 8{,}640{,}184^s.542T_U + 0^s.0929T_U^2 \qquad (1)$$

where T_U = number of Julian centuries of 36,525 days of *UT* elapsed since 1900 Jan. 0, 12^h*UT*.

The hour angle of this point is $\theta_M - R_U(UT)$, where

θ_M = Greenwich mean sidereal time, the Greenwich hour angle of the mean equinox of date.

Hence, *UT* is a function only of θ_M:

$$\theta_M = UT + R_U(UT) + 12^h \qquad 0 \leq \theta_M, \mathrm{UT} \leq 24^h \qquad (2)$$

(Note that any integer multiple of 24 hr may be added to the right-hand side, and hence the $+12^h$ term could also be written as -12^h.)

UT is obtained from meridian transits of stars by the U.S. Naval Observatory. At the instant of observation, the right ascension of the observing station is equal to that of the observed star, relative to the true equator and equinox of date. Subtracting the east longitude of the observing station gives the true Greenwich sidereal time θ at the instant of observation:

θ = true Greenwich sidereal time, the Greenwich hour angle of the true equinox of date.

Subtracting the nutation in right ascension (Ref. 1, p. 43) gives Greenwich mean sidereal time, θ_M. Solving Eq. (2) gives the value of *UT* at the instant of observation. Each observing station has a nominal value of longitude used for computing *UT*; if this nominal value is used, the resulting *UT* is labeled *UT0*. Due to wandering of the pole, the latitude and longitude of a fixed point on the Earth are a function of time. Using the true longitude of the observing station at the observation time, the resulting *UT* is labeled *UT1*. *UT1* has predictable seasonal fluctuations; if these are removed, the resulting time is labeled *UT2*.

The DPODP uses only *UT1*. It takes the value of *UT1* supplied by the U.S. Naval Observatory and computes θ_M from Eq. (2). Adding the nutation in right ascension gives θ which is used to compute the position of a tracking station relative to the true equator and equinox of the date of observation.

d. Broadcast Universal Time, UTC. This is Greenwich civil time which is an approximation of *UT2*. *UTC* is derived from the U.S. Frequency Standard at Boulder, Colorado, and deviates from *UT2* by a known amount having a maximum of about 0.200 sec. It is broadcast from several National Bureau of Standards and U.S. Naval Observatory stations, such as WWVL, WWV, and WWVH. The seconds pulses are of length 9,192,631,770(1-S) cycles of cesium. For the years 1960 to 1966, the annual values of S were -150, -150, -130, -130, -150, -150, and -300×10^{-10}, respectively. The value of S is changed annually by international agreement. Several times a year, as required, an even fraction of a second, typically 0.100

sec, is added to or subtracted from *UTC* so that it will not deviate from *UT2* by more than 0.100 to 0.200 sec. The step changes to broadcast *UTC* are announced in advance by the U.S. Naval Observatory.

e. Station Time, ST. This is obtained at each DSIF station by counting cycles of a rubidium atomic frequency standard. The difference between *ST* and *UTC* is tabulated by each station.

3. Transformations Between Time Scales

The transformation between *A.1* time and *ET* is given by

$$(ET - A.1) = \Delta T_{1958} - \frac{(\text{J.D.} - 243{,}6204.5)\,(86{,}400)}{9{,}192{,}631{,}770} \times \Delta f_{cesium} + \frac{2e\,(\mu a)^{1/2}}{c^2} \sin E \qquad (3)$$

where

ΔT_{1958} = *ET-UT2* on 1 January 1958, $0^h0^m0^s$ *UT2* minus the periodic term in (3) above evaluated at this same epoch.

J.D. = Julian date.

243,6204.5 = Julian date on 1 January 1958, $0^h0^m0^s$.

Δf_{cesium} = correction to $f_{cesium} = 9{,}192{,}631{,}770$ cycles of cesium per ephemeris second.

μ = gravitational constant of Sun, $1.327{,}154{,}45 \times 10^{11}$ km^3/sec^2.

a = semi-major axis of heliocentric orbit of Earth-Moon barycenter, 149,599,000 km.

e = eccentricity of heliocentric orbit of Earth-Moon barycenter, 0.01672.

c = speed of light at infinite distance from Sun, 299,792.5 km/sec.

E = eccentric anomaly of heliocentric orbit of Earth-Moon barycenter.

Substituting numerical values, the coefficient of the periodic term in (3) above is 1.658×10^{-3} sec. For an accuracy of 10^{-6} sec in the value of the periodic term, the eccentric anomaly E may be computed from the following approximate solution to Kepler's equation:

$$E \approx M + e \sin M \qquad (4)$$

where the mean anomaly M is given by (Ref. 1, p. 98)

$$M = 358°28'33''.04 + 129{,}596{,}579''.10T - 0''.54T^2 - 0''.012T^3 \qquad (5)$$

where

T = number of Julian centuries of 36525 days of *ET* elapsed since 1900 Jan 0, 12^h *ET*

To sufficient accuracy, the T^2 and T^3 terms can be evaluated for $T = 0.7$ and subtracted from the constant term of (5) giving

$$M = 358°28'32''.77 + 129{,}596{,}579''.10T \qquad (6)$$

The first term of (3) arises since *A.1* was set equal to *UT2* at the beginning of 1958. The second term accounts for the difference between the lengths of the *ET* and *A.1* seconds (if Δf_{cesium} is non-zero). The periodic term of (3) arises from general relativity. It accounts for the fact that *A.1* time (as well as *UTC* and *ST*) is a measure of *proper time* observed on Earth and that *ET* is a measure of *coordinate time* in the heliocentric (strictly barycentric) space – time frame of reference.

The parameters ΔT_{1958} and Δf_{cesium} are solve-for parameters in the DPODP.

The remaining transformations between the various time scales are specified by linear or quadratic functions of time t. The coefficients of these polynomials are specified by time block and the argument t is seconds past the start of the time block.

$$UTC\text{-}ST = a + bt + ct^2 \qquad (7)$$

$$A.1\text{-}UTC = d + et \qquad (8)$$

$$A.1\text{-}UT1 = f + gt + ht^2 \qquad (9)$$

To a sufficient degree of accuracy, each of Eqs. (3) and (7) to (9) may be used to transform in either direction, the right-hand side being evaluated with the known time. For instance, Eq. (7) may be evaluated at a *ST* epoch in order to transform to *UTC*. Also, it may be evaluated at a *UTC* epoch in order to transform to the corresponding *ST* epoch.

The coefficients a through c are solve-for parameters in the DPODP; a-priori values are supplied in time blocks by each DSIF station. The U.S. Naval Observatory supplies weekly values of *A.1-UTC* and *A.1-UT1*. Curve

fitting techniques are used to obtain the polynomial coefficients d through h by time block, normally of 1 month's duration. Real-time reduction of data is accomplished using extrapolated polynomials for the current month.

The observables are recorded in ST. In order to obtain the computed values of the observables, the ephemerides of the probe, planets, and Moon which affect the observables must be interpolated at the ET epoch of observation, obtained from the ST epoch by using Eqs. (7), (8), and (3). The angular position of the Earth at the observation time is computed from Eq. (2) using the $UT1$ epoch of observation obtained from the ST epoch using Eqs. (7), (8), and (9).

J. Accuracy of the SPACE Trajectories Program for a *Lunar Orbiter*

J. F. Gallagher

The *Lunar Orbiter* is a somewhat different mission from those with which JPL has had experience in that it consists of from 1000 to 2000 orbits about a primary body, whereas lunar and planetary missions are tracked for less than one orbit. This new situation requires a reexamination of the accuracy of the single-precision space trajectories program, SPACE (Ref. 6). Regarding the mathematical model and physical constants as exact, we can study the numerical integration error of SPACE and seek answers to questions such as:

(1) How does the integration error grow as a function of time or number of orbits?

(2) What is the best integration step size?

(3) What is the running time behavior of the program?

With answers to these questions one can answer such project-related questions as:

(1) How many orbits of data should be fit at one time in the orbit determination process?

(2) For how many orbits can sufficiently accurate station predicts and occultation times be calculated?

(3) Over how many orbits can SPACE accurately locate the position of the spacecraft so that the selenographic position of the photographed areas can be accurately determined?

(4) How much time must be allocated in mission operations for trajectory computation?

Ref. 7 gives the results of an extensive study of the accuracy behavior of the single-precision space trajectories program, SPACE, for orbiters. Portions of that report have been selected for presentation here.

The work described in Ref. 7 used a *Lunar Orbiter* trajectory as the subject for study. It is a final or photographic orbit and is described by:

Injection epoch June 29, 1966, $1^h33^m5^s$ GMT

$a = 2686.0785$ km

$e = 0.33577167$

$T_p =$ June 28, 1966, $23^h49^m1^s$ GMT

The orientation angles referred to the mean Earth equator and equinox of 1950.0 are:

$i = 34.169866$ deg

$\Omega = 17.290042$ deg

$\omega = 19.832598$ deg

These angles referred to the true lunar equator and lunar vernal equinox of date are:

$i = 15.000036$ deg

$\Omega = 352.45055$ deg

$\omega = 348.76693$ deg

The true anomaly at injection is:

$v = 179.96654$ deg

The attempt was to discover the effect of the integration step size and the number of orbits upon the accuracy and running time of the program. All other quantities

of the program such as the masses of the planets and Moon were held fixed. The first half of the study used a spherical Moon and no n-body perturbations in order to have an analytical accuracy standard available. The second half used a trajectory with all of the perturbations included except solar pressure. Comparing the two halves of the study confirmed that the accuracy behavior of SPACE is the same whether or not perturbations are included, and thus the accuracy results from the first half of the study, for which a standard was available, are applicable to the perturbed trajectories which, of course, are the ones actually flown by the spacecraft.

The trajectory program introduces error in a very simple way. In position, the error is an "in-track" error, i.e., the simulated spacecraft travels on essentially the same ellipse as the actual spacecraft but falls behind, the distance between the two being greatest at perilune, least at apolune and the average separation growing with each succeeding orbit. In velocity, the error vector is directed radially outward from the Moon, and its greatest magnitude occurs at perilune, its least magnitude at apolune and the average value increases from orbit to orbit. (For

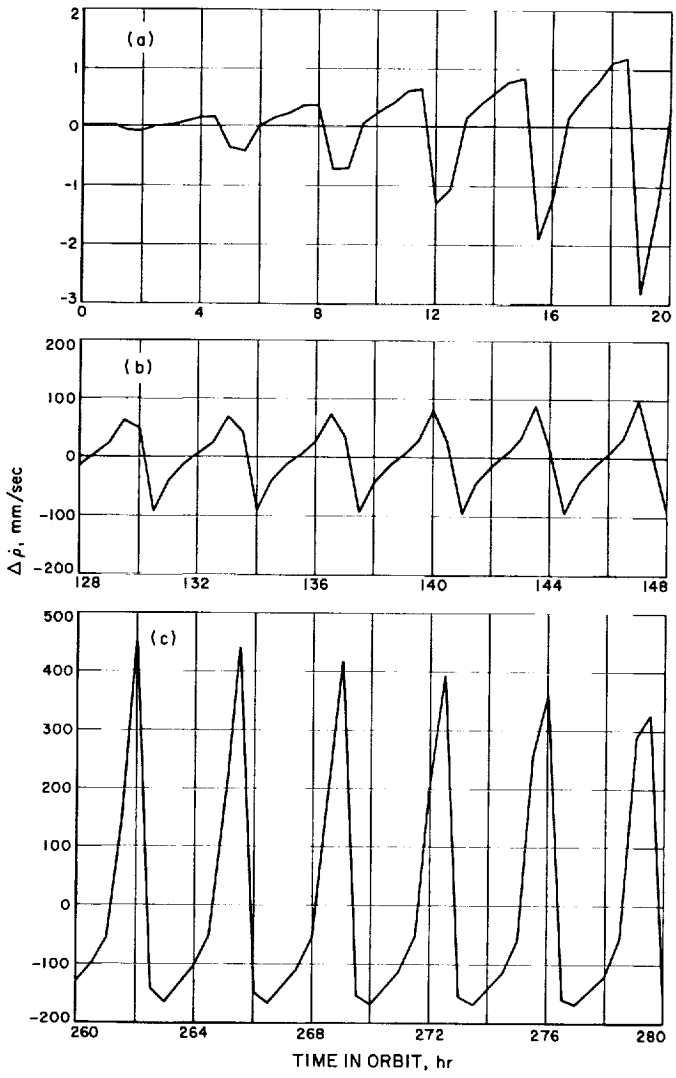

Fig. 30. Range-rate error with 30-min data interval, $\Delta t = 60$ sec

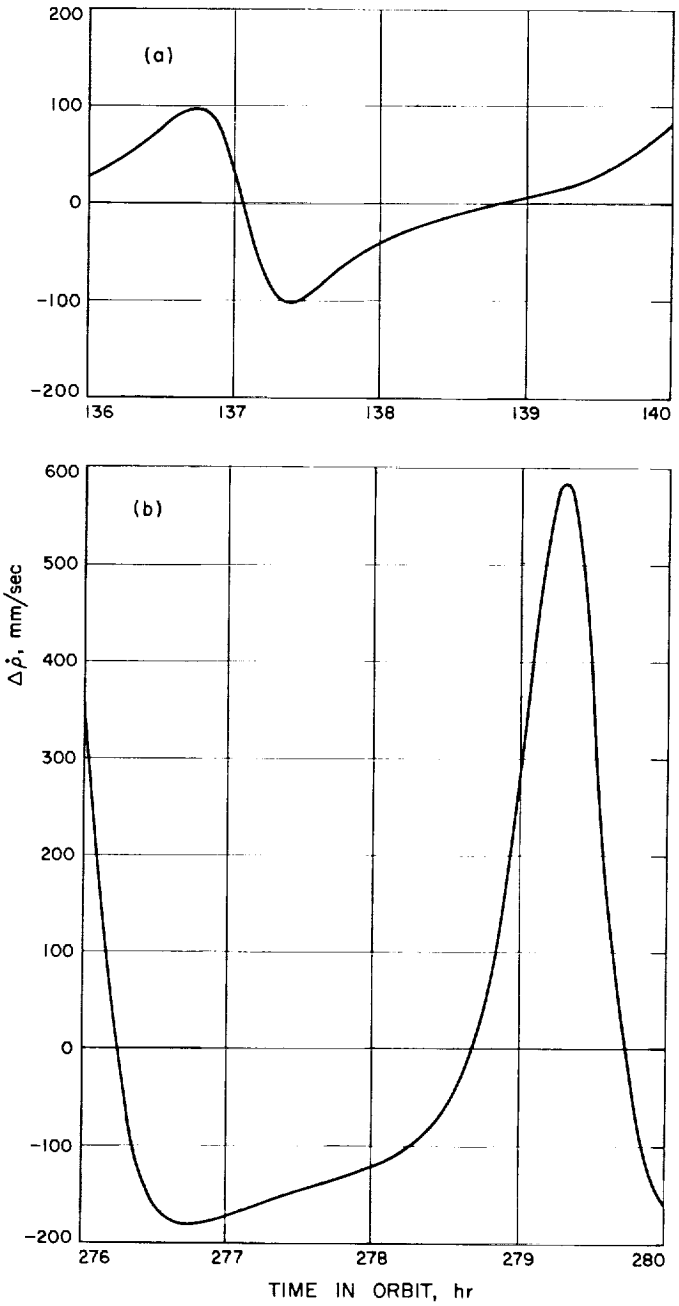

Fig. 31. Range-rate error with 10-min data interval, $\Delta t = 60$ sec

integration step sizes of 80 sec and more, the situation is reversed. The position error is a leading type in track error rather than a lagging, and the velocity error is radially inward toward the Moon.)

The effect of the integration error upon the geocentric range rate is shown in Figs. 30 and 31. In these figures, time is measured from injection into the final orbit. The plots show the error in the range rate at a given time. The Moon was regarded as transparent. The integration step size used in these plots was 60 sec. These curves are typical of other range rate error curves for other integration step sizes. They differ only in the magnitude of the error, not in the shape. Three 20-hr segments from a 280-hr trajectory are shown in Fig. 30: 0–20, 128–148, and 260–280-hr. These plots were done at 30-min data intervals. Fig. 31 data plots were done at 10-min intervals over a 4-hr period and give one a better idea of the true shape of the error curves. The changing shape of the curves is due to the changing relationship of the Earth, Moon and perilune point.

From Fig. 30, we see that the maximum range rate error for $\Delta t = 60$ sec is about 2.8 mm/sec during the first 20 hr. A step size of 40 sec was found to produce the most accurate trajectories, showing a maximum range rate error of about 1.4 mm/sec during the first 20 hr. The DSIF is capable of more accuracy than this, and the OD process must strike some sort of balance between the length of the data arc used and the statistics on the DSIF data.

For 1500 integration iterations and more, the running speed was very consistent at about 675 iterations per minute for the A machine, which is an IBM 7094 Model I. The Model II machines in the Space Flight Operations Facility (SFOF) showed running times nearly twice as fast at about 1200 iter/min. Integration of the variational equations increases the running time by about 50%, i.e., the running rate is decreased to about 800 iter/min on the Model II machines when variational equations are done.

Combining the results of Ref. 7, samples of which are given in this article, with information from the project allows one to answer project-related questions such as those given above. For example, having information on the error build-up in the range rate assists the OD analyst in selecting a set of weights to be applied to the doppler data so that the bias introduced by the integrator can be absorbed in the OD solution statistics and the number of orbits to be fit in one pass can be chosen.

K. *Apollo* Project Support

D. W. Curkendall

The task reported here has as its objectives to provide the systems analysis effort to support the development of Unified S-band to be used in the *Apollo* program, to develop the capability to participate in the *Apollo* S-band qualification tests, and to assist the Manned Spaceflight Center (MSC) and Goddard Spaceflight Center (GSFC) in the planning and execution of the navigation aspects of the *Apollo* lunar landing mission. Specific items under this task will be selected each report period for further discussion.

1. Tracking and Navigational Accuracy Analyses

The *Apollo* task includes, but only partially funds items reported under Tracking and Navigational Accuracy Analyses found elsewhere in Sect. G of this volume. In that Section, D. Curkendall contributes the second of a series of articles investigating the ability to estimate a probe's velocity with doppler data corrupted by noise of a specific character. In the first article (*SPS 37-38*, Vol. III, pp. 20–24), the doppler data was assumed to be corrupted by stationary white, or uncorrelated, range noise. This restriction is relaxed in the present article, and the analysis is made assuming a stationary but exponentially correlated noise model. On the basis of this analysis, it is concluded that (1) so-called "destructive counting mechanisms" (as opposed to continuously integrating the doppler signal) should not be used in precision tracking systems, and (2) the possibility of using the total count in the doppler counter as a data type rather than differencing adjacent counter readings is an attractive possibility in certain circumstances.

2. Unified S-Band Qualification Tests

JPL is participating with GSFC and MSC in the development and performance of the Unified S-Band qualification tests. Starting with the sub-orbital *Apollo* SA 202 mission, S-band equipment will be carried on a series of *Apollo* flights for testing and evaluation under operational conditions. These tests will form the basis for qualifying the S-band systems to become the prime communications and tracking system for later missions.

In order to be able to process the tracking data, JPL is modifying its trajectory programs to include an atmospheric drag model compatible with MSC's and is building the capability to accept the MSFN tracking data formats and data types in the single precision data editing and orbit determination programs.

L. *Pioneer* Project Support

D. W. Curkendall, R. Ball, and J. E. Ball

1. Introduction, D. W. Curkendall

The *Pioneer* program consists of a series of spacecraft whose purpose is to gather scientific information concerning the deep-space environment in the region near the ecliptic plane and at a distance from the Sun varying from 0.8 to 1.2 AU. The DSN is committed to track the *Pioneer* spacecrafts, obtain engineering and scientific telemetry, determine the orbit of each probe, and provide facilities to the Project within the SFOF and the DSIF for the conduct of the mission and reduction of data. Specific items under this task will be selected during each report period for further discussion.

In this issue, the high-frequency tracking-data noise obtained from the *Pioneer* probe is analyzed. The behavior of the magnitude of the high-frequency noise as a function of round-trip light time to the probe (Fig. 32) is presented and discussed.

The effects of an observed gas leak upon the orbit of the *Pioneer VI* probe are also presented. TRW Systems, a subcontractor to the *Pioneer* project, is attempting to extend this analysis. For this purpose JPL has supplied them with 10 days of raw tracking data during the early portion of flight.

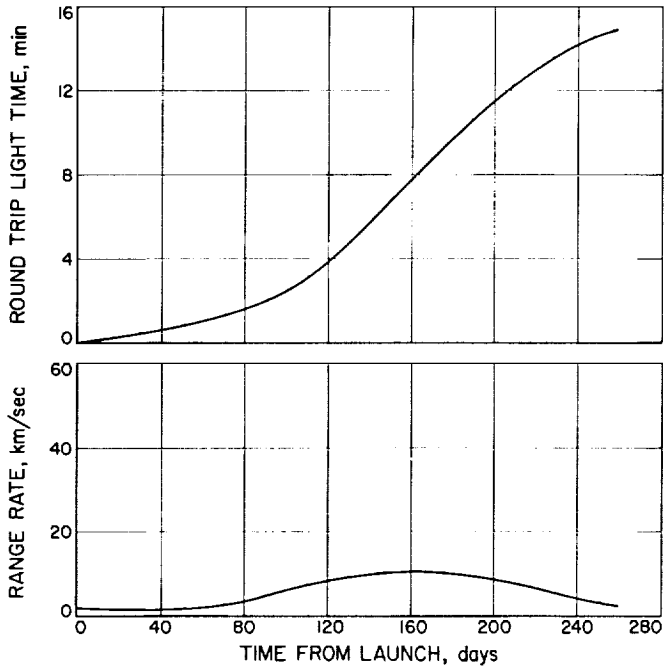

Fig. 32. *Pioneer VI* range and range rate versus time from launch

2. Pioneer VI High-Frequency Doppler Noise, R. Ball

Estimates of the high-frequency noise present in the *Pioneer VI* tracking data have been computed by removing from the doppler the effect of the rotating Earth and fitting the resultant with a third- to tenth-order polynomial. A previous report (*SPS 37-38*, Vol. III, pp. 90–92) of the same title by W. D. Chaney presented the results of this analysis up to 30 January 1966; this report updates the data to 15 April 1966.

The data included in this report is 60-sec sampled continuous count doppler from Deep Space Stations 12, 41, 42 and 51. Stations (DSS) 11 and 61 took insufficient data of the type used in this report and so are not included.

This doppler data is of three types. Times-one ($\times 1$) data was taken at DSS 41 and 51. Times-two ($\times 2$) data was taken at DS 42, and Resolver data was taken at DSS 12 (see *SPS 37-38*, Vol. III, for details). Fig. 33 shows the results of the noise estimation procedure on this data. These estimates are formed from the standard deviation of the difference between observed doppler and the polynomial mentioned above.

All data used here after 18 January 1966 is of special form called Plan B, which was taken for orbit determination and inherent accuracy reasons. Plan B's precepts (as compared to Plan A) are:

(1) Sampling rates will be 10 sec for about 0.5 hr at rise, zenith, and set.

(2) Data shall be as high quality and as continuous as possible.

(3) Orbital calculations and noise statistics will be based on this data.

Fig. 32 gives the round-trip light time ($2 \cdot Range/c$) and $\dot{R}$ for the *Pioneer VI*. Fig. 33 shows that even at a round-trip light time of 4.5 min, the stability of the rubidium standard is good enough that no appreciable increase in noise can be observed. It can also be readily seen from Fig. 33 that space noise, due to increasing range, is not yet the controlling influence in the high-frequency doppler noise. It should be noted that up until mid-April, the transmitted power level was continuously increased such that received power at the spacecraft has

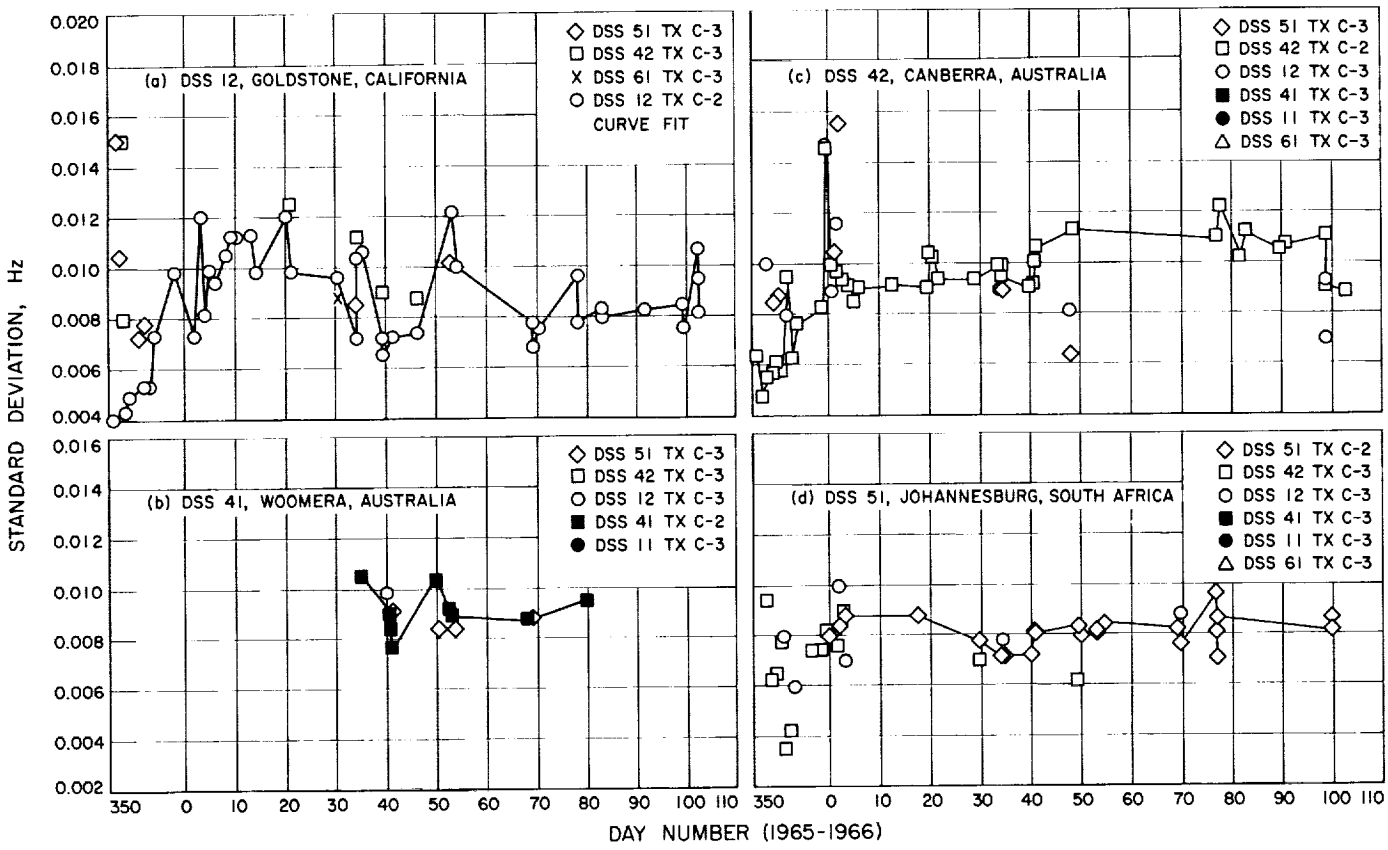

Fig. 33. High-frequency doppler noise versus day number

remained constant. This transmitter power level reached 10 kw (the station's limit) in mid-April; and from now on the spacecraft received power will decrease. This decreased uplink power plus increased range effects should begin to increase high-frequency noise.

3. *The Effect of the Gas Leak on the Pioneer VI Orbit,* J. E. Ball

A study was undertaken to investigate the gas leak on board the *Pioneer VI* spacecraft for its perturbing effect on the trajectory. Stored on board the spacecraft was bottled nitrogen gas initially at 3200 lb/in^2. The gas after going through a gas regulator is directed through a low-pressure (50 lb/in^2.) chamber and out through a nozzle. This pneumatic subsystem serves as the orientation system for properly aligning the spacecraft's spin axis with respect to the Sun-Earth line. After the spacecraft performed its orientation maneuvers, a gas leak was observed and a plot of the nitrogen gas pressure versus time is shown in Fig. 34. TRW Systems fitted the exponential curve

$$P = 1740e^{-0.027t}$$

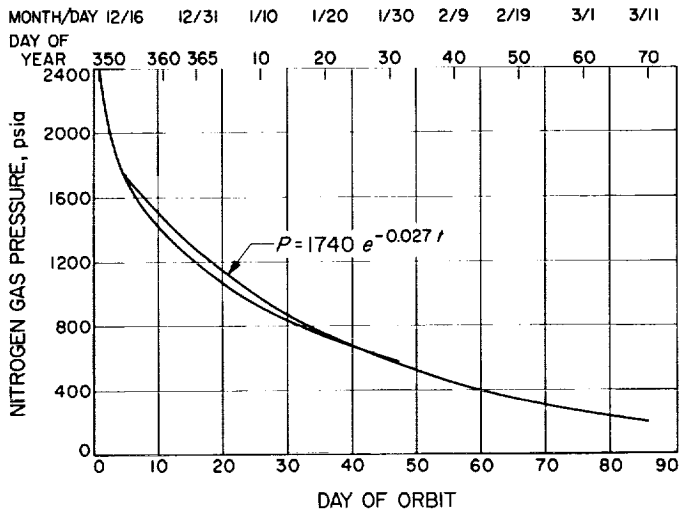

Fig. 34. *Pioneer VI* nitrogen gas pressure versus time from launch

to the points, and this fit is also shown in Fig. 34. Since the gas pressure is following an exponential curve, the gas leak is assumed to be in the high-pressure side. The

spacecraft is spinning at the rate of approximately one revolution per second and the spin axis is nearly perpendicular to its orbit plane (also the ecliptic plane). If the leak is continuous, the only component of the force that would perturb the trajectory is the component along the spin axis since the other component would be averaged to zero by the spinning.

JPL's single-precision orbit determination program (SPODP) does not presently have the capability of solving for or including in the trajectory model an exponentially decaying perturbative force. The results of fitting a trajectory to a short arc of the *Pioneer* data using a restricted model, allowing only constant perturbative forces, is presented in Fig. 35. Two-way doppler data (CC3), sampled one point every 10 min, was collected over a period of 9 days starting at December 18, 1965 and ending at December 27, 1965. An orbit was obtained by fitting to this data using JPL's single-precision orbit determination program. The numerical difference between the observed CC3 and its calculated value is the residual. The residuals shown in Fig. 35 represent a typical 6-hr frame for the Goldstone station. As can be seen in Fig. 35, the residuals lie very close to zero. This indicates that the models used in the SPODP describing the "fit" world for a 9-day period agrees with what is occurring in the "real" world.

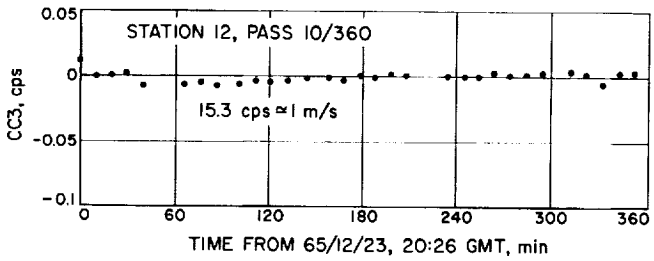

Fig. 35. Fit of 9 days of two-way doppler data to the trajectory model

Data was allowed to accumulate for 28 days, and at that time a comparison was made between the actual two-way doppler data from Canberra (Station 42) on January 13 and the value predicted by the SPODP from the orbit of the 9-day fit for Canberra on January 13. Fig. 36 shows these residuals. If our prediction orbit were accurately describing the actual orbit of the spacecraft, then the residuals should lie along the zero residual line, and should *not* have the pattern of residuals shown in Fig. 36.

A new orbit estimate was obtained using the SPODP by fitting to the 28 days of tracking data. Fig. 37 is a plot of the CC3 residuals. Notice, in the 9-day orbit fit (Fig. 35), the residuals lie close to the zero residual line while in the 28-day orbit fit (Fig. 37) the doppler residuals display a dish-shape pattern and are displaced by as much as 0.05 cyc/sec.

Fig. 38 shows the results when two-way doppler observables calculated from an orbit estimate using the 28 days of tracking data are compared to the actual two-way doppler data for a Canberra pass on January 22, 1966 (35 days out). The pattern of the residuals is identical to the pattern of the previous residuals, which indicates that some long-term acceleration effect is acting on the spacecraft that is not accounted for in our model.

Since the orbit determination program used for *Pioneer* is the same orbit program used for *Mariner IV*, the *Pioneer* two-way doppler residuals should look the same as the *Mariner IV* doppler residuals in the absence of such modeling errors. Fig. 39 shows a typical frame of the *Mariner IV* fit of 30 days of data 6 months from launch. The *Pioneer* residuals are not behaving in the same manner as the *Mariner IV* residuals and it is probable that the gas leak is causing this anomaly.

If all of the gas is leaking through a nozzle of 100% efficiency, directed through the center of gravity and

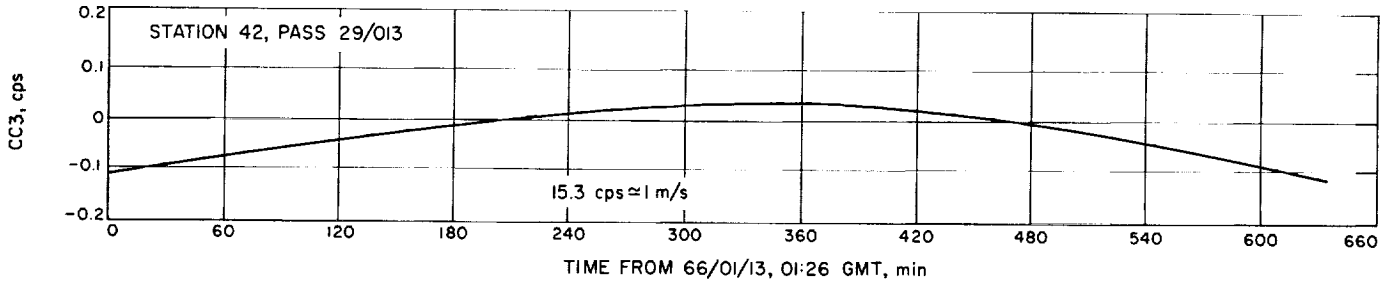

Fig. 36. Comparison of range rate residuals of 9-day orbit fit to the tracking data at 28 days

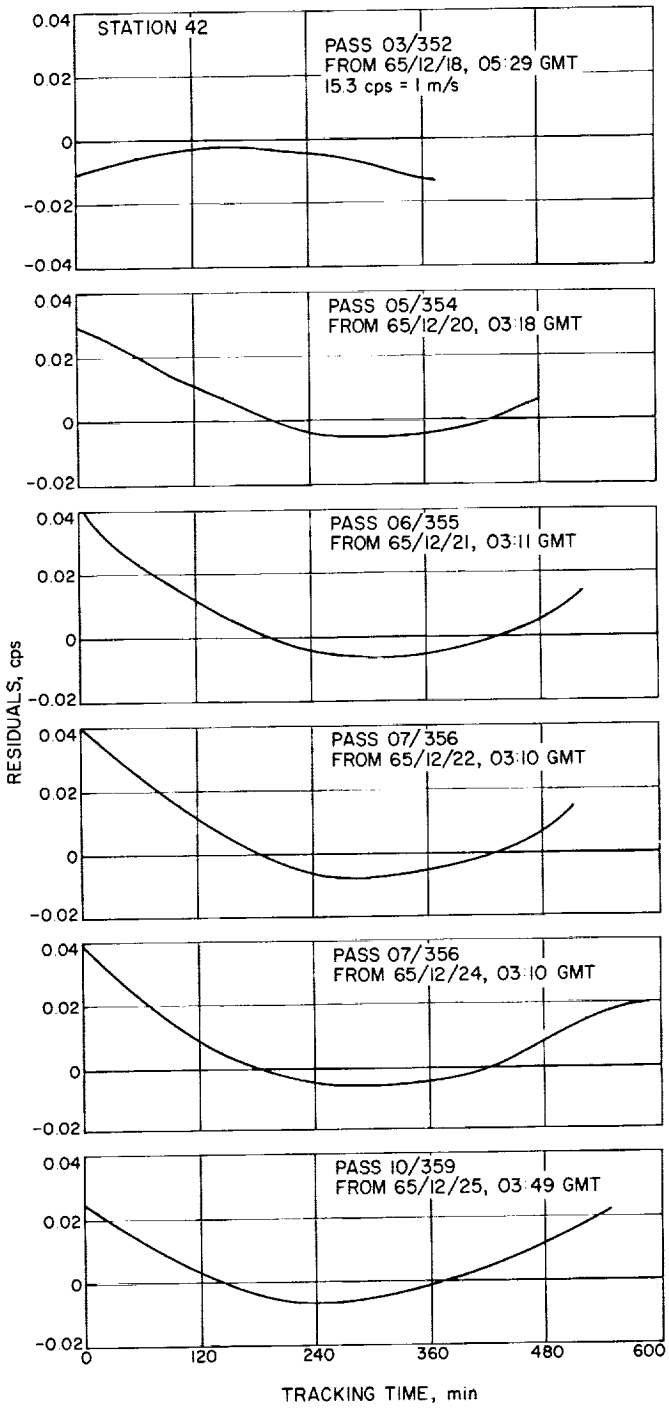

Fig. 37. Fit of 28 days of two-way doppler data to trajectory model

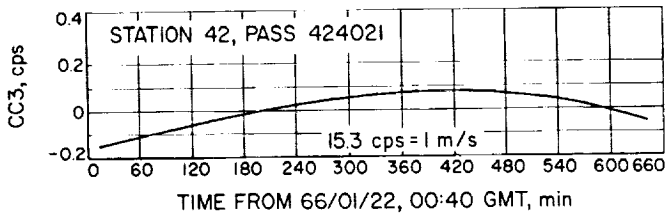

Fig. 38. Comparison of range rate residuals of 28-day orbit fit to the tracking data at 35 days

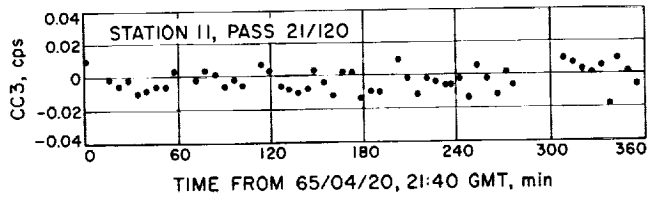

Fig. 39. Typical *Mariner IV* fit of 30 days of data 6 months from launch

parallel to the spin axis, then the maximum average acceleration from end of Type II maneuver to 60 days later is 0.42×10^{-6} m/sec^2. This constant perturbing acceleration was then inserted into the SPODP to test the effect of the perturbing acceleration on the doppler residuals. The procedure was to generate artificial tracking data displaced by the amount of the gas leak acceleration. The artificial tracking data was then used by the SPODP to calculate an orbit from a model that did not account for a gas leak effect. The residuals from the first 10 days are presented in Fig. 40.

Fig. 40 shows the effect of the fit on the doppler residuals when a constant 20% of the maximum gas leak acceleration is applied parallel to the spin axis. Fig. 40 also shows the effect of applying only 2% of the gas leak acceleration parallel to the spin axis. Comparing the doppler residual plots of the 20% gas leak acceleration and the 2% gas leak acceleration residual plots to the *Pioneer* 28-day orbit residual plots (Fig. 37), the residual plots are identical except for the magnitude of the displacement of the residuals from the zero residual line. From the results of the two simulated cases, they show that the amplitude of the residual curve is linear. By interpolation it is concluded that about 10% of the total acceleration acting along the spin axis could cause the trajectory of the *Pioneer* spacecraft to change enough to explain the difference between the orbit calculated by the SPODP and the *Pioneer* orbit. This perturbation is not large enough to affect the trajectory to an extent that will degrade the primary scientific mission, but they make the task of solving for the astronomical constants such as the AU and the Earth's ephemeris more challenging.

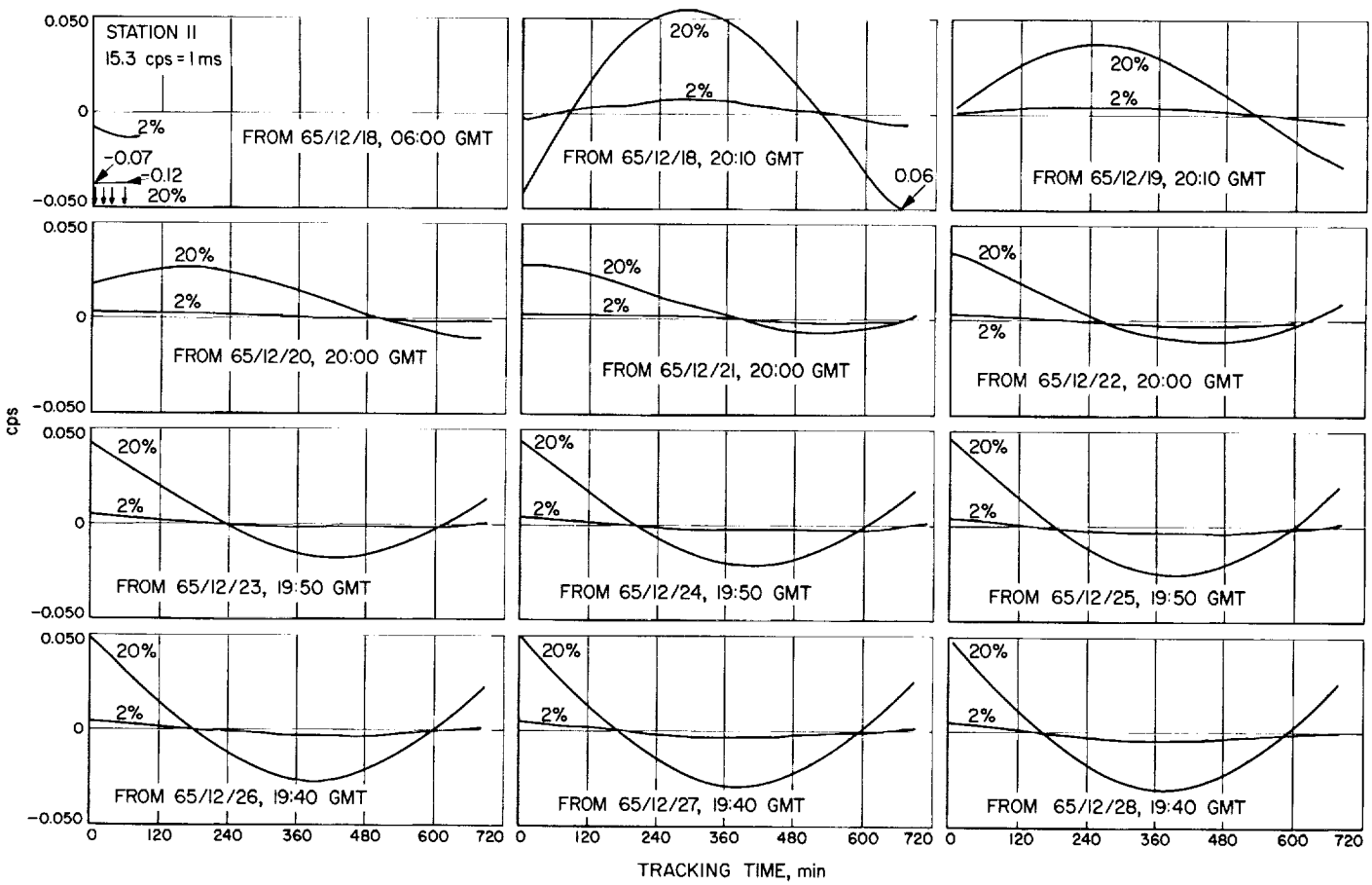

Fig. 40. Fit of 67 days of simulated gas leak data to model

References

1. *Explanatory Supplement to the Ephemeris*, see all indexed references under "Time," Her Majesty's Stationers Office, London 1961.

2. US Naval Observatory, Washington, D.C.; 202-696-8421. For practical timekeeping and observations, time theory, and lunar *ET* determinations, write or call Dr. W. Markowitz, Dr. C. A. Lidback, or Dr. G. Hall.
   Some samples of USNO publications:
   The Atomic Time Scale, W. Markowitz, Reprint 34, US Naval Observatory, Washington, D.C.
   The Second of Ephemeris Time, as above, Reprint 14.
   Rotation of Earth, as above, Reprint 2.
   Motion of the Pole, as above, Reprint 11.
   Ephemeris Time, G. Clemence, as above, Reprint 1.
   Tidal Variations in Earth Rotation, E. Woolard, as above, Reprint 3.

References (Cont'd)

3. National Bureau of Standards, U.S. Department of Commerce, Bolder, Colorado 80301. For publications and reference services, write *U.S.F.S.*, J. A. Barnes, Atomic Frequency and Time Standards, or *V.L.F.*, D. H. Andrews, Chief of 251.2 Frequency-Time Broadcast Services.
4. Munk, W. H., Macdonald, G. J. F., *The Rotation of the Earth*, Cambridge University Press, 1960.
5. Carpenter, R., "Ranging System Evaluation," *Research Summary No. 36-13*, pp. 42–44, Jet Propulsion Laboratory, Pasadena, California, March 1, 1962.
6. Holzman, R. E., *Users' Guide to the Tracking Data Processor and Orbit Data Generator Programs*, Reorder 65-205, Jet Propulsion Laboratory, Pasadena, California, May 27, 1965.
7. Warner, M. R., Nead, M. W., Hudson, R. H., *The Orbit Determination Program of the Jet Propulsion Laboratory*, Technical Memorandum 33-168, Jet Propulsion Laboratory, Pasadena, California, March 18, 1964.
8. Warner, M. R., Nead, M. W., *SPODP-Single Precision Orbit Determination Program*, Technical Memorandum 33-204, Jet Propulsion Laboratory, Pasadena, California, February 15, 1965.
9. *Explanatory Supplement to the Ephemeris*, Her Majesty's Stationery Office, London, 1961.
10. White, R. J., et al, *SPACE-Single Precision Cowell Trajectory Program*, TM 33-198, Jet Propulsion Laboratory, Pasadena, Calif., January 15, 1965.
11. Gallagher, J. F., *Accuracy and Running Time Study of SPACE for a Lunar Orbiter*, TM 312-620, Jet Propulsion Laboratory, Pasadena, Calif., November 22, 1965.
12. Gallagher, J. F., *A Few Further Results on Unperturbed Orbits and Accuracy Results on Perturbed Orbits for a Lunar Orbiter*, TM 312-620 Addendum 1, Jet Propulsion Laboratory, Pasadena, Calif., February 17, 1966.

IV. Communications Research and Development

A. Efficient Data Systems: Teletype Coding Experiment

H. N. Fredricksen and E. C. Posner

This is the status report of a continuing project to develop and demonstrate an error-correcting coding and decoding system for DSN teletype. The program is now at a stage in which single error correction has been demonstrated.

1. Review

Commands are sent on the DSN ground communication system (GCS) from the SFOF to the DSIF sites for transmission to spacecraft. Errors in such messages can be disastrous to a mission; hence, some form of error correction for teletype is needed. Experiments were performed at JPL (*SPS 37-34*, Vol. III, pp. 64–68) to determine the error characteristics of the GCS teletype circuits. An error-correcting code was chosen which corrects both character and synchronization errors. The code takes 32 binary bits, regarded as 8 characters of the 16-element field, and a ninth synchronization character, and encodes them into a word of length 15 over the 16-element field. The four positions of the characters from the 16-element field are regarded as the first four teletype levels. The fifth level is taken as even parity on the first four, because of special requirements in the NASCOM communications processor and in the overseas repeating stations (*SPS 37-35*, Vol. III, pp. 71–76).

The goal is to take a worst-case teletype channel in which the bit error probability is 10^{-2} and create a reliable teletype channel with a bit error probability of 10^{-9}. This is accomplished by correcting all single and double character errors, and detecting all synchronization errors and all error patterns of five or less. In this mode, the bit error probability is the required figure of 10^{-9} or less, whereas the probability of an error detected but not correctable is still small, less than 10^{-4}. In this latter case, repeat transmission must be requested.

2. Status

The encoder–decoder, a Scientific Data Systems 910 computer, has been installed at JPL in the Information Processing Laboratory and will function as the prototype communications processor (PCP).

The PCP talks to the teletype lines through a teletype interface console (TIC) which performs the functions of a teletype transmitter and receiver under 910 control. The TIC has been installed and is in the acceptance phase.

A full-duplex teletype line between the SFOF Communications Center and the Information Processing Lab has been installed. This will allow on-line encoding and decoding. A Teletype Corp. Model 28 chassis has been installed to allow testing and monitoring of the experimental program.

The encoding program has been written; the decoding program is written as far as the double error-correction feature. Using the theory of error-correcting codes, this subprogram has proved to be workable.

B. Efficient Data Systems: A Multipurpose Digital Autocorrelator for the DSN

W. Tveitan

1. Summary

A compact, multipurpose spectrum analysis system has been designed, built, installed at Goldstone, and tested. The system consists of assorted bandpass filters, a digital autocorrelator, autocorrelator-to-computer interface equipment, a SDS 920 computer, computer programs, a digital-to-analog converter, and an *X-Y* plotter. The available spectrum bandwidths range from 11 to 2100 cps, and the cumulation capacity of the correlator is 8 hr, minimum. This autocorrelator is the result of an attempt to provide an initial standard DSN autocorrelator design.

2. Over-all System

Sensitive and flexible spectrum analysis equipment is needed in the Deep Space Network for tracking weak spacecraft signals, as well as for station spectrum monitoring: the spectrum monitoring serves to detect signals leaking from station equipment, and also external extraneous signals that interfere with proper station operation.

A multipurpose autocorrelator has been designed and built in JPL Section 331, to provide a spectrum analysis capability when used in conjunction with an SDS 920 computer. The autocorrelator is installed in the alidade room at the Mars Station. The spectrum analysis system, including both the program of the SDS 920 computer and the spectrum plotting equipment, has been operationally tested and appears to work as intended. Features providing complete computer control of the autocorrelator operation (presently manually controlled) are being prepared for immediate installation.

3. Design

The correlator design is quite simple, and most of its hardware was salvaged from earlier Section 331 projects (several bandpass filters with a center frequency of 1050 cps were on hand). The filter bandwidths are 400, 200, 100, 50, and 10 cps. The correlator is designed to be compatible with these filters and to accommodate spectrum bandwidths of 700 and 2100 cps.

The correlator has a basic sampling period of 238 μsec, which corresponds to a sampling frequency of 4201.68 samples/sec. Table 1 relates the various available sampling periods to: the corresponding sampling frequencies, the bandwidths, and the orientation of the resulting spectrum after the Fourier transformation of the autocorrelation function is performed. (A reversed spectrum results when a harmonic of the sampling frequency lies at the upper end of the band-limited input spectrum, instead of at the lower end.)

The autocorrelation function of the input signal is calculated for 238 discrete and equidistant values of time shifts. This large number permits high resolution in the spectrum analysis. The basic increment of the time shift varies with the sampling rate and is equal to the sampling

Table 1. Autocorrelator characteristics

Sampling period, msec	Sampling rate, samples/sec	Sampling bandwidth, cps	Filter bandwidth, cps	Spectrum type	Spectrum center, cps
0.238	4201.68	2100.8	NA[a]	Normal	1050.4
0.714	1400.5	700.3	NA[a]	Reversed	1050.4
1.19	840.3	420.2	400	Normal	1050.4
2.142	466.9	233.4	200	Normal	1050.4
4.522	221.1	110.6	100	Reversed	1050.4
9.282	107.7	53.9	50	Reversed	1050.4
45.458	22	11	10	Reversed	1050.4

[a] Not available.

period. In order to make use of the high resolution potential, a large cumulation capacity has been provided so that the autocorrelator can operate for approximately 8 hr, even at its highest sampling rate, before overflow and consequent loss of information can occur. In other words, data output transfer is not required more often than once every 8 hr to prevent loss of information in the autocorrelator.

The output of the autocorrelator is in the form of 3-bit symbols, which are accepted by the computer. These symbols can be transferred at a rate of 4200/sec, which is sufficient to complete a transfer of all the autocorrelation information in less than 0.5 sec. Any rate lower than this is also possible.

The dimensions of the autocorrelator are approximately 19 in. wide by 5¼ in. high by 7 in. deep. Also, there is a filter mounting and display panel, which is 3½ in. high. The volume of later versions may be reduced to approximately one-third of the present volume through the use of microelectronic shift register storage instead of magnetostrictive delay line storage. The lengths of the acoustic (magnetostrictive) delay line storage elements presently used were standardized to three different lengths for ease of spare parts maintenance, although this results in some loss of logical efficiency.

C. Digital Communication Tracking: Resolving the DSN Clock Synchronization Error

W. L. Martin

1. Introduction

As space missions become more sophisticated, the need for correlating data received at different tracking stations grows more important. Typically, data is recorded at a station for later processing at JPL. Each station records a time code derived from its local master clock. Unfortunately, in the past it has not been possible to synchronize these clocks more accurately than several milliseconds, because of the lack of a stable, wide-band communications channel over which synchronization signals can be sent. The DSN has relied upon independent synchronization to radio station WWV; but noise, multipath problems, and bandwidth limitations have combined to produce uncertainties of several milliseconds. This report discusses a method for reducing the synchronization error by approximately two orders of magnitude using closed loop ranging to supply the missing communications link.

Each tracking station is being equipped with the Mark I ranging subsystem: a pseudonoise ranging device capable of resolving lunar distances to a few meters. It seems natural that the potential power of this device could be brought to bear on the clock synchronization problem. Accordingly, the following discussion outlines a procedure for quantifying, to a few microseconds, the synchronization error existing between DSN stations. The technique is operative whenever two or more DSN stations can simultaneously view a single satellite containing a turnaround ranging transponder. Furthermore, there is no limit to the number of stations that can participate, the only requirement being an overlapping view period and the availability of the ranging subsystem.

2. Procedure

Referring to Fig. 1, assume that Station 1 is ranging in the conventional manner. This implies the transmission of a pseudonoise code to which the ground equipment is locked when the signal returns from the satellite. Thus, the correct range is held in the Station 1 range tally. Station 2 also locks its receiver ranging coder to the returning signal; however, it does not transmit. Because Station 2's transmitter ranging coder is asynchronous with respect to the one located at Station 1, the range information available at the second station is incorrect and should be ignored.

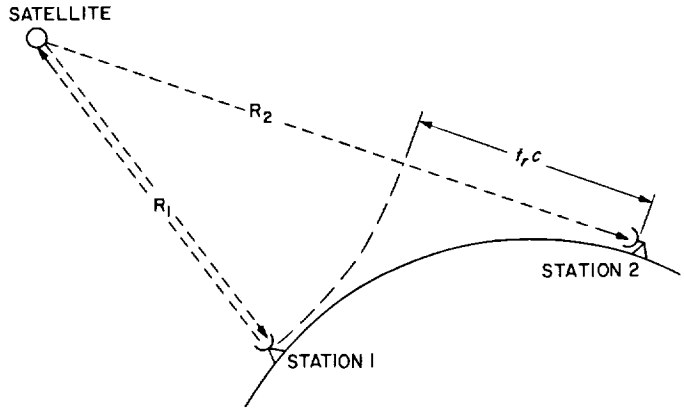

Fig. 1. Clock synchronization scheme

The Mark I receiver coders are designed to produce a marker pulse whenever a particular code vector (111 . . . 1 vector) appears. These pulses, which are not coherent with the station clock, occur at approximately 3-sec intervals (Fig. 2).

In addition to the code marker pulses, each station independently generates timing signals. Assuming the rubidium frequency standards to be accurate, these timing pulses will differ by some arbitrary but constant phase from one station to another (Fig. 2). It is this difference that must be measured.

At Station 1, an elapsed time counter is started by a specific timing pulse (e.g., the first second of each minute during a common view period). This counter accumulates a time interval t_1, until the appearance of the next code marker which terminates the process. Time is measured by counting cycles of a precise 10-Mc frequency which occur between the time and code marker pulses.

Station 2 emulates this procedure using the equivalent local time tick and code marker pulses to measure an interval t_2. Now, if the station timing signals were perfectly synchronized ($t_s = 0$) the difference between the intervals ($t_2 - t_1$) should exactly equal the difference in range between the satellite and the respective stations. To the extent that this is untrue, the clock synchronization error will be known. Specifically

$$(t_2 - t_1) = t_s + t_r + t_e$$

where

t_s = the synchronization error to be determined

t_r = time corresponding to the range difference

t_e = various system errors

a. Errors. This technique is predicated upon an ability to accurately predict the range from Station 2 to the spacecraft. Typical orbit determination programs indicate an upper limit of 150-m uncertainty if the range from Station 1 to the spacecraft can be measured to 25 m. In practice, typical prediction errors can be expected to be far less, hence the corresponding time uncertainty should fall well below 0.5 μsec.

An additional error is introduced by the Earth's rotation (Fig. 3). A slight range change occurs during the signal's down-link flight time. If the distances are specified at the instant when the signal leaves the satellite, then the predicted arrival times will be in error. The worst case occurs for two stations on the equator in the configuration shown. Were no corrections made, a total discrepancy of 3.5 μsec (1100 m) might be possible. In practice, range increments are accounted for in the orbit determination program, rendering errors from this source negligible.

Equipment calibration is another possible source of uncertainty. Existing procedures call for the calibration of the entire system as a single unit, including: transmitter, transponder, receiver, and ranging equipment. Presently it is impossible to quantify each component's

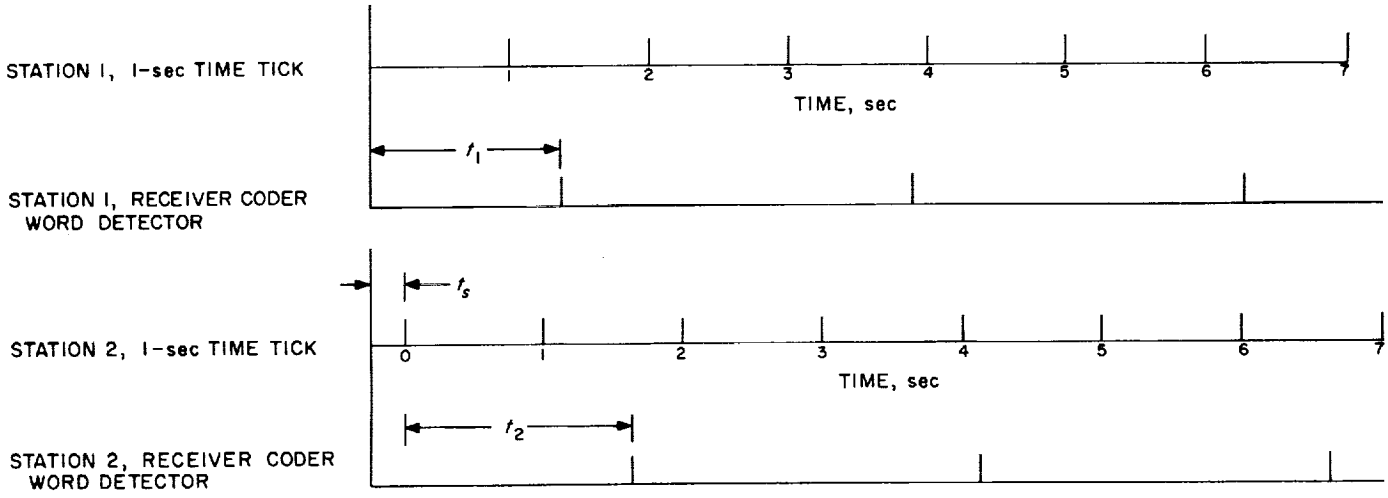

Fig. 2. Timing chart

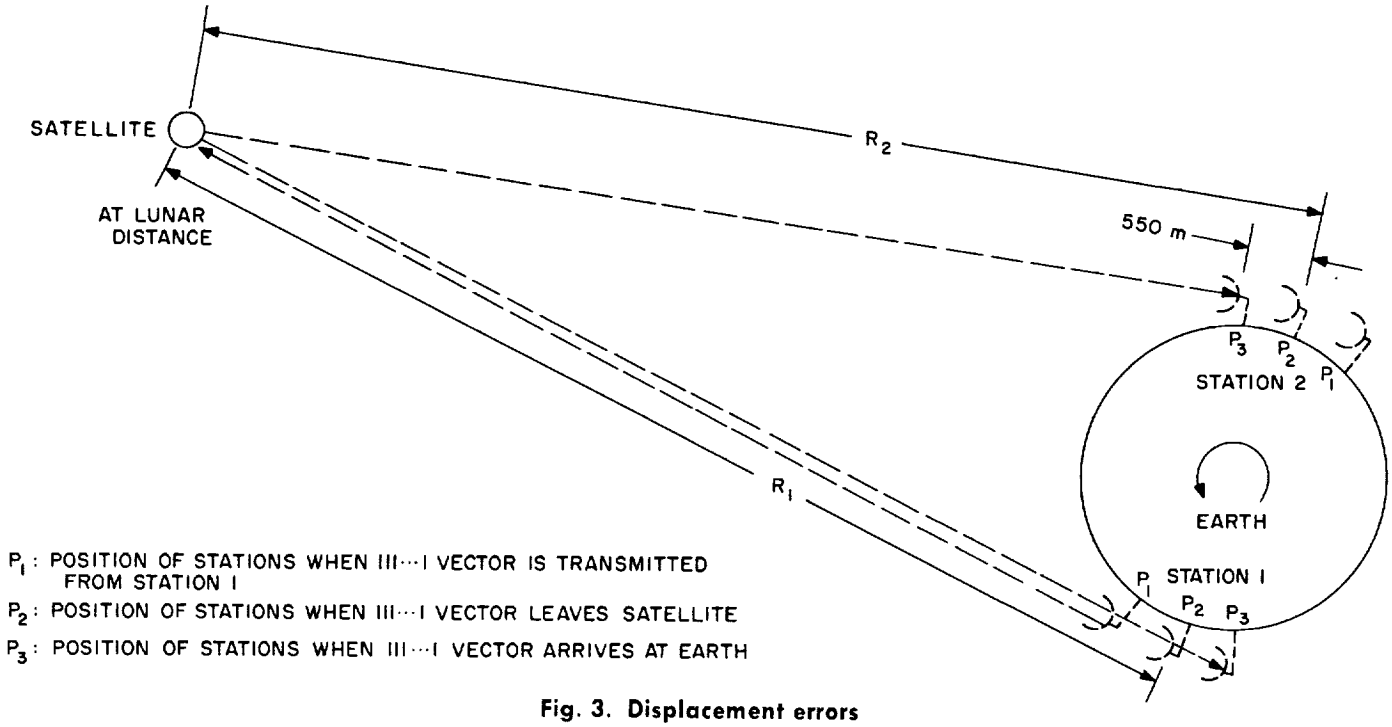

Fig. 3. Displacement errors

individual contribution. This is unfortunate since the synchronization measurement is only dependent upon delays occurring in the receiver and ranging systems. Again taking the worst case, the maximum uncertainty cannot exceed the total system delay which is on the order of 2 μsec. With some effort it might be possible to devise a method for calibrating the receiver and ranging equipment separately. This failing, some better estimates of the delay distribution would help immeasurably in reducing the uncertainties. In any event, this particular error is amenable to reduction through improved procedures.

The final errors arise in the time interval measurement. Here, rise times of the counter start–stop pulses are important as well as the counter's quantization level. Because the counted frequency is derived from the rubidium standard, no significant errors are introduced by this source. Pulse rise times are reported not to exceed 0.1 μsec, which is also the quantization interval. Thus, even the most pessimistic estimates cannot exceed 0.5 μsec for the total error. Since two stations make this measurement simultaneously, a total cumulative error not exceeding 1.0 μsec would be possible. By establishing standard threshold voltages for counting, it would be possible to reduce the uncertainties to 0.3–0.5 μsec.

For convenience, the errors are summarized in Table 2.

Table 2. Summary of maximum errors

Range prediction	0.5 μsec
Earth rotation (2 stations)	3.5 μsec
Equipment calibration	2.0 μsec
Interval measurement (2 stations)	1.0 μsec
Total worst-case error	7.0 μsec

b. Implementation. A 10-Mc counter is available in the Mark I ranging equipment for the time interval measurements. Time ticks of 1 sec and coder word detector pulses are also available, although the former requires connecting an additional wire from the logic block area to the counter. To initiate a time interval measurement, an operator must press a reset button on the counter's front panel. A problem lies in the timing of this act if, for example, it is decided to take a sample on the first second of each minute. Then, sometime after the 59th sec, but before the 0th sec, the button must be pushed to enable the counter's start input. After the sample is taken, the operator must log the result. Since this procedure is repeated at all stations participating in the calibration, it is apparent that there is ample opportunity for error. The problem can be alleviated to some extent by using 10-sec or 1-min time ticks to initiate measurement. In the latter case, the operator can reset

the counter at any time during the preceding minute. While reducing the operator timing requirements, this procedure parries the question of accurate data recording.

A better solution is afforded by constructing a small, separate time interval measuring subsystem (Fig. 4). Basically this consists of a high quality digital counter, printer, and a small amount of digital logic.

When in the *operate* mode, this equipment automatically measures the time tick-code marker interval once each minute. The result, together with the corresponding time, would be printed on a paper tape. In addition to power, the only inputs required would be the station time tick, code marker pulse, station time code, and the frequency standard. Should the extra equipment be deemed undesirable, one of the on-site SDS computers could be used to initiate and record the measurements, relieving the operator of the responsibility for timing and data recording.

c. Advantages. Synchronization measurements utilizing the Mark I satellite ranging system offer several advantages:

(1) Simple operation.

(2) High resolution.

(3) Inherent stability (only delays in receiver and ranging equipment are important and are likely to be invariant).

(4) Low cost (equipment already exists).

(5) Simultaneous calibration of several stations is possible.

d. Disadvantages. Some of the more apparent disadvantages are:

(1) Satellite with ranging transponder is required.

(2) Satellite must be distant enough to provide reasonable visibility from two or more stations.

(3) Operator error is possible unless system is automated.

(4) Measurements must be used as postflight corrections (insufficient information available at individual stations for clock adjustments).

e. Conclusions. On the basis of preliminary investigations, satellite calibration of the clock synchronization error appears to be entirely feasible. With minimal care, the measurements should resolve the discrepancy to

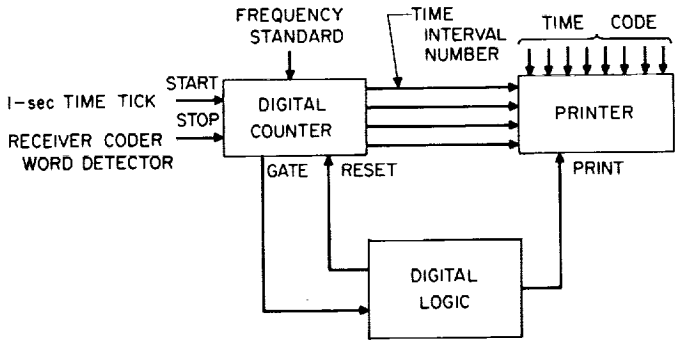

Fig. 4. Time interval measuring subsystem

10 μsec or better; slightly more effort could reduce the ambiguity to the 1–2 μsec region. The scheme is doubly attractive since all equipment required for its implementation already exists.

D. Digital Communication Tracking: Interfacing With SDS 900 Series Computers

W. L. Martin

Several Scientific Data Systems (SDS) 900 series computers have been purchased recently by JPL in order to expand the DSN's capability. Generally, these computers include a central processor augmented by a carefully selected set of peripheral equipment. One of the computer's primary jobs is to control various subsystems—often from different manufacturers. So the question exists as to the best way of connecting external devices to the computer.

The computer's structure requires that a 24-bit word be decoded to determine which of several external subsystems is being addressed. Two approaches are immediately apparent. The first is the construction of a device to decode the required word (called an *EOM*) and to produce a signal at one of several external subsystem connectors. Such a decoder is called a "J-box." The alternative is to examine each piece of external equipment and fabricate a specialized decoder for its specific requirements. Because the latter design is simpler than the J-box, it can be constructed on a single card and can be plugged directly into the computer. Borrowing from the earlier terminology, this device will be known as a "J-card."

Resolution of the J-box versus J-card question is based on both technical and philosophical considerations. Technically, since the J-card is made for a specific piece of equipment it can be designed more efficiently. Special features (to be illustrated later) can be included with the basic decoding. Philosophically, a system of maximum flexibility is desirable. Making each device a wholly independent subsystem allows its connection, at will, to any computer. Thus, if succeeding requirements necessitate modification of the system's basic configuration, changes could be made with minimum effort. After due consideration, it was decided to construct the interface–decoders on a single card located on one end of a cable connecting the peripheral device with the main computer.

1. Computer Description

Before considering the design of a specialized J-card, more information is needed regarding the computers' characteristics. The following discussion is relevant mainly to the SDS 925/930/9300 computers. The major differences between these and the 910/920 machines are: machine cycle time; absence of a *SKS* clocking signal (*Skss*); and different duty cycles of the clock signals Q_1 and Q_2 from the corresponding ones (Q_q1 and Q_q2) in the 930/9300 series. It must be emphasized that these differences are relatively minor and their existence does not preclude building interface cards which will work on all SDS 900 series machines.

Fig. 5 is a block diagram depicting the major communications channels (Ref. 1). Note that there are three types which comprise two distinct classifications: those which operate in conjunction with the central processing unit, and those which communicate directly with memory. The first class includes the parallel input–output channel (*PIN–POT*) and the time multiplexed communications channels (TMCC); the second class comprises the direct access communications channels (DACC).

The TMCC is a time multiplexed input–output channel for communication between peripheral devices and the computer. Its operation is designated "time multiplexed" because it gains access to the computer's memory through the same path used by the central processing unit, and therefore, must interrupt computation. Up to four TMCC channels can be connected to one computer and all may be active simultaneously, although only one channel at a time communicates with memory.

Utilization of TMCC for standard interfacing suffers from several disadvantages. First, the TMCC channels are optional and most computers will be equipped with

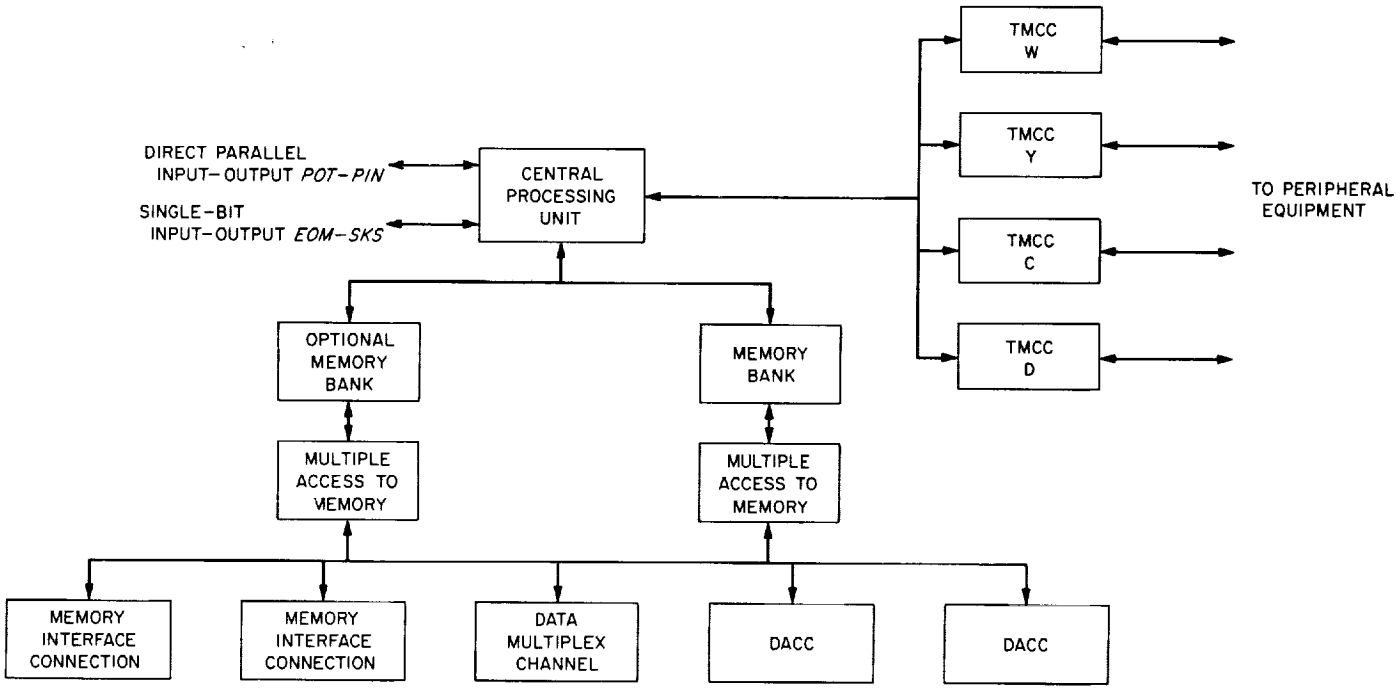

Fig. 5. Communications channels, SDS 925/930/9300 computers

only the W-buffer which is designed to be used with typewriters, printers, tape readers, etc., all of which are character-oriented. Since the buffer can handle only 6 bits at a time, its utility is sharply limited. Second, use of the W-buffer for interfacing is likely to slow the machine's operation markedly. It is often desirable to perform two operations simultaneously, such as outputting a character to the typewriter while communicating with another device. This can be accomplished by loading the W-buffer with the character to be typed and then communicating with the external equipment. Since typewriters are relatively slow, the two operations will overlap. Obviously, efficient operation precludes using the W-buffer for standard interface operations.

Another possibility is the DACC which provides a means of direct memory access under interlace control that can be either simultaneous or time multiplexed with computation. The memory access will be simultaneous only if the memory bank being accessed by the DACC is not being addressed for computation. In the event of a conflict, the operation becomes time multiplexed. Simultaneous access requires the computer to have two or more memory banks which restricts this type of channel to the SDS 930/9300 multiple bank machines.

Use of the DACC for standard interfacing is impractical because it restricts interface design to SDS 930/9300 computers and because the majority of such machines purchased by JPL do not include this option. Since standardization is a prime consideration, the best choice seems to be a parallel input–output operation through the computer's C-register. Clearly, this is the method intended to be used for general communication.

Parallel input–output operations, where a data transfer is involved, consist of two instructions. Before the transfer can occur, an energize output medium (*EOM*) must be given to alert the specific external device that an exchange is imminent. The following instruction will be either a parallel output (*POT*) for data leaving the computer, or a parallel input (*PIN*) if the transfer is to be into the computer. It must be understood that all *POT*, *PIN* operations are to be preceded by an *EOM*; however, an *EOM* can be used alone to initiate some action in an external device.

2. EOM Instruction

Because the distinction between these instructions is important for efficient interface design, it is worthwhile to consider them in greater detail.

An *EOM* is an instruction in the form of a computer word which signals an external device. This word is held in the computer's C-register for one machine cycle. The instruction's 24 bits are available on several connectors in the TMCC block.

The *EOM* word format adopted by JPL is shown in Fig. 6. Significance of the particular bits is as follows:

Bits 0,1,2; 18,19,20 form two octal digits which designate the class of external device being addressed. *Note*: Bit 2 will always be 0. Table 3 summarizes present unit assignments made in an effort to standardize all interface design (32 different device classifications exist in the *EOM* word structure).

Bits 3,4,5; 6,7,8 form a two-digit op-code which designates the instruction as an *EOM*. These two digits will always be 02.

Bits 9,10,11 specify the type of *EOM* (Table 4). All but 011 (Octal 3) are reserved for use within the computer. It is necessary to decode Bit 9 in the external equipment to insure that it is 0. However, Bits 10 and 11 are decoded

C-REGISTER

CLASS FIRST OCTAL DIGIT		0[a]	*EOM* OP - CODE FIRST OCTAL DIGIT			*EOM* OP - CODE SECOND OCTAL DIGIT			*EOM* TYPE			FUNCTION FIRST OCTAL DIGIT			FUNCTION SECOND OCTAL DIGIT			CLASS SECOND OCTAL DIGIT			UNIT I DIGIT		
0	1	2	3	4	5	6	7	8	9	10	11	12	13	14	15	16	17	18	19	20	21	22	23

[a]BIT 2 IS ALWAYS 0

Fig. 6. *EOM* instruction word format

Table 3. Device classification codes

Type first octal digit bits 0,1,2	Code second octal digit bits 18,19,20	Equipment to which code is assigned
0	0	Programmed exciters
0	1	X-Y plotters
0	2	Digital display units
0	3	Miscellaneous, one-of-a-kind devices
0	4	Miscellaneous, one-of-a-kind devices
0	5	Computer-computer communications
0	6	Correlators
0	7	SKS identification cards
2	0	Not yet assigned
2	1	
2	2	
2	3	
2	4	
2	5	
2	6	
2	7	
4	0	
4	1	
4	2	
4	3	
4	4	
4	5	
4	6	
4	7	
6	0	
6	1	
6	2	
6	3	
6	4	
6	5	
6	6	
6	7	

Table 4. *EOM* classifications

Bits			*EOM* type
9	10	11	
0	0	0	Buffer control (*buc*)
0	0	1	Input–output control (IOC)
0	1	0	Internal control
0	1	1	System type *EOM* (*Sys*)
1	1	1	Special SDS peripheral equipment

within the computer, and when they are both 1 a system pulse appears at the system signal (*Sys*) pin of the output connector. Instruction timing is shown in Fig. 7. Note that the contents of the C-register will be stable during an *EOM* instruction.

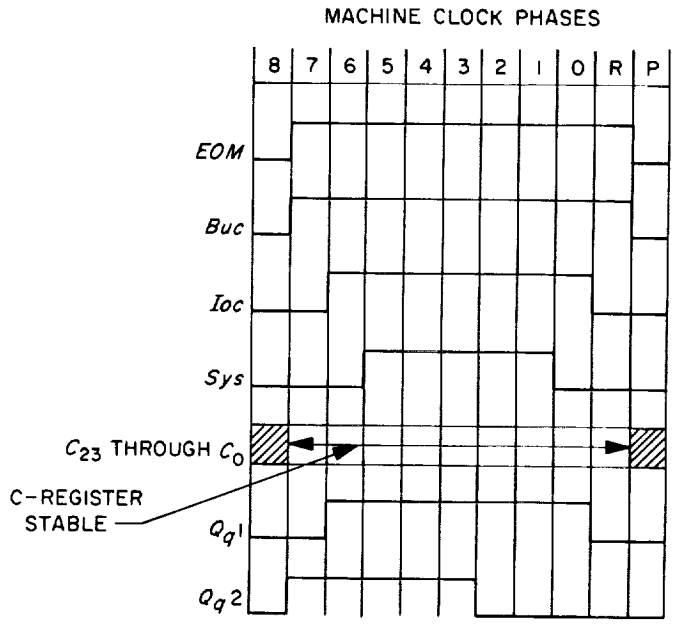

Fig. 7. *EOM* instruction timing, SDS 925/930/9300 computers

Bits 12,13,14; 15,16,17 comprise the two octal digits specifying the function that the addressed unit is to perform. Thus, each unit can be sent a maximum of 64 different commands.

Bits 21,22,23 indicate the particular unit within a class which is being addressed. For example, within the general category of displays one might address Display 1, Display 2, etc. Each class can contain a maximum of 8 units.

Fig. 8 provides a graphic interpretation of the *EOM* structure for external devices. To summarize, there are 64 different operation commands for each of 8 different units in each of 32 device classifications.

EOM's are used for two distinct purposes: to signal a data transfer to or from the computer, and to command external devices to perform specific functions. It is this instruction which allows the computer to operate as a system controller. To be useful, the *EOM* instruction must be decoded. Bits 2 through 8, 10, and 11 are decoded by the computer into a *Sys* signal. In other words, a *Sys* signal will only be present when the current instruction is an *EOM* of the type meant for external devices. Bit 9 (C_9) must also be included in the decoding matrix to insure that it is 0 (see Table 4). Logically, an *EOM* embodies the following characteristics:

$$EOM = (Sys) \cdot (\overline{C_9}) \cdot (Class) \cdot (Unit) \cdot (Function) \quad (1)$$

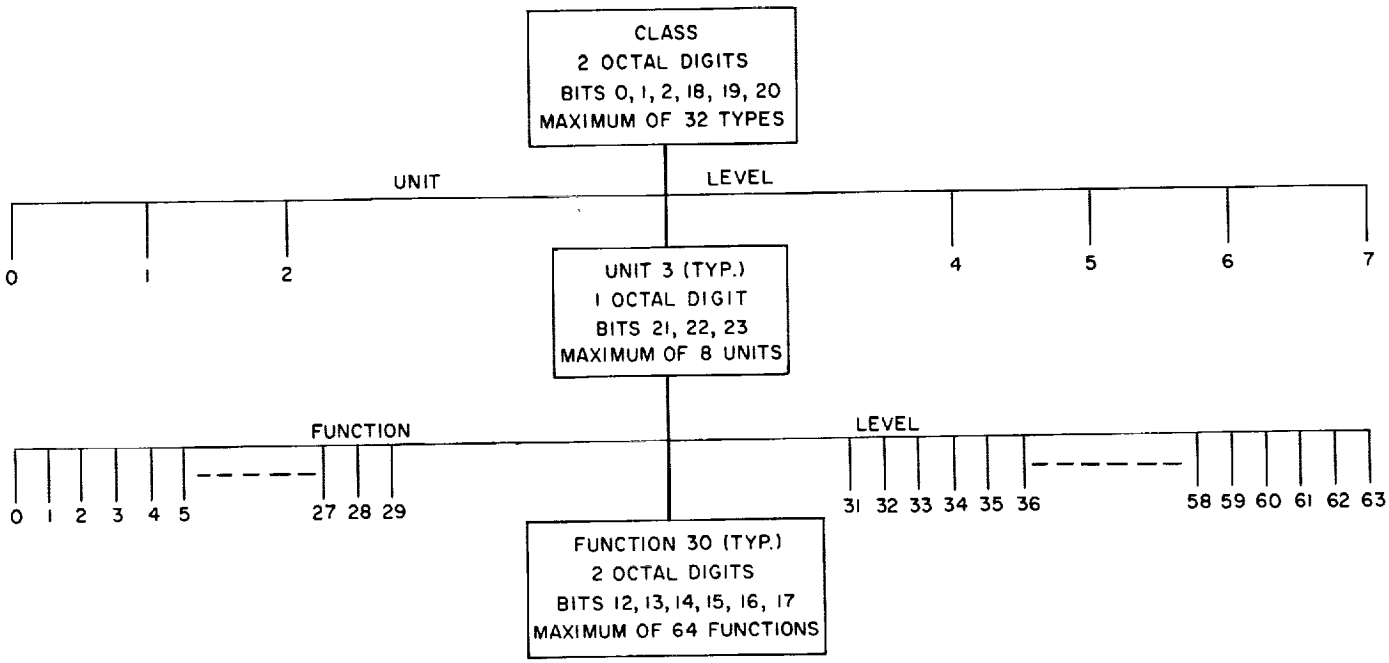

Fig. 8. Decomposition of a system *EOM*

While the C-register is stable for 9/11 of a machine cycle (Phases 7 through *R*, Fig. 7) the *Sys* strobe pulse is only present for 5/11 of a cycle (Phases 5 through 1). This precludes the use of slow speed logic or logic with excessive delays.

3. *Data Output*

Data transfer operations are always preceded by an *EOM*. The transfer instructions are: *POT* for data transmission from the computer, and *PIN* for data entry into the computer.

The *POT* instruction provides a means of direct parallel transfer of up to 24 bits from memory to an external device via the C-register of the central processor. Each word transfer is under direct program control. During a *POT* instruction, the computer accesses the word to be transferred from a location of memory specified by the effective address. The computer then proceeds to a wait phase.

The wait phase consists of an integral number of computer cycles. During this time all computation ceases and the C-register output lines (C_0–C_{23}) are stable (unless a time-share operation occurs) and contain the 24-bit word to be transferred to the external device. The computer remains in the wait phase until receipt of a ready signal ($\overline{R_t}$), which is generated by the external device. This signal is normally true (+8 v) and must be made false (0 v) for a minimum of one computer cycle. Since all external devices connect to a common $\overline{R_t}$ line, it must remain in a normally true condition.

The $\overline{R_t}$ line is sampled during Phases T_7–T_3 of each computer cycle. If $\overline{R_t}$ is false, the computer exits from the wait phase at the conclusion of the present cycle. Even when the external device is ready, prior to entering the wait phase, the computer will spend at least one cycle in this mode.

POT instructions require two machine cycles prior to entering the wait phase. Thus, the total time required is given by:

$$T_{POT} = (2 + n)\, t_m \qquad (2)$$

where

t_m is the length of one machine cycle

n is the number of cycles spent in the wait phase

Machine timing during a wait phase is depicted in Fig. 9. There are two signals generated in the central processing unit by a *POT* instruction.

POT 1 is true during the entire wait phase of the *POT* instruction and false at all other times. *POT 1* being true

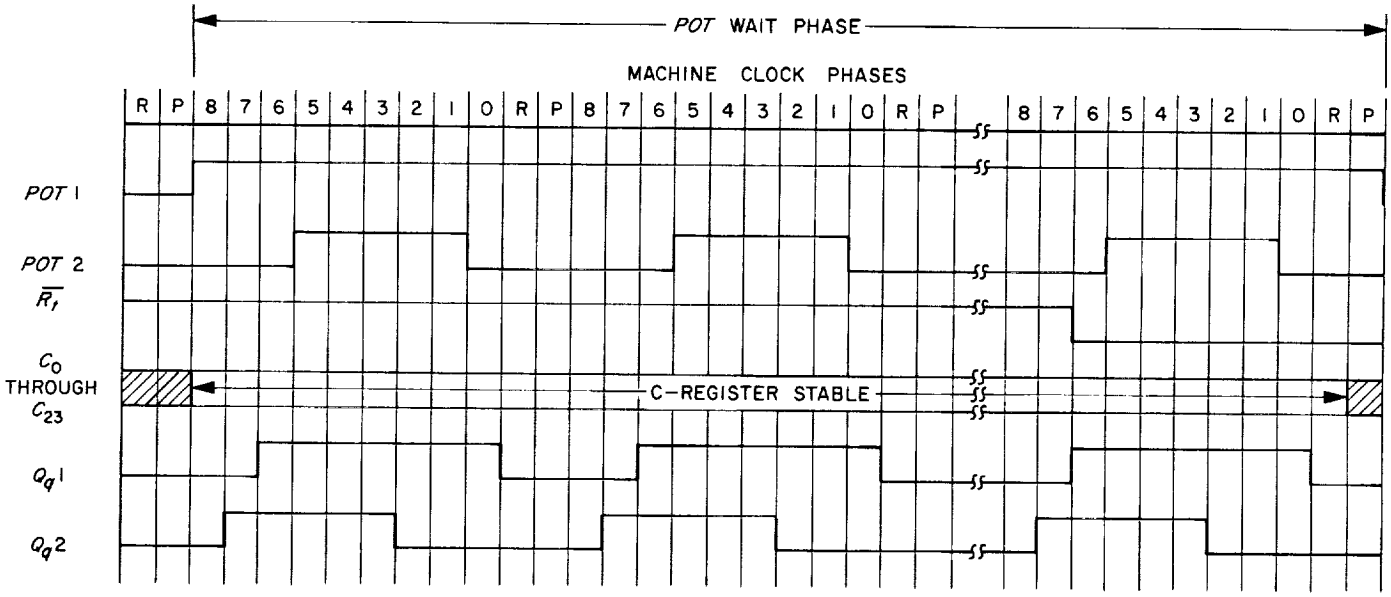

Fig. 9. POT instruction timing, SDS 925/930/9300 computers

indicates that the C-register output lines are stable and the 24-bit word is ready to be transferred. *POT 1* going false indicates to the external device that the computer has acknowledged the ready signal and has exited the wait phase.

POT 2 is true from T_5–T_1 of every machine cycle during the wait phase and false at all other times. *POT 2* may be used as a strobe by the external device to interrogate the C-register output lines, C_0–C_{23}.

NOTE: A *POT* instruction can be preempted at the end of any machine cycle by a time-share operation. If this occurs, *POT 1* remains true, *POT 2* is inhibited, and the C-register is undefined. At the completion of the time-share operation, *POT 2* and the C-register return to normal and, depending upon the condition of $\overline{R_I}$, at least one more cycle of wait phase will occur. Under certain unusual circumstances, a time-share operation can occur during every other machine cycle. Therefore, it is most desirable that the external equipment be designed to accept a data transfer within one machine cycle. This insures that once the wait phase is reached, the transfer will occur immediately.

Two other signals which are useful in interface design are generated by the communications channels.

Q_q1 is a clock pulse true from T_6–T_0 of every computer cycle and false at all other times.

Q_q2 is a clock signal true from T_7–T_3 of every computer cycle and false at all other times. Q_q2 may be used during the *POT* wait phase to indicate to the external device that the $\overline{R_I}$ line is being sampled.

NOTE: Both Q_q1 and Q_q2 are continuous and not associated specifically with *POT* operations. As a result they are ideally suited to the function of clocking external equipment.

4. Data Input

The *PIN* instruction provides a means for direct parallel transfer of up to 24 bits of data from an external unit into the computer's C-register. Like the *POT* operation, a *PIN* instruction must be preceded by an *EOM*. Similarly, during execution, the computer proceeds to a wait phase which is almost identical to that of a *POT* instruction. Data transfer is accomplished by first resetting the C-register and then copying information on input lines $\overline{C_d0}$–$\overline{C_d23}$ into the register. This process of resetting the C-register and strobing the data repeats once every machine cycle during the wait phase of a *PIN* instruction.

NOTE: The C-register input lines ($\overline{C_d0}$–$\overline{C_d23}$) are inverted before they are strobed into the computer. Therefore, at the conclusion of a *PIN* instruction, the register will hold the *ones* complement of the data on its input lines.

Upon receipt of a ready signal ($\overline{R_t}$ going false from the external device) the computer exits the wait phase and continues computation. The wait phase terminates at the completion of the machine cycle, during which the ready signal was acknowledged by the computer. Therefore, a *PIN* instruction must go through at least one wait phase cycle. The total time is given by:

$$T_{PIN} = (3 + n)\, t_m \qquad (3)$$

Machine timing during a wait phase is illustrated in Fig. 10. There are two signals generated in the central processing unit by a *PIN* instruction.

PIN is true from T_7–T_0 of every computer cycle during a *PIN* wait phase and false at all other times. *PIN* indicates to the external equipment that the input lines are being strobed into the C-register and therefore must be held stable.

$\overline{R_{ti}}$ is a signal from the computer which goes false for 1.4 μsec (T_7–T_0), indicating that the machine has exited the wait phase $\overline{R_{ti}}$ going false indicates that the ready signal has been acknowledged and the computer has accepted the 24 data bits.

NOTE: Should a time-share operation occur during the wait phase, the *PIN* signal is inhibited. When the time-share operation is completed, depending upon the condition of $\overline{R_t}$, at least one more cycle of wait phase will occur. If a time-share operation occurs immediately following the last wait phase cycle, $\overline{R_{ti}}$ is inhibited until the time-share operation is completed.

5. Skip If Signal Not Set (SKS)

An *SKS* instruction can be used as a ready test for external equipment. Depending upon the status of a signal line ($\overline{Ssc}$), the computer may or may not skip the next instruction. Specifically, if the line is false the next instruction is skipped, while if it is true, the next instruction in the sequence is obeyed by the machine.

This instruction is similar to an *EOM*. The primary difference being that *EOM's* are concerned with transferring information out of the computer, while *SKS*'s respond to a single bit entering the machine. Like *EOM*'s, the C-register's class and unit digits are decoded to determine which device is being addressed. The function digits specify which of 64 possible tests are being made. External subsystems respond with an appropriate level (0 or +8 v) on the $\overline{Ssc}$ line.

Bits 10 and 11 of the instruction word are decoded internally to determine the type of *SKS*. Setting should be the same as for a system *EOM* (i.e., $C_{10} = C_{11} = 1$). An *SKS* instruction generates one internal signal in the SDS 930/9300 computers.

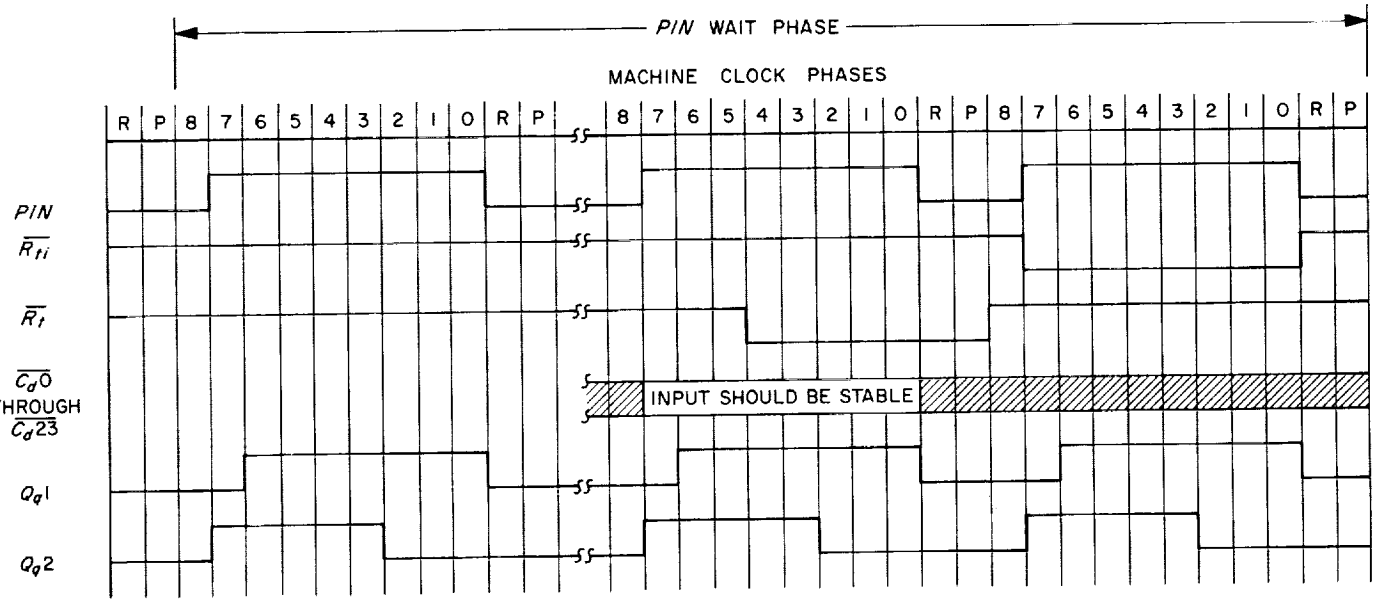

Fig. 10. *PIN* instruction timing, SDS 925/930/9300 computers

SKS clocking signal (*Skss*) is true from T_6–T_R of the second cycle if bit C_9 is true, or from T_7 of the first cycle to T_R of the second cycle if C_9 is false (Fig. 11). An *Skss* pulse indicates to the external device that the machine is executing an *SKS* instruction and that the $\overline{Ssc}$ line will be tested at time T_R of the second cycle.

An *SKS* instruction requires two computer cycles if no skip is performed, and three if one is performed. During the first two cycles the C-register is held stable for decoding by the external equipment.

NOTE: If a time-share operation occurs during either of the first two phases of an *SKS* instruction, both phases will be repeated at the completion of the time-share operation. During this interval the *Skss* signal will be inhibited.

6. Interface Design

With the machine's characteristics defined, an interface can be designed to perform a specific job. As an example, consider the connection of an *X-Y* plotter (Mosley, Model 6SA) and a digital-to-analog converter to an SDS 930. In this case the available converter was also made by SDS alleviating signal level compatibility problems. Input requirements are summarized in Table 5.

Table 5. Signals required for SDS digital-to-analog converters

Input signals	Direct coupled	Transformer coupled
Data		
Binary "1"	0 v ±2 v	−8 v ±2 v swing from common
Binary "0"	+6 to +20 v	–
Pulse width	0.3 μsec (min.)	0.5 to 6 μsec
Fall time (max.)	–	1 μsec (max.)
Nominal load	6 ma	17 ma
Channel select		
Quiescent voltage	+6 to +20 v	–
Pulse voltage	0 v ±2 v	−8 v ±2 v swing from common
Pulse width	0.3 μsec (min.)	0.5 to 6 μsec
Fall time (max.)	–	1 μsec (max.)
Nominal load	6 ma	17 ma
Convert		
Quiescent voltage	+6 to +20 v	–
Pulse voltage	0 v ±2 v	−8 v ±2 v swing from common
Pulse width	0.3 μsec (min.)	0.5 to 6 μsec
Fall time (max.)	–	1 μsec (max.)
Nominal load	6 ma	17 ma
Clear		
Quiescent voltage	+6 to +20 v	The clear signal is always direct coupled
Pulse voltage	0 v ±2 v	
Pulse width	0.5 μsec (min.)	
Fall time (max.)	–	
Nominal load	6 ma	

This converter accepts 9 data bits (8 bits plus sign) and accomplishes the conversion in two steps. During Step 1, the 9 bits are loaded from the computer in parallel into a hold register in the converter. Energizing the appropriate channel-select line determines which channel receives the data. Step 2 causes the conversion to be made. Here data in the hold register is transferred in parallel to a second bank of flip-flops by a convert command. This second group of flip-flops feeds a summing network whose output current is proportional to the binary number in the register.

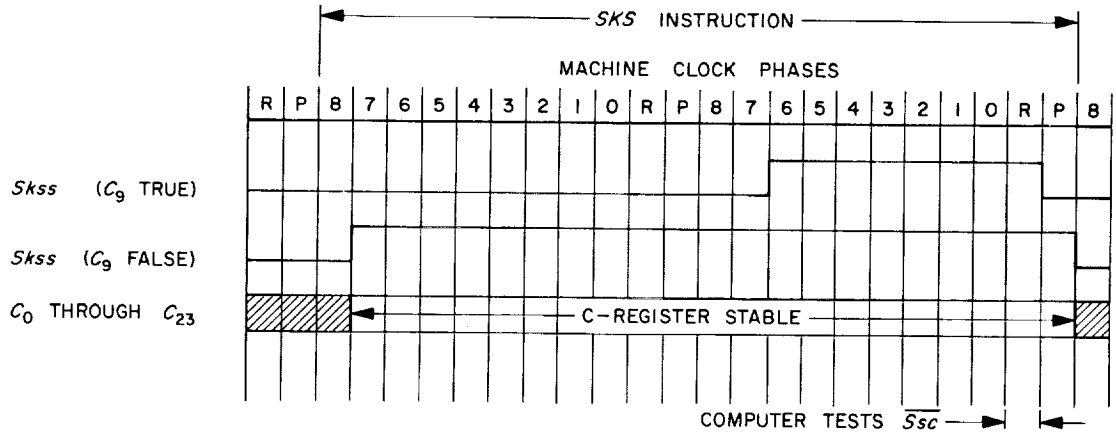

Fig. 11. *SKS* instruction timing, SDS 925/930/9300 computers

The X-Y plotter also has two functions requiring control. The recording pen can be raised and lowered electrically, and the chart paper (supplied in large rolls) can be advanced automatically. It was deemed desirable to put both of these operations under program control.

Finally, a SKS which tests plotter readiness was included. For the plotters having a servo null indicator, the SKS instruction can be used to speed the data output. If no such indicator is available, this command is still useful to indicate the existence of the plotter subsystem. Thus, the user can have general programs which simply test for the availability of various subsystems with a response to an SKS being indicative that the unit exists and is operative.

It must be emphasized that interface design philosophy requires the construction of a most general device which will be usable without modification in all similar applications. Thus, a particular subsystem can be added to any computer by merely duplicating an existing interface card. Costly and time-consuming reengineering is thereby replaced by the relatively minor problems of production. For this reason, it is imperative that the first card of a series be given exceptional care in its specification, design, and fabrication.

Previously it was stated that there are distinct advantages to placing all interface circuits on a single cable connector card. While slightly more costly in design, the potential benefits are apparent when it is realized that all peripheral equipment exists as separate, independent subsystems. Such devices can be connected to any 900 series computer by simply plugging in the cable card.

Fig. 12 is a block diagram of the X-Y plotter interface. Class and unit decoding are accomplished by the amplifier-gate combination on the left; function decoding by the center group and generation of operational commands by the flip-flop amplifier units on the right. Single

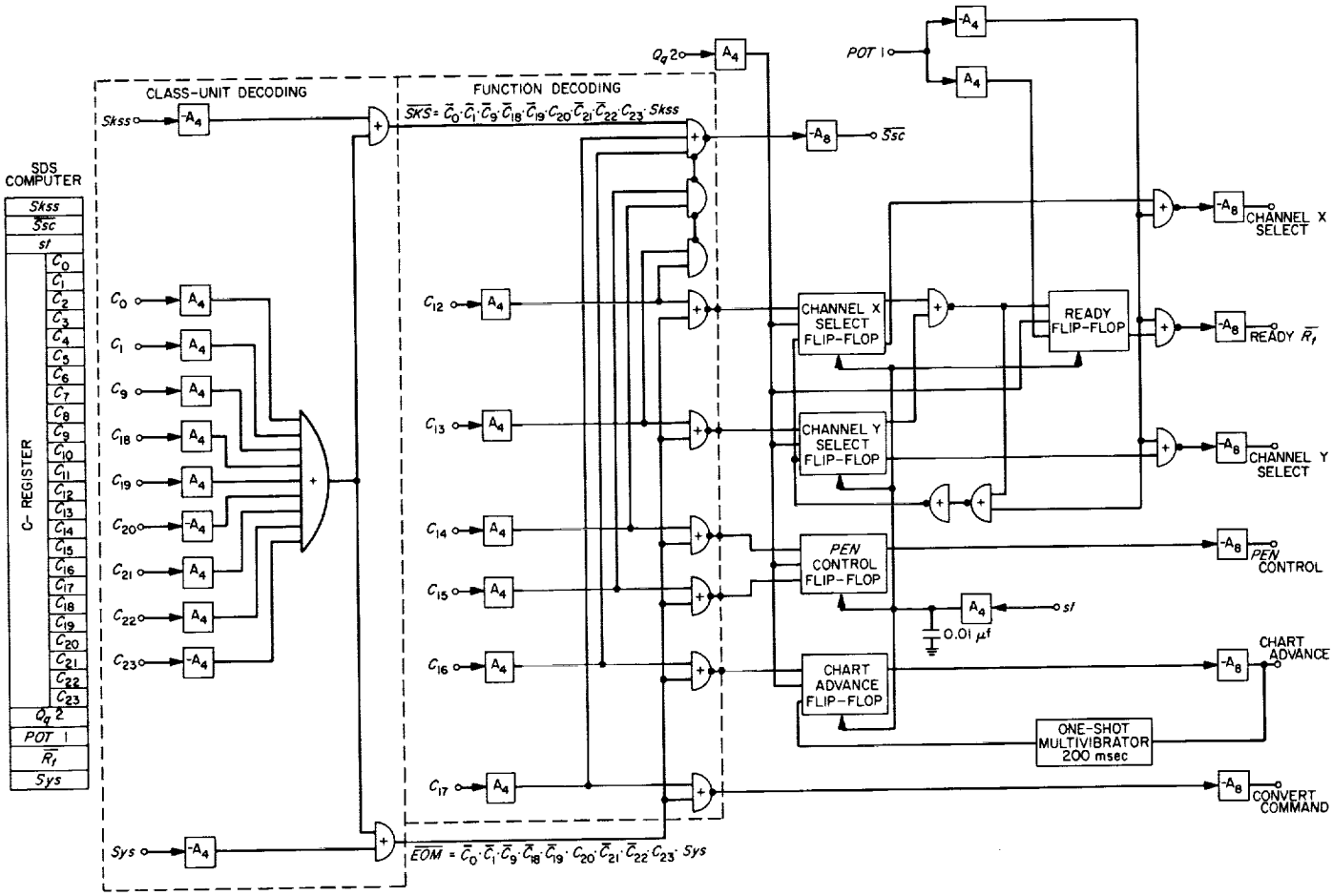

Fig. 12. X-Y plotter interface (J-1 card)

transistor amplifiers are included in all computer interconnecting lines to minimize problems of loading and rise-time degradation.

Except for class-unit decoding, all logic is implemented using Fairchild *or/nor* microcircuits. Because these microcircuits operate at a lower voltage than the computer (3.6 versus 8 v), some voltage limiting or amplification is required in all computer interconnecting lines. Fortunately, these characteristics could be embodied in the isolation amplifiers placed in each line. An appropriate designation is required since these amplifiers can have outputs of either 4 or 8 v and can be either inverting or noninverting. Accordingly, the subscript indicates the output voltage while a minus sign implies phase inversion (Fig. 12).

Class-unit decoding is accomplished by a unique circuit employing complementary transistors (Fig. 13). The circuit combines *SKS*, *EOM* decoding with isolation, amplification, and signal-limiting in a single set of transistor amplifiers. Each amplifier consists of an epoxy-encapsulated transistor and a resistor. Logically the two outputs can be represented as:

$$\overline{SKS} = \overline{C_0} \cdot \overline{C_1} \cdot \overline{C_9} \cdot \overline{C_{18}} \cdot \overline{C_{19}} \cdot C_{20} \cdot \overline{C_{21}} \cdot \overline{C_{22}} \cdot C_{23} \cdot Skss^1 \quad (4)$$

and

$$\overline{EOM} = \overline{C_0} \cdot \overline{C_1} \cdot \overline{C_9} \cdot \overline{C_{18}} \cdot \overline{C_{19}} \cdot C_{20} \cdot \overline{C_{21}} \cdot \overline{C_{22}} \cdot C_{23} \cdot Sys \quad (5)$$

Function decoding determines which of several operations is to be performed. An *SKS* gives rise to an *Ssc* feedback signal if

$$\overline{Ssc} = \overline{C_{12}} \cdot \overline{C_{13}} \cdot \overline{C_{14}} \cdot \overline{C_{15}} \cdot \overline{C_{16}} \cdot \overline{C_{17}} \cdot \overline{SKS} \quad (6)$$

where

$\overline{SKS}$ is given by Eq. (4)

To maximize decoding efficiency, each of the remaining operations is determined on the basis of a single function bit. Since *or* gating is used, a considerable saving can be realized if all logic bits except the one representing the desired operation are true.

A gate's output will be false only if the function bit *and* and $\overline{EOM}$ signal are false. Except during an *EOM* instruction, the $\overline{EOM}$ line will be true, dissatisfying all function gates.

The gates are used to enable several operation flip-flops which are of a JK type and are designed so that their enable inputs are active when at ground potential. Flip-flop triggering is accomplished with the computer's clock, Q_q2, and occurs when this signal goes to ground. Thus all interface operations are timed to Phase 2 of the machine cycle (Fig. 8).

The flip-flops are reset from several sources. Presence of a chart advance command is sensed by a one-shot multivibrator, causing its output which is normally false to become true for 200 msec. At the end of this period its output again becomes false allowing Q_q2 to reset the chart advance flip-flop.

A common signal derived from the two-channel select flip-flops is normally true except when one of the flip-flops is set. This, together with *POT*-1 (Fig. 8) is used as a

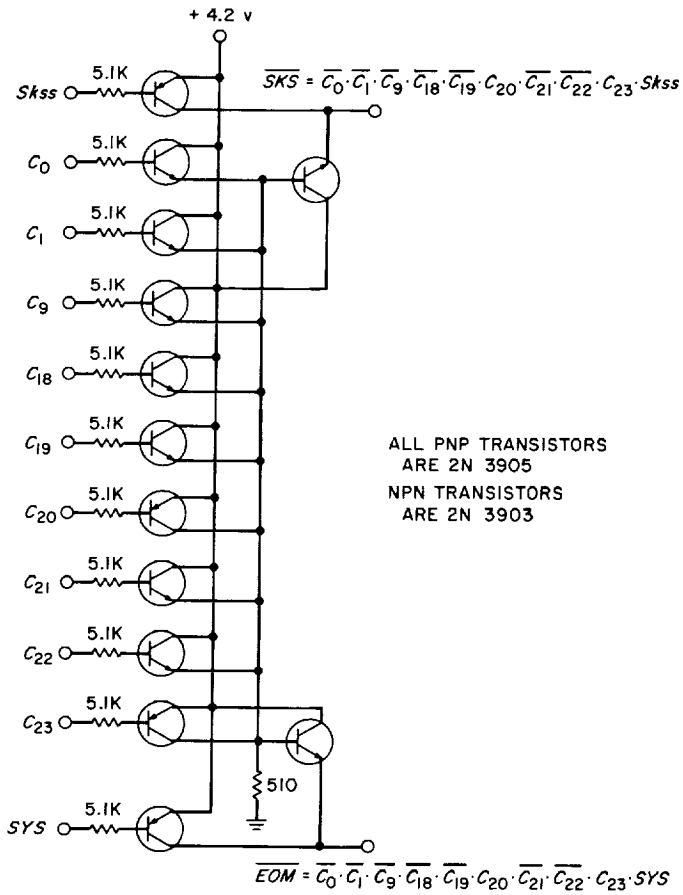

Fig. 13. Class-unit decoding

[1] *Skss* is available only in 930/9300 machines. For 910/920 computers this term is simply omitted.

reset enable for both flip-flops. Gating with *POT* 1 insures that the flip-flops are not reset prematurely.

The common channel select signal is also used to enable a ready flip-flop which provides a feedback signal ($\overline{Rt}$) to the computer. This flip-flop is reset by *POT* 1 going false, which indicates that the computer has acknowledged the ready signal and has exited the *POT* wait phase. Logical expressions for the various flip-flops can be written directly.

$$CHX = \overline{C_{12}} \cdot \overline{EOM} \cdot \overline{Q_q 2}$$
$$\overline{CHX} = (CHX + CHY) \cdot POT \cdot \overline{Q_q 2}$$
Channel X Select flip-flop (7)

$$CHY = \overline{C_{13}} \cdot \overline{EOM} \cdot \overline{Q_q 2}$$
$$\overline{CHY} = (CHX + CHY) \cdot POT\,1 \cdot \overline{Q_q 2}$$
Channel Y Select flip-flop (8)

$$PEN = \overline{C_{14}} \cdot \overline{EOM} \cdot \overline{Q_q 2}$$
$$\overline{PEN} = \overline{C_{15}} \cdot \overline{EOM} \cdot \overline{Q_q 2}$$
Pen control flip-flop (9)

$$CTA = \overline{C_{16}} \cdot \overline{EOM} \cdot \overline{Q_q 2}$$
$$\overline{CTA} = \overline{OS} \cdot \overline{Q_q 2}$$
Chart advance flip-flop (10)

where *OS* is the one-shot multivibrator's output

$$RDY = (CHX + CHY) \cdot \overline{Q_q 2}$$
$$\overline{RDY} = \overline{POT\,1}$$
Ready flip-flop (11)

EOM in the above is as specified earlier in Eq. (5).

In addition to the automatic reset signals specified in Eqs. (7)–(11), it is possible to manually reset all interface flip-flops. The DC reset inputs on each flip-flop have been wired to a common bus which is activated by the *start* button (*st*) located on the computer's control panel. This serves to initialize the J-card whenever power is first applied to the computer.

Continuing, interface card outputs can be written as:

$$\text{Not Channel X select line} = CHX \cdot POT\,1$$
$$\text{Not Channel Y select line} = CHY \cdot POT\,1$$
$$\text{Not ready signal } (\overline{Rt}) = RDY \cdot POT\,1$$
$$\text{Not pen control} = PEN$$
$$\text{Not chart advance} = CTA$$
$$\text{Not convert command} = \overline{C_{17}} \cdot \overline{EOM} \quad (12)$$

In the course of interface development it became necessary to design several circuits. A primary requirement was simplicity since the entire unit was to be packaged on a single card. The three different types of amplifiers employed in the design are shown in Fig. 14.

The particular transistors selected were from a silicon complementary series having low leakage and a high beta. Beta is guaranteed to be not less than 50 at room temperature. Another outstanding characteristic of these epoxy encapsulated transistors is their low cost: 50¢ each in quantities of 100 or more.

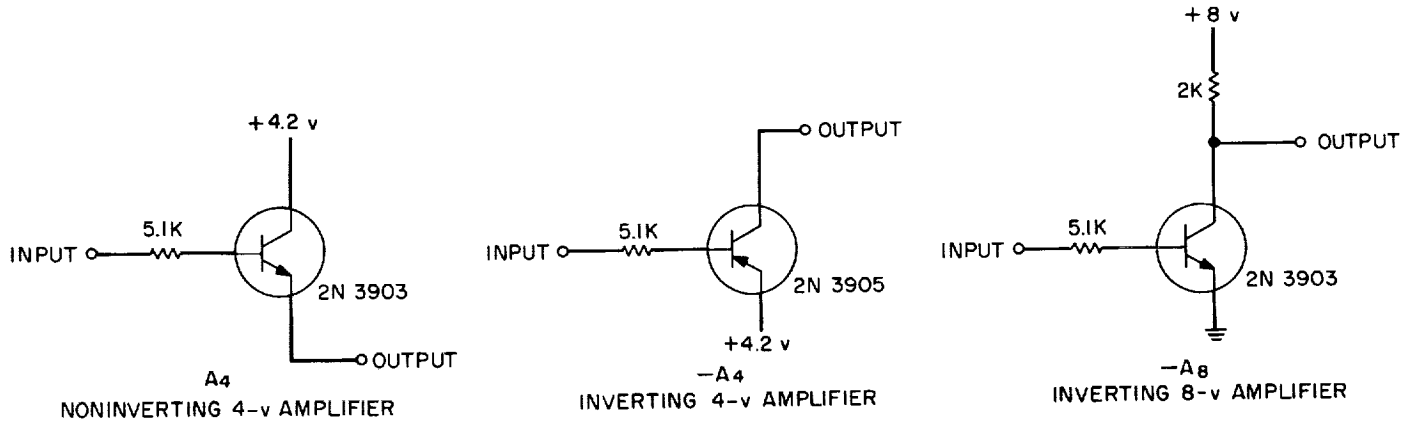

Fig. 14. Interface amplifiers

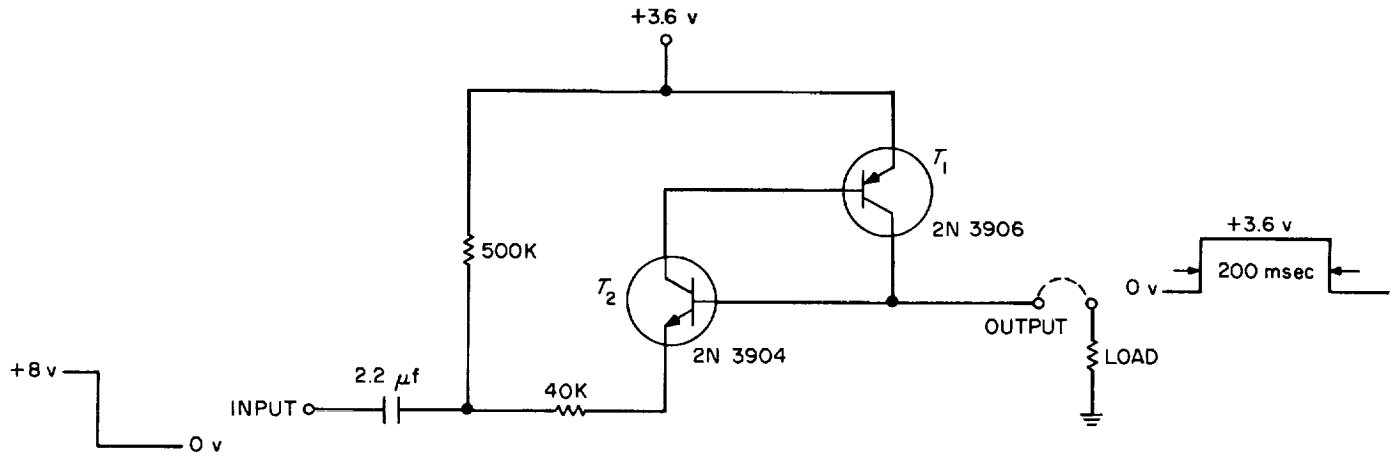

Fig. 15. One-shot multivibrator (200 msec)

The one-shot multivibrator is shown in Fig. 15. In the quiescent state both transistors T_1 and T_2 are off, causing the output to be at ground. A 4.4 v charge is established on the capacitor by the 500K resistor to the +3.6 v. When the chart advance signal occurs, the input which is normally at +8 v suddenly goes to ground, resulting in a corresponding drop in voltage on the other side of the capacitor causing T_2 to turn on when its emitter voltage reaches approximately −0.6 v. As T_2 begins to turn on, its collector starts to drop which activates T_1. T_1's collector rises rapidly toward 3.6 v forcing T_1 to turn on even harder. The output voltage is now about 3.5 v where it stays until the charge drains from the capacitor. At this point T_2 begins to turn off, removing the drive from T_1 which causes its collector to fall towards 0 v. As a result, T_2 is turned off further and the output voltage returns to its quiescent value. Total *on* time for the circuit with the values shown is approximately 200 msec. In addition to being compact, the circuit has the decided advantage of needing no standby power; current only flows during the brief interval when the output is at +3.5 v.

The power supply (Fig. 16) is a pair of conventional emitter followers whose input is regulated by a Zener diode. Local regulation has the added advantage of reducing noise on the power supply lines which can be a source of problems in microcircuit systems.

In addition to the special circuits designed for inclusion on the interface card, two others are required to operate the pen and advance the chart in the *X-Y* plotter. Both had to operate solenoids directly; the pen mechanism requiring approximately 100 ma and the chart advance approximately 1 amp. Because the plotter utilized PNP circuitry, its power supply produced a negative voltage with respect to ground. This aggravated the situation, since it forced the driver amplifiers to embody level shifting as well as current amplification.

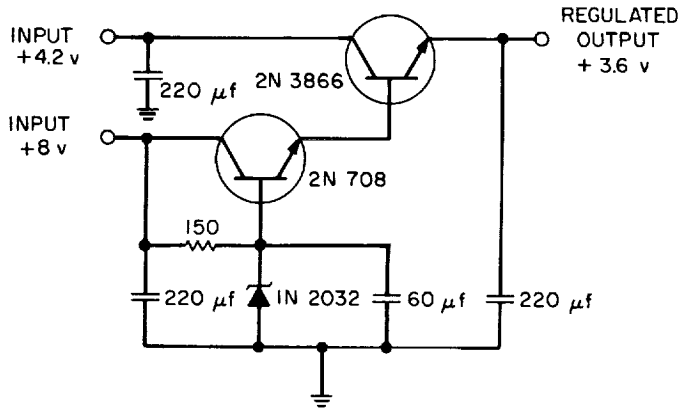

Fig. 16. Interface power supply

The driver amplifier is shown in Fig. 17. Both the pen and chart advance employ identical circuits which are capable of providing over 1 amp of current. Again, local regulation was used to reduce noise found on the power supply lines. The two amplifiers are packaged on a single card which is housed inside the plotter cabinet. By locating these circuits at the receiving end, noise problems and difficulties associated with transmitting high currents over long lines were avoided.

As previously noted, the interface subsystem was constructed with Fairchild series 900 microcircuits. Fig. 18 shows the completed product. Although there are 51 separate and distinct circuits on the card, the total parts

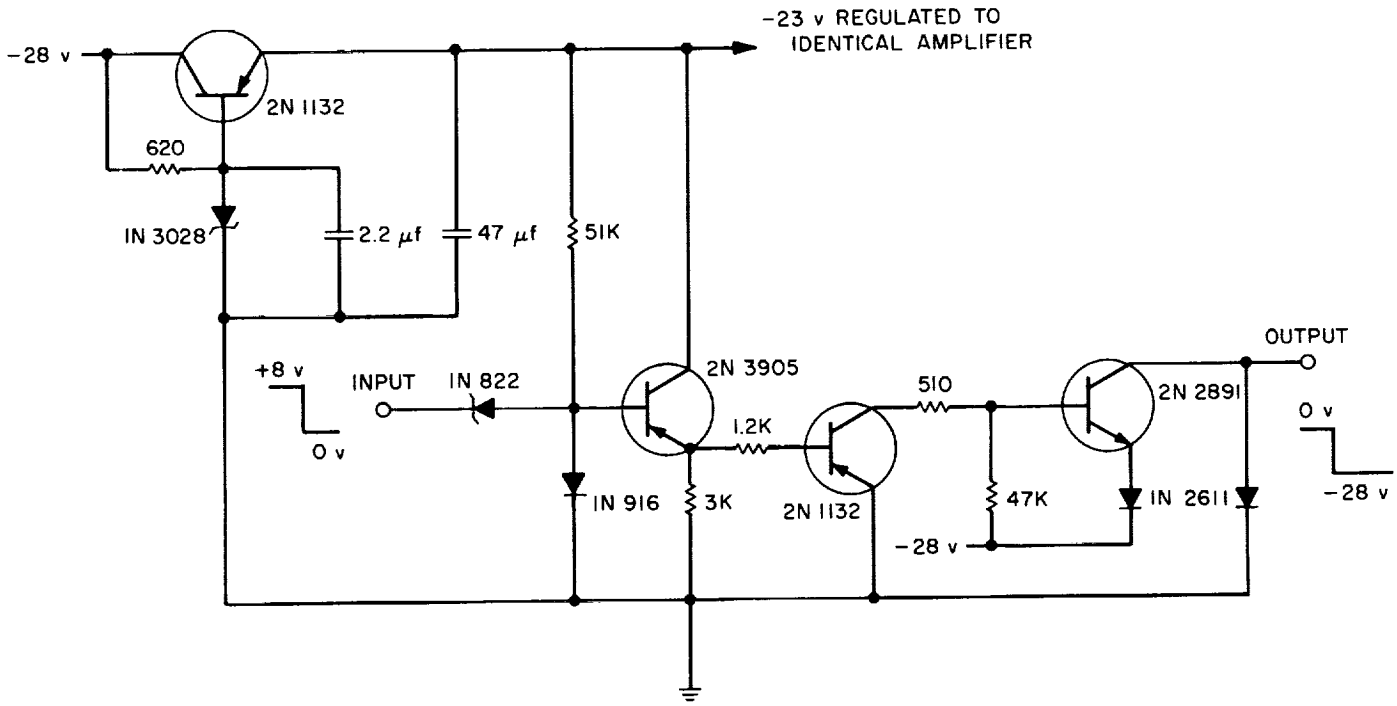

Fig. 17. X-Y plotter, pen and chart advance solenoid driver amplifier

cost was only approximately $100. Thus, besides occupying less space and being inherently more reliable, microcircuits are also very inexpensive—the average cost being approximately $3.50 per circuit. Although comparisons are difficult to make, construction of a device to perform the same functions, using standard SDS module cards, would require approximately one-third of a 25-card block.

The interface card is designed to plug directly into the cable card slot of the digital-to-analog converter, while the opposite end plugs into one of the *POT* connectors in the computer.

7. Programming

Instructions for the plotter are as follows:

00233711	Load Channel X
00235711	Load Channel Y
00237611	Convert
00236711	Pen down
00237311	Pen up
00237511	Chart advance
04030011	*SKS*

Operations can be combined into a single instruction by setting the appropriate function bits to zero. For example, 00237111 simultaneously raises the pen and advances the chart. Approximately 2 sec are required to fully advance the chart. Therefore, there must be incorporated in the program a delay which will prevent resumption of plotting before the chart has stopped. An internal interlock always raises the pen when the chart is advanced.

8. Summary

The J-card approach to interfacing was undertaken in part as an experiment in microcircuit design, and in part to test the philosophy of fully independent subsystems. Experience to date indicates remarkable success in both areas. Although the components used were of an inexpensive "industrial" quality, no failures have yet occurred. The independent subsystem concept will be more fully appreciated in time. Already, the 9-bit capability of the present digital-to-analog converter is becoming insufficient and a 12-bit replacement unit has been ordered. When it arrives, the existing converter can be moved to *any* SDS series 900 computer and it will become operative immediately.

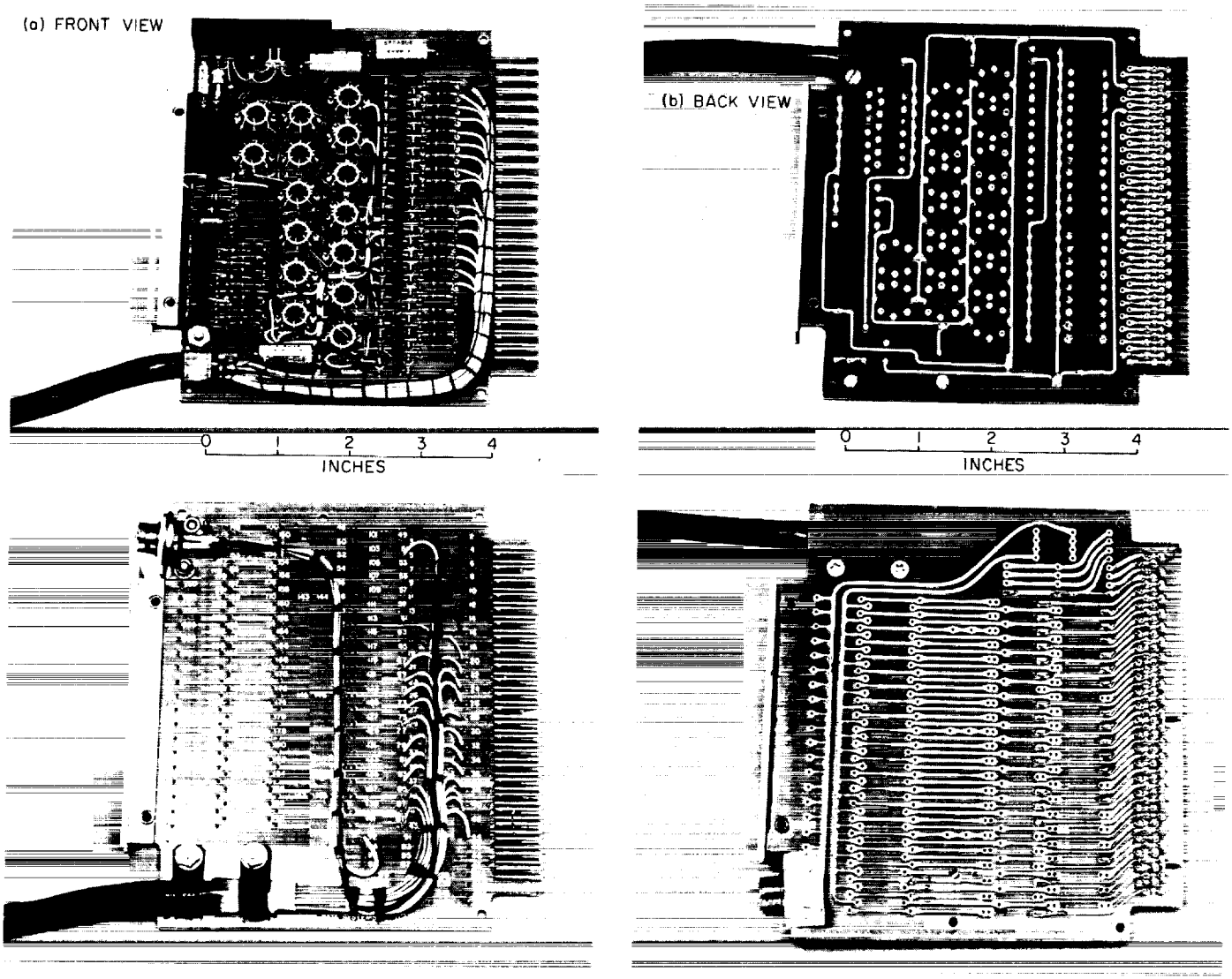

Fig. 18. Plotter interface card

E. Frequency Generation and Control: S- and X-Band Central Frequency Synthesizer

G. U. Barbani

Wiring of the entire central frequency synthesizer (CFS) system has been completed and initial check out of all subsystems has begun. A tracking filter to meet the requirement of smooth bandwidth transition, and a voltage vigilant system (VVS) to monitor all DC power and phase-lock loop functions were developed.

1. System Description

Wiring consisted of power supply cabling, distribution system, DC signal lines, and RF coaxial cables. Fig. 19 shows cable guide for main DC power cable and coaxial lines and the DC distribution system. Taper pin connections were used from the main DC cable to the RF modules. Strain reliefs eliminated connectors and provided a sufficient number of power cords. Fig. 20 shows DC signal lines, coaxial cables, module identification, location and output code.

Fig. 19. Details of DC power distribution and coaxial cable guide

Contractual help was obtained to wire the central frequency synthesizer. The entire system was turned on for a subsystem test where power supply levels were adjusted, power consumption was checked, and all wiring has proved satisfactory. The voltage controlled oscillators were set on frequency and all loops recorded in-lock condition except the 31.44 and 35.075 Mc phase-locked loops (refer to *SPS 37-36*, Vol. III, p. 68 for block diagram). Both loops were cycling between in-lock and out-of-lock condition, periodically. As the bandwidth relay in the tracking filter made transitions from wide bandwidth to narrow, relay chatter was enough to drive the VCO out-of-lock.

All system tracking filters were modified by removing the bandwidth relay and installing a photoconductive cell (Fig. 21) that changed the bandwidth smoothly from a wide loop to a narrow loop position. This is accomplished by taking advantage of the large resistive change in the photoconductive cell as a function of light intensity. A long-life bulb triggered from the in-lock detector supplies the illumination needed for the required bandwidth change (Figs. 21 and 22).

The voltage vigilant system was developed to remotely sense all DC output power variations. Eight voltrips with stable resistors were used to set minor and major alarm points. Power voltages in excess of ± 0.5 v rms for the 15-v system automatically turn on the minor alarm (yellow lamps). Variations greater than $\pm 10\%$ turn on the major alarm (red lamps). The 30-v alarms are analogous to the 15-v system. Voltrips and circuits with front panel removed are shown in Fig. 23.

All phase-lock loop functions, i.e., in-lock, out-of-lock, and excessive phase error are registered on separate lamp indicators. They are: red lamps for out-of-lock condition, yellow for excessive phase error, and one master green lamp for all loops in-lock indication. Any loop out-of-lock shuts off the master green lamp. Excessive static phase error > 0.5 v rms triggers the yellow lamp. This is accomplished with *or* gate circuitry, shown in Fig. 24. Lamp indications and alarms are shown in Fig. 25.

Alarm to the station recording system includes parallel closures from all phase-lock loops, the rubidium frequency standard, and all DC power supply major alarms.

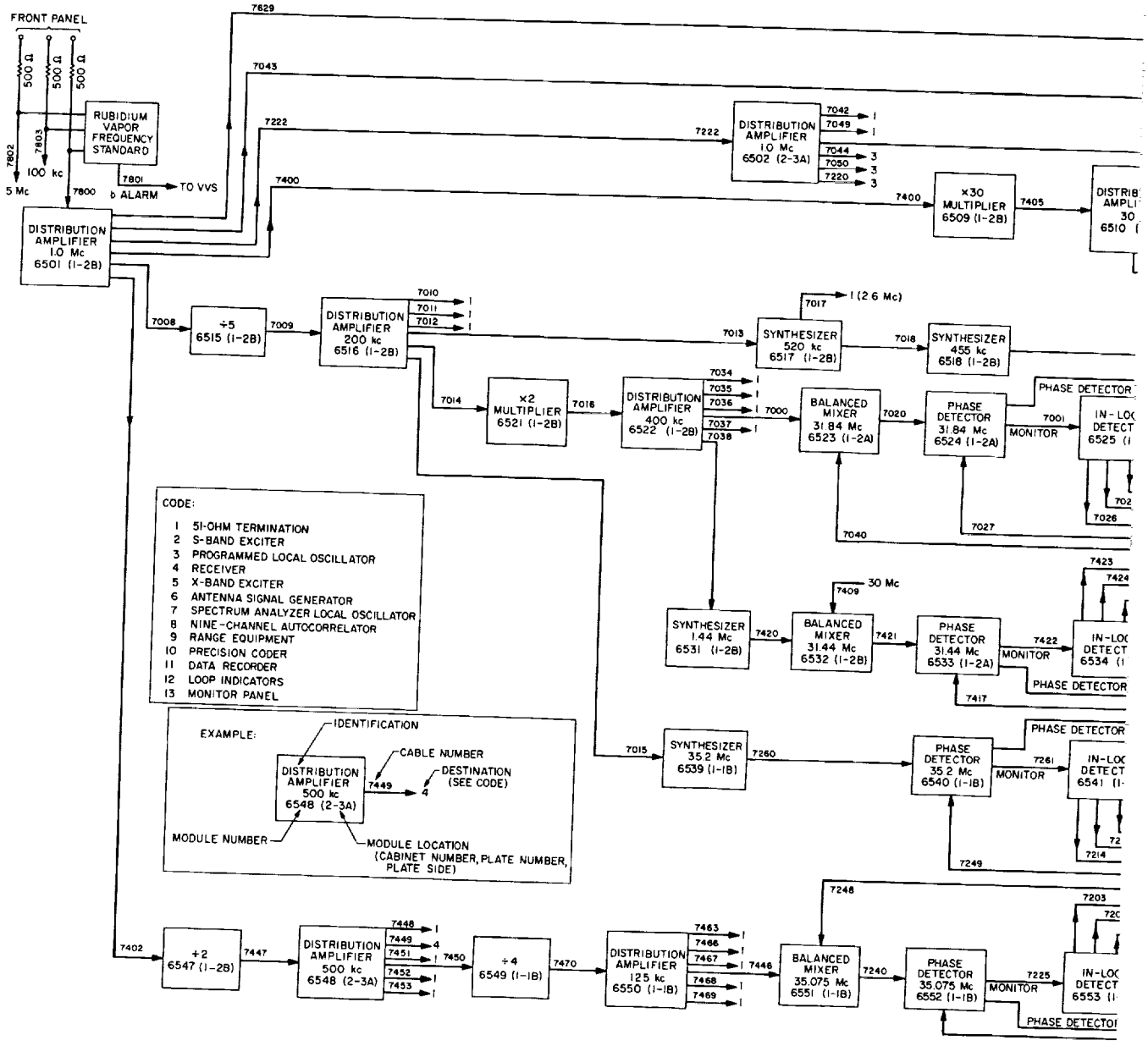
FRONT PANEL
500 Ω
500 Ω
500 Ω
RUBIDIUM VAPOR FREQUENCY STANDARD
7802
7803
100 kc
5 Mc
7800
7801
b ALARM
TO VVS
7629
7043
7222
7400
DISTRIBUTION AMPLIFIER 1.0 Mc 6501 (1-28)
7008
÷5 6515 (1-28)
7009
DISTRIBUTION AMPLIFIER 200 kc 6516 (1-28)
7010
7011
7012
7014
×2 MULTIPLIER 6521 (1-28)
7016
DISTRIBUTION AMPLIFIER 400 kc 6522 (1-28)
7034
7035
7036
7037
7038
7000
BALANCED MIXER 31.84 Mc 6523 (1-2A)
7020
PHASE DETECTOR 31.84 Mc 6524 (1-2A)
7001
MONITOR
PHASE DETECTOR
IN-LOC DETECT 6525 (1
7026
7027
7040
DISTRIBUTION AMPLIFIER 1.0 Mc 6502 (2-3A)
7042
7049
7044
7050
7220
×30 MULTIPLIER 6509 (1-28)
7405
DISTRIB AMPLI 30 6510 (
7017
1 (2.6 Mc)
SYNTHESIZER 520 kc 6517 (1-28)
7013
7018
SYNTHESIZER 455 kc 6518 (1-28)
CODE:
1 51-OHM TERMINATION
2 S-BAND EXCITER
3 PROGRAMMED LOCAL OSCILLATOR
4 RECEIVER
5 X-BAND EXCITER
6 ANTENNA SIGNAL GENERATOR
7 SPECTRUM ANALYZER LOCAL OSCILLATOR
8 NINE-CHANNEL AUTOCORRELATOR
9 RANGE EQUIPMENT
10 PRECISION CODER
11 DATA RECORDER
12 LOOP INDICATORS
13 MONITOR PANEL
EXAMPLE:
IDENTIFICATION
CABLE NUMBER
DESTINATION (SEE CODE)
DISTRIBUTION AMPLIFIER 500 kc 6548 (2-3A)
7449
4
MODULE NUMBER
MODULE LOCATION (CABINET NUMBER, PLATE NUMBER, PLATE SIDE)
7409
30 Mc
SYNTHESIZER 1.44 Mc 6531 (1-28)
7420
BALANCED MIXER 31.44 Mc 6532 (1-28)
7421
PHASE DETECTOR 31.44 Mc 6533 (1-2A)
7422
MONITOR
PHASE DETECTOR
IN-LOC DETECT 6534 (1
7423
7424
7417
7015
SYNTHESIZER 35.2 Mc 6539 (1-1B)
7260
PHASE DETECTOR 35.2 Mc 6540 (1-1B)
7261
MONITOR
PHASE DETECTOR
IN-LOC DETECT 6541 (1-
7214
7249
7402
+2 6547 (1-28)
7447
DISTRIBUTION AMPLIFIER 500 kc 6548 (2-3A)
7448
7449
7451
7450
7452
7453
÷4 6549 (1-1B)
7470
DISTRIBUTION AMPLIFIER 125 kc 6550 (1-1B)
7463
7466
7467
7446
7468
7469
7248
BALANCED MIXER 35.075 Mc 6551 (1-1B)
7240
PHASE DETECTOR 35.075 Mc 6552 (1-1B)
7225
MONITOR
PHASE DETECTOR
IN-LOC DETECT 6553 (1
7203

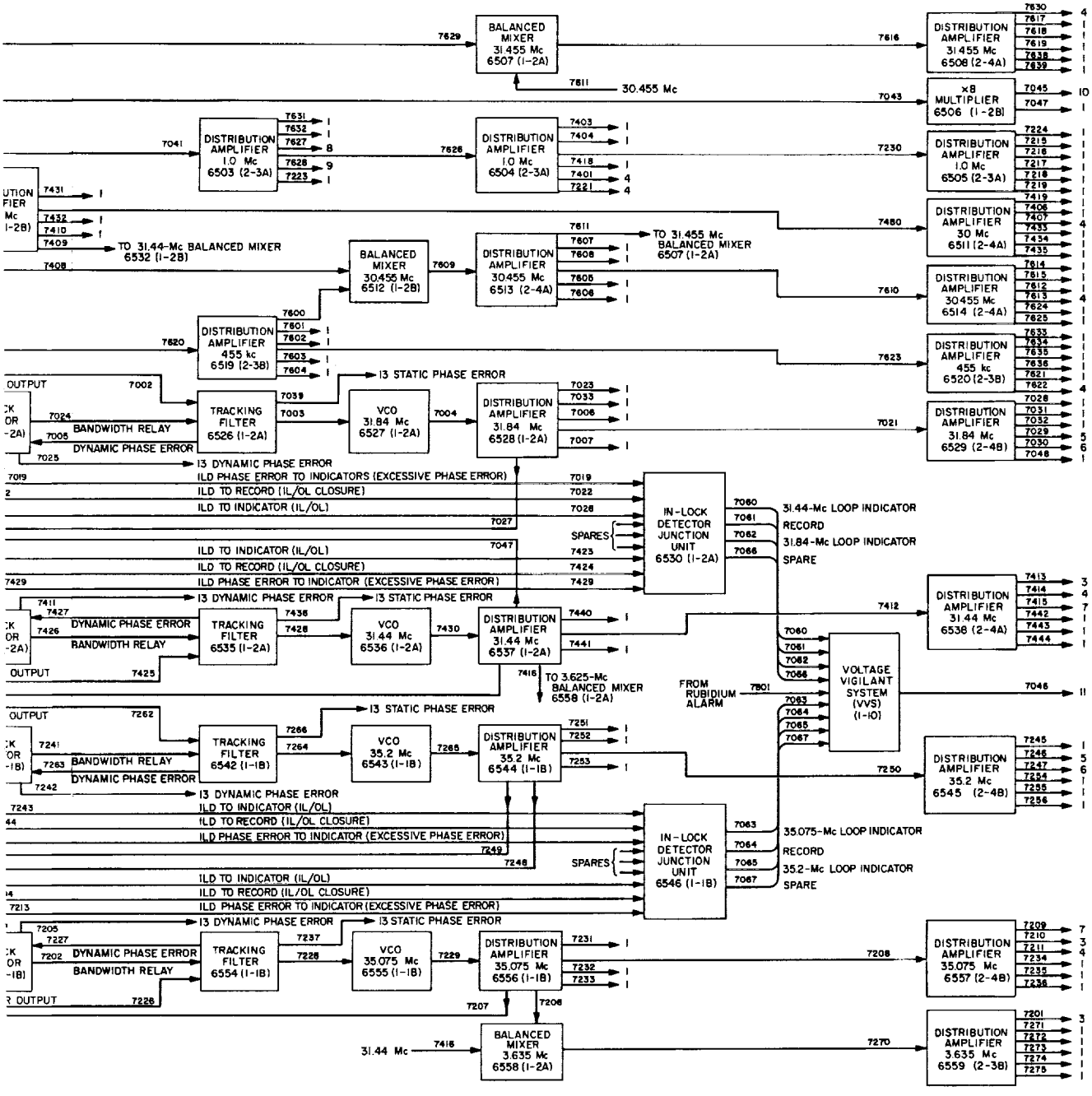

Fig. 20. Central frequency synthesizer, Mod I, wiring block diagram

Fig. 21. Partial view of tracking filter showing photoconductive cell

A closure from any subsystem mentioned will alarm the data-record station.

The CFS has been functioning as a system for 1221 hr and the rubidium frequency standard for 4874 hr. Modifications and tests are continuing to improve system reliability and progress is being made toward an early delivery date.

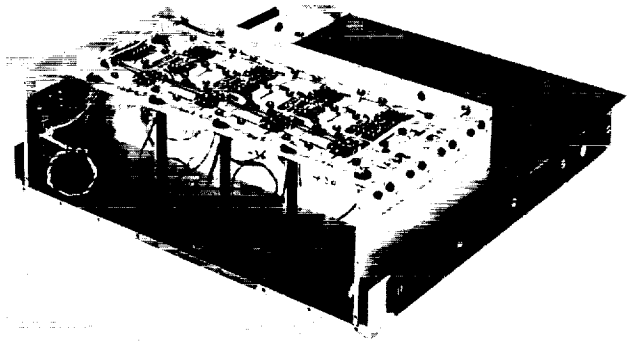

Fig. 23. Voltage vigilant system with front panel removed

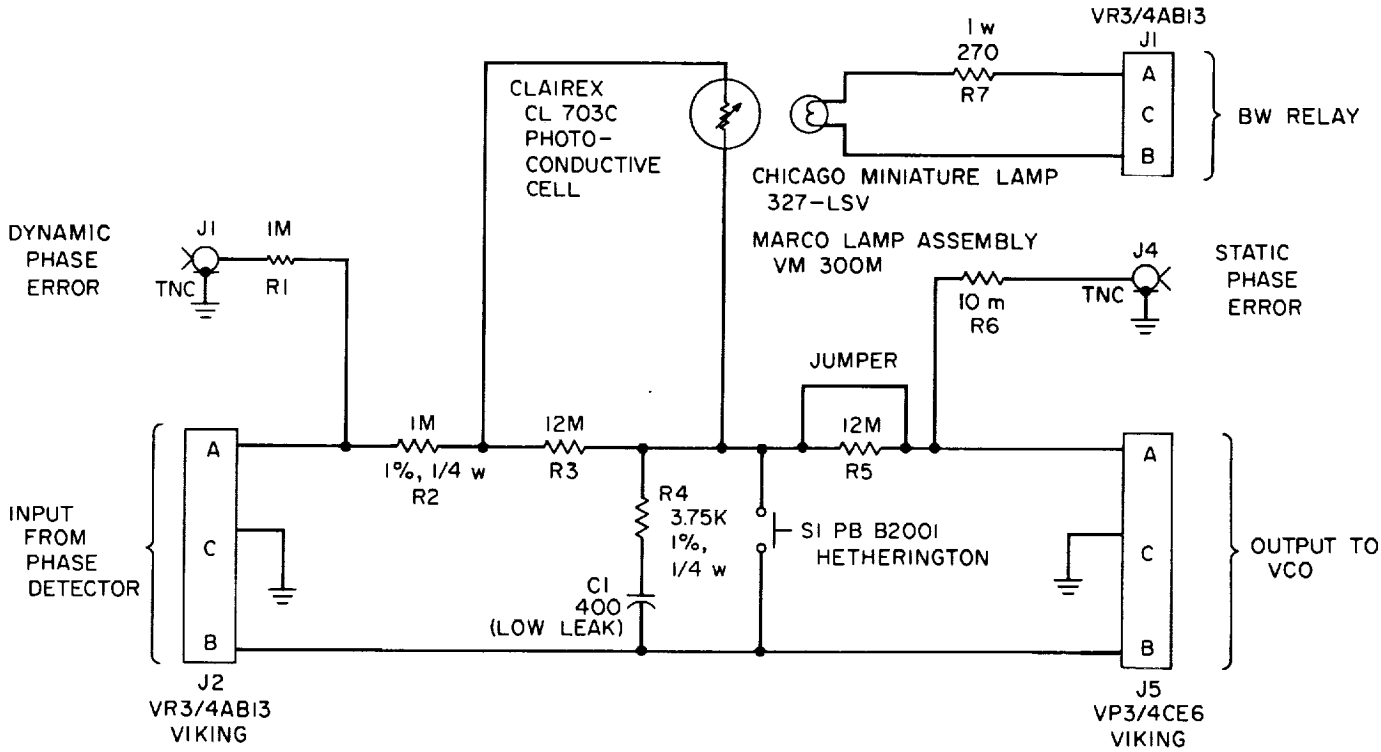

Fig. 22. Tracking filter $2B_L$ = 1 cps, central frequency synthesizer

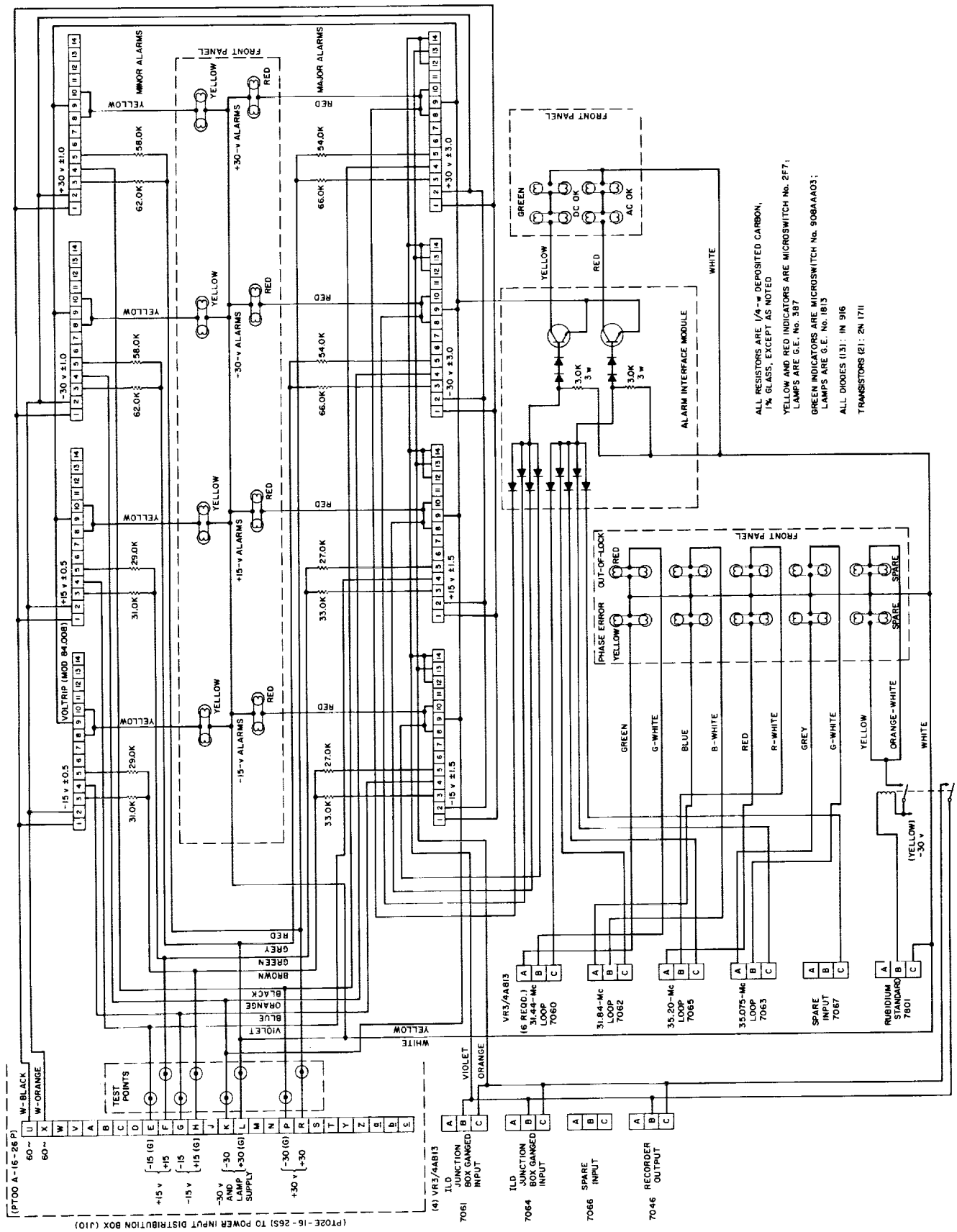

Fig. 24. Voltage vigilant and central alarm system

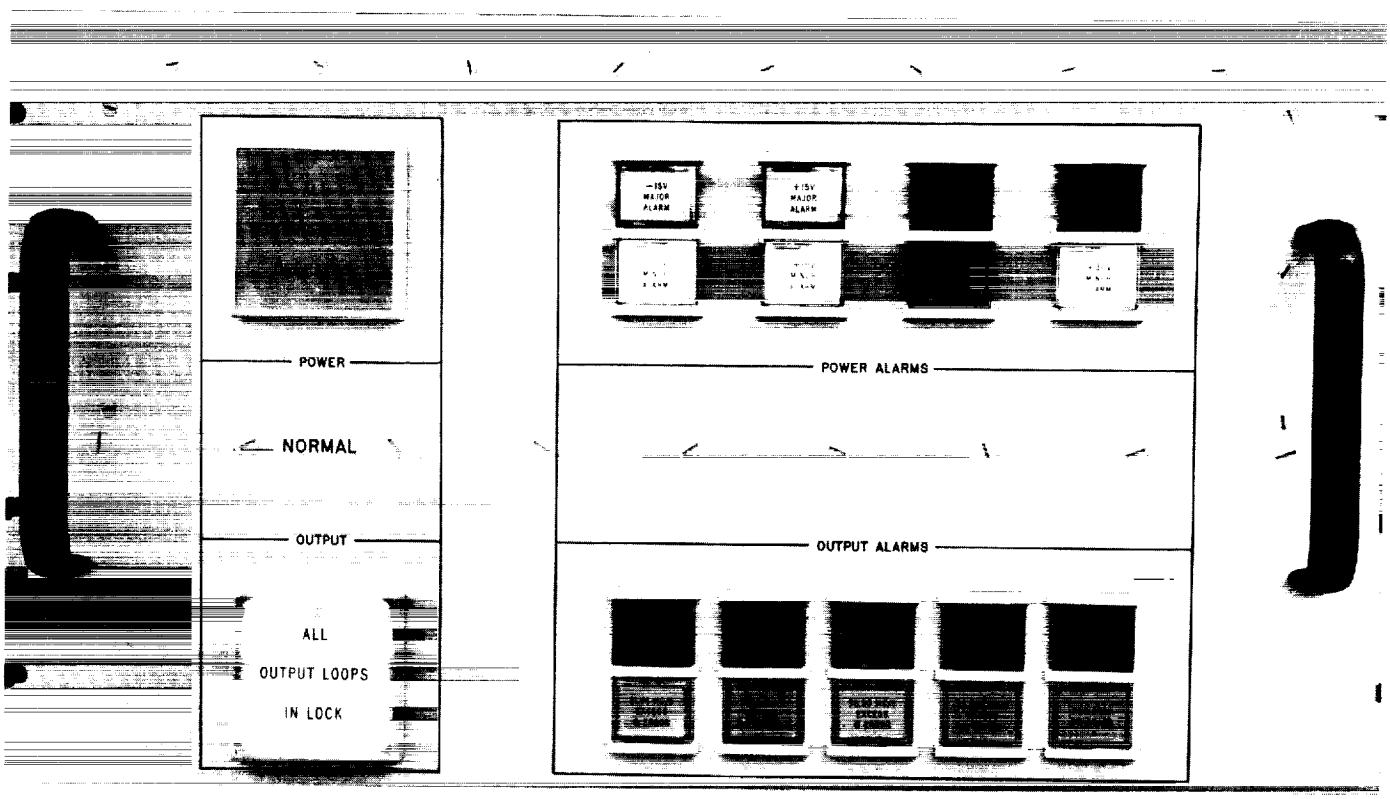

Fig. 25. Voltage vigilant system front panel

F. Digital Development: Mod V Programmed Oscillator

R. Emerson, E. S. Fábián, and G. Thompson

During February and March, the Mod V programmed oscillator (PO) was completed and installed at the Mars Station (Fig. 26). The computer used to control the PO is an SDS 920 with a card reader and 16 arming priority interrupts.

The control program for the Mod V PO accomplishes the following:

(1) Accepts data in the form of polynomial constants for the evaluation of the received frequency.

(2) Determines the receiver frequency and translates it to the local oscillator requirements once per second.

(3) Tunes the local oscillator to the required frequency and controls the PO to track the required frequency.

(4) Provides communication between the PO system and the operator to determine proper operation and to signal any malfunction, real or apparent, of the PO without interrupting the operation of the PO.

The program consists of a minimal main line (base load) program with almost all actions occurring on interrupt requests. Fig. 27 is a block diagram of the program.

The main program loop updates the display, commands the PO to maintain a given configuration, monitors the error indicators and requests for the typewriter, and controls the typewriter mode (input or output).

The 1-sec, 0.5-sec, and count interrupt routines service each type of interrupt. These interrupts are generated by the PO when it is in the computer-controlled mode.

The load interrupt routines are enabled by the LOAD and LSYN commands which read and format data to be used by the program.

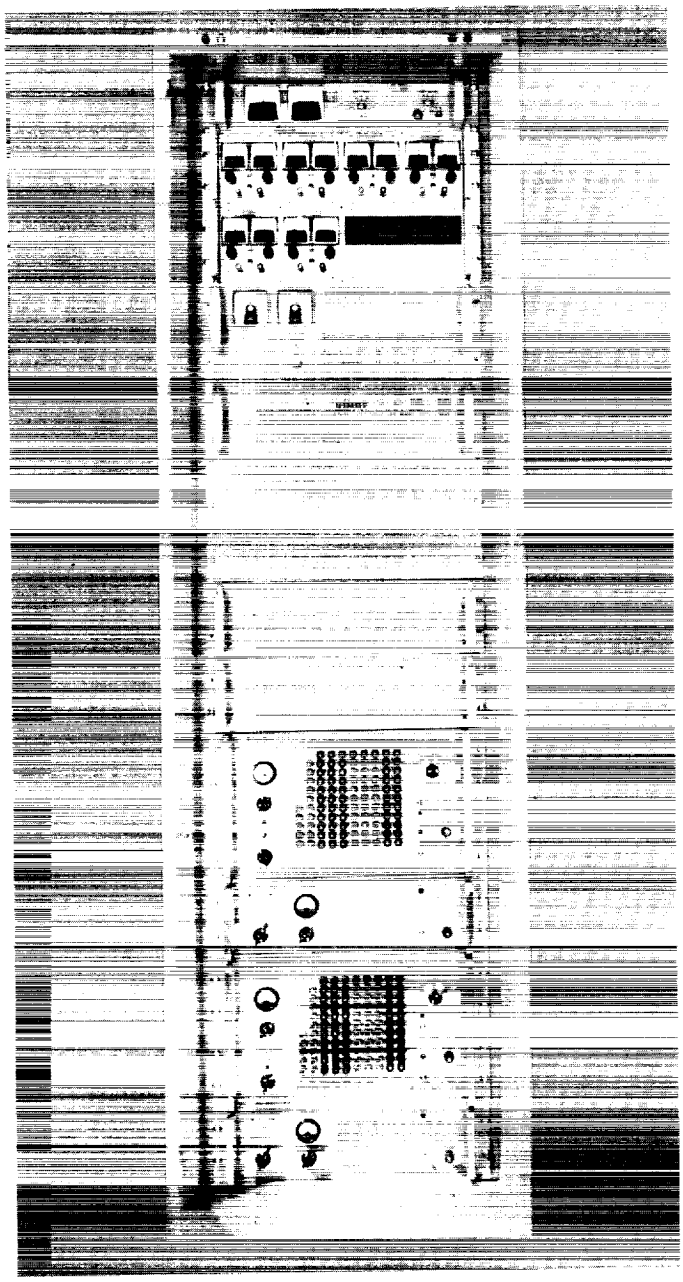

Fig. 26. Mod V programmed oscillator

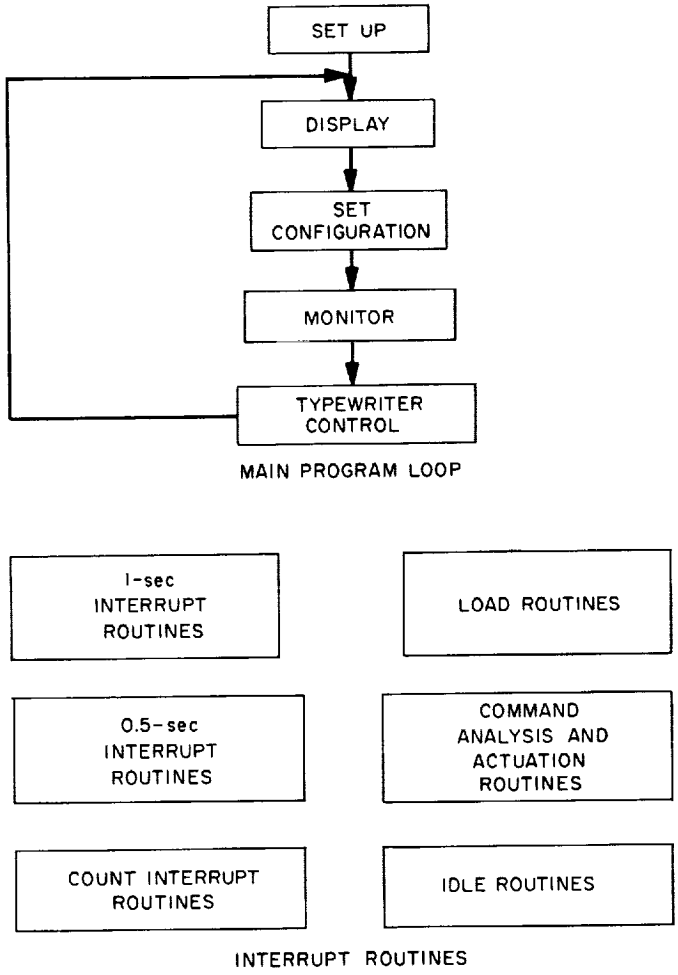

Fig. 27. Computer program block diagram

The command analysis and actuation routines form the link between the operator and the control program. The idle routines are used when the PO is not being commanded in closed loop. The portion of the program that is used as an interface with the operator will be explained more fully.

To obtain control of the console typewriter, the operator sets break-point Switch 1. If the program does not need the typewriter for messages, a carriage return will signal the operator that he can enter commands. Commands are strings of letters and numbers followed by a period. After the computer has acknowledged and acted upon a command, it signals the completion by a carriage return. A list of commands is given in Table 6. The commands are grouped into two classes: operation and test.

For normal operation of the program, the following sequence is followed.

(1) Load program with all break-point switches reset.

(2) Set break-point Switch 1.

(3) Load the card reader with a deck containing the 6 doppler cards and a Synfreq card, in that order.

(4) Give the following commands in order:

  (a) LOAD

  (b) LSYN

(c) SETC

(d) SYNC

(e) If the configuration of the PO is correct as indicated by the lights, reset break-point Switch 1.

(f) If not, correct by one of each of the paired commands:

X or S: Output 1 or 2

T or R: transmit or receive

ONE or TNTH: sample rate (one or ten per sec)

H or L: gain setting (high or low)

OPEN or SA: open loop or synchronous assist

If anything should malfunction during the normal operation of the PO a message will be typed, indicating the type of failure. Table 7 gives these messages; most are self-explanatory. "Select error" refers to the readiness of the PO to accept computer commands. "Histogram complete" signals the operator upon completion of that request.

1. Control Panel

The controls on the PO (Fig. 28) serve only as indicators during the computer-controlled operation of the PO. During manual operation they replace the computer commands. The controls are:

Sync: The sync indicator is lighted after a sync command has been given and until the 1-sec "Tick" from the station synchronizes the equipment to the station time.

Set Decade, Set D/A, Set High, Set Low: Controls for manual operation only.

High–Low: High–low lights indicate the gain setting used with the integrator.

One–Tenth: Indicates the sampling rate used (one per second or ten per second).

Manual–Computer: Indicates the control status of the PO and will only be set to *computer* when all control switches are set to *remote*.

Count (on-off): Indicates that the PO is being commanded in closed loop to tune to the required frequency.

Table 6. Commands

Type	Command	Effect
Operational	LOAD	Loads polynomial constants
Operational	LSYN	Loads Synfreq number
Operational	SYNC	Syncs PO to station time and starts tracking
Operational	DSET	Sets up display
Operational	SETC	Sets last configuration used
Operational	T	Commands transmit option
Operational	R	Commands receive option
Operational	X	Commands Output 1 option
Operational	S	Commands Output 2 option
Operational	OPEN	Commands open loop option
Operational	SA	Commands synchronous assist option
Operational	TNTH	Commands 0.1-sec sample option
Operational	ONE	Commands 1-sec sample option
Operational	H	Commands high-gain option
Operational	L	Commands low-gain option
Operational	BIAS	Sets an offset in frequency
Test	KILL	Resets program to idle state
Test	SET	Adjusts gain of control loop
Test	SETF	Sets constant frequency as reference
Test	RSET	Resets to tracking mode (frequency reference) from SETF command
Test	HIST	Initiates a 1-hr histogram of frequency error
Test	A	Sets address for W, IW, ST, and STI commands
Test	W	Write out the contents of cell specifics by last A command
Test	ST	Store octal number on this line in address called by A
Test	IW	Increment A and write as in W
Test	STI	Store as in ST and increment A

Table 7. Computer messages

Select error 00:00:00
Station time error 00:00:00
Time out of poly range 00:00:00
Card read error 00:00:00
1-sec check error 00:00:00
0.5-sec check error 00:00:00
Histogram complete 00:00:00
Counter check error 00:00:00

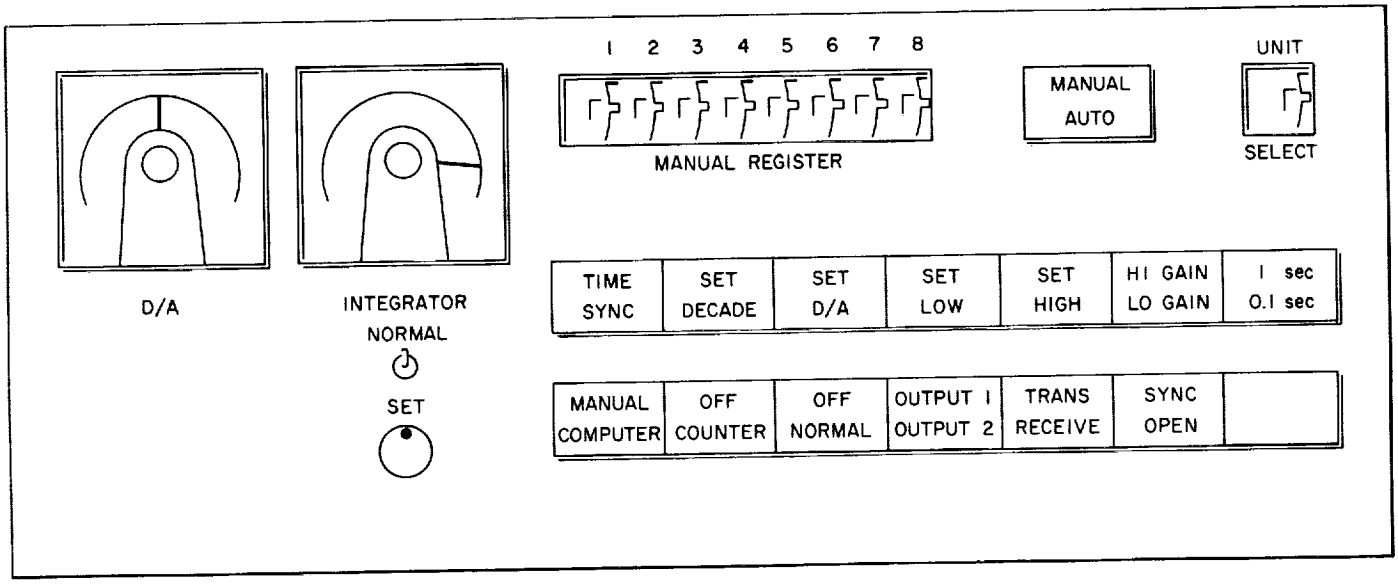

Fig. 28. Control panel

Normal (on-off): Indicates that the PO and computer are operating properly (no recognized malfunctions).

Transmit-Receive: Indicates the mode of the PO (exciter or local oscillator).

Output 1–Output 2: Shows the unit to which the PO is connected (S and X are used to command this option from the keyboard).

Open Loop–Sync Assist: Indicates the mode of the reference feeding the PO.

2. Auxiliary Equipment

The auxiliary equipment consists of an interface to buffer computer output signal, an interface to permit input of the station time information into the computer, and a light display to assist real-time operations. Both the hardware and the software associated therewith are operational. Further information regarding the PO may be found in *SPS 37-36,* Vol. III, pp. 54–63.

a. Computer interface. The system is built with only one circuit connected to each of the computer output signals, and uses Schmitt triggers on all strobe signals for noise rejection. The data signals, C_0 through C_{23}, are each prevented from going negative by a diode to ground to eliminate ringing, and are connected to the node of the microcircuit package by an isolation diode, thus preventing the 8-v computer output signals from damaging the microcircuits, which have an 8-v breakdown voltage.

The amplitude of the strobe signals is reduced by a voltage divider, and the reduced amplitude signal is used to drive the inputs of the Schmitt trigger microcircuits.

This interface presents both the inverted data signals and the buffered (twice inverted) signals on the output pins, thus eliminating the need for inverting most signals at several different locations within the system.

b. Time interface. The station time is brought to the PO through the cable wrap up from the Datex-built external equipment called frequency and timing subsystem (FTS) in 31-bit, binary-coded decimal days, hours, minutes, and seconds format (−13, ONE; ground, ZERO). Each of these signals, excepting day, is connected to a gated microcircuit inverter via a levelshift network (Fig. 29). Since the output of the inverter is

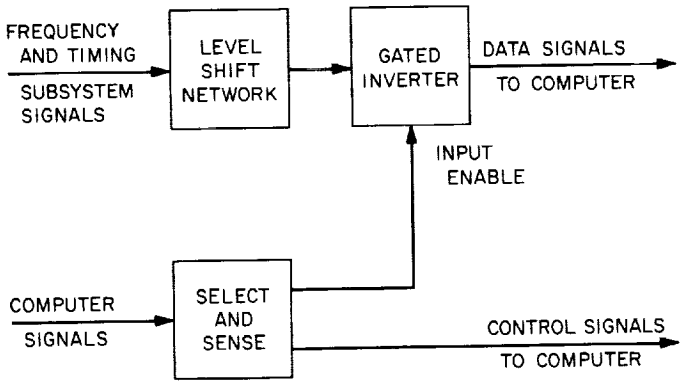

Fig. 29. Time interface block diagram

ground, representing ONE when the FTS signal is ground, an exclusive *OR* (EOR) instruction is used within the computer after inputing the data to convert it to standard binary-coded decimal (BCD) format.

c. Display. MIDGILITE Model 04-30 miniature readout lamps are used (Fig. 30 shows a typical connection).

Depression of the TEST switch lights all filaments without changing the contents of the display control registers.

The program may test the existence and/or operational status of the unit by a *skip if signal not set (SKS)* command.

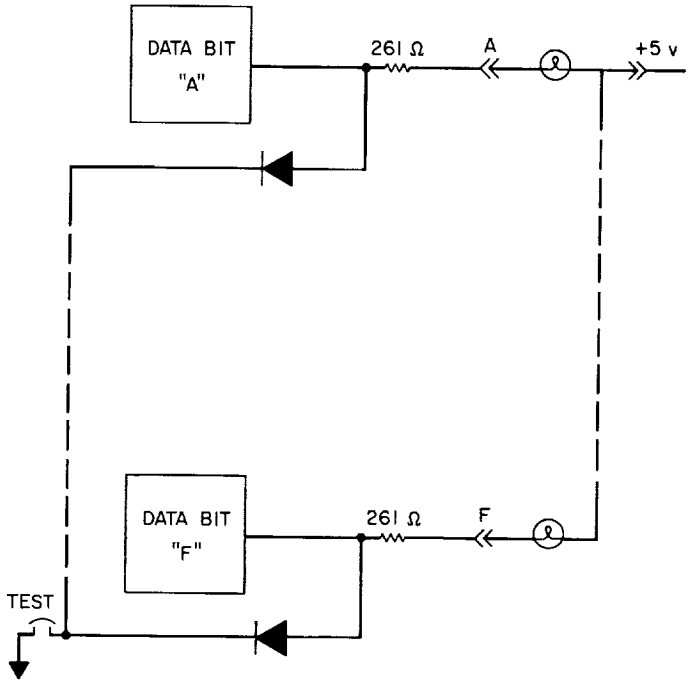

Fig. 30. Lamp drive, typical configuration

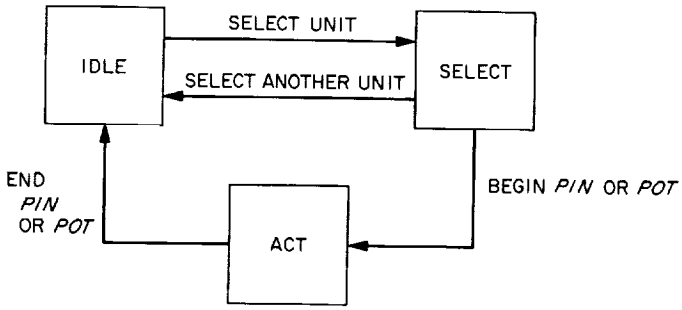

Fig. 31. Simplified phase-state diagram

A computer energize output *M (EOM)* command with the appropriate unit number selects the display unit which then returns a ready signal and the status of the DISPLAY SELECT toggle- and thumbwheel-switch. This selection is terminated by any of the following: another system *EOM* selecting a different unit, a parallel input (*PIN*) command to read the selection, or a parallel output (*POT*) command to set up new information. Fig. 31 is the phase-state diagram.

The display unit stores the information to be displayed in 8 registers of 7 bits each. One character of the display is controlled by each register and is selected by the low-order bits of the computer *POT* word (Fig. 32). The individual bits of the register are loaded from bits 13 through 19 of the same *POT* word, and drive the filaments of the associated character directly, thus necessitating program translation from computer to MIDGILITE code.

d. Software. Various display formats have been programmed as parts of the common DISPLAY subroutine. A table-look up is performed to determine the memory locations where the information is stored, as well as the choice of format. Binary information may be displayed

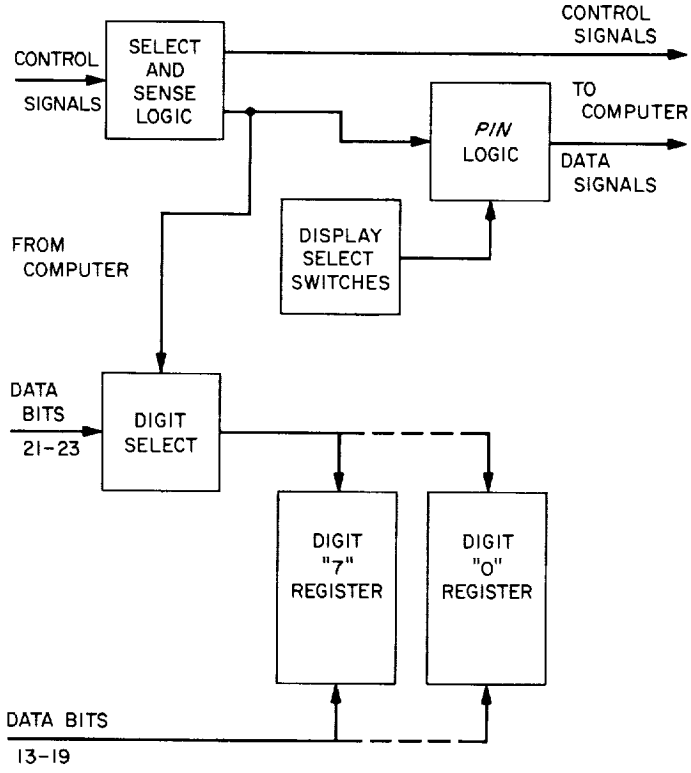

Fig. 32. Display block diagram

as 8-digit octal, or may be converted to signed ("P" for plus) 7-digit decimal format. Inputs from the time interface are displayed in this typical format: 21-57-13; 4- or 6-bit per character BCD data may be displayed as 8 characters. The DSET console typewriter command may be used to associate any one of the 16 display select codes with memory locations and display formats.

3. Performance Characteristics

The Mod V PO has been operational since March 1966, at the Goldstone Mars Station. The system has been tested for the performance characteristics listed in Table 8. The statistics listed there apply to a PO output frequency of 35 MHz which is approximately the nominal frequency of operation for the S-band experimental receiver at the Mars Station. The specifications in Table 8 were generated from the performance characteristics of the X-band Mod IV programmed local oscillator (*SPS 37-30*, Vol. III, pp. 69–71).

The Mod V PO phase noise was measured in a phase-locked loop at 35 MHz with a double-sided noise bandwidth of 5 Hz. The worst-case situation exists when the computer is maintaining the search oscillator at a constant frequency. Under these conditions, the phase noise was measured to be 0.03 deg rms. This is not appreciably worse than when the search oscillator is not used. Therefore, the digital control of the PO does not increase the system phase noise.

Table 8. Mod V PO performance characteristics

Characteristic	Specification	Performance	Units
Phase noise $2B_L = 5$ Hz	0.04	0.03	deg rms
Frequency stability, σ	5×10^{-11}	1×10^{-11}	—
Total doppler range	—	100 kHz to 50 MHz	—
Continuous doppler coverage	100	100	Hz
Maximum doppler rate	0.3	0.5	Hz/sec
Minimum frequency increment	1.0	0.5	mHz

The Mod V PO can provide doppler coverage from 100 kHz to 50 MHz at rates up to 0.5 Hz/sec (32 Hz/sec at Mars Station S-band frequency). With the search oscillator in the 10-Hz column, the range of continuous doppler coverage is 100 Hz. Since switching transients have been shown to endure on the order of 200 μsec, this limitation is acceptable at present (Ref. 2).

The inherent instability of the search oscillator limits the range of continuous doppler coverage for a given stability requirement on the system. As mentioned previously, the search oscillator has a stability of 1 part in 200,000 or 5 Hz in 1 MHz. Operating in the 10-Hz column, this instability has a net effect on the output frequency of 5×10^{-4} Hz. At 50 MHz this is 1 part in 10^{11}. At 1 MHz this is 5 parts in 10^{10}. Therefore, to obtain stabilities of 5 parts in 10^{11} the synthesizer has to be used above 25 MHz and the maximum range of the search oscillator will be 100 Hz.

It should be noted that both the rate of coverage and the range of continuous coverage can be increased by a factor of ten if a sacrifice in phase noise and frequency stability is made. This mode is readily available by simply controlling the search oscillator in the 100-Hz column instead of the 10-Hz column.

The ability of the digital logic to control the output frequency is determined by making a histogram (Fig. 33) of the frequency deviation of the search oscillator. The standard deviation of this graph is ⅓ MHz, or a stability of 1 part in 10^{11} at 35 MHz for a 1-sec averaging time.

The non-zero mean of the histogram is caused by a residual offset in the digital-to-analog converter. With the present method of frequency control this represents a limit to the accuracy of setting the output frequency of the PO. This accuracy represents 1 part in 10^{11}. However, since the counter continuously counts the search oscillator frequency, the PO can be programmed to phase track a continuous frequency function. The phase tracking would then insure that the inaccuracy of the output frequency approaches zero after a long period of time.

The digital logic can control the output frequency of the PO with the accuracy and the short-term stability of a rubidium frequency standard. Any worthwhile improvement in frequency control requires better atomic frequency standards, as well as improved digital control.

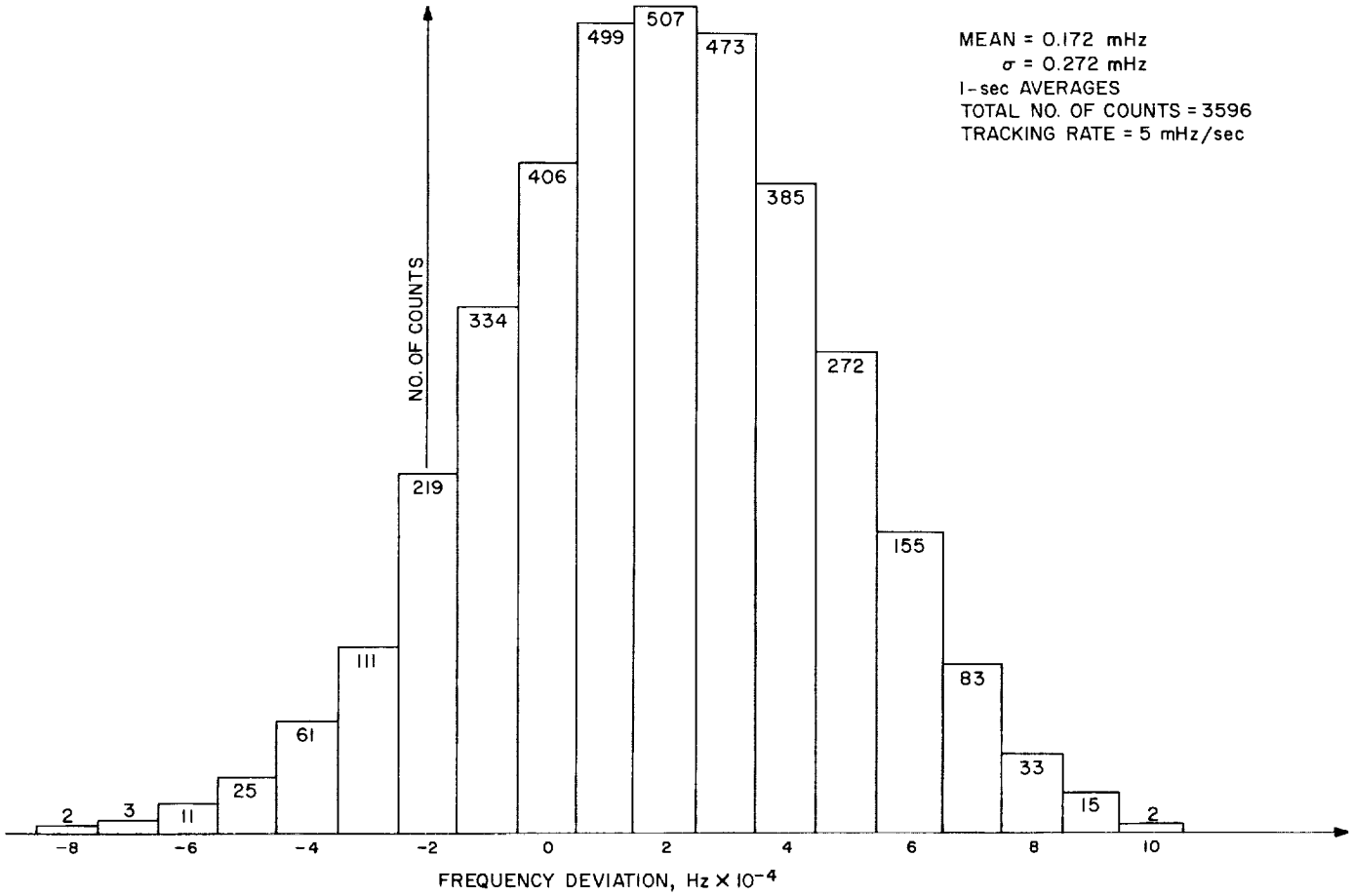

Fig. 33. Histogram of Mod V PO frequency stability

G. Digital Development: Frequency Divider

E. Lutz

This report describes a frequency divider featuring a digital countdown system in combination with an analog gate.

When used to divide a high stability reference frequency, this method maintains phase noise characteristics of the input signal without significant deterioration. Referring to Fig. 34, a signal of known frequency is simultaneously applied to the inputs of the gate and the counter. The counter, in turn, provides a control (blanking) signal which causes the gate to conduct at specific time intervals. Therefore, depending upon the blanking period, the fundamental output frequency can be made any submultiple of the input frequency.

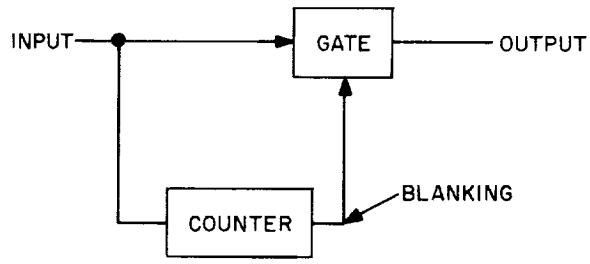

Fig. 34. Basic frequency divider

This hybrid arrangement is preferred for a number of reasons. A straight digital countdown system has the wide-band capability and reliability not easily achieved in analog schemes. On the other hand, the phase stability of a digital counter leaves something to be desired because of the numerous temperature-sensitive voltage thresholds and other unpredictable parameters. In conjunction with the more predictable semianalog gate, a

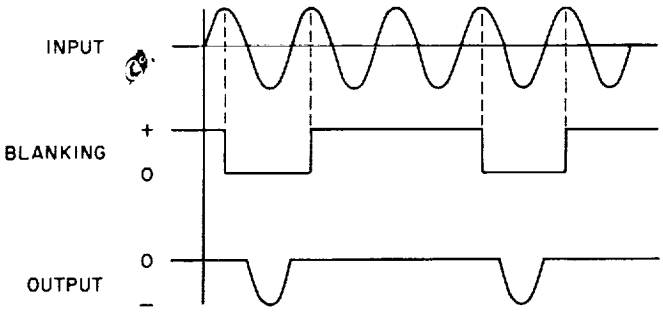

Fig. 35. Timing diagram

substantial improvement is achieved. The timing diagram in Fig. 35 shows the actual operation.

1. Gate

a. Description. Fig. 36 shows the gate circuit configuration. The input signal is terminated into approximately 50 Ω at the input of the buffer stage Q_1. The blanking signal is applied to the fast PNP switch Q_2 which translates positive logic into negative levels. Transistor Q_2 operates in the common base mode and, depending upon the state of Q_3, its bias varies from light to heavy cutoff. When in light cutoff, negative portions of the input signal are allowed to conduct Q_2 and will therefore be seen at the output of buffer stage Q_4. During the time Q_2 is in heavy cutoff, the output remains static.

In order to avoid excessive feedthrough noise in Q_2, due to switching transients at the base, an RF transistor (such as 2N 918) with exceedingly low leakage capacitances is recommended. In addition, the collector of Q_2 is clamped to approximately +4.5 v, thus removing any remaining feedthrough and power supply noise.

b. Test setup. The operating conditions are listed in Table 9. Fig. 37 shows the test setup from which are

Table 9. Operating conditions

		Minimum	Typical	Maximum	Units
Input	Sine wave (50-Ω source)	—	5	7	Mc
Blanking	t_r t_f (200-Ω source)	— —	20 20	40 40	nsec nsec
Output	V_i = 1 v rms f = 5 Mc R_L = 1K		3.5		v

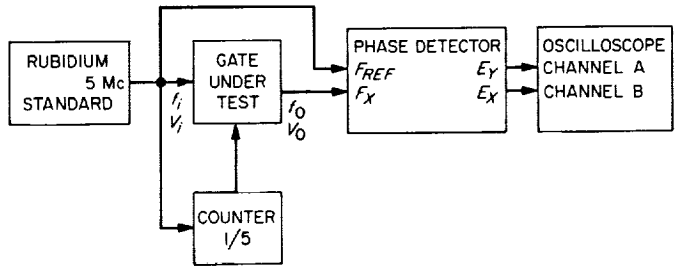

Fig. 37. Test setup

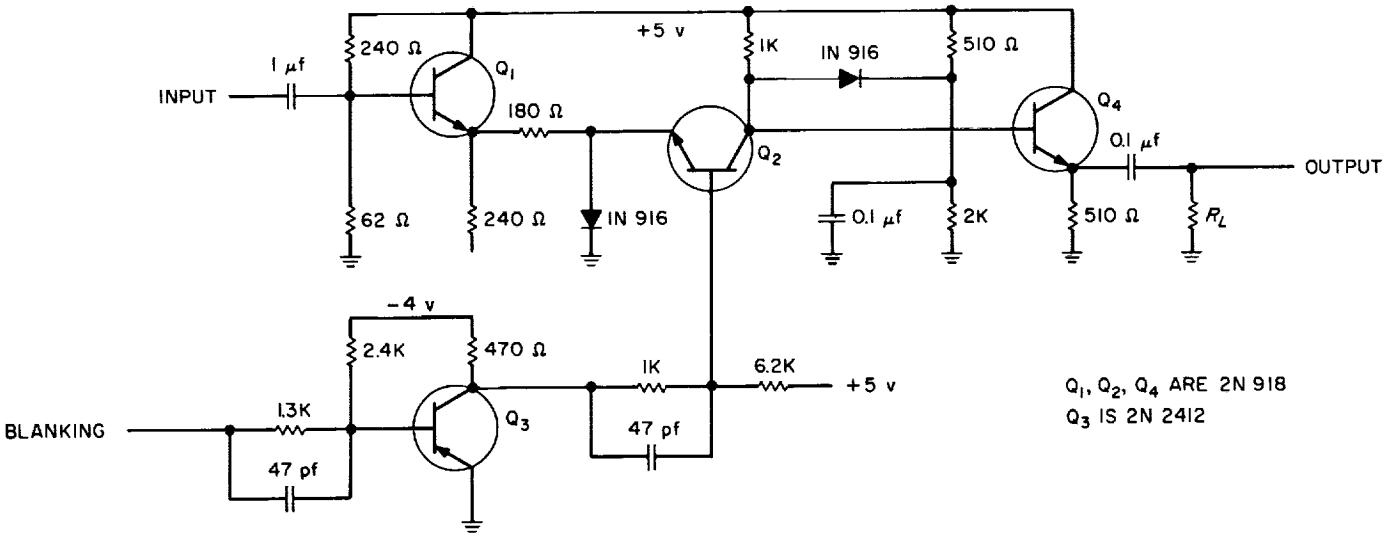

Fig. 36. Gate

derived the various phase measurements that are performed differentially by comparing the output signal to the input in the Parzen 104 frequency comparator. The input signal is obtained from a Varian rubidium standard at 5 Mc, while the blanking signal was arranged to countdown to 5. After proper calibration, the Parzen phase detector outputs were connected to a Tektronix 545A oscilloscope for visual error display.

c. Definition of terms. *Static phase jitter* ϕ_{JS} is defined as the total amount of random phase modulation in degrees, measured differentially between the output and the input of the gate. ϕ_{JS} is specified in terms of f_i, V_i, f_0 and V_0.

Dynamic phase jitter ϕ_{JD} is defined as the total amount of dynamic phase modulation or crosstalk in degrees, measured differentially between the output and the input of the gate when the blanking signal is phase modulated sinusoidally by an amount ϕ_{JB}. ϕ_{JD} is now specified in terms of f_i, V_i, f_0, V_0 and ϕ_{JB}.

d. Results of measurements. Table 10 shows the static phase jitter ϕ_{JS}, and Fig. 38 is a typical graph for the dynamic phase jitter ϕ_{JD}. As a result of the dynamic phase jitter measurements, an average improvement of 15 times was obtained.

Table 10. Static phase jitter

Parameter	Test conditions	Minimum	Typical	Maximum	Units
ϕ_{JS}	f_i=5 Mc, V_i=1 v rms f_0=1 Mc, V_0=3.5 v, peak-to-peak Readout time=0.3 msec	—	0.001	0.002	deg

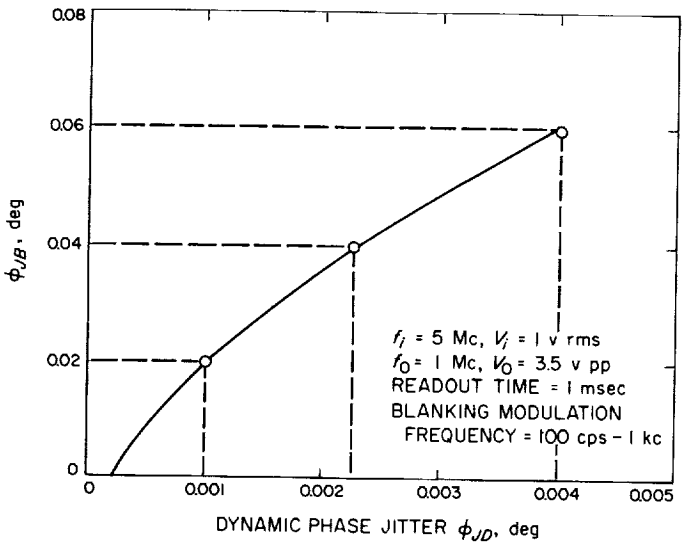

Fig. 38. Dynamic phase jitter

2. Conclusion

The over-all performance capabilities of this type of frequency divider were found to be satisfactory. This system will prove useful in applications where wide bandwidths and large frequency ratios are required, i.e., frequency synthesis in the DSIF and the doppler extractor.

It must be noted that measurements made at 1 Mc show a static phase jitter not exceeding 0.002 deg, from which it is assumed that if this frequency is multiplied up to 3 Gc, the total jitter will not exceed 6 deg.

H. Experimental Closed Cycle Refrigerator for Masers

W. Higa and E. Wiebe

An alternative approach to a second generation closed cycle refrigerator (CCR) has been developed which solves two major problems associated with the gas-balancing engine used in the earlier version (*SPS 37-31*, Vol. III, p. 38). In the new approach, an A. D. Little paramp cooler is used to provide the cooling necessary for the Joule-Thompson (J-T) expansion of gaseous helium to produce refrigeration at 4.2°K. Only minor changes were required to transfer the existing J-T circuit to the new machine.

The principal difficulty with the gas-balancing engine has been that of inconsistent performance because of its sensitivity to changes in friction in the moving parts. This difficulty has been noted in a given machine as a function of time and also in comparing the performance of two identical separate units. The other difficulty is a practical one of commercial nonavailability.

Both difficulties have been solved by the successful conversion of the A. D. Little paramp cooler (Model 340L) to a 4.2°K refrigerator. Fortunately, only minor changes were required to make the transition from the old to the new configuration. Fig. 39 shows schematically how the J-T circuit is added to the paramp cooler. The helium gas is cooled to 70°K, then to 15°K, and finally to 4.2°K, by a J-T expansion process.

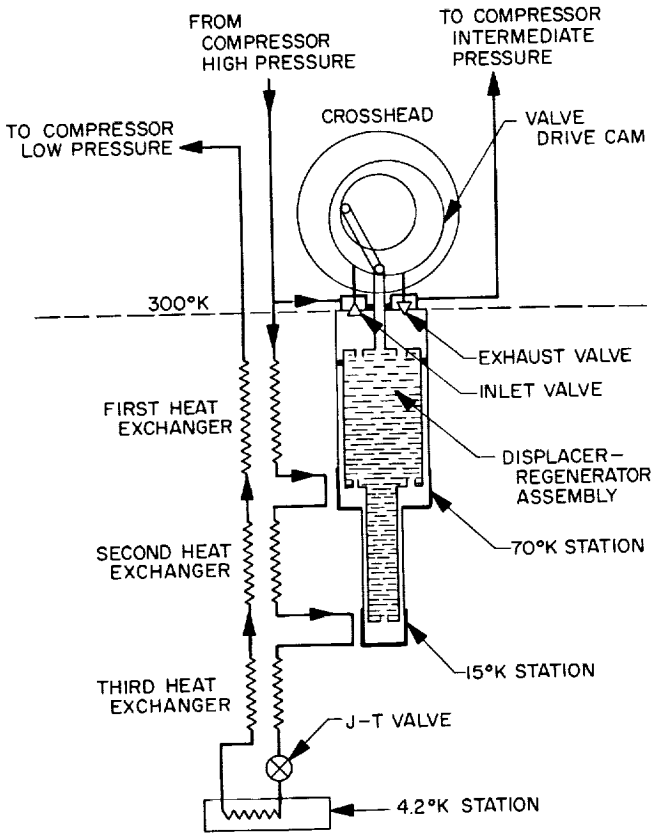

Fig. 39. Schematic diagram of cryogenic refrigerator

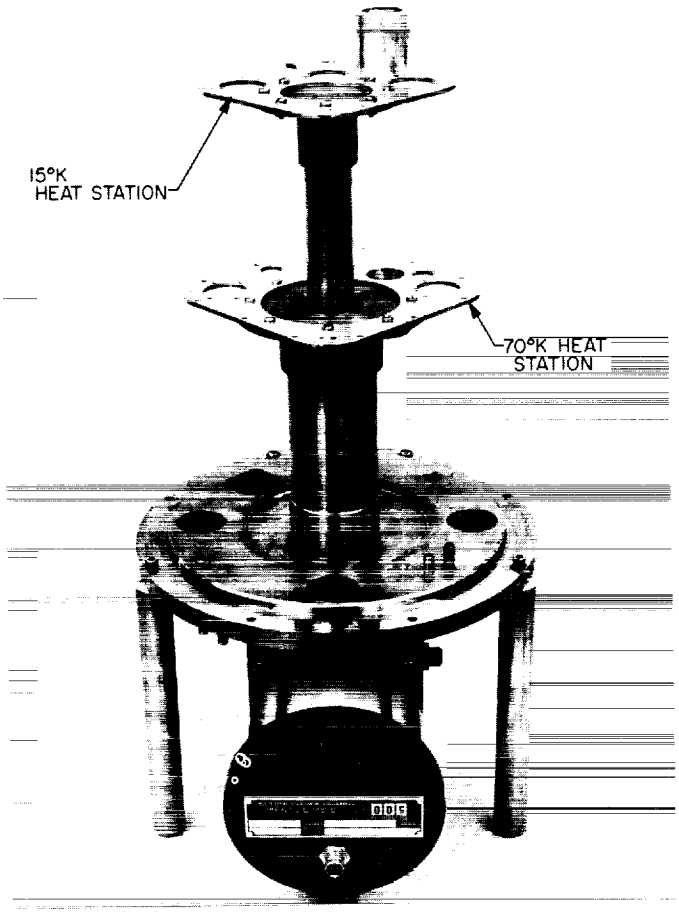

Fig. 40. Basic paramp cooler with heat stations mounted

Fig. 40 shows the basic Model 340L refrigerator with the addition of the two heat stations at 70 and 15°K. The complete CCR with traveling wave maser (TWM) installed is shown in Fig. 41. The complete TWM/CCR assembly is shown in Fig. 42 ready for installation in the listening cone of the advanced antenna system (AAS). (The TWM which is tunable from 2275 to 2400 Mc is described on p. 83.)

The thermodynamic cycle for the Model 340L is essentially the same as for the gas-balancing machine (*SPS 37-31*, Vol. III, pp. 38–44) and need not be repeated here. The significant difference between the two machines is in the way the reciprocating displacer is moved. In the Model 340L, a definite phase relationship between the displacer position and the inlet and exhaust valve positions is assured by the electromechanical driver (crosshead). In the gas-balancing machine, the phase relations are governed by the amount of friction at the displacer seals; this friction is understandably a variable quantity and leads to the aforementioned difficulties.

The performance of the new refrigerator is similar to that of the pneumatically driven machine. The performance characteristics of the machine are summarized in Table 11.

Cool-down time (with maser) was 3.2 hr with liquid nitrogen precooling and around 7 hr without liquid nitrogen.

At the time of this reporting, a total of 2200 hr has been logged for the new refrigerator.

Table 11. Performance characteristics of the new CCR

Supply pressure, psia	J-T flow rate, SCF/min	Temperature, °K	Capacity without maser, mw	Capacity with maser, mw
250	1.3	4.4	800	600
275	1.3	4.4	950	—

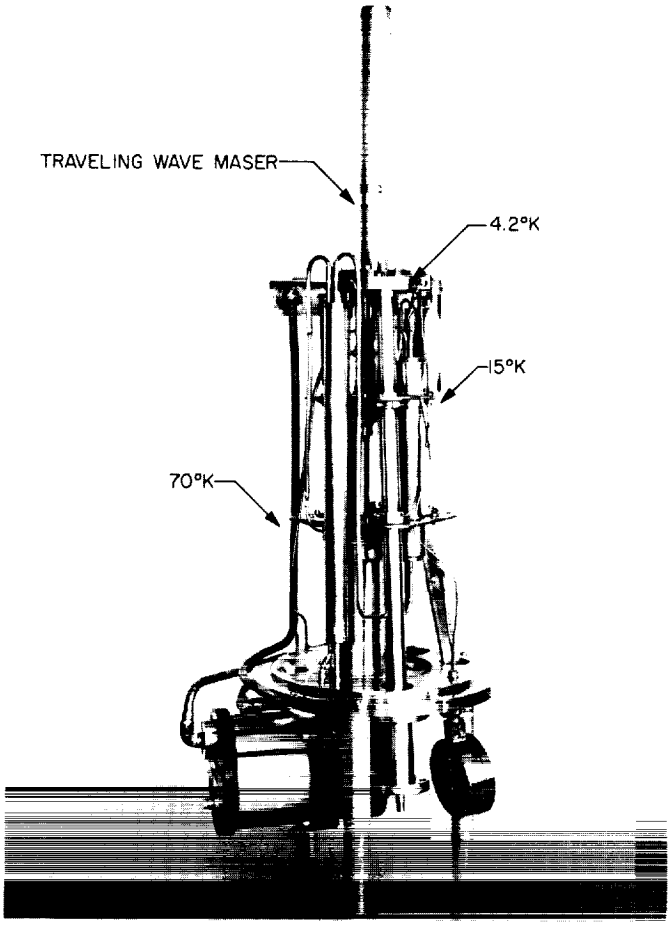

Fig. 41. 4.2°K refrigerator with TWM mounted (radiation shield removed)

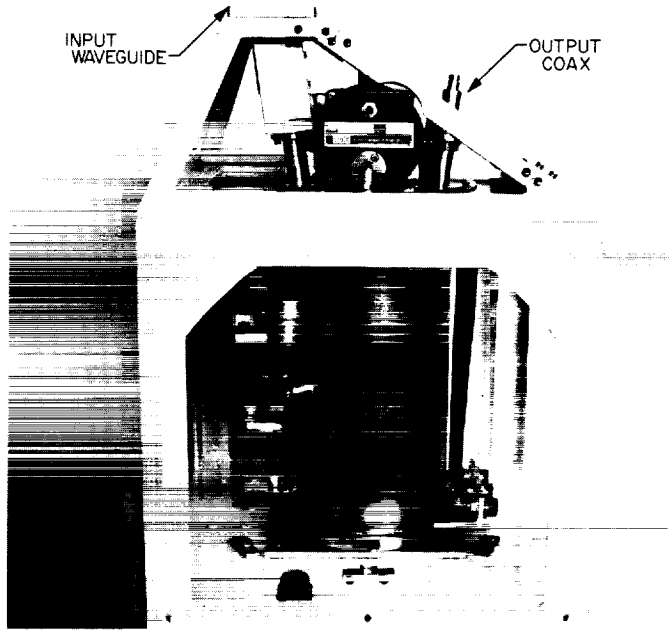

Fig. 42. Complete TWM/CCR assembly ready for cone installation

I. Continuous Wave Signal Power Calibration With Thermal Noise Standards

C. T. Stelzried and M. S. Reid[2]

1. Introduction

An attempt to improve the accuracy of the calibration of the continuous wave (CW) received signal power in the DSN is presently underway. A convenient measure of a spacecraft received power level is the received AGC voltage, which is calibrated for absolute received power, defined at the receiver input, with a calibrated test transmitter. The theory, method of data acquisition, and equipment have been discussed previously (SPS 37-35, Vol. III, p. 58; SPS 37-36, Vol. III, p. 44; SPS 37-37, Vol. III, p. 35; SPS 37-38, Vol. III, p. 41).

One of the important considerations in this method of CW power calibration is the measurement of system temperature. In this report, the method of system temperature measurement used in the CW power calibration experiments is discussed and compared with the nominal DSIF station methods.

2. The Measurement of System Temperature

CW power calibrations were carried out over an extended period of time on the *Mariner IV* spacecraft. As these calibrations were made at two stations (DSIF 11 and DSIF 12), it was important for comparison purposes that both stations should use the same method of measuring system temperature. There were several other constraints on the measurement of system temperature. Among these were: (1) the requirement for reliability and repeatability, as the experiments continued over an extended period of time, and (2) the need for a quick and simple method because of the limited time available during the precalibration routine. In view of these con-

[2]On leave of absence from National Institute for Telecommunications Research, Johannesburg, South Africa.

straints, a Y-factor method was chosen; also, an ambient load was used because this met the requirements of reliability and stability. Switching the maser input between the antenna at zenith and the ambient load yielded the Y-factor. Each station measured five Y-factors daily during the precalibration routine and just prior to the CW power calibration. An average system temperature for each station was computed each day from these measurements. This method requires a knowledge of the thermal temperature of the termination. If an ambient termination is used, the thermal temperature can easily be measured with sufficient accuracy.

An error analysis of system temperature measurement has been carried out by this method (*SPS 37-36*, Vol. IV, p. 268). This analysis has shown that with the given probable error in receiver temperature, the system temperature probable error is a minimum for thermal load temperatures between ≈150 and 400°K.

Table 12 is a summary of system temperature measurements defined at the maser input for DSIF 11 and DSIF 12 during the period that the *Mariner IV* spacecraft CW power was calibrated by microwave noise standards. The nominal DSIF methods refer to the system temperatures as measured by the normal station procedures and reported to the SFOF.

Table 12. System temperature measurements at the Pioneer (DSIF 11) and Echo (DSIF 12) Stations

Station	Y-factor method		Nominal DSIF method	
	Average, °K	Standard deviation, °K	Average, °K	Standard deviation, °K
Pioneer (DSIF 11)	44.8	0.55	41.3	0.99
Echo (DSIF 12)	43.6	1.18	48.3	2.60

Fig. 43 is a plot of system temperature against time for the two stations. The solid lines connect the data points derived by the ambient load Y-factor method, and the dotted lines correspond to the nominal station data. The averages from Table 12 are also shown in this figure.

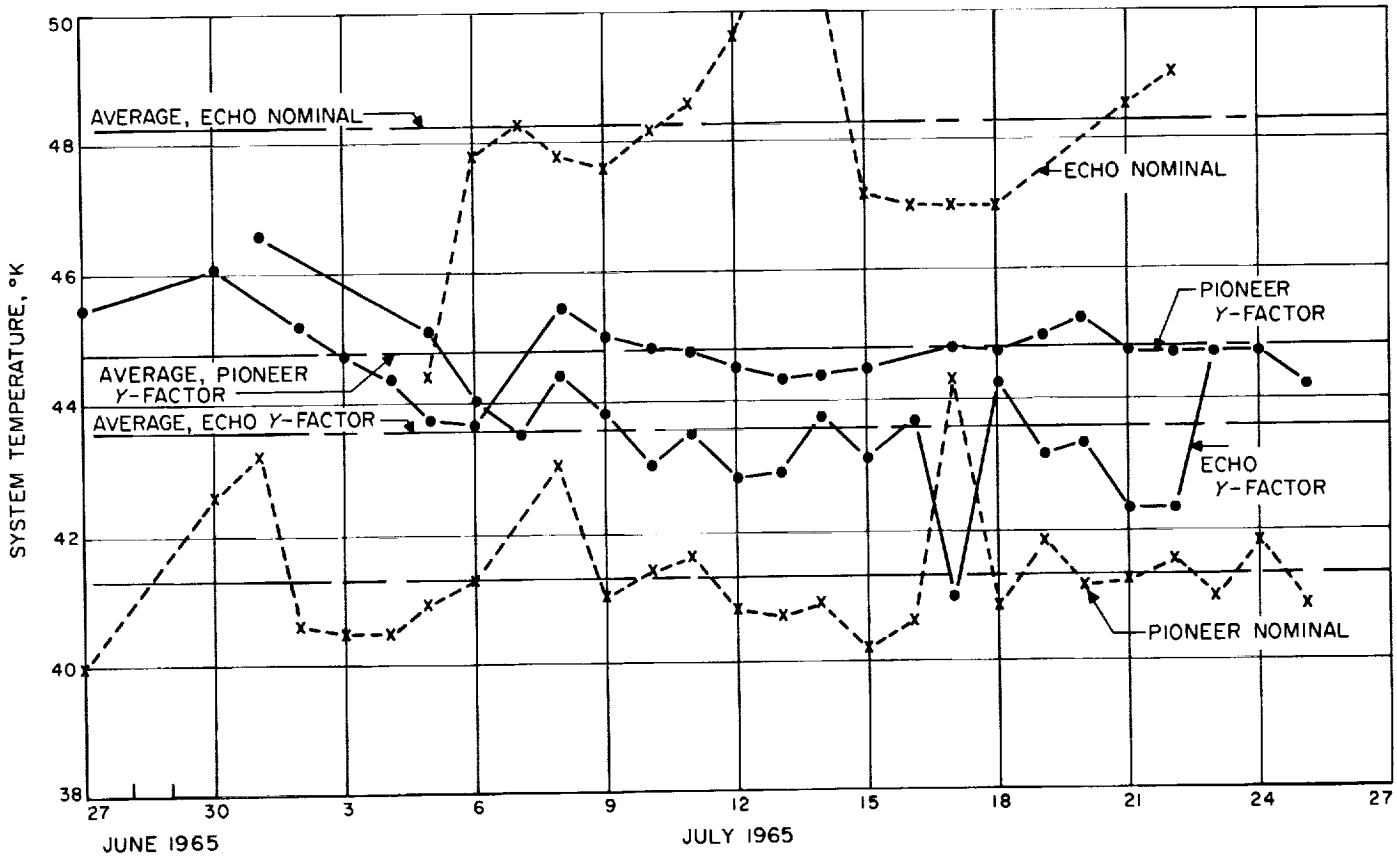

Fig. 43. System temperature measurements at the Pioneer (DSIF 11) and Echo (DSIF 12) Stations

It must be noted that the system temperature measurements by the ambient load Y-factor method were made through a narrowband filter (about 10 kc 3 db BW). The resolution would be considerably improved if this narrowband filter were not used. For example, at the Mars Station, where system temperature is measured by an ambient load Y-factor method without a narrowband filter, the 1 σ of one month's data was 0.12°K after adjustment for equalizing the number of data points.

3. Summary

Even though a narrowband filter was used for these measurements, the 1 σ of the measurement data was considerably reduced over that of the nominal data. Furthermore, by comparison, the mean noise temperatures between stations appear to be more consistent.

Table 13. Traveling wave maser performance

Center frequency, Mc	Net gain, db	Forward loss, db	Measured inversion ratio	Slowing factor
2275	59	34	—	165
2285	62	27	3.4	125
2295	60	22	3.4	125
2310	57	18	3.4	125
2330	54	14	3.4	115
2350	50	13	3.5	110
2370	46	15	3.6	110
2388	40	18	3.6	110
2400	38	21	3.9	115
2415	34	25	3.9	125

J. Microwave Maser Development

R. Clauss

1. Summary

An electronically tunable traveling wave maser (TWM) has been completed and is being used on the 210-ft antenna at the Goldstone Mars Station. The TWM operates in a new closed cycle helium refrigerator at 4.4°K (p.79). Net gain in excess of 40 db is available over a tunable range from 2275 to 2388 Mc. A gain adjustment trades gain for instantaneous bandwidth. The equivalent input noise temperature of the TWM is approximately 7°K.

2. Maser Characteristics

The slow wave comb structure (Fig. 44) and loading techniques have been described previously (*SPS 37-37*, Vol. III, p. 44; *SPS 37-38*, Vol. III, p. 51). Ruby is the maser material used. Polycrystalline YIG isolator discs provide the reverse loss necessary for stable amplification. Table 13 shows the results of measured values which describe the TWM performance. Both magnetic field and pump frequency have been optimized to give maximum gain at the individual frequencies listed. The 3-db bandwidth of the amplifier at maximum gain is approximately 13 Mc, and the pump frequency for 2295-Mc signal frequency

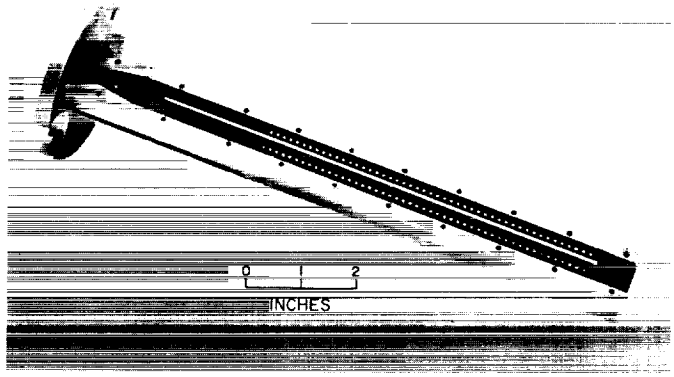

Fig. 44. Maser comb structure

is 12.7 kMc. For maximum gain the pump must be retuned at the rate of 1.6 Mc per Mc signal frequency change. Since the klystron now in use is not tunable over the range required to cover signal frequencies of 2295 and 2388 Mc, it is necessary to change pump klystrons when tuning over this range.

3. Magnetic Field Adjustment

A uniform magnetic field of 2500 gauss is required for maser operation. This field is supplied by a 150-lb alnico magnet. The field strength may be adjusted electrically by the use of two trim coils. This adjustment determines the center frequency of operation for the maser.

In order to provide an efficient gain adjustment (one which trades excess gain for additional bandwidth), a

second set of trim coils is used. The gain adjustment coils change the magnetic field across a total of one-half the amplifying length of the maser. This field change slightly shifts the resonance frequency and results in a stagger tuning of the resonance line. Fig. 45 shows how one step in the magnetic field provides five separate sections of amplification alternately operating at two separate frequencies. As the current through the gain adjustment coil is increased, the separation between F_1 and F_2 is increased, the bandwidth increases, and the overall net gain is reduced. Stagger tuning of the resonance line has been discussed in detail by Siegman (Ref. 3). The results of stagger tuning are shown in Figs. 46 and 48.

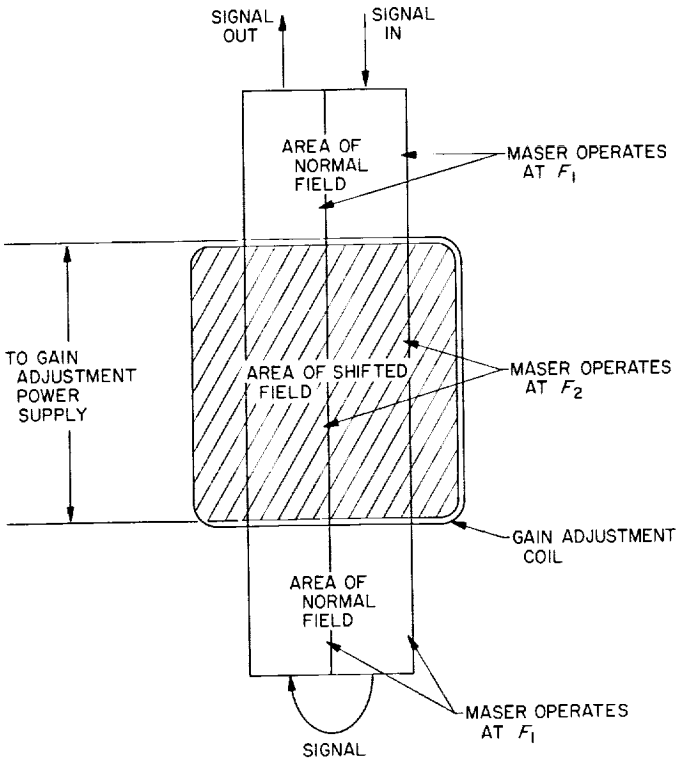

Fig. 45. Gain adjustment coil field change

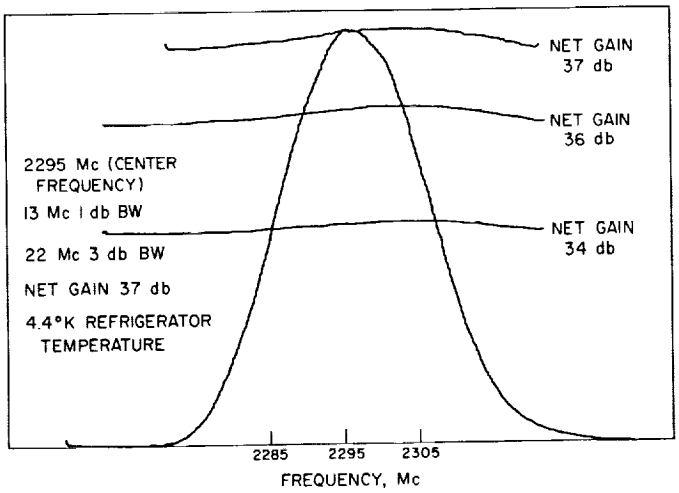

Fig. 46. Stagger tuned maser at 2295 Mc

4. TWM Noise Temperature

The equivalent input noise temperature of a TWM assembly is determined by the amplifier and the signal in-

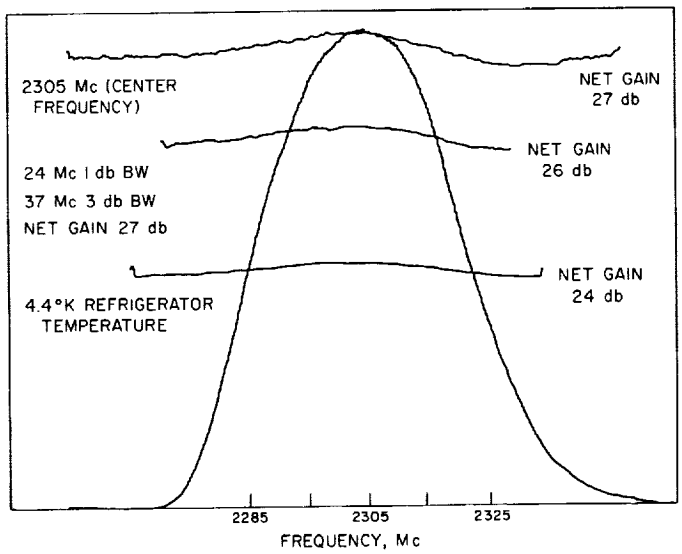

Fig. 47. Stagger tuned maser at 2305 Mc

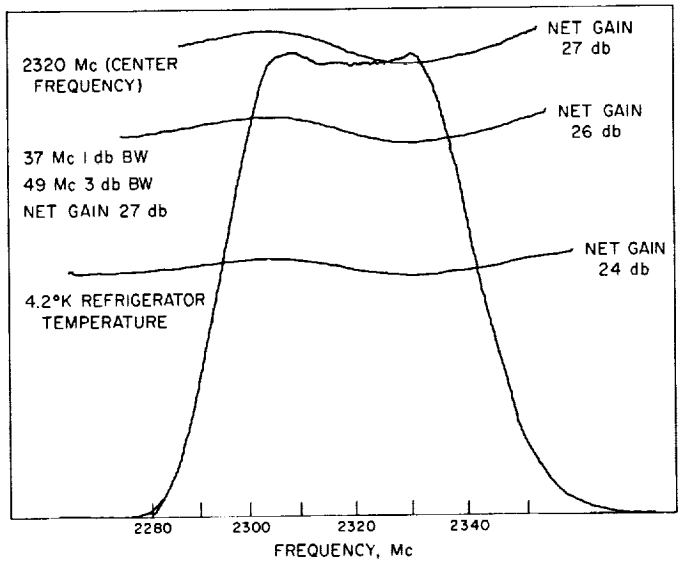

Fig. 48. Stagger tuned maser at 2320 Mc

put line. Insertion loss measurements of components in the signal line have been made. Table 14 gives a summary of the results and lists the equivalent noise contribution to the TWM temperature. An 18-in. length of ⅞-in. coaxial line carries signal power from a waveguide transition to the 4.4°K flange of the maser. The noise contribution of this coaxial line has been reduced by using refrigeration from the 4.4°K flange to cool the center conductor. Fig. 49 is a drawing of the center conductor and vacuum seal. The 7½-in. plated stainless steel section prevents excessive heat leak from the room temperature waveguide to the 4.4°K flange of the maser. The equivalent noise contribution of the partially cooled coaxial line is approximately 1°K. The maser noise temperature T_m is predicted from measured loss and gain values (Ref. 4)

$$T_m \simeq T_0 \frac{\rho + \beta}{1 - \beta} \tag{1}$$

where

T_0 = refrigerator temperature

$$\rho = \frac{1}{\text{measured inversion ratio}}$$

$$\beta = \frac{\text{forward loss in db}}{\text{electronic gain in db}}$$

When the maser is operated in a uniform magnetic field at maximum gain, the forward loss and gain are assumed to be uniformly distributed. An increase in maser noise temperature caused by stagger tuning was measured at 2295 Mc. A reduction of net gain from 69 to 40 db caused an increase in noise temperature across the bandwidth, as shown in Fig. 50.

The predicted maser temperature, including the increase caused by stagger tuning and the signal input line contribution, indicates that an equivalent input noise temperature of 6°K should be achieved at 2295 Mc at 40-db net gain. Cryogenic and ambient reference loads were used to measure the receiver and system noise temperatures on the 210-ft antenna at Goldstone. The lowest measured TWM equivalent input noise temperature at 2295 Mc is 7.2 ± 0.6°K.

Table 14. Loss and noise contributions of components in signal line

Component	Measured loss, db	Calculated loss, db	Noise contribution, °K
Waveguide to ⅞-in. coaxial line transition	0.01	—	0.7
Half-wavelength teflon vacuum seal with neoprene O-ring	0.02	—	1.4[a]
Half-wavelength teflon vacuum seal with silicone rubber O-ring	0.005	—	0.4
⅞-in. coaxial line at (°K)	Measured loss, db/ft	Calculated loss, db/ft	Noise contribution, °K/ft
290	0.03	—	2
170	—	0.022	1
120	—	0.017	0.5
70	—	0.01	0.16

[a]Neoprene O-ring replaced with silicone rubber O-ring.

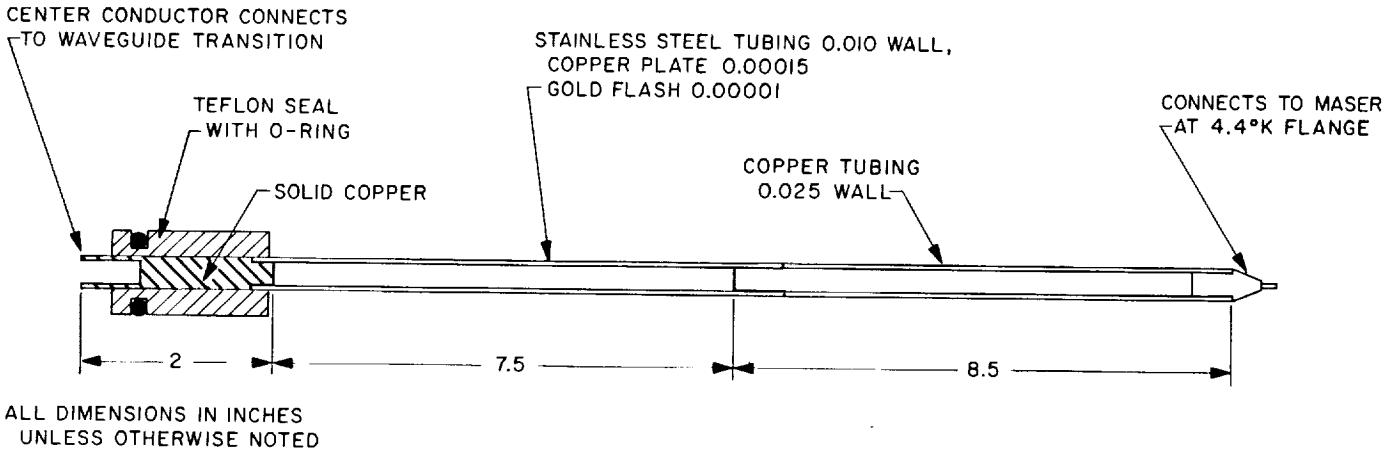

Fig. 49. Input line center conductor

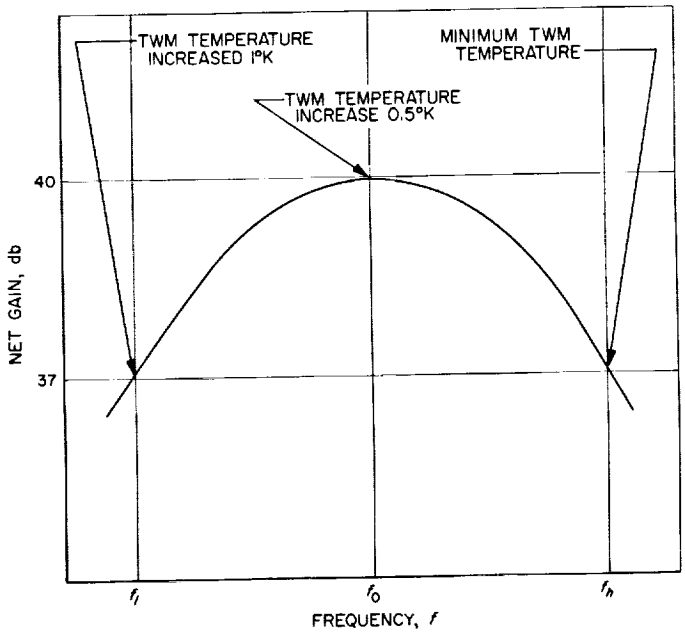

Fig. 50. Increased maser noise temperature caused by stagger tuning

K. RF Techniques

C. T. Stelzried and T. Y. Otoshi

1. Listening Cone

a. Listening cone RF instrumentation. The listening cone RF instrumentation block diagram for the Mars Station 210-ft antenna is shown in Fig. 51. This instrumentation provides for remote measurements of waveguide load reflection coefficient, system noise temperatures, and maser gain. It also provides calibration for AGC curves, radio sources, and antenna gain measurements.

Maser gain is measured by comparison of a CW signal provided by the signal generator switched in front of and behind the maser. Reflectometer measurements are made by comparison of the CW signal injected into the maser and then into the load under evaluation. The side arm of the 26-db waveguide coupler at the maser input is provided with a waveguide-to-coax transition with a built-in isolator and tuning screws (MMC Model SR 8126) to match up the reflectometer.

Noise instrumentation is provided by (1) switching in waveguide between the antenna and the cryogenic loads, and (2) firing two gas tube noise sources of approximately 37 and 4°K. The low noise source will be especially useful when measuring low-level radio sources.

b. Listening cone noise temperature calibrations. Before the listening cone was installed on the 210-ft-diameter antenna, a testing program was initiated to evaluate the cone noise temperature system. Transmission line loss measurements, noise temperature calibrations, and preliminary cone RF instrumentation checkout tests were made at JPL (on the roof of Building 238). Results of insertion loss measurements at 2295 and 2388 Mc have been presented in *SPS 37-38*, Vol. IV, p. 180. The cone noise temperature calibration measurements are discussed here.

(1) *Measurement technique and error analysis.* System noise temperature measurements are made by the Y-factor method which consists of adjusting the precision IF attenuator for the same output power level indication after switching noise source terminations or firing a gas tube noise source. In order to determine receiver and antenna temperature, it is necessary to make two different Y-factor measurements. These involve the use of two reference noise source standards and switching between the antenna and the standards. The two precision noise source standards for the listening cone are the waveguide liquid-nitrogen-cooled load and waveguide ambient load. The less precision noise standards are the high and low gas tube excess noise temperatures.

Fig. 52 shows a block diagram of the basic noise temperature system for the cone. The double-primed symbols indicate temperatures defined at the maser input reference flange; all single-primed symbols refer to temperatures defined at the antenna output reference flange. The double- and single-primed temperatures are related by the dissipative losses of the interconnecting transmission lines.

The notations used are defined as follows (the primes have been dropped for generality):

T_C = cryogenic load effective temperature, °K

T_R = receiver temperature, °K (includes effect of the post amplifier)

T_A = antenna temperature, °K

T_{02} = physical and effective noise temperature of the ambient load, °K (the physical temperatures of the transmission lines are also assumed to be at temperature T_{02})

T_E = excess noise temperature of the gas tube injected into the maser amplifier, °K

T_{SA}, T_{SC}, T_{S0} = system temperatures when switched to the antenna, cryogenic load, and ambient load, respectively, °K

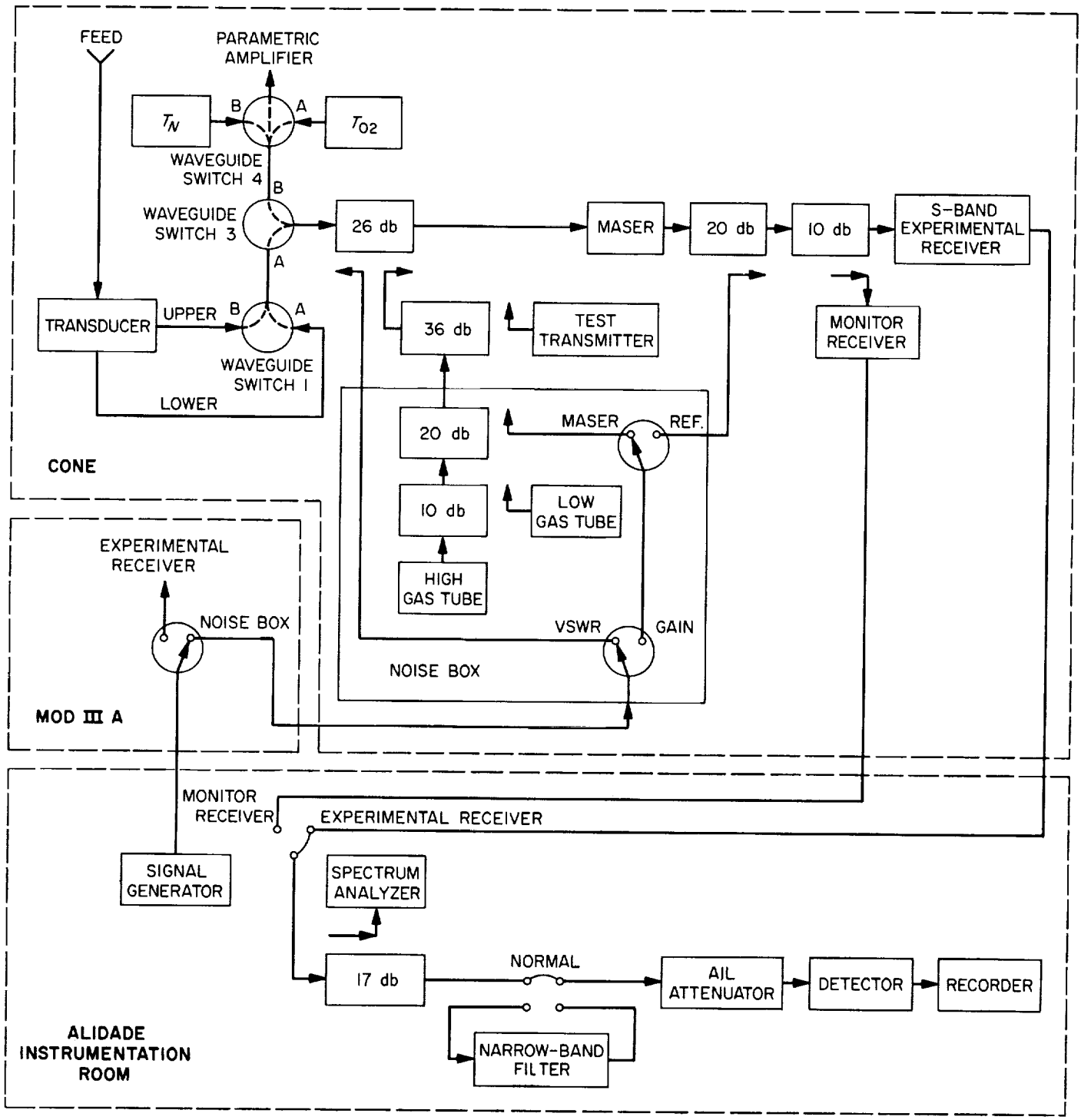

Fig. 51. Receiving system RF instrumentation for the Mars Station 210-ft dish/listening cone

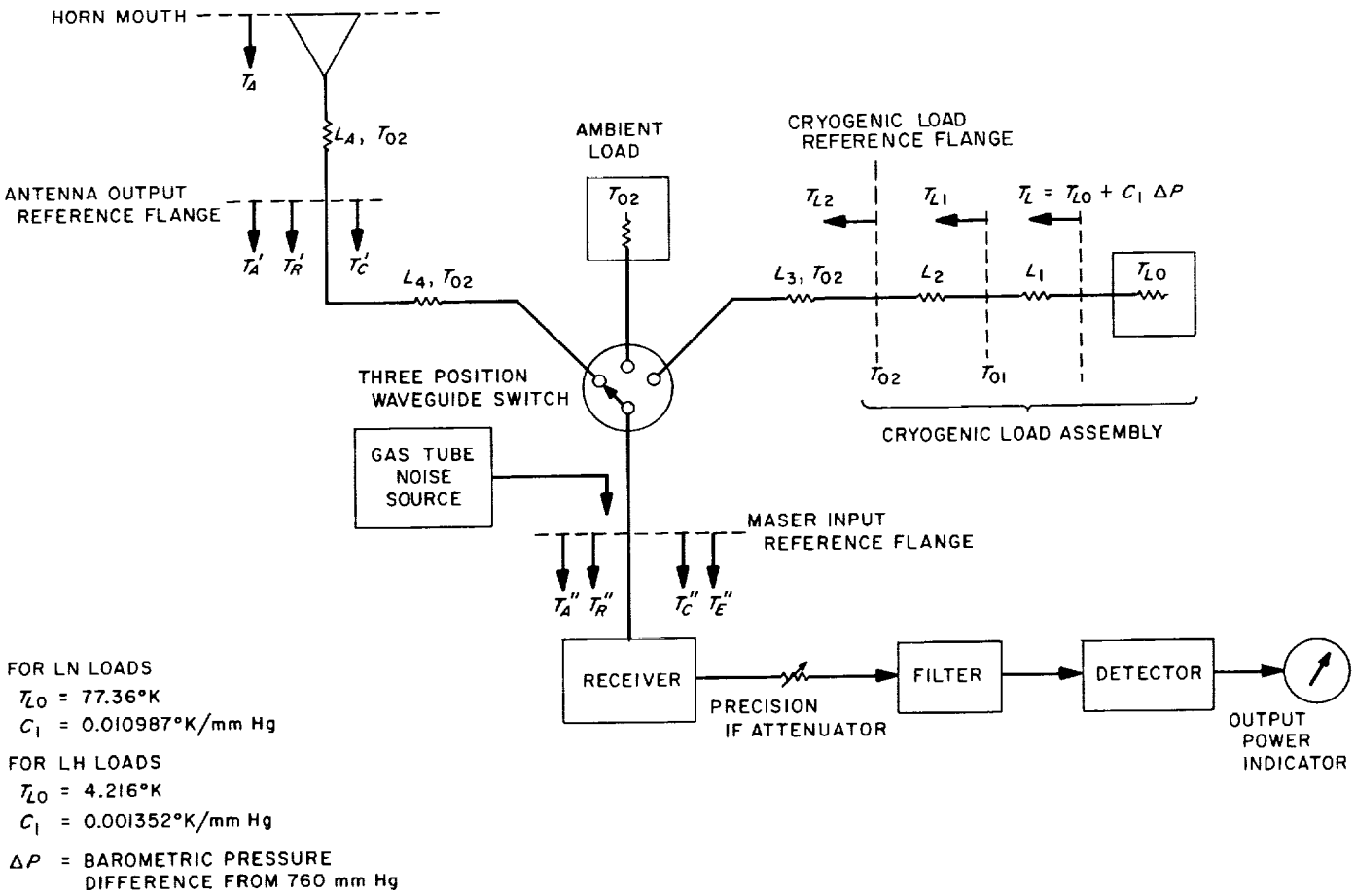

Fig. 52. Block diagram of noise temperature measurement system

The Y-factors as determined with the precision IF attenuator when switched in sequence to the antenna, cryogenic load, and ambient load are represented by the equations

$$Y_{AC} = \frac{T''_{SC}}{T''_{SA}} = \frac{T''_C + T''_R}{T''_A + T''_R} \tag{1}$$

$$Y_{C0} = \frac{T''_{S0}}{T''_{SC}} = \frac{T_{02} + T''_R}{T''_C + T''_R} \tag{2}$$

A third Y-factor which can be obtained in terms of the two preceding Y-factors is

$$Y_{A0} = \frac{T''_{S0}}{T''_{SA}} = Y_{AC}\, Y_{C0} \tag{3}$$

The Y-factor as determined by firing the gas tube when the receiver input is switched to the cryogenic load is given by

$$Y_C = \frac{T''_C + T''_R + T''_E}{T''_C + T''_R} \tag{4}$$

Manipulation of Eq. (2) yields

$$T''_R = \frac{T_{02} - Y_{C0} T''_C}{Y_{C0} - 1} \tag{5}$$

and manipulation of Eq. (1) and substitution of Eq. (5) yields

$$T''_A = \left[\frac{T''_C (Y_{AC} Y_{C0} - 1) - T_{02} (Y_{AC} - 1)}{Y_{AC} (Y_{C0} - 1)}\right] \tag{6}$$

Manipulation of Eq. (4) and substitution of Eq. (5) gives

$$T''_E = (T_{02} - T''_C)\left(\frac{Y_C - 1}{Y_{C0} - 1}\right) \tag{7}$$

Examination of Eqs. (5), (6), and (7) reveals that the noise temperatures of interest involve measurements of the ambient load temperature, the cryogenic load temperature, and the Y-factors.

The effective cryogenic load temperature referred to the maser input flange is determined from the expression

$$T''_C = (1 - L_3^{-1})\, T_{02} + L_3^{-1}\, T_{L2} \tag{8}$$

where

L_3 = dissipative line loss factor of the transmission line between the cryogenic load and maser input reference flanges ($L_3 > 1$)

T_{02} = physical temperature of the noise temperature system transmission lines, °K

T_{L2} = effective temperature of the cryogenic load defined at the cryogenic load reference flange, °K

The effective temperature T_{L2} is calculated from an expression involving the barometric pressure, physical temperatures T_{01} and T_{02}, and cryogenic load lines losses L_1 and L_2 (*SPS 37-25*, Vol. IV, p. 119).

Of special interest to antenna design engineers are the noise temperatures referred to the antenna reference flange near the feed horn. To refer noise temperatures from the maser to the antenna reference flange, the dissipative loss of the interconnecting transmission line must be known. The noise temperatures are related as follows:

$$T''_C = (1 - L_4^{-1})\, T_{02} + L_4^{-1}\, T'_C \tag{9}$$

$$T''_A = (1 - L_4^{-1})\, T_{02} + L_4^{-1}\, T'_A \tag{10}$$

$$T''_R = -(1 - L_4^{-1}) T_{02} + L_4^{-1}\, T'_R \tag{11}[3]$$

$$T''_E = L_4^{-1}\, T'_E \tag{12}$$

where

L_4 = dissipative line loss factor of the transmission line between the antenna output and maser input reference flanges ($L_4 > 1$).

[3]Derivation of this equation was given in Section 333 Interoffice Memo 3333-66-046, C. T. Stelzried to P. D. Potter, *Receiving System Equivalent Noise Temperature Translation*, March 29, 1966.

Substitution of the above equations into Eqs. (1), (2), and (4) gives

$$Y_{AC} = \frac{T'_C + T'_R}{T'_A + T'_R} \tag{13}$$

$$Y_{C0} = \frac{T_{02} + T'_R}{T'_C + T'_R} \tag{14}$$

$$Y_C = \frac{T'_C + T'_R + T'_E}{T'_C + T'_R} \tag{15}$$

Manipulation of Eqs. (13), (14), and (15) yields

$$T'_R = \frac{T_{02} - Y_{C0}\, T'_C}{Y_{C0} - 1} \tag{16}$$

$$T'_A = \frac{T'_C\,(Y_{AC}Y_{C0} - 1) - T_{02}\,(Y_{AC} - 1)}{Y_{AC}\,(Y_{C0} - 1)} \tag{17}$$

and

$$T'_E = (T_{02} - T'_C)\left(\frac{Y_C - 1}{Y_{C0} - 1}\right) \tag{18}$$

It may be seen that these equations for the noise temperatures defined at the antenna reference flange differ from those for the maser reference case only in regard to the single- and double-primed notations.

The effective cryogenic load temperature T'_C defined at the antenna output flange can be calculated directly in terms of T_{L2} using the expressions

$$T'_C = \left(1 - \frac{L_4}{L_3}\right) T_{02} + \left(\frac{L_4}{L_3}\right) T_{L2} \tag{19}$$

The losses L_3 and L_4 can be measured separately or directly as a ratio L_3/L_4. Although a direct measurement is more accurate, separate measurements are required for defining noise temperatures at the maser input.

The total probable errors associated with the measured average receiver and antenna temperature values are expressed in terms of the probable errors of the independent variables as follows (the primes have been omitted from the notations for generality):

$$PE_{T_R} = \left\{\left[PE_{T_C}\left(\frac{\partial T_R}{\partial T_C}\right)\right]^2 + \left[PE_{T_{02}}\left(\frac{\partial T_R}{\partial T_{02}}\right)\right]^2 + \left[PE_{Y_{C0}}\left(\frac{\partial T_R}{\partial Y_{C0}}\right)\right]^2 + (PE_{T_{RM}})^2 + [PE_{mismatch\ (Y_{C0})}]^2\right\}^{1/2} \tag{20}$$

$$PE_{T_A} = \left\{ \left[PE_{T_C} \left(\frac{\partial T_A}{\partial T_C} \right) \right]^2 + \left[PE_{T_{02}} \left(\frac{\partial T_A}{\partial T_{02}} \right) \right]^2 + \left[PE_{Y_{AC}} \left(\frac{\partial T_A}{\partial Y_{AC}} \right) \right]^2 + \left[PE_{Y_{C0}} \left(\frac{\partial T_A}{\partial Y_{C0}} \right) \right]^2 + (PE_{T_{AM}})^2 + [PE_{mismatch\ (Y_{AC},\ Y_{C0})}]^2 \right\}^{1/2} \quad (21)$$

where

PE_{T_C} = probable error of the effective cyrogenic load temperature. This probable error is dependent upon the accuracy of the reference load temperature T_{L2}, the accuracy of T_{02}, and the accuracy of the line loss value between the cryogenic load reference flange and the reference flange at which T_C is defined.

$PE_{T_{02}}$ = probable error of the ambient load effective noise temperature (estimated to be 0.05°K for the particular load and temperature readout system used).

The terms $PE_{Y_{AC}}$ and $PE_{Y_{C0}}$ are the probable errors of the Y_{AC} and Y_{C0} power ratios as determined with the precision IF attenuator. For the particular AIL attenuator used, these Y-factor probable errors were calculated from the expressions

$$PE_{Y_{AC}} = Y_{AC} \left(\frac{\ln 10}{10} \right) \left\{ (0.003)^2 + [0.00354\,(Y_{AC})_{db}]^2 \right\}^{1/2} \quad (22)$$

$$PE_{Y_{C0}} = Y_{C0} \left(\frac{\ln 10}{10} \right) \left\{ (0.003)^2 + [0.00354\,(Y_{C0})_{db}]^2 \right\}^{1/2} \quad (23)$$

where the *db* subscripts refer to the Y-factor ratios expressed in decibels. The probable errors $PE_{T_{RM}}$ and $PE_{T_{AM}}$ are respectively the probable error of the measured average receiver and antenna temperatures calculated from the following expressions. For convenience, these terms will be referred to as the measurement precision index.

$$PE_{T_{RM}} = \frac{0.6745}{\sqrt{N}} \left[\frac{\sum_{i=1}^{N} (T_{R_{AVG}} - T_{Ri})^2}{N-1} \right]^{1/2} \quad (24)$$

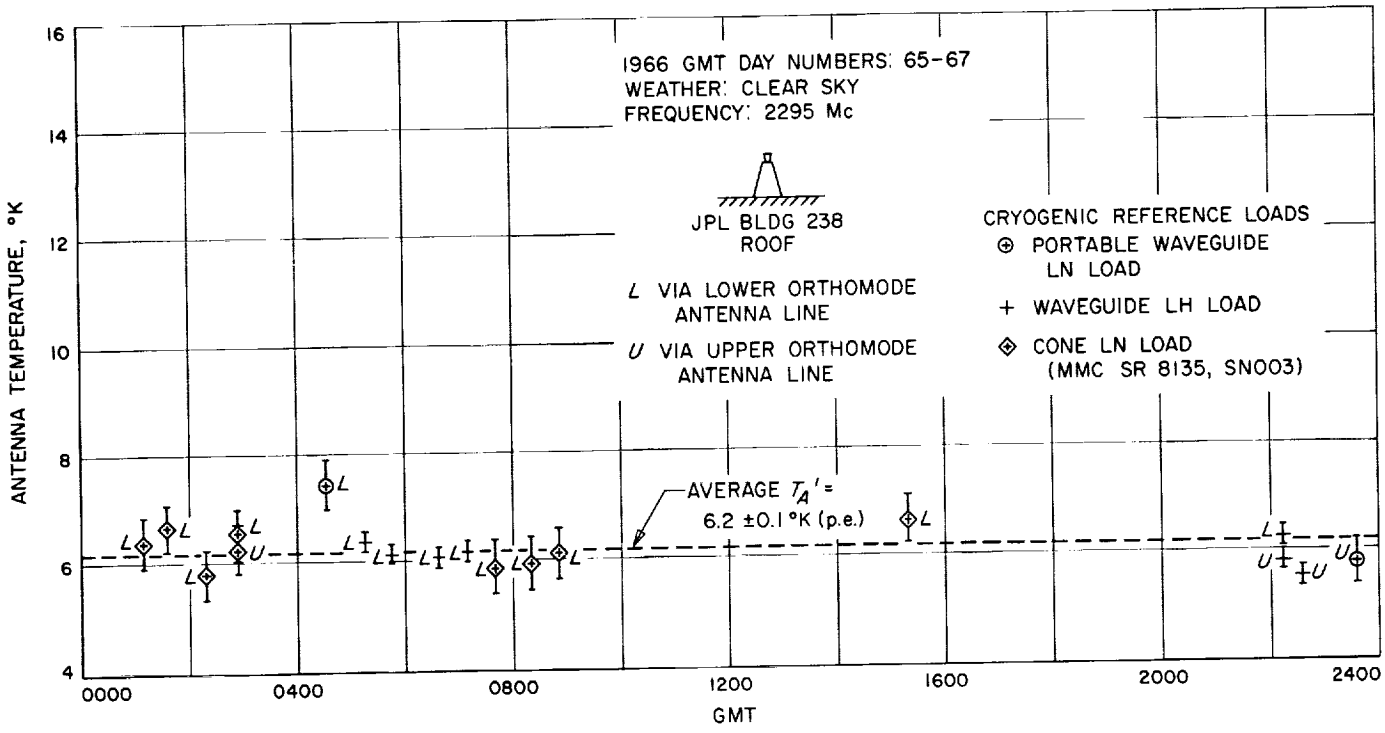

Fig. 53. Listening cone zenith antenna temperature defined at antenna reference flange

$$PE_{T_{AM}} = \frac{0.6745}{\sqrt{N}} \left[\frac{\sum_{i=1}^{N} (T_{A_{AVG}} - T_{Ai})^2}{N-1} \right]^{1/2} \quad (25)$$

The probable error $PE_{mismatch\ (Y)}$ in Eqs. 20 and 21 is the probable temperature error due to a nonzero reflection coefficient value of the receiver (looking into the receiver at the maser flange) and nonzero reflection coefficients of the noise sources involved in the particular Y-factor measurement(s). The nonzero reflection coefficients of noise source and receiver assemblies will interact with the transmission line reflection coefficients to produce mismatch errors which are often difficult to analyze.

After differentiating the equations for T_R and T_A, as given respectively by Eqs. (5) and (6) or (16) and (17) with respect to the independent variables, substitution into Eqs. (20) and (21) gives the resultant expressions from which the total probable errors were calculated.

(2) *Experimental results.* Figs. 53 and 54 show the results of the cone noise temperature calibrations which were made at JPL on the roof of Building 238. Fig. 53 shows a plot of measured zenith antenna temperature as defined at the antenna output reference flange; Fig. 54 shows the measured antenna, receiver, and gas tube temperatures as defined at the maser input flange.

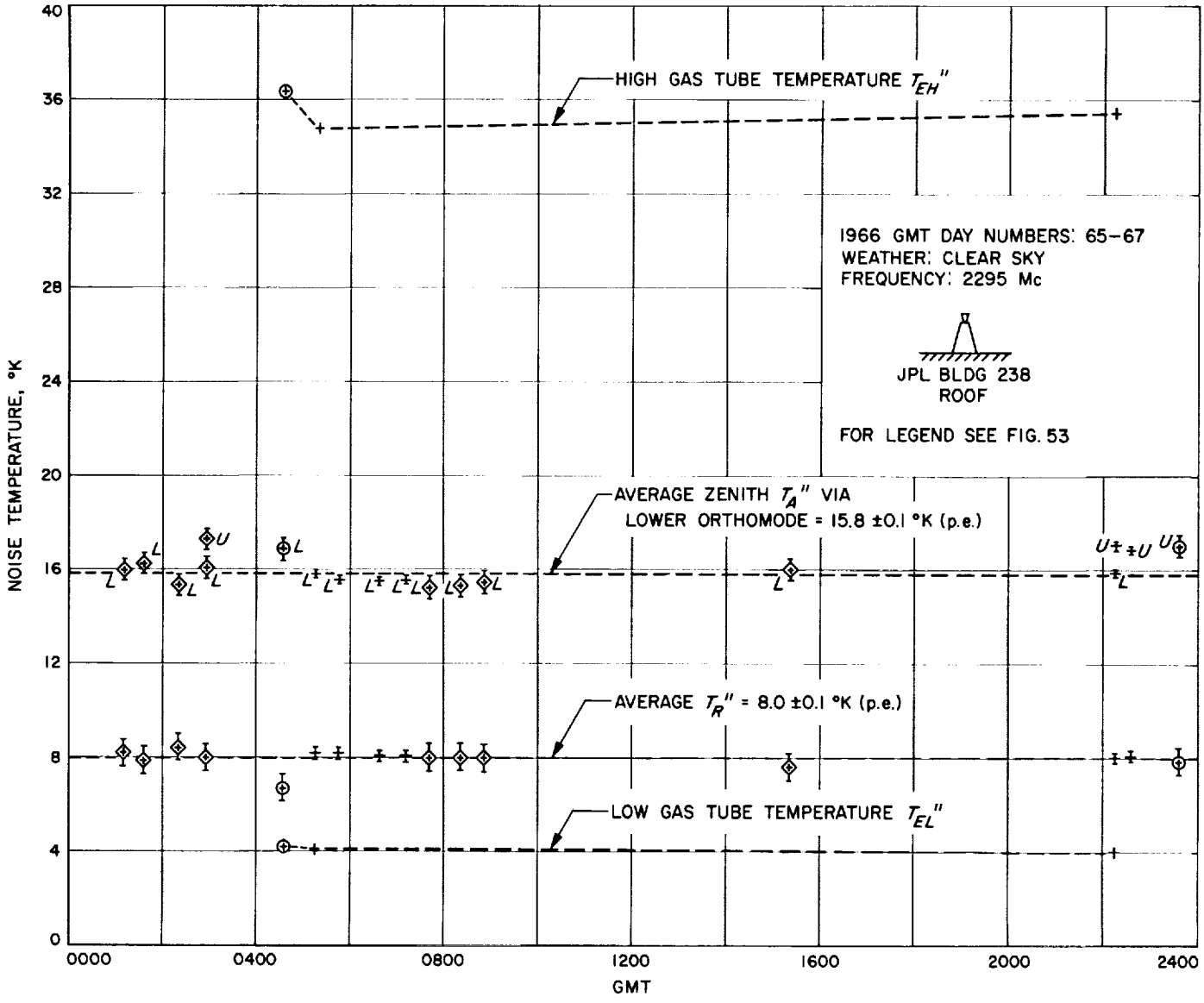

Fig. 54. Listening cone noise temperatures defined at maser input flange

The center of each data point in Figs. 53 and 54 represents the average calculated value based on 10 sets of Y-factor measurements, while the deviations from the average represent the total probable error calculated from Eqs. (20) and (21), except for the omission of the mismatch probable error term. The error analysis due to mismatch was not completed in time for this reporting.

An overall average measured value of 6.2 ±0.1°K (p.e.) was found for the zenith antenna temperature as defined at the antenna reference flange. This overall average was determined from the average values of the 18 data points shown in Fig. 53. The probable error is the measurement precision index of the overall average. It can be noted from Fig. 53 that at the antenna reference flange, the antenna temperature via the lower and upper orthomode transmission lines have nearly identical values, as would be expected if the insertion losses were properly accounted for.

At the maser input flange the overall average measured antenna temperature via the lower orthomode was 15.8 ±0.1°K (p.e.). The zenith antenna temperature at the maser input via the upper orthomode line is slightly higher due to the slightly higher line loss through this path. The overall average measured receiver temperature defined at the maser flange was 8.0 ±0.1°K (p.e.). These probable errors are the measurement precision indices of the overall averages.

For this cone evaluation, three different cyrogenic reference loads were used. These cryogenic loads were (1) a portable liquid-nitrogen-cooled waveguide load (*SPS 37-33*, Vol. IV, pp. 46–50), (2) a liquid-helium-cooled waveguide load (*SPS 37-25*, Vol. IV, pp. 120–121), and (3) the cone liquid-nitrogen-cooled waveguide load which was fabricated by the Maury Microwave Corporation (MMC) for JPL. The design of this load was described in *SPS 37-31*, Vol. IV, pp. 283–284. It can be seen from the experimental results that the cone noise temperature data, as obtained through the use of three different loads, were reasonably consistent.

2. The Mars Station 210-ft Dish/Listening Cone

a. Weekly noise temperature calibrations. Following cone calibrations at JPL, the listening cone was shipped to the Mars Station at Goldstone and installed on the 210-ft antenna system.

To check the stability of the AAS antenna and receiver temperatures over a period of time, a weekly calibration procedure has been initiated. The weekly calibrations require that the cone liquid nitrogen load assembly be filled and used in the calibrations. Y-factor data are taken in a systematic manner on a data sheet which has been set up for ease of key punching the data onto IBM cards. A sample weekly calibration data sheet and data for Run 2 of day 94 are shown in Fig. 55. The punched IBM cards are run through an IBM 1620 computer which computes and prints out (1) receiver temperature and probable errors, (2) antenna temperature and probable errors, (3) system temperature, (4) gas tube excess temperatures, and (5) follow-up receiver temperature. These temperatures are calculated for both maser input and antenna output reference flange cases. Fig. 56 is a sample output page from the computer program for the input data of Fig. 55.

Results of the weekly calibrations of the Mars Station 210-ft dish/listening cone system are shown in Figs. 57 and 58. On day 73, the noise temperature measurements were made at a lower than normal maser gain. At this time, the antenna system was not completely operational and the hyperboloid was not yet focused. Data on day

RECEIVING SYSTEM NOISE TEMPERATURE WEEKLY CALIBRATION

Sea Level Bar. Pressure (In.Hg.) 29.80 — Nit.Load Plate Temp T_{01},°C 31.6 — Maser on-off Y_{oo},db 26.9

Year 1966 — Day No 094 — Time,GMT 0400.0 Z — Run No 2

D.L.O.F.T.D.J.S.M.L.I.S.T. C.O.N.E. M.A.R.S. S.I.T.E. 3.T.S. M.M.C. S.N. 3. L.N.L.O.A.D

Maser Gain GM(db) 40.7 — Reflectometer Measurements: Antenna L. 38.3 — Antenna U. — Nitrogen Load 38.7 — Amb. Load 40.7

Time Nit. Load filled, GMT 0330.0 Z — LN Level, in. —

Operator KAMRATH — Weather CLEAR

Comments

No data pts. 10 — Freq 2 — Station 14

Antenna L	Antenna U	LN Load	LN Load + GT, low	LN Load + GT, high	AMB Load	Ambient Temp T_{02}, °C
	AIL ATTENUATOR READING					
6.92	—	12.05	12.26	13.62	17.45	24.50
6.89	—	12.04	12.25	13.60	17.45	24.48
6.92	—	12.05	12.27	13.65	17.48	24.46
6.92	—	12.06	12.28	13.63	17.48	24.45
6.91	—	12.07	12.27	13.63	17.47	24.43
6.92	—	12.07	12.28	13.65	17.46	24.41
6.94	—	12.10	12.29	13.67	17.49	24.39
6.94	—	12.11	12.29	13.66	17.47	24.38
6.94	—	12.09	12.29	13.65	17.49	24.36
6.95	—	12.09	12.30	13.67	17.50	24.34

* 2 for 2295 Mc, 3 for 2388 Mc

Fig. 55. Sample weekly calibration data sheet

LOWER ORTHOMODE
FREQ = 2295 MC

DATA REDUCTION
RECEIVER AND ANTENNA NOISE TEMPERATURE MEASUREMENTS

NITROGEN LOAD CASE YEAR 1966 DAY 94 TIME 400 GMT RUN 2

210 FT DISH LIST. CONE MARS SITE GTS MMC SN 3 LNLOAD
MASER GAIN 40.7 DB, RETURN LOSS ANT L 38.3 DB, ANT U 0.0 DB, NIT L 38.0 DB, AMB L 40.7 DB
TIME NIT L FILLED 330 GMT LN LEVEL 0.0 IN
KAMRATH CLEAR

ALL TEMPERATURES ARE DEFINED AT MASER INPUT

T02 (DEG C)	A1DB (DB)	A2DB (DB)	A3DB (DB)	Y1DB (DB)	Y2DB (DB)	Y3DB (DB)	TRPI (DEG K)	TAPI (DEG K)	TCPI (DEG K)	Y1	Y2
24.500	6.920	12.050	17.450	5.130	5.400	10.530	7.8015	19.2352	80.2944	3.25836	3.46736
24.480	6.890	12.040	17.450	5.150	5.410	10.560	7.5094	19.3138	80.2941	3.27341	3.47536
24.460	6.920	12.050	17.480	5.130	5.430	10.560	6.9365	19.8346	80.2938	3.25836	3.49141
24.450	6.920	12.080	17.480	5.160	5.400	10.560	7.7823	19.0622	80.2937	3.28095	3.46736
24.430	6.910	12.070	17.470	5.160	5.400	10.560	7.7747	19.0675	80.2934	3.28095	3.46736
24.410	6.920	12.070	17.460	5.150	5.390	10.540	8.0525	18.9363	80.2931	3.27341	3.45939
24.390	6.940	12.100	17.490	5.160	5.390	10.550	8.0448	18.8795	80.2928	3.28095	3.45939
24.380	6.940	12.110	17.470	5.170	5.360	10.530	8.9046	18.2192	80.2926	3.28851	3.43557
24.360	6.940	12.090	17.490	5.150	5.400	10.550	7.7478	19.1477	80.2923	3.27341	3.46736
24.340	6.950	12.090	17.500	5.140	5.410	10.550	7.4558	19.4122	80.2921	3.26587	3.47536

INPUT DATA
BPISL = 29.800 INCHES HG
ALT = 3437.0 FT
T01N = 31.60 DEG C
PE(TCP)= .100 DEG K
PE(T02)= .050 DEG K
L1DB = .0152 DB
L2DB = .0076 DB
L3DB = .0622 DB
L4DB = .1456 DB
YONOFF = 26.900 DB

RECEIVER
AVG TRP = 7.8010 DEG K
TOTAL PE = .5796 DEG K

E(TCP) = .14052 DEG K
E(Y2P) = .55159 DEG K
E(T02) = .02026 DEG K
E(NTR) = .10773 DEG K (MEAS TERM)

FOLLOW UP RECEIVER
TFP = .6226 DEG K

CRYOGENIC LOAD
AVG TCP = 80.2932 DEG K
E(NTC) = .00017 DEG K (MEAS TERM)

AVG TL2 = 77.1588 DEG K
E(MTL2) = 0.00000 DEG K (MEAS TERM)

ANTENNA
AVG TAP = 19.1108 DEG K
TOTAL PE = .4286 DEG K

E(TCP) = .12809 DEG K
E(Y1P) = .11458 DEG K
E(Y2P) = .38236 DEG K
E(T02) = .01404 DEG K
E(MTA) = .08868 DEG K (MEAS TERM)

SYSTEM
AVG TSAP = 26.9119 DEG K

Fig. 56. Sample output page of IBM 1620 computer data reduction program for weekly calibrations

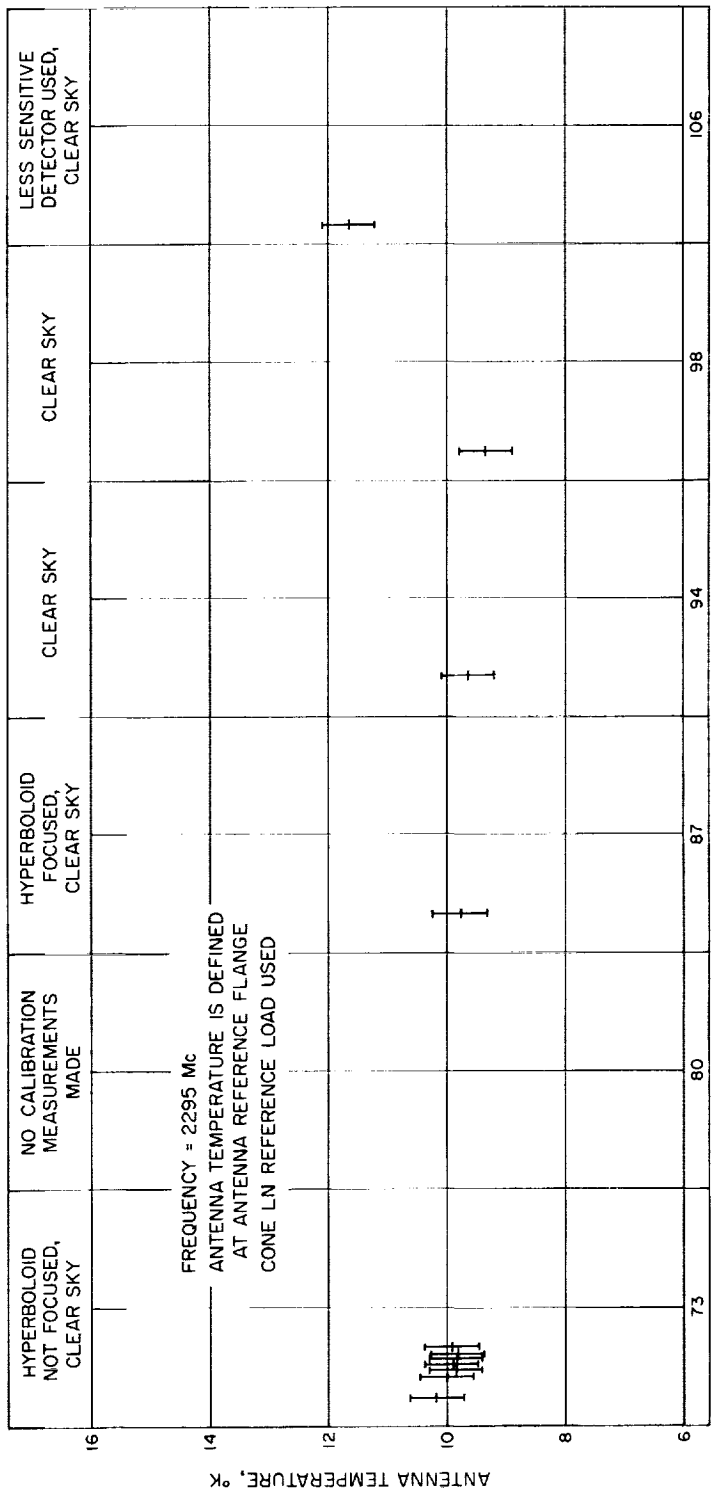

Fig. 57. Zenith antenna temperature via lower orthomode for the Mars Station 210-ft dish/listening cone system (weekly calibration data)

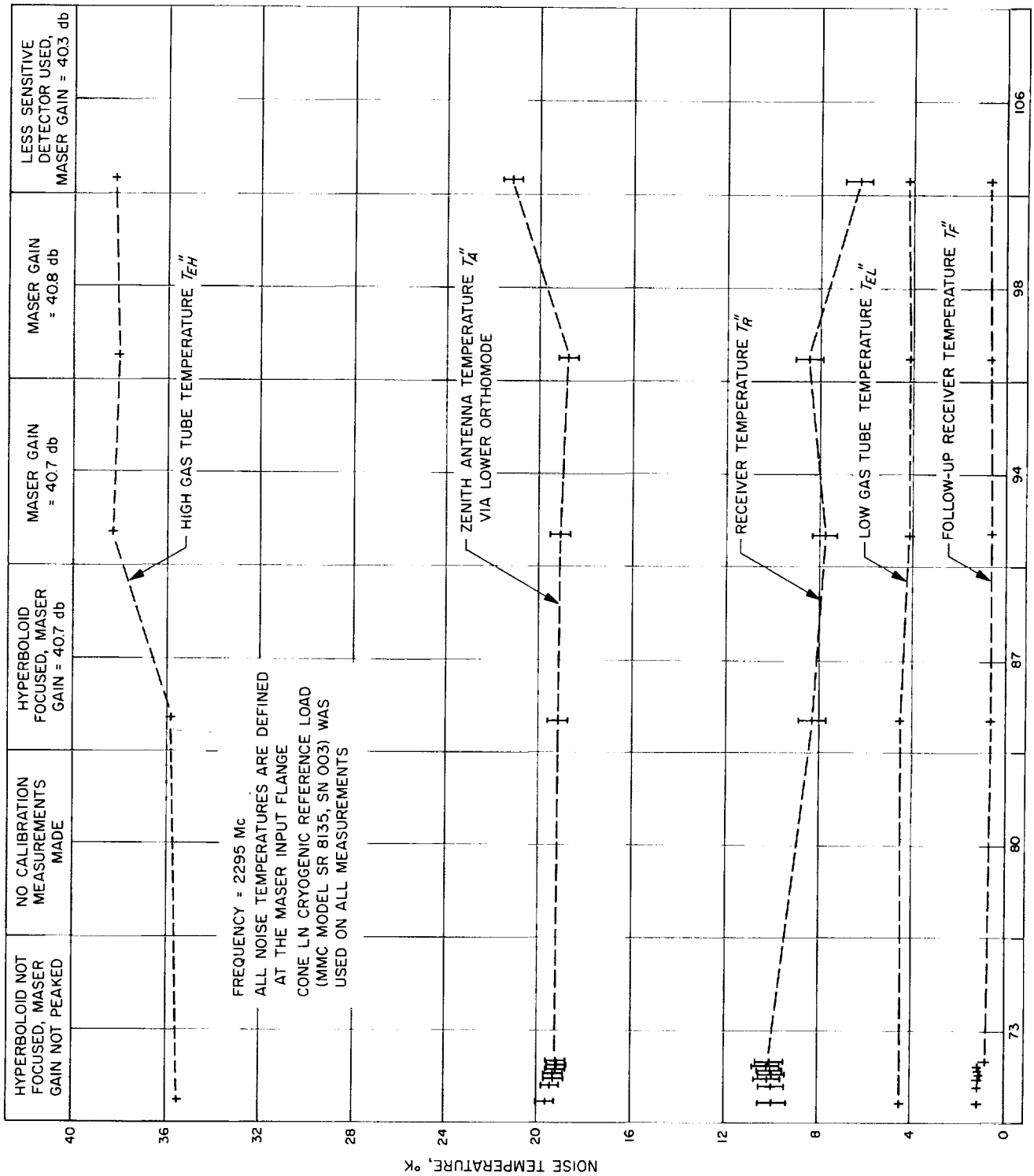

Fig. 58. Noise temperatures for the Mars Station 210-ft dish/listening cone system (weekly calibration data)

number 106 were significantly different from normal (based on previous weekly calibration data). The cause of the deviation is presently being investigated.

The overall average noise temperature values for the 210-ft dish/listening cone, based on the data taken on day numbers 87, 94, and 98, are given in Table 15. These values may be used in conjunction with data obtained from daily calibrations. The probable error of each average shown in Table 15 includes only the measurement precision index term based on the three data points.

Table 15. Summary of 210-ft dish/listening cone noise temperatures (weekly calibration data)

Noise source	Reference flange	Average noise temperature, °K
Antenna via lower orthomode	Antenna output	9.6 ± 0.1 (p.e.)
	Maser input	19.1 ± 0.1 (p.e.)
Receiver	Maser input	8.2 ± 0.2 (p.e.)
Follow-up receiver contribution	Maser input	0.6
High gas tube	Maser input	37.4 ± 0.5 (p.e.)
Low gas tube	Maser input	4.3 ± 0.1 (p.e.)

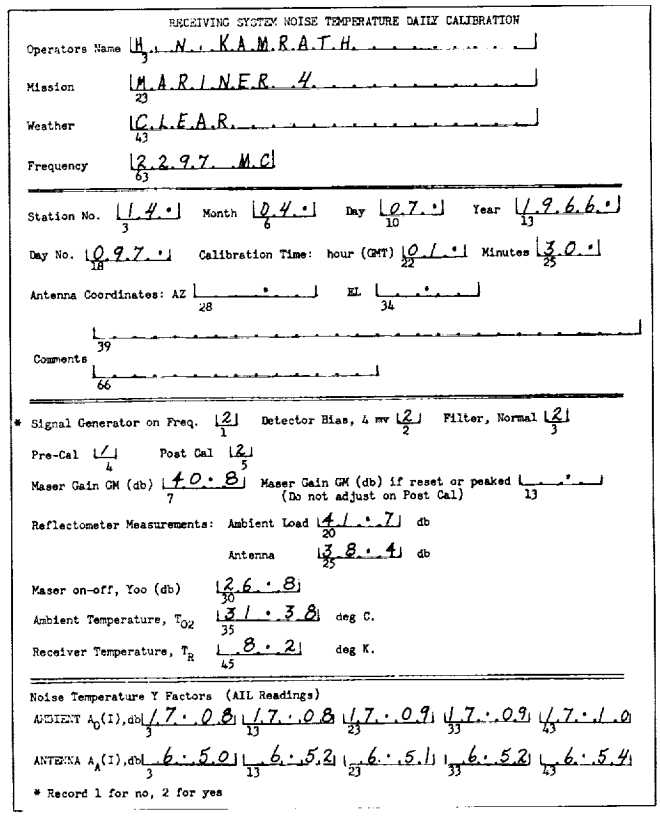
RECEIVING SYSTEM NOISE TEMPERATURE DAILY CALIBRATION

Operators Name H. N. KAMRATH

Mission MARINER 4

Weather CLEAR

Frequency 2297 MC

Station No. 14 Month 04 Day 07 Year 1966

Day No. 097 Calibration Time: hour (GMT) 01 Minutes 30

Antenna Coordinates: AZ EL

Comments

* Signal Generator on Freq. 2 Detector Bias, 4 mv 2 Filter, Normal 2

Pre-Cal 1 Post Cal 2

Maser Gain GM (db) 40.8 Maser Gain GM (db) if reset or peaked (Do not adjust on Post Cal)

Reflectometer Measurements: Ambient Load 41.7 db

Antenna 38.4 db

Maser on-off, Yoo (db) 26.8

Ambient Temperature, T_{O2} 31.3 deg C.

Receiver Temperature, T_R 8.2 deg K.

Noise Temperature Y Factors (AIL Readings)

AMBIENT $A_0(I)$,db	17.08	17.08	17.09	17.09	17.10
ANTENNA $A_A(I)$,db	6.50	6.52	6.51	6.52	6.54

* Record 1 for no, 2 for yes

Fig. 59. Sample copy of data sheet for receiving system noise temperature daily calibration

b. Daily system noise temperature calibrations. The receiving system noise performance was evaluated on a daily basis from March 17 to April 12, 1966. The measurement technique consisted of switching the waveguide switch S3 between the antenna pointed at zenith and the ambient load. Waveguide switch S1 was left on position A through the lower waveguide run to the mode transducer providing right hand circular polarization. The AIL attenuator was adjusted to give the same noise level on the recorder when switched between these positions. The daily noise temperature calibration sheet is shown in Fig. 59, filled in for a typical calibration check. Computer data cards are punched directly from this data sheet. These data include the follow-up receiver noise temperature, maser gain, and reflectometer measurements of the ambient load and antenna. A computer program has been written to simplify data reduction. The daily maser gain and reflectometer readings of the waveguide ambient load and antenna through the switch position A are shown in Fig. 60. Although there appears to be some correlation between the reflectometer readings on the ambient load and antenna (indicating some systematic error in the measurements), the system is satisfactory for this application. Divergent reflectometer readings between the antenna and ambient load would indicate an unstable situation in either the ambient load or antenna. Correlated changes probably indicate problems in the reflectometer. The averages and probable errors of the individual measurements of the reflectometer readings for the ambient load and antenna are 42.1 ±0.7 (p.e.) and 39.9 ±1.2 db (p.e.), respectively. This is the difference between the return signal and a signal applied at the maser input in the forward direction. The errors are the daily statistical measurement errors.

An individual system temperature measurement $T_{SA}(I)$ defined at the maser input flange is found from the individual AIL readings $[A_0(I)]_{db}$ on the ambient load and $[A_A(I)]_{db}$ on the antenna. The difference is the Y-factor in decibels

$$[Y_{A0}(I)]_{db} = [A_0(I)]_{db} - [A_A(I)]_{db} \tag{26}$$

The Y-factor ratio is given by

$$Y_{A0}(I) = 10^{[Y_{A0}(I)]_{db}/10} \tag{27}$$

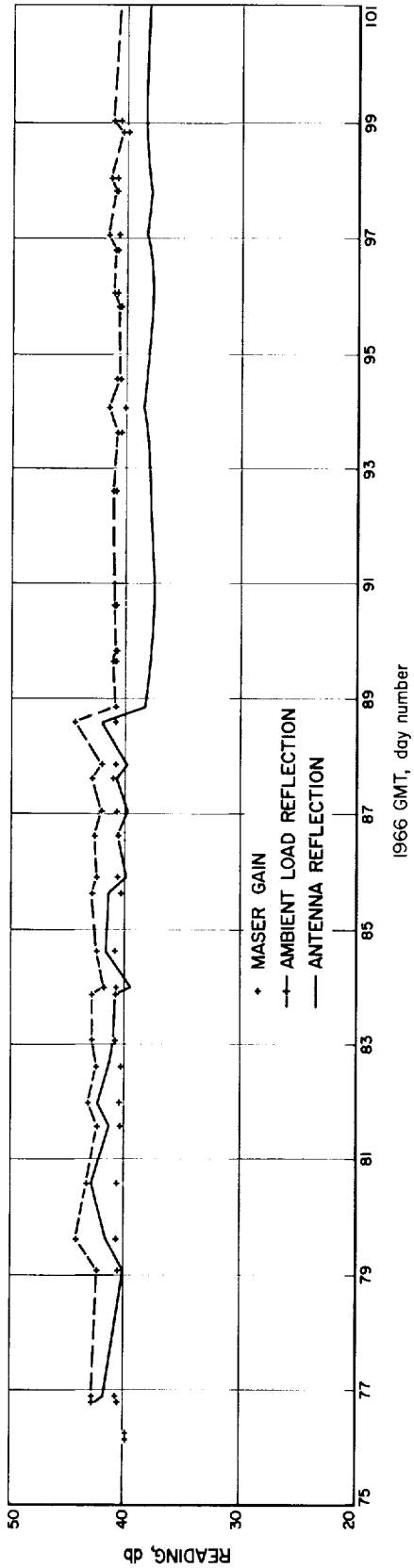

Fig. 60. Mars Station 210-ft dish/listening cone 2297-Mc maser gain and reflectometer readings

The individual system temperature measurements, found from a temperature ratio, are

$$T_{SA}(I) = \frac{T_{02} + T_R}{Y_{A0}(I)} \tag{28}$$

where

T_{02} = ambient load temperature, °K

T_R = receiver temperature defined at the maser input (the double primes have been dropped for convenience)

$Y_{A0}(I)$ = Y-factor ratio for an individual set of readings obtained by switching between the ambient load and antenna

The receiver temperature is considered a constant as obtained from the weekly calibrations. An error analysis of this technique (*SPS 37-36*, Vol. IV, p. 269) shows that an overall measurement probable error of less than 1% should be expected, with a 1°K probable error in the receiver temperature. The average measured system temperature for the set is

$$T_{SA} = \frac{\sum_{i=1}^{N} T_{SA}(I)}{N} \tag{29}$$

For the individual measurements and for the measured average, the statistical measurement probable errors from Eqs. (28) and (29) are

$$PE_{T_{SA}}(M, I) = 0.6745 \left\{ \frac{\sum_{i=1}^{N} [T_{SA} - T_{SA}(I)]^2}{N - 1} \right\}^{1/2} \tag{30}$$

$$PE_{T_{SA}}(M) = \frac{PE_{T_{SA}}(M, I)}{\sqrt{N}}$$

The composite system temperature probable error found by differentiating Eq. (28) and accounting for the statistical measurement error is

$$PE_{T_{SA}} = \left[PE^2_{T_{SA}}(M) + (PE^2_{T_{02}} + PE^2_{T_R}) \left(\frac{1}{Y_{A0}} \right)^2 + PE^2_{Y_{A0}} \frac{(T_{02} + T_R)^2}{Y^4_{A0}} \right]^{1/2} \tag{31}$$

where, from the measurement data,

$$Y_{A0} = \frac{\sum_{i=1}^{N} Y_{A0}(I)}{N}$$

and, from the attenuator characteristics,

$$PE_{Y_{A0}} = Y_{A0} \left(\frac{1}{10 \log_{10} e} \right) [a^2 + b^2 (Y_{A0})^2_{db}]^{1/2}$$

(the constants from the AIL attenuator specifications are $a \simeq 0.0030$ and $b \simeq 0.00354$) where for this system $PE_{T_{02}} \simeq 0.1$°K, $PE_{T_R} \simeq 1$°K. The composite system temperature probable error estimates the total absolute error and reflects the actual measurement statistical error.

The contribution of the follow-up noise receiver to the system temperature defined at the maser input is given approximately by

$$T_F = \frac{T_{02} + T_R}{Y_{00}} \tag{32}$$

where

Y_{00} = maser amplifier *off-on* Y-factor = $10^{(Y_{00})_{db}/10}$

The computer output from the data given in the daily calibration sheet is shown in Fig. 61. A plot of the daily system temperature measurements for the operational period is shown in Fig. 62. The average of all these data points is 27.7 ±0.4°K (p.e.). The probable error refers to the daily statistical variation. The overall system temperature measurement accuracy problem error $PE_{T_{SA}}$ for a daily calibration is typically 0.3°K. The average of the daily measurement errors $PE_{T_{SA}}(M)$ from the data sheets is 0.03°K. The actual statistical variation in system temperature (0.4°K), which is greater than the daily resolution (0.03°K), is probably an actual receiver temperature change not necessarily due to the measurement system. The maser gain was not peaked each day in order to determine long term gain stability. It is shown (p. 83) that maser temperature is sensitive to tuning.

It appears that the Y-factor measurement method used with the ambient load and antenna provides a very reliable measurement scheme, with an overall measurement accuracy probable error of 0.3°K, which does not entail the daily use of a cryogenic waveguide termination or a gas tube.

```
OPERATORS NAME  H.N.KAMRATH                    MISSION  MARINER 4
       WEATHER, CLEAR                        FREQUENCY, 2297 MC
STATION NO.  14     MONTH   4  ,DAY  7  ,YEAR 1966     DAY NO.   97
CALIBRATION TIME, HOUR(GMT)   1,MINUTES   0   COMMENTS
MASER GAIN  40.8  PEAKED MASER GAIN
REFL.MEAS., AMB.LOAD  41.7  ANTENNA  38.4
MASER ON-OFF,YOO(DB)  26.8   AMB.TEMP.,TO2(DEG.C)  31.38
REC.TEMP TR(DEG.K)   8.2

 AO(I)     AA(I)     YOA(I)     TSA(I)
 17.08      6.50     10.58     27.364
 17.08      6.52     10.56     27.490
 17.09      6.51     10.58     27.364
 17.09      6.52     10.57     27.427
 17.10      6.54     10.56     27.490

TSA=  27.427,DEG.K
TF=      .653,DEG.K
PETSA(M,I)= .042,DEG.K
PETSA(M)=   .019,DEG.K
PETSA=      .253,DEG.K
```

Fig. 61. Sample daily noise temperature calibration computer printout

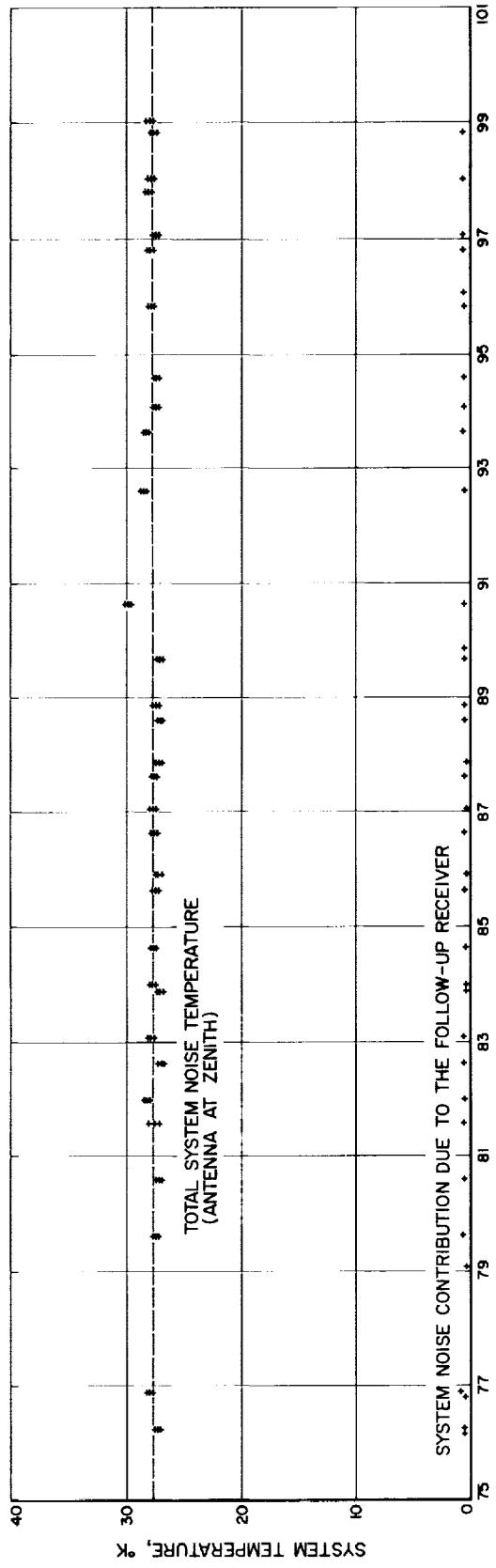

Fig. 62. System and follow-up receiver noise temperatures for the Mars Station 210-ft dish/listening cone

L. Venus Station Operations

E. B. Jackson and A. L. Price

1. Experimental Activities

During the period of February 11 through April 13, 1966, the major activities at the Venus Station (summarized in Table 16) were S-band planetary radar experiments with Venus as the target, and *Mariner* Mars 1964 tracking and command transmission, including the *Mariner* Sun occultation experiment (bistatic with the Mars Station).

Table 16. Summary of Venus Station activity (February 11–April 13, 1966)

Activity	Hours	Percent
Venus planetary radar experiments	255	17.23
Mariner experiments Transmission, reception, and testing (includes time required to change Cassegrain feed cone)	183	12.36
Testing, calibration, construction, and scheduled maintenance	1042	70.41
Total	1480	100.00

a. Planetary radar. The S-band planetary radar system continued to operate with Venus as the target. Experiments performed were open-loop ranging and mapping, closed-loop ranging, open-loop total spectrum (normal and crossed polarization), and phase-locked loop doppler experiments.

b. Mariner Mars 1964. The monthly reception from the *Mariner* spacecraft continued, with signals being successfully received on March 1, 1966 at a signal level (carrier only) of approximately −178.6 dbm. On March 17, the Venus Station was again placed into the *Mariner* configuration for the Sun occultation experiment. In this experiment, the Venus Station transmits to the *Mariner* spacecraft, thus keeping it in the two-way mode. By means of a specially designed Cassegrain feed cone and associated receiving equipment, the Mars Station receives the spacecraft signal and transmits the receiver output via the microwave link to the Venus Station, where the spectrogram processing is accomplished. The character of the spectrograms is observed as the spacecraft moves toward, near to, and away from the Sun. From these data, conclusions can be drawn regarding the medium through which the signals have passed. The standard frequency reference for the Mars Station during this experiment is obtained from the Venus Station via a microwave link.

On March 25, 1966, the Venus Station transmitted a set of five DC-17 commands to up-date the Canopus sensor on board the *Mariner* spacecraft. Unfortunately, the Mars Station was unable to receive from the spacecraft at that time, and commands were transmitted "in the blind." However, on April 12, 1966, the Venus Station again transmitted DC-17, this time as a set of six commands; reception by the Mars Station and signal processing at the Venus Station verified two-way RF lock prior to, during, and subsequent to command transmission. Because additional work was required on the Mars antenna, the Sun occultation experiment was also terminated on this date. Next scheduled reception from the *Mariner* spacecraft is May 2, 1966, with reception planned to continue at monthly intervals thereafter.

Some sample spectrograms from the *Mariner* spacecraft are shown in Figs. 63 and 64. Although no direct comparison can be made between these two figures (which were obtained under very different conditions), some comments can be made.

Fig. 63, taken on March 1, 1966, depicts the spacecraft in one-way mode. (In this one-way mode, a crystal oscillator on board the spacecraft is used as the frequency source for the spacecraft transmitter.) In all these spectrograms, the X-axis is frequency, with zero in the center, plus-frequency to the right, and minus-frequency to the left. The Y-axis is power and is unlabeled because the instrumentation gain used to produce these spectra varies from display to display. Fig. 63(a) was obtained by integrating the spacecraft carrier alone through a narrow (29.4 Hz) bandwidth filter for 15 min. Fig. 63(b), also a 15-min integration through the same filter, was taken after a lapse of approximately 15 min. Note that the average received frequency has drifted to the left (downward) approximately 1.5 Hz and the nature of the frequency jitter has changed. Fig. 63(c) represents a 15.5-min integration through a wider (480.8 Hz) bandwidth filter. Within this greater bandwidth, the upper and lower telemetry subcarriers can be seen at the nominal 150-Hz spacing from the carrier. Here the width of the subcarriers is greater than the width of the carrier, indicating that telemetry modulation is still being generated. A longer integration period would have reduced the amplitude of the noise fluctuations and enhanced the resolution of the spectrogram.

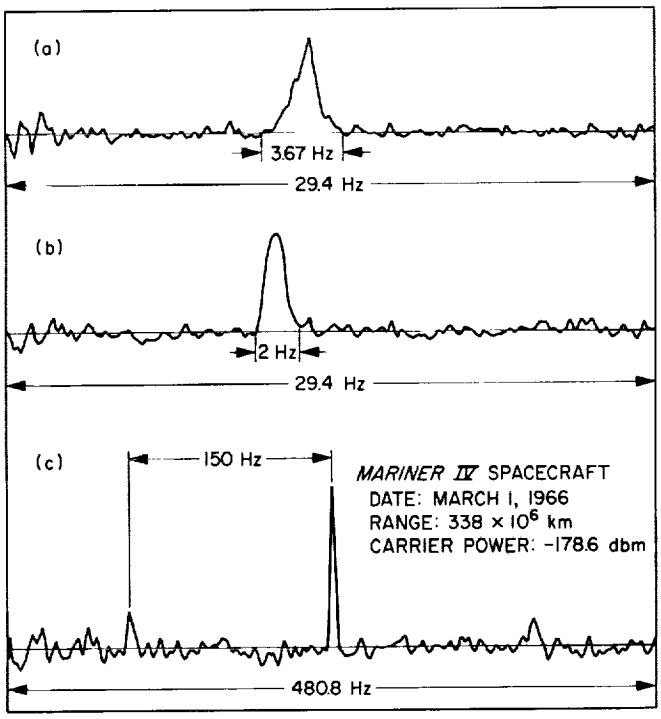

Fig. 63. Power spectrum from *Mariner IV* spacecraft, one-way mode

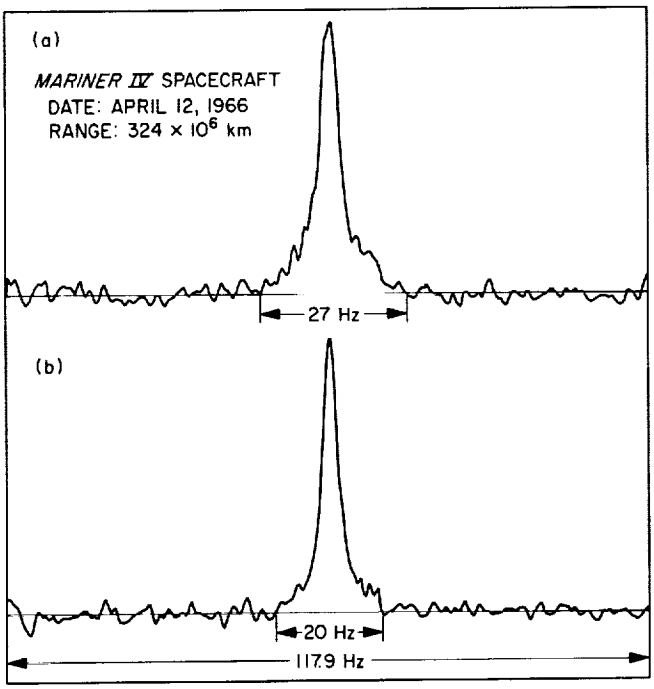

Fig. 64. Power spectrum from *Mariner IV* spacecraft, two-way mode

Fig. 64, taken on April 12, 1966, depicts the spacecraft in two-way mode. (In this mode, the spacecraft transmitted frequency is generated by multiplying the ground transmitter frequency by the ratio 240:221). In this mode, the spacecraft transmit frequency is controlled by the ground transmitter frequency, and frequency drift in the spacecraft crystal oscillator is no longer a factor. The width of the received spacecraft carrier spectrum will be determined primarily by (1) jitter in the ground transmitted frequency, (2) jitter in the spacecraft phase-locked loops, (3) jitter in the ground receiver, and (4) broadening, if any, caused by the propagation characteristics of the medium through which the signals have passed.

Fig. 64(a) was obtained by integrating the spacecraft received carrier through a 117.9-Hz bandwidth filter for 30 min. The spectrum is approximately 27 Hz at the baseline; however, because of noise fluctuations, it is difficult to make an accurate assessment. How much of this width is attributable to each of the effects mentioned is not known at this time. The difficulties encountered in baseline spectrum width evaluation can be conceived by observing Fig. 64(b), which is also a 30-min integration taken through the same filter, starting approximately 35 min after the spectrogram depicted in Fig. 64(a) was completed. A baseline carrier width of approximately 20 Hz is noted, as compared with the 27 Hz previously obtained. The character of the spectrum has also changed, particularly around the baseline. It is probable that broadening of the spectrum due to jitter is not as much of a factor in this spectrum as was true in Fig. 64(a).

2. Subsystem Performance

a. 100-kw transmitter. During this period, the R&D and the *Mariner* transmitters were in extensive use. Except for difficulty with back power instrumentation, operation was reliable throughout. Certain corrective measures have been taken to shield and isolate the back power instrumentation from interfering signals, and no difficulty has been experienced during the last 14 days of *Mariner* operation.

b. Receiving systems. During this period, the S-band (2388 MHz) system was used in the Venus planetary experiment, and the *Mariner* receiver (2295 MHz) was used in the reception of signals from the *Mariner* spacecraft. The *Mariner* reception was again accomplished by crosspatching the 30-MHz signal from the *Mariner* receiver into the S-band receiver. A portion of the S-band receiver was also used in the *Mariner* Sun occultation experiment. This was accomplished by feeding the 455-

kHz signal from the Mars Station *Mariner* receiver, via microwave, into the AM channel of the Venus Station S-band receiver. This configuration permitted signal spectrum analysis in either the closed- or open-loop modes.

The X-band receiver (8448 MHz) was maintained in a standby condition throughout this period.

There was no lost tracking time due to receiver equipment failure during this period. A low-level leakage signal has been detected in the AM channel of the S-band receiver. Preliminary trouble-shooting indicates that the leakage is confined to the AM channel and can be eliminated by the rerouting of the 30-MHz mixer AGC and signal cables. Trouble-shooting is continuing. In preparation for the site shut-down period, the S-band cone receiver power supply has been removed and returned to JPL.

c. Programmed local oscillator (PLO). While no failures occurred and no modifications were made in the RF portion during this period, the digital portion was troubled by continuing tape reader problems. These problems were found to be caused by (1) improperly punched doppler tapes and (2) poor alignment of the tape as it passes through the tape reader due to a badly worn aperture plate. The tape reader has now been overhauled and operation is normal. The display lamp power supply has been repaired and re-installed in the PLO.

d. Central frequency synthesizer (CFS). The specific gravity adjustment of the rubidium frequency standard standby batteries has been completed, and the correct float voltage has been determined. The CFS now furnishes a coherent 1-MHz reference signal to the Mars Station. It is sent to Mars by means of the microwave link.

3. System Improvements

No major receive-system modifications were made during this period. Most of the work effort was directed toward the installation and checkout of the Mars Station *Mariner* receiver.

References

1. *SDS 925/930/9300 Computers Input–Output*, Scientific Data Systems, Santa Monica, California, January 1965.
2. Van Duzer, V. E., "A 0-50 Mc Frequency Synthesizer with Excellent Stability, Fast Switching, and Fine Resolution," *Hewlett-Packard Journal*, Vol. 15, No. 5, May 1964.
3. Siegman, A. E., *Microwave Solid-State Masers*, McGraw Hill Book Co., Inc., New York, 1964, pp. 326–331.
4. Higa, W. H., *Noise Performance of Traveling Wave Masers*, Technical Report No. 32-506, Jet Propulsion Laboratory, Pasadena, California, January 1964.

V. Communications Development Engineering

A. S-Band Implementation for the DSIF: Acquisition Aid for the Spacecraft Guidance and Command Station (DSIF 72)

D. Neff

An S-band acquisition aid (SAA) system (*SPS 37-36*, Vol. III, p. 22) for the 30-ft antenna system at the Spacecraft Guidance and Command Station (DSIF 72) has been designed, constructed, installed, and tested. Electrical performance is well within predicted limits. Several improvements in the mechanical design have been initiated to compensate for the environmental conditions at Ascension Island.

Mechanical installation was completed in November 1965; however, the February 1966 electrical checkout revealed that the subsystem coaxial transmission lines were in poor physical condition. Severe corrosion was evident at several of the coaxial connectors. Rust and electrolysis from dissimilar metals, caused by the rain, mist, and salt spray, made cleaning and replacement of the coaxial system mandatory. An example shown in Fig. 1 is a ⅞-in. coaxial cable to N connector. This connector was located in a bulkhead plate at the elevation axis cable wrap-up. The inside of the connector cavity was filled with salt water, and a bridge of material had been deposited between the inner and outer conductor. Vise grips were required to remove the connectors, resulting in destruction of the mating Type N connector. These were replaced and the new connection was coated with silicone grease. Many of the ½-in. receiver hard line cables mounted on the bulkhead plate also had water in the connectors.

The ⅞- coax, 1⅝-in. hard line, and waveguide joints had been protected with a silicone rubber compound; unfortunately, the material had been applied during wet weather and did not adhere to the damp surfaces, allowing moisture to seep in at the edges. The joints were cleaned and the silicone rubber was re-applied and covered with silicone grease.

Fig. 1. Corroded coaxial connector

The interior surfaces of the subsystem were well protected by the nitrogen pressure system. This system will be equipped with an alarm indicator, which is scheduled for installation and delivery in July 1966. It is expected that with this improvement, moisture damage to the microwave system caused by a radome failure or supply system pressure loss will be prevented.

Field work performed in February and March 1966 completed the necessary RF testing (boresighting, VSWR, insertion loss, noise temperature, and receiver/servo tests).

Boresighting (per test procedure DZQ-1158-TP) consisted of aligning the receiver error channels, positioning to the optical boresight, and adjusting the SAA to the RF null position in both axes. Final data are shown in Table 1.

Table 1. Collimation tower boresight coordinates

Boresight	Azimuth, deg	Elevation, deg
Optical	316.104	359.652
Radio frequency	316.076	359.672

Snap-on tests were made to verify operation of the SAA system. Azimuth locked on satisfactorily with up to a 9-deg offset. Elevation tests operated satisfactorily, but were more restricted because of the final limit switch position.

Reference channel (sum) gain was measured to the electronics room interface (ERI), with transmission line losses subtracted. Sum and error channel gain and pattern characteristics are included in Table 2.

Table 2. SAA antenna characteristics

Channel	Gain, db	Error channel null depths, db	Sum channel 3-db beamwidth, deg	Error channel peak separation, deg
Sum channel at 7/8 ERI	+17.93	—	16.5	—
Azimuth channel at Type N ERI	+15.6	−32	—	22.5
Elevation channel at Type N ERI	+15.7	−39	—	22.5

The VSWR and insertion loss data of the SAA (measured per test procedure DZQ-1149-TP) are shown in Table 3.

The SAA subsystem noise temperature measured by the receiver/paramp equipment at DSIF 72 varied from 80 to 118°K, depending on the particular setup used for the calibration. The SAA noise temperature measured at JPL (*SPS 37-36*, Vol. III, p. 27) was 62.2 ± 1.5°K at

Table 3. SAA system VSWR and transmission line losses

Parameter	VSWR			Transmission line losses to ERI, db
	2290 Mc	2295 Mc	2300 Mc	
Sum channel at ERI	1.34	1.09	1.32	−0.88
Sum channel at paramp No. 2 input	1.35	1.32	1.29	−1.56
Azimuth channel at receiver input	1.10	1.20	1.13	−1.28
Elevation channel at receiver input	1.30	1.36	1.20	−1.15
Collimation tower	1.12	1.09	1.06	−11.79

zenith. The predicted temperature, including the transmission line loss, is 131°K. A compromise value of 125 ± 15°K will be used for the sum channel noise temperature until the measurement problem is resolved at the site.

VSWR and insertion loss measurements were not made on the low power SAA transmitting horn at DSIF 72. The VSWR had been measured at the Pioneer Station (DSIF 11) through the S-band Cassegrain (monopulse) feedhorn and bridge system (SCM) transmit switch, and was less than 1.07 from 2100 to 2120 Mc. Because of the low values (−0.2 db) and test equipment stability problems, insertion loss measurements are impractical. Electrical characteristics of the transmitter horn (Fig. 2) are given in Table 4.

Table 4. Electrical characteristics of the low gain acquisition aid transmitter horn

Horn characteristics	Value
VSWR with any horn section 2115 ±5 Mc	1.07 ±0.5
Gain, db	
Section 1	16.0 ±0.4
Section 2	17.6 ±0.4
Section 3	19.2 ±0.4
Section 4	21.2 ±0.4
Beamwidth, deg	
Section 1	31
Section 2	24
Section 3	20
Section 4	15
Ellipticity, db	0.4 ±0.1

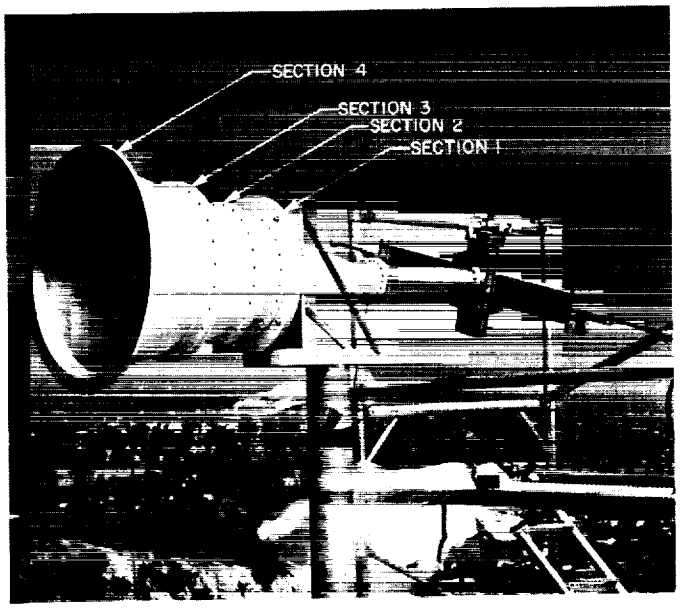

Fig. 2. Transmitter horn

Maintenance of antenna-mounted equipment at DSIF 72 will be a very high priority project. A complete supply of spares for the subsystem, including a second SAA tracking antenna, will be provided. A tar and felt-tape preparation has been found to protect the hard line and waveguide connectors; however, its use is limited to semi-permanent joints.

B. Evaluation of Microwave Link Between Venus and Mars Stations

R. B. Crow

A microwave link was established to furnish communications and data handling capability between the Mars Station and the other Goldstone tracking stations.

This link consists of two paths—Venus to Echo, and Echo to Mars—and was first used to furnish a coherent reference frequency between the Venus and Mars Stations for the *Mariner* occultation experiment. Before the Echo-to-Mars microwave link was completed, preliminary investigations were made on the existing Venus-to-Echo link. As originally installed, the Venus-to-Echo path suffered severe phase transients caused by automobile interference. This path was changed and the problem of traffic modulation was eliminated. However, tests indicate that a 1-Mc signal can have 0.1-deg peak-to-peak phase transients caused by wind modulation. Fig. 3 shows the test setup to measure both wind and traffic modulation.

The terminal microwave equipment used on the Venus-to-Echo path (P_0 = 100 mw, vacuum tube receiver) was investigated to determine methods of minimizing phase noise. The drive level into the transmitter modulator was found to be critical. Too much drive causes the reflex klystron to generate noise, and too little signal reduces the signal-to-noise ratio. Further, there is less noise when the relay point is connected so that the receiver drives the

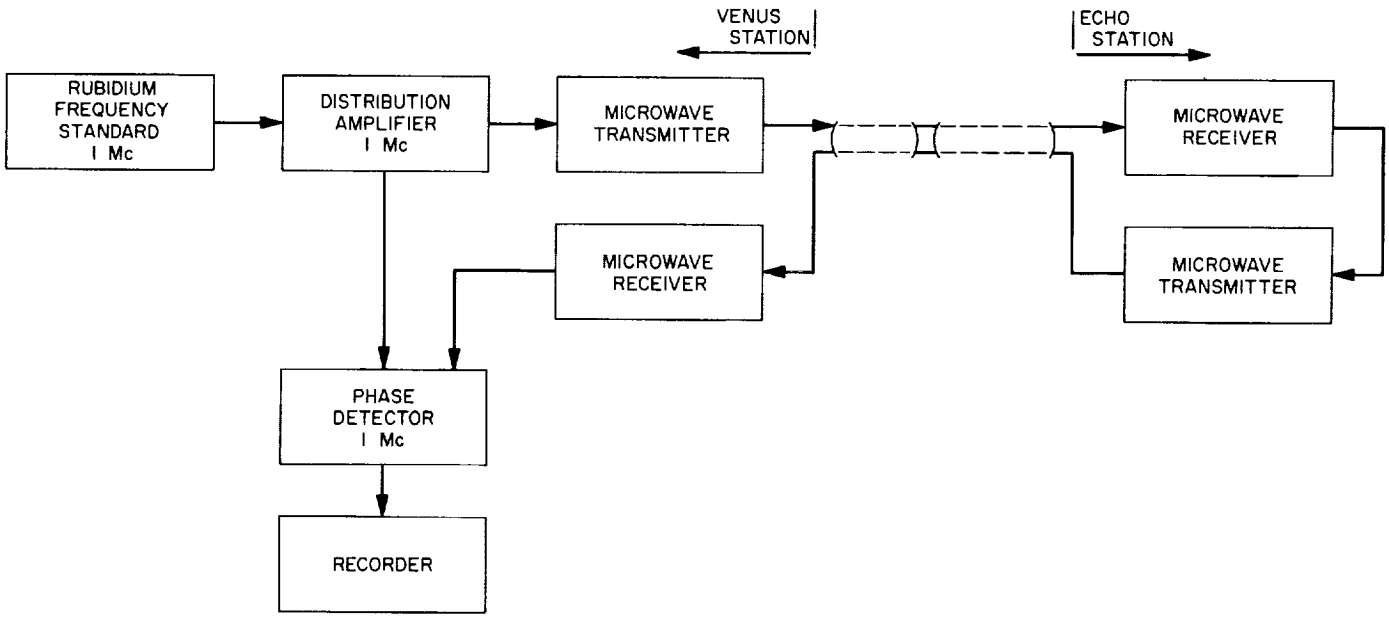

Fig. 3. Test setup to measure wind modulation

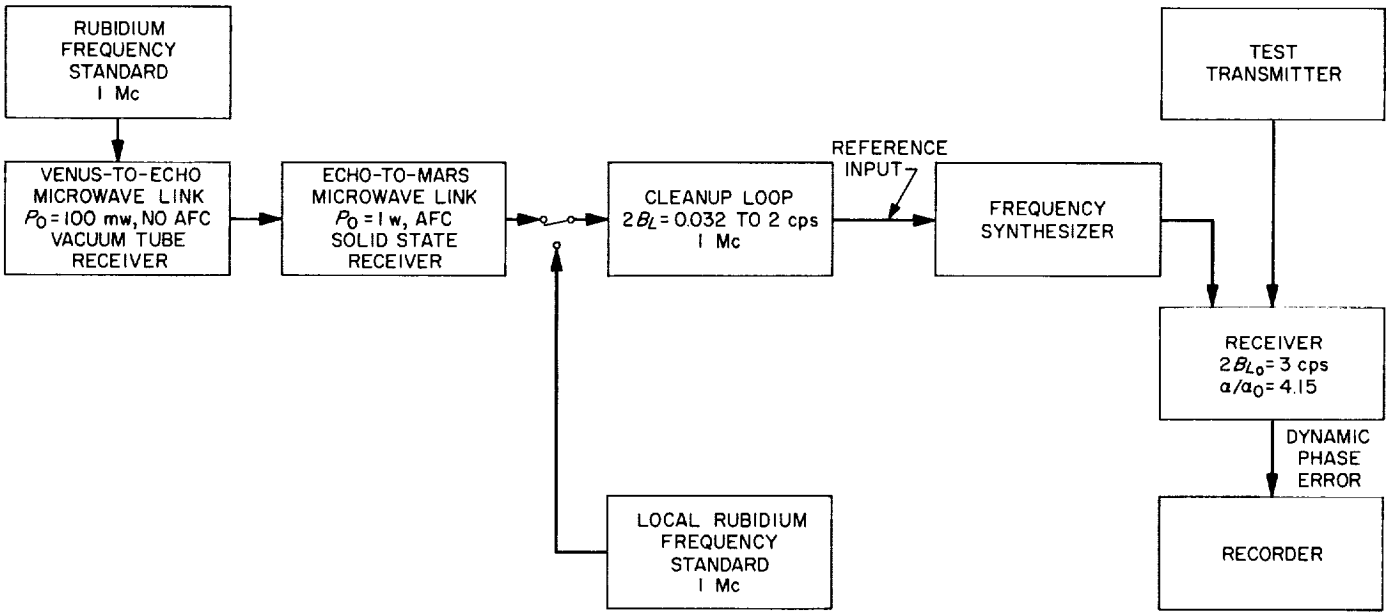

Fig. 4. Test setup to measure receiver jitter as a function of 1-Mc reference source

transmitter directly than when the de-emphasis and pre-emphasis circuits that are part of the microwave system are used.

The complete path was investigated and connected as shown in Fig. 4. The bandwidth of the 1-Mc cleanup loop was optimized by observing the dynamic phase error (DPE) of the receiver (when the receiver was locked to a local test transmitter). The results of this test (Fig. 5) indicate that a $2B_L$ of 0.25 cps or less will allow the Venus 1-Mc rubidium frequency standard to be used with no degradation to the Mars receive system. The 1-Mc cleanup loop is presently operating with a design $2B_L$ of 0.032 cps.

The 100-mw equipment used in the present microwave link between Venus and Echo has no automatic frequency

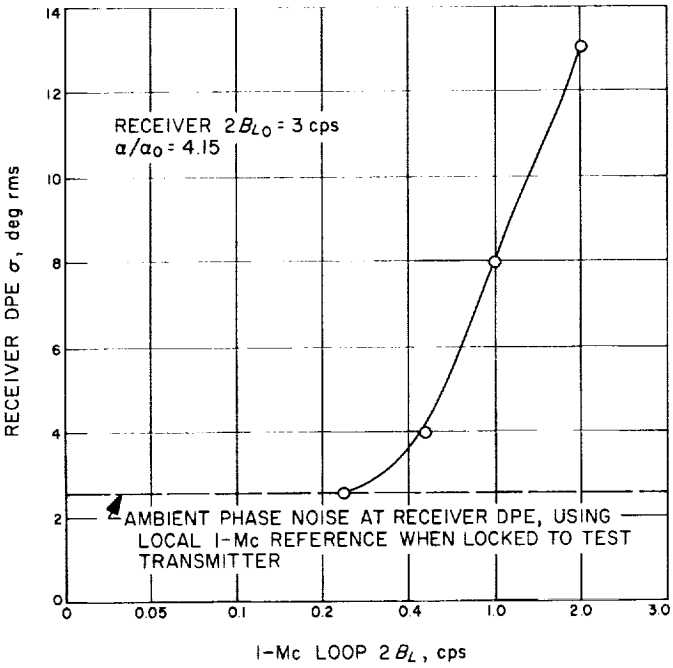

Fig. 5. Jitter on dynamic phase error of receiver as a function of 1-Mc clean-up loop bandwidth

control (AFC) on the transmitter. The resultant circuit outages have created a reliability problem. This problem has apparently been eliminated in the new, solid state, 1-w equipment used between Echo and Mars. Added flexibility is available in the new equipment since it has a 6½-Mc bandwidth, in contrast to the 4½-Mc bandwidth of the 100-mw system.

C. Ascension Island Microwave Installation

R. W. Hartop

Installation and check-out of the complete microwave system for the 30-ft antenna at Ascension Island has been completed. The S-band Cassegrain monopulse (SCM-30) cone assembly (shown in Fig. 6 on a pallet at the manufacturer's facility) is a major component of the microwave system. This cone assembly is 86 in. high, has a base diameter of 50 in., and weighs 820 lb. The acquisition aid subsystem for the DSIF 72 antenna has been reported separately (*SPS 37-36*, Vol. III, p. 22).

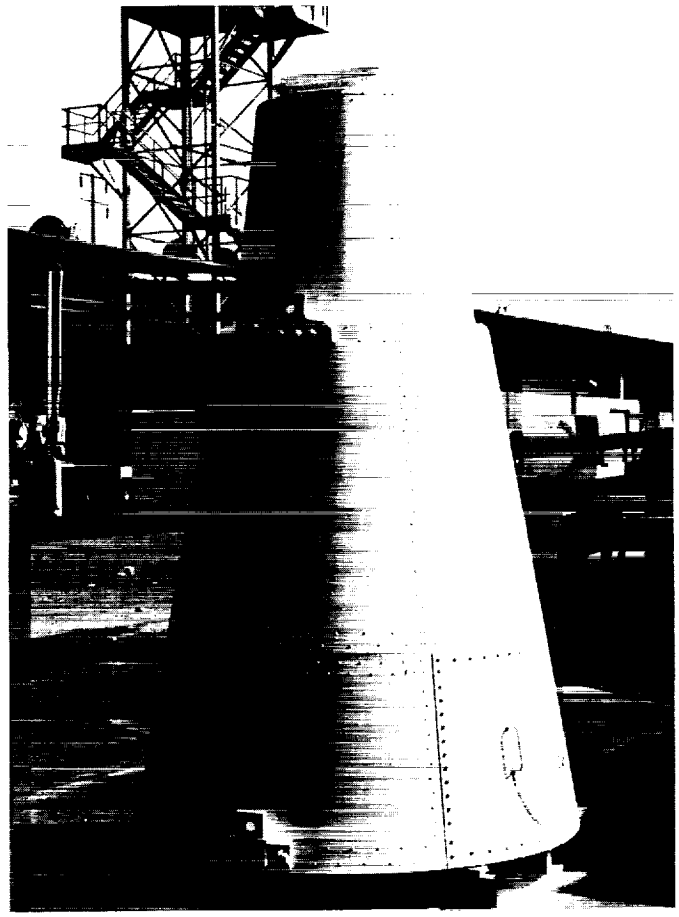

Fig. 6. SCM-30 cone assembly

Although much of the S-band equipment for the 30-ft antenna project is identical to that of a Goldstone duplicate standard (GSDS) 85-ft installation, the microwave equipment differs necessarily. In addition to a completely new tracking cone assembly, the antenna-mounted microwave equipment required a completely new layout with carefully designed waveguide runs and supporting bracketry. Only certain microwave components such as the waveguide switches, diplexer, and waveguide filters are unmodified GSDS units.

The SCM-30 cone assembly was constructed by Hughes Aircraft Co., Fullerton, according to JPL specifications.[1] The tracking feed within the cone (Fig. 7) is based upon the SCM feed for the 85-ft antenna. The dual bridge circuitry is essentially identical, but changes were made in the multimode portions of the feed to conform to the

[1]This included specifications for the base diameter of the cone and control of the Cassegrain system optics.

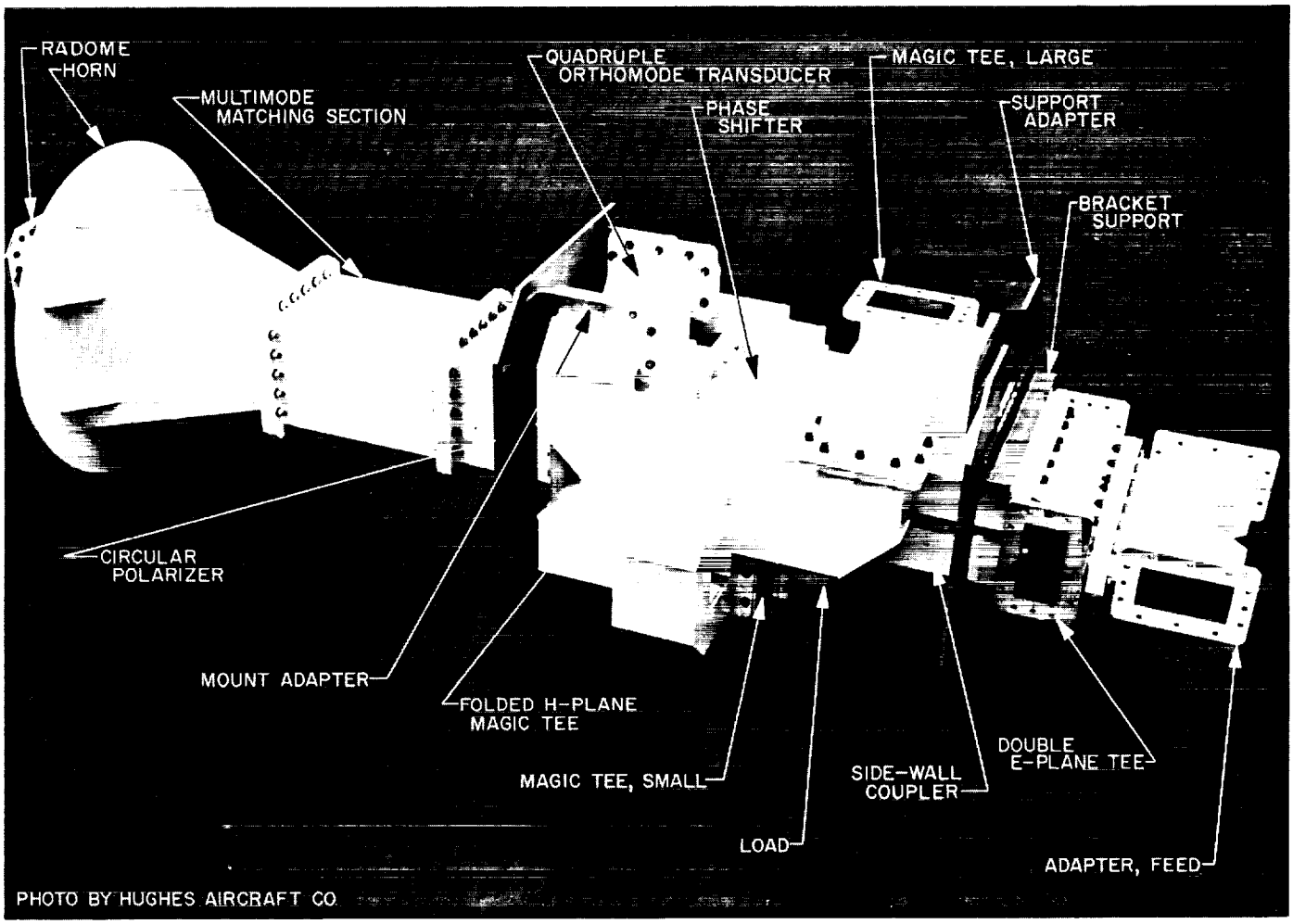

Fig. 7. SCM-30 feed assembly

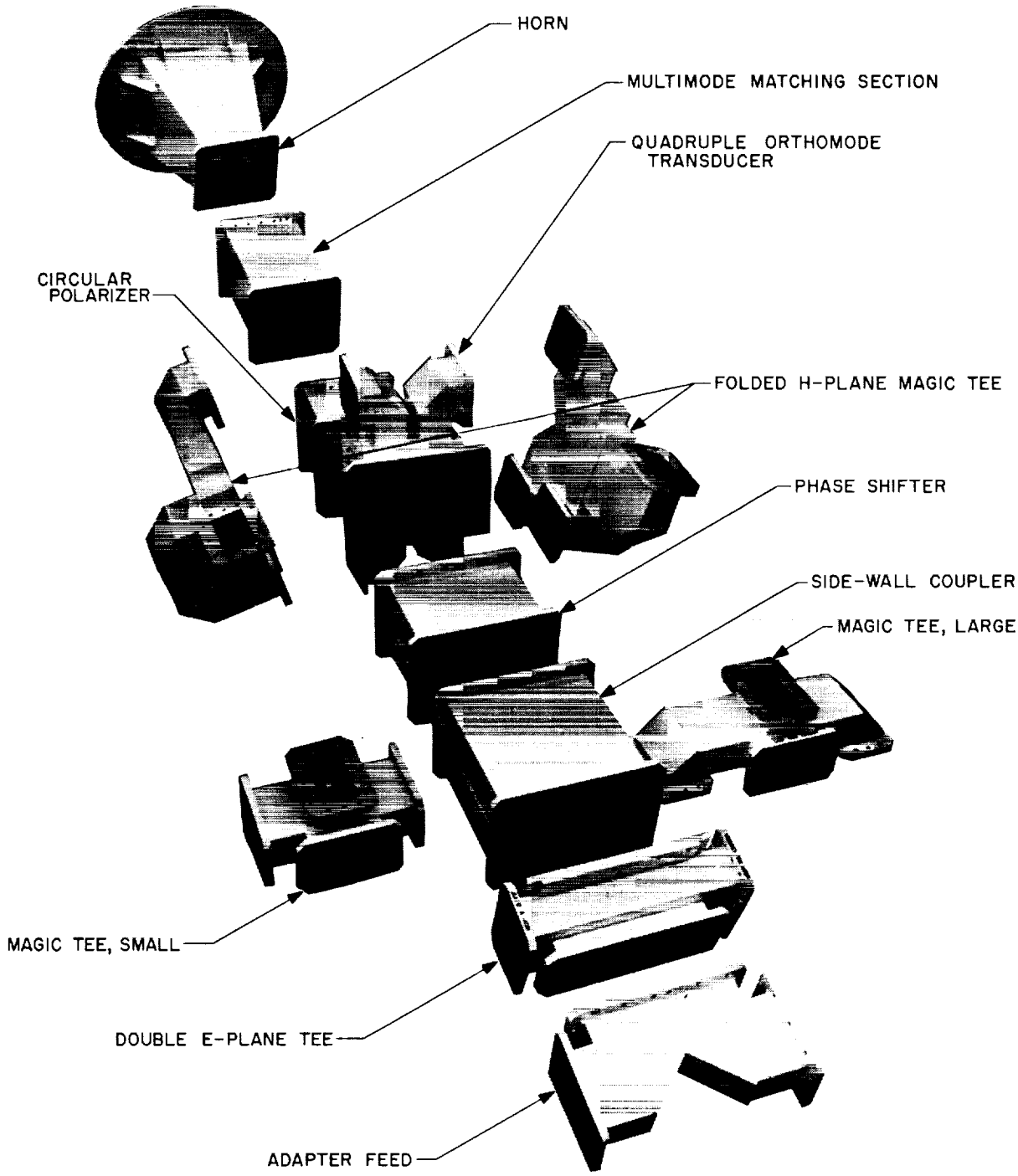

PHOTO BY HUGHES AIRCRAFT CO.

Fig. 8. SCM-30 feed, exploded view

30-ft antenna requirements, and the horn is much smaller. Fig. 8 is an exploded view of the feed.

Upon completion of the elevation equipment room layout and detail drawings, all necessary microwave components and mounting hardware were procured and test-fitted on the 30-ft antenna mock-up at the Pioneer Station, Goldstone. The Serial No. 1 SCM-30 cone assembly (a spare cone assembly has since been delivered) was mounted on the mock-up and integrated with the elevation room installation. Following minor modifications to several of the mounting brackets, the design was shown to be satisfactory. Before disassembling the equipment for shipment to Ascension Island, VSWR measurements were made on all waveguide runs over the operating frequency bands. No tuning was necessary.

The microwave installation was completed at Ascension Island in less than two weeks, and an additional two weeks (approximate) were spent in thoroughly testing the subsystem. Table 5 presents some of the measured data. The antenna gains were measured by the net path loss method, using a gain-calibrated GSDS S-band test antenna (STA) on the 100-ft collimation tower which is approximately 4208 ft from the 30-ft antenna. Without a maser, it was considered impractical to attempt gain measurements by radio sources with such a small antenna. Fortunately, the collimation tower at Ascension Island is located across a deep ravine, providing a relatively reflection-free environment; unlike the 85-ft antenna ranges, the collimation tower is very nearly in the far field of the 30-ft antenna.

Table 5. Measured data on DSIF 72 antenna

Parameter	Frequency, MHz	
	2295	2110
Antenna gain (including waveguide component insertion losses), db	42.5 ±0.5	42.0 ±0.5
Ellipticity, db	0.5 ±0.2	0.8 ±0.2
Beamwidth, half-power, deg	0.98 ±0.02	1.04 ±0.02
Highest sidelobe level, db	−16	−14
Error channel peak level, relative to sum peak, db	−4.7 ±0.3	—
Error channel peak separation, deg	1.35 ±0.03	—
Error channel ellipticity, db	1.0 ±0.3	—
Error channel minimum null depth, db	−26	—
Null plane orthogonality, deg	90 ±2	—
Null plane rotation, deg	+6	—

Following completion of the microwave tests, the proper operation of the microwave subsystem, in conjunction with the receiver, transmitter, and servo subsystems, was verified. The antenna system was diplexed at 10-kw CW without degradation to the paramp-receiver subsystem performance. Collimation tower snap-ons were completed, and later autotracking of an instrumented airplane verified the overall system performance.

VI. Tracking Stations Engineering and Operations

A. Flight Project Support

J. Orbison

1. Mariner IV Mission

On March 17, 1966, the Mars Station 210-ft antenna successfully acquired and tracked both the *Pioneer VI* and the *Mariner IV* spacecraft. An R&D receiver was mounted in the antenna alidade control room (Fig. 1), and a radiometric Cassegrain cone was mounted on a special adapter to mate it with the lower half of the 210-ft antenna cone. Tracking of the *Mariner IV* spacecraft continued until April 12. The Venus Station provided the transmitter and command capability, and via the intersite microwave link, processed and recorded the received signal from Mars Station. Since the termination of the *Mariner IV* daily tracking on October 1, 1965, the Venus Station has continued to track the spacecraft on the first of each month.

2. Pioneer VI Project

Tracking of the *Pioneer VI* spacecraft has continued on a 3- to 5-day week since Pass 30 on January 15, 1966. Operation has been nominally routine, with all subsystems functioning well. The nature of the *Pioneer VI* mission has allowed for comprehensive training in systems operation for new personnel.

Special tests were performed during the *Pioneer VI* tracking periods to determine equipment operation, using the spacecraft carrier signal as a reference. Typical tests performed were:

(1) Doppler resolver tests with the tracking data handling (TDH) subsystem

(2) Channels 6 and 7 offsets and phase jitter with the receiver subsystem

(3) Spacecraft AGC curve fit using the digital instrumentation subsystem (DIS)

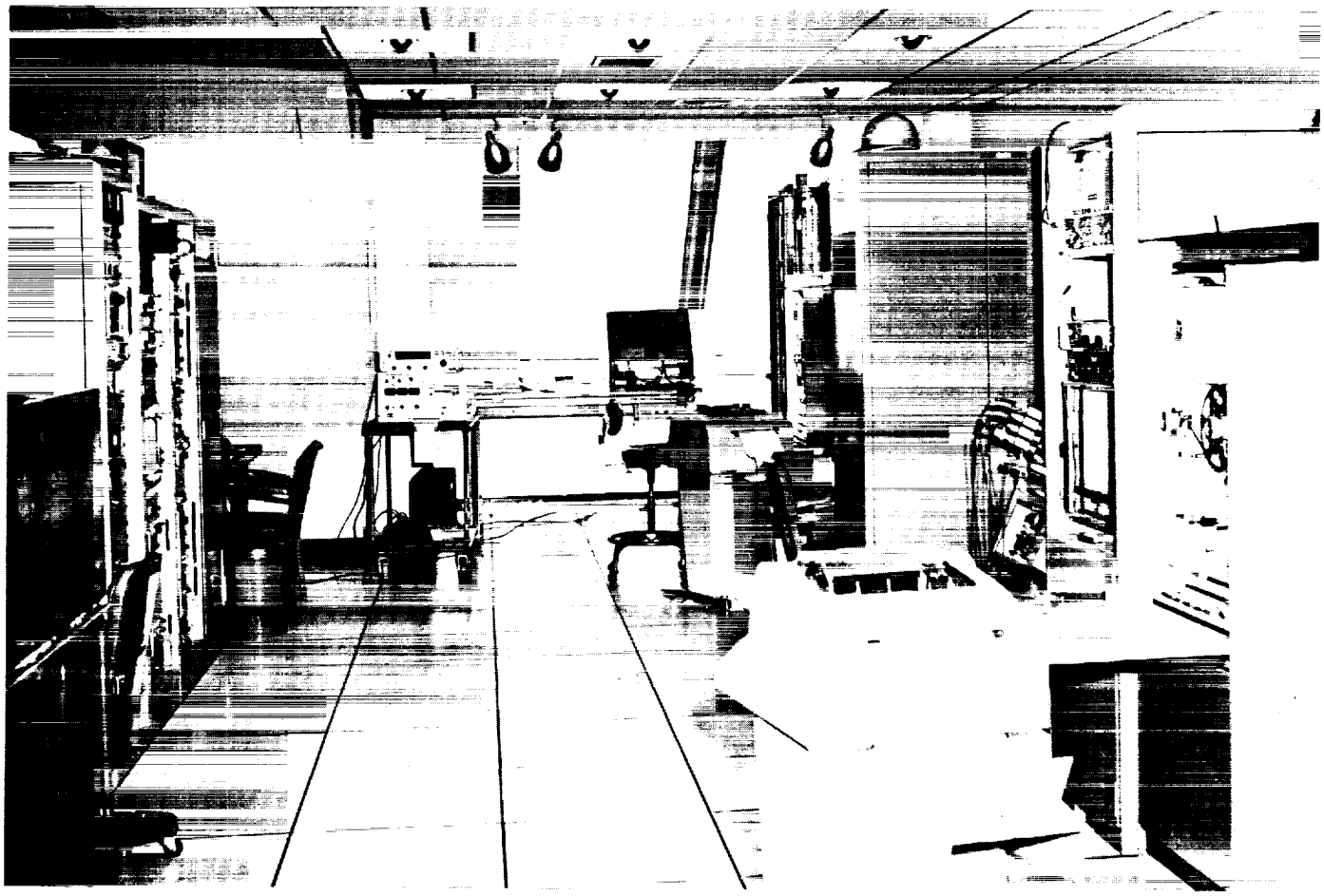

Fig. 1. R&D receiver in alidade control room

Pioneer VI was tracked by the Pioneer Station a total of 32 hr, on March 2 and 9, as scheduled.

3. Surveyor Project

Preparation for the *Surveyor* mission continued to be the prime activity for the Pioneer Station. On March 21, the *Surveyor* T-21 test model spacecraft was returned to Goldstone and installed in the Spacecraft Test Facility (p. 117). Although the test model was intended primarily for training of new personnel at the Pioneer Station and the Space Flight Operations Facility (SFOF), it is also being used for system testing of the *Surveyor* ground operational equipment and the S-band system. The latter testing is a result of the move of the S-band system from its former location into the east wing of the Pioneer Station control room (*SPS 37-37*, Vol. III, p. 55; *SPS 37-38*, Vol. III, p. 84).

Concurrent with the *Surveyor* testing, the Pioneer Station participated in the *Atlas–Centaur 8* Project. The resulting Earth orbit of the vehicle was tracked for two passes. First acquisition was at 02:29:00 GMT, until loss of signal at 02:34:15 GMT; second acquisition was at 04:01:27 GMT, until loss of signal at 04:08:00 GMT. Both a post-calibration and pre-calibration were performed on the system between the two passes.

4. Lunar Orbiter Project

The *Lunar Orbiter* testing has been performed concurrently with the tracking of *Pioneer VI*. In the interim period following the post-calibrations and prior to tracking countdown, *Lunar Orbiter* personnel, assisted by Echo Station personnel, have conducted subsystem tests. These included the ranging subsystem jitter, threshold, and interface tests, as well as NASCOM high-speed data line operations, operational procedures, and engineering evaluation. During this time, SFOF and Echo Station personnel training programs were conducted and practice countdowns were performed.

B. Facility Construction and Equipment Installation

J. Orbison and C. Chatburn

1. Mars Station, J. Orbison

Mars Station dedication ceremonies were held on April 29, 1966. The inherent capability of this facility to receive and track a spacecraft had been demonstrated earlier in the solar occultation experiment of March 1966.

Installation of the DSIF S-band system in the control room on the second floor of the pedestal (Fig. 2) is progressing, with approximately 75% of the system on hand. The servo electronics subsystem was the first operational subsystem to be installed, and allowed antenna-driving during the final phases of assembly. The second subsystem to be installed was the digital instrumentation subsystem (DIS), followed by the tracking data handling (TDH) and the frequency and timing subsystems. During the solar occultation experiment tracking, the antenna-drive coordinates were produced by the DIS which also drove the antenna. The S-band receiver has been installed and preliminary operational testing is in progress.

With the dismantling of the 315-ft tower crane in mid-March, heavy construction at the site was completed. The access road to the station has been extended and now terminates in an asphalt-paved circle extending 50 ft outward from the pedestal base. A fence, 9½ ft out from the base, provides an unobstructed area for movement of the alidade stairwell as the antenna rotates in azimuth.

2. Echo Station, J. Orbison

Installation of two microwave systems is in process. One, the new microwave telephone system (*SPS* 37-38, Vol. III, p. 84) for Goldstone, is scheduled for completion in early fall. The other, the microwave system for relay of tracking data between the Mars and Echo Stations, is currently in the final operational testing stages. The latter provides a system of five channels with 6-Mc bandwidth; each channel can further be divided into 12 channels of multiplex operation. The link is operated using passive dish and billboard antennas to cover the approximate 10-mi distance between the two stations.

An hour angle low-speed electric drive has been installed on the Echo Station 85-ft antenna (Fig. 3).

3. Pioneer Station, J. Orbison

Modification of the generator building is progressing. All remnants of the former steel structure have been removed. Two concrete pads have been completed: one,

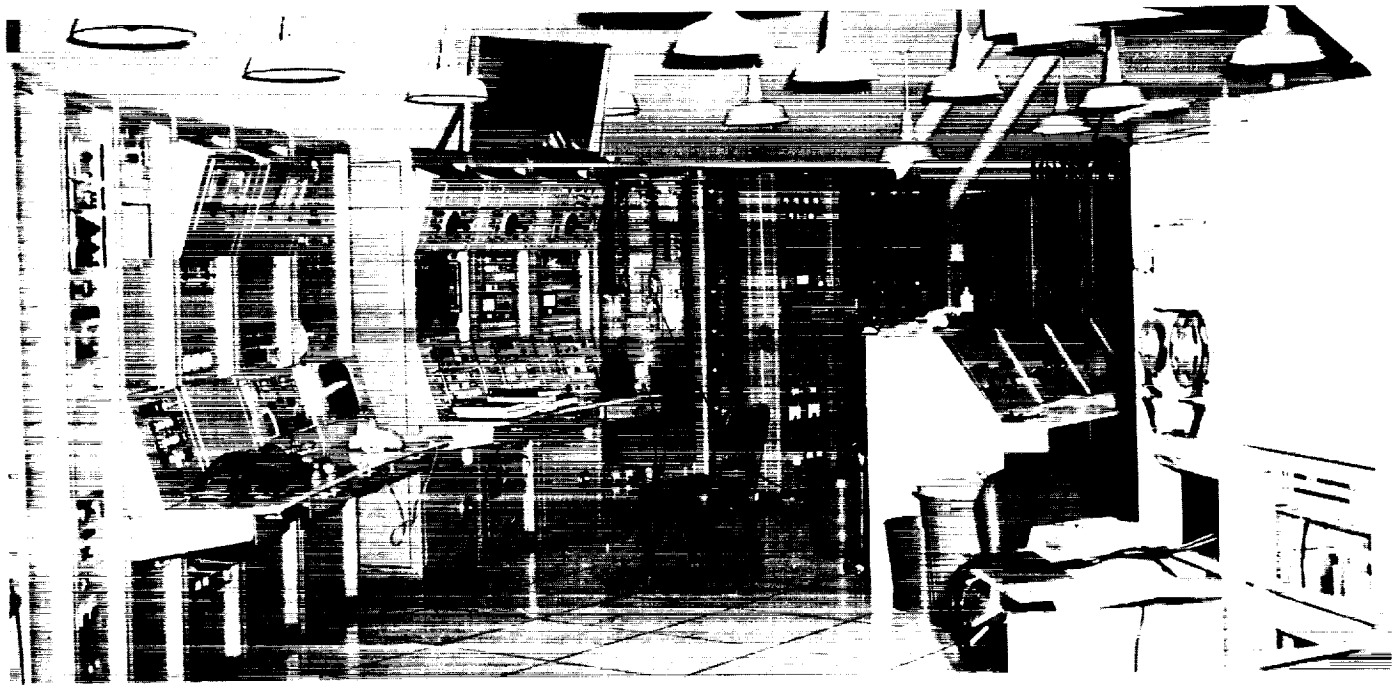

Fig. 2. S-band system control room

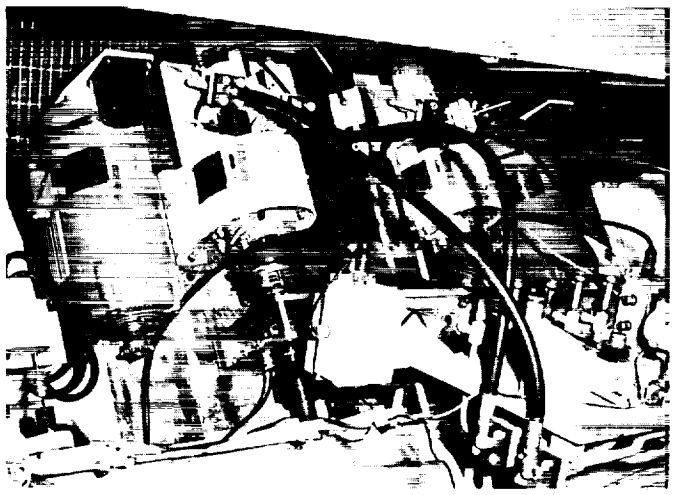

Fig. 3. HA low-speed electric drive installation

a 22 × 36 ft base, was placed inside the building to support the four diesel generator units; the second, a 9 × 42 ft base, was placed outside the building to support the generator radiators and the starting batteries.

a. Cebreros Station. Disassembly and preparation for packing of the Cebreros Station (DSIF 62) S-band system began April 18, with shipment to Madrid, Spain, scheduled for early May.

b. Deep Space Instrumentation Facility Training Center. A formal, 16-week training program for selected personnel from DSIF stations was instituted at the Pioneer Station on January 30, 1966. The operation and maintenance of area working standards is currently being taught to nine students by one instructor; however, two more teachers will soon join the staff. A typical student work area is shown in Fig. 4.

4. Goldstone Spacecraft Test Facility,

J. Orbison and C. Chatburn

Preparation for the *Ranger* Block III missions included compatibility testing at simulated lunar distances between DSIF 12 (Echo Station) and the PTM spacecraft. To house the spacecraft and to allow lunar distance simulation, a 12 × 12 × 18 ft shield room (Fig. 5) was installed in September 1963 near the base of the DSIF 12 collimation tower, approximately 1 mi east of the 85-ft antenna. A *Ranger* PTM was installed and connected to the existing collimation tower antenna. Tests were performed simulating cruise mode, midcourse maneuver

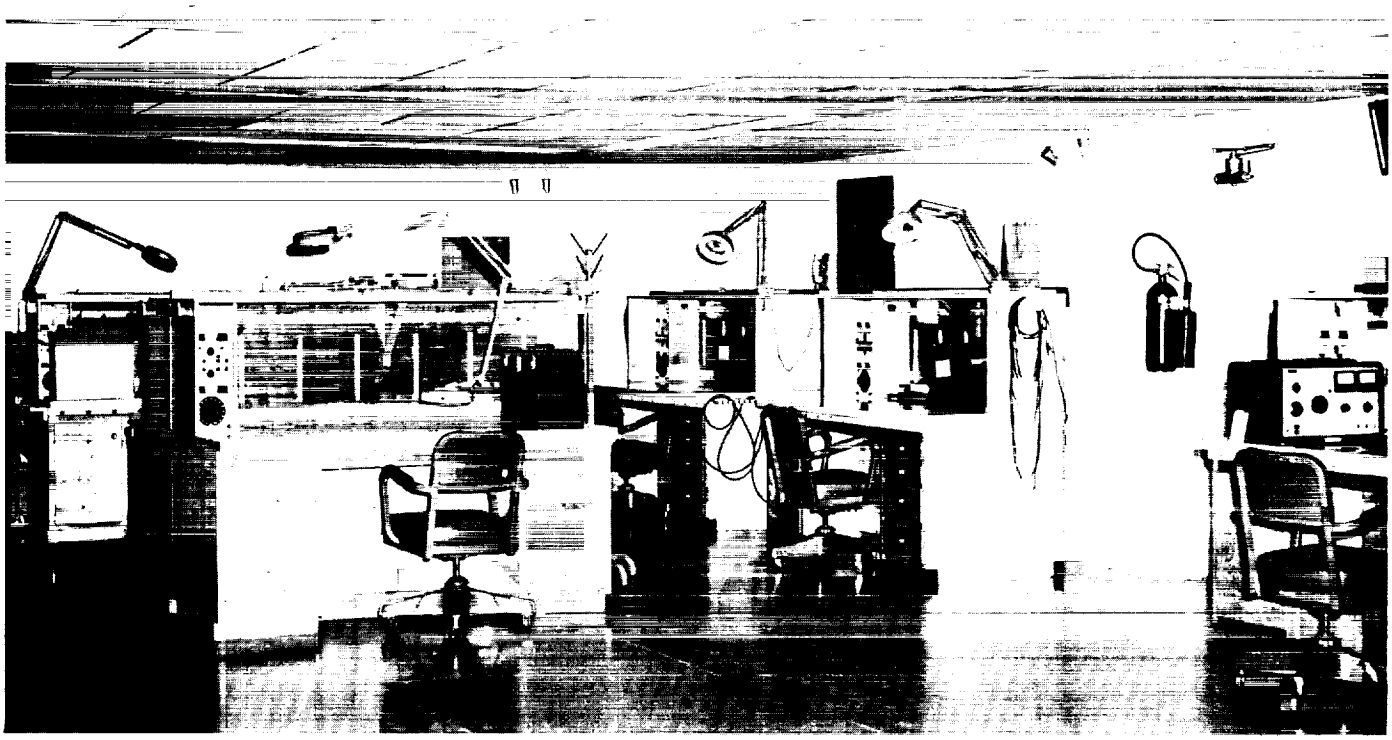

Fig. 4. DSIF training center student work area at Pioneer Station

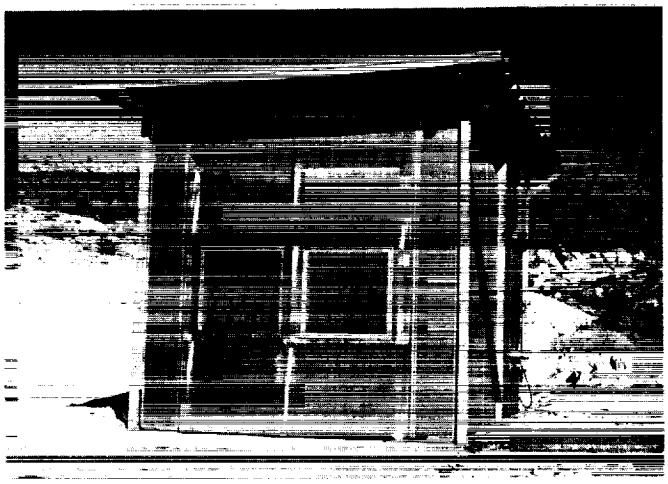

Fig. 5. Original shield room installation near DSIF 12

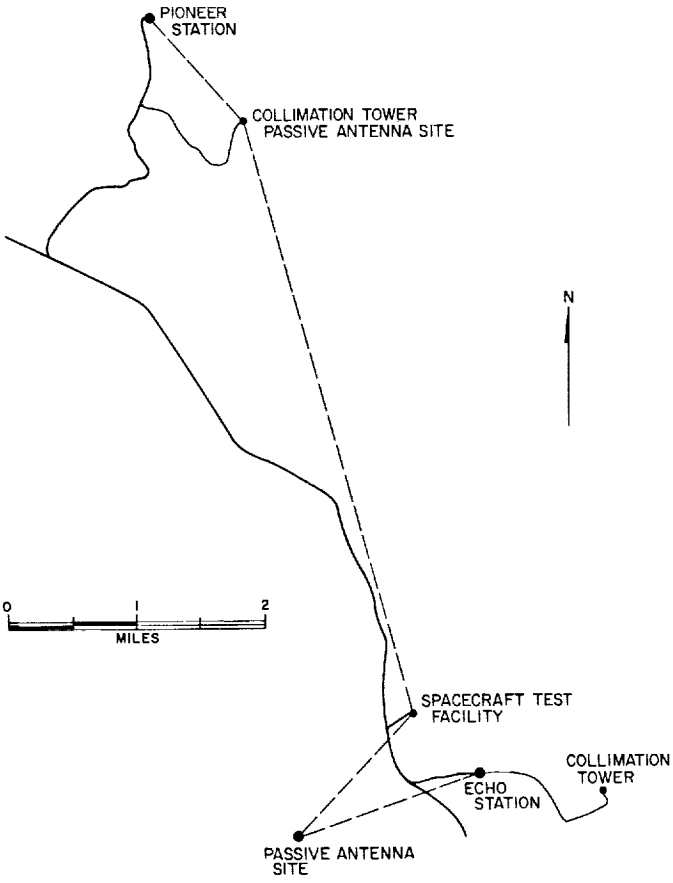

Fig. 6. Goldstone Spacecraft Test Facility location

command sequences, and pre-impact photography in both normal and emergency operation.

In May 1964, the shield room was moved to a site approximately 200 ft northwest of the Microwave Test Facility (Fig. 6), which provided easier access and made possible a passive RF link to both DSIF 11 (Pioneer) and DSIF 12 (Echo).

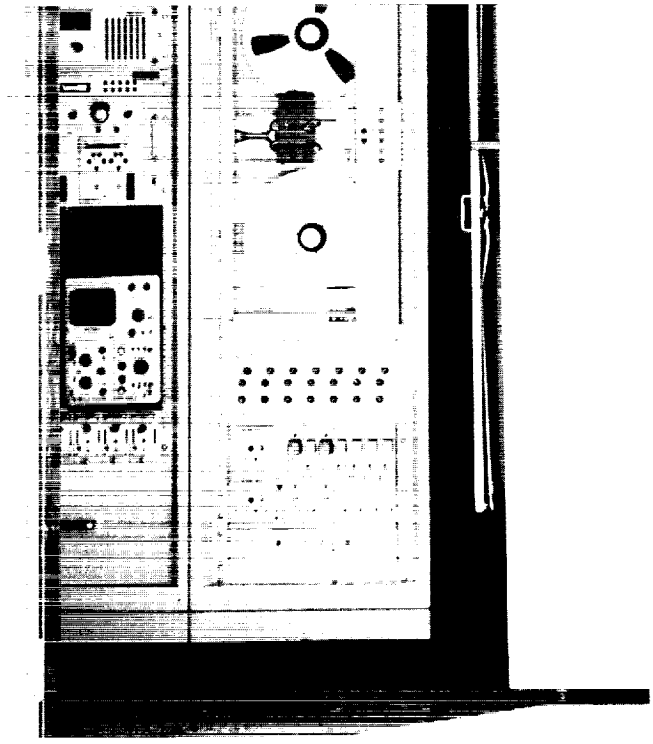

Fig. 7. *Mariner* transponder installation at Spacecraft Test Facility

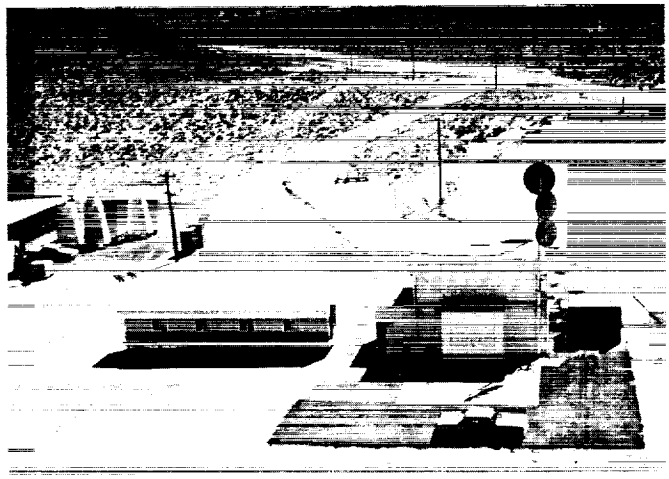

Fig. 8. Aerial view of Spacecraft Test Facility

In June 1964, a *Mariner IV* transponder along with associated support equipment was installed in the shield room. An RF link to the Pioneer Station was established via back-to-back antennas mounted on the Pioneer collimation tower and an antenna mounted next to the shield room. A series of tests was performed for acquisition, two-way lock, telemetry data transmission, and receipt of and simulated action to command signals from DSIF 11.

Because of the extremely crowded conditions created by the support equipment used in *Mariner* testing (Fig. 7), the shield room was enlarged (Fig. 8) to its present dimensions (28 × 28 × 20 ft) in June 1965.

Three spacecraft tests have been performed in the enlarged test facility. The first, in August 1965, involved the *Surveyor* T-21 (Fig. 9). Training and tests included simulated flight, landing and post-landing operations, and full exercise of command transmissions and telemetry processing. The second test, with the *Lunar Orbiter* Test Model C (Fig. 10), was begun in December 1965. Two-way operation was performed at both near-Earth and simulated lunar distances. Flight components associated with the ground command reconstruction equipment were used. All three modes covering telemetry and video transmission from the spacecraft were tested with the facilities of the SFOF, DSIF 12, and the *Lunar Orbiter*. The spacecraft picture-scanning equipment was tested

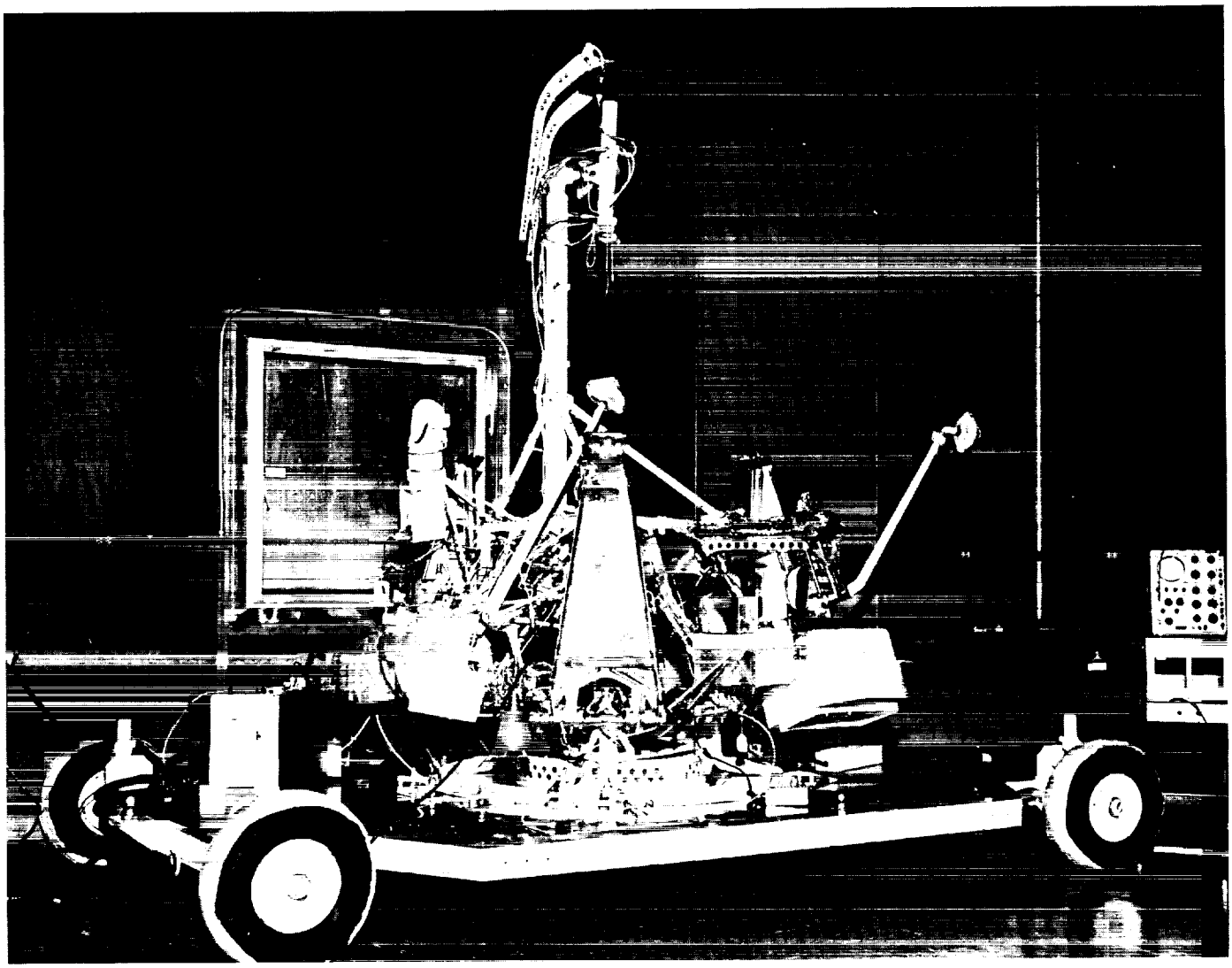

Fig. 9. *Surveyor* T-21 spacecraft installation in Spacecraft Test Facility

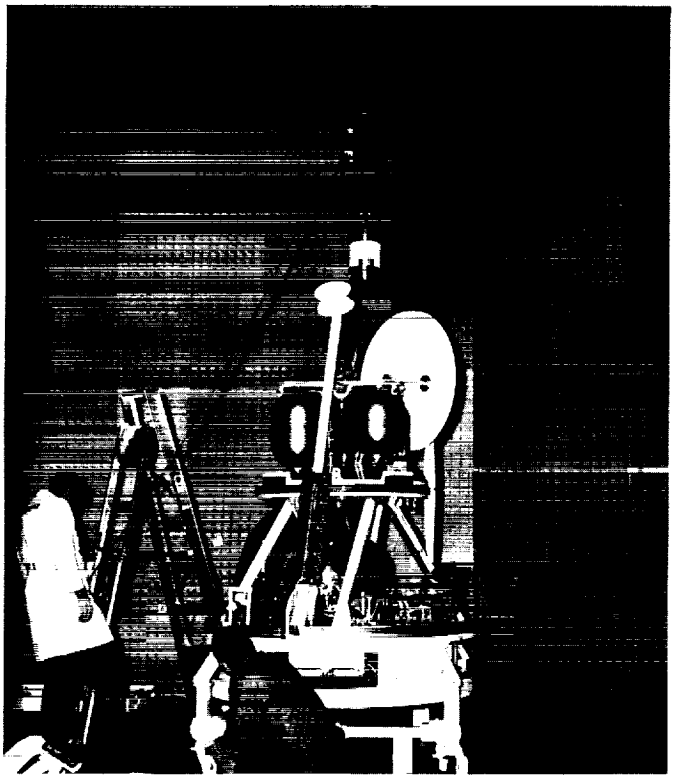

Fig. 10. *Lunar Orbiter* installation in Spacecraft Test Facility

using a pre-exposed film of a lunar landscape model (made from *Ranger IX* pictures) which was transmitted to the Echo Station for recovery and processing. These tests were completed in February 1966.

The third spacecraft test, currently in progress, involves *Surveyor* T-21 use for DSIF training exercises.

The shield room is constructed of ¾-in. marine-plywood modular panels, bonded with galvanized steel sheeting. The individual panels are clamped together to form a tight electrical seal, and all exterior seams are sealed with waterproof tape. The interior is unobstructed, permitting handling of spacecraft with solar panel extension diameters of 25 ft, and heights up to approximately 18 ft. A 4-in. double-capped opening in the ceiling permits a cable drop for lifting and handling of heavy subassemblies.

The front wall is protected by an exterior enclosure with 10 × 12 ft double doors, opening onto a 30 × 30 ft concrete pad. A 10 × 12 ft entrance room on the right wall protects a 30 in. × 7 ft personnel access door, and provides storage space for necessary test equipment. A sloping sunroof protects the flat ceiling, and is accessible by a permanently installed ladder. On both sides and in front of the building, 20-ft wide asphalt-paved areas are provided.

The building is equipped with a 5-ton air-conditioning unit with 5-ton backup capability. All air ducts are located on the left wall outside the building. Heating is supplied by 3000-w strip heaters, with 3000-w backup, within the units.

In June 1965, test performance revealed a nominal 110-db attenuation at currently used S-band frequencies. In November 1965, the room interior was covered with an RF anechoic material that attenuates wall reflection by 40 db.

All power, communications, and signal lines entering the building are shielded and filtered to maintain attenuation integrity of 110 db or better. Primary power available is 37.5 kva, three phase, at 480/208/120 v. Four filtered lead-through lines provide external/internal connections for special power and control circuits, as needed. Six unfiltered, shielded, coaxial lead-throughs provide coupling from the spacecraft electronics to the roof-mounted antennas.

Two 4-in.-diameter steel masts corner-mounted on the roof are able to support 8-ft-diameter dish-type reflectors which can be readily directed toward either of the two current passive antenna sites.